PNS PREDICTIONS OF EXTERNAL/INTERNAL HYPERSONIC FLOWS FOR NASP PROPULSION APPLICATIONS

BILAL A. BHUTTA and CLARK H. LEWIS

VRA, Inc.

Post Office Box 50

Blacksburg, Va 24063

Phase II Final Report for Period

May 1988 to May 1990

SBIR 1986 Phase II

June 1990

PROJECT SUMMARY

The 1986 State-of-Union address by President Reagan clearly stated the need for a new "Orient Express" (hypersonic transport), and laid the foundation for a National Aero-Space Plane (NASP) technology development program. Due to a lack of flight data and limited experimental capabilities, the development of NASP propulsion technology (as well as the airframe design) program, in its first three phases, has to heavily rely upon the CFD support provided. Thus, a keen need exists for developing accurate, reliable and computationally efficient numerical schemes for predicting large angle-of-attack, supersonic/hypersonic external flows over realistic (3-D) NASP configurations. In this SBIR Phase II study a new three-dimensional fully iterative PNS scheme has been developed to study hypersonic external flows over 3-D lifting configurations. In addition, it has been demonstrated that this baseline PNS scheme can also be extended to predict 2-D/axisymmetric supersonic/hypersonic internal flows. This work was done by VRA, Inc., for the NASA Lewis Research Center under contract number NAS3-25450. Dr. Clark H. Lewis was the principal investigator for this work, and Mr. Tom Benson of NASA Lewis Research Center served as the contract monitor.

The three-dimensional PNS scheme developed under this SBIR Phase II effort is inherently stable in the subsonic as well as the supersonic flow regions and, thus, does not require any sublayer approximation. Furthermore, it has the capability of treating perfect-gas, equilibrium-air and nonequilibrium-air gas models in a unified manner. A fourth-order crossflow and a second-order streamwise smoothing approach are used to damp the solution oscillations. In addition, a pseudo-unsteady approach is used to dramatically improve the solution efficiency without compromising the solution accuracy. The scheme is formulated in terms of a general curvilinear coordinate system, and is capable of treating cylindrical, parabolic, body-normal, a modified body-normal and elliptic grid-generation algorithms for highly nonaxisymmetric configurations. A new fully implicit and crossflow-coupled shock-fitting approach has also been developed. With this solution approach the shock is fully coupled in the crossflow direction, while within the shock-layer the solution is obtained using a new predictor-corrector solution scheme which can treat strong crossflow solution-coupling effects. The resulting overall computing times are of the order of the noniterative PNS schemes using Approximate Factorization, because apart from being numerically efficient the present solution scheme allows much larger marching steps to be taken. In addition to these mathematical and numerical developments, significant effort was also spent in developing a vectorization strategy for this 3-D PNS scheme. Furthermore, in this SBIR Phase II study, it has also been shown that this baseline PNS scheme for external flows can be extended to study 2-D/axisymmetric supersonic/hypersonic internal flows.

Six cases were considered to test this new PNS scheme for external and internal hypersonic flows. The first three test cases were for the 5-deg angle-of-attack flow over a 3-D lifting configuration at Mach 20 and 125 kft altitude. Perfect-gas, equilibrium-air and nonequilibrium-air gas models were used to study these cases, and it was observed that the type of gas model used had a significant influence on the flowfield predictions. The next three test cases considered 2-D supersonic/hypersonic internal flows through different channel configurations. In each of these internal flow cases, comparisons were also made with the predictions obtained using classical 2-D inviscid theory, and the agreement between inviscid and viscous predictions was found to be excellent. In general, the results of these numerical tests were very encouraging and substantiated the accuracy, efficiency and stability claims of the PNS scheme developed under this Phase II effort.

TABLE OF CONTENTS

LIST OF ILLUSTRATIONS

LIST OF TABLES

NOMENCLATURE

CA	=	axial-force coefficient
CFS	=	streamwise skin friction coefficient
CI,C_i	=	mass fraction of i-th species
C_p	=	specific heat at constant pressure
D_{ij}	=	diffusion coefficient for the i-th species with respect to the j-th species
DSHK	=	linear distance from the body to the corresponding shock-point location
h	=	static enthalpy of the mixture
h_i	=	static enthalpy of the i-th species
J	=	determinant of the transformation Jacobian
$(J_i)_j$	=	x, y and z component of the mass-flux vector of the i-th species for j = 1, 2 and 3, $(Le\frac{\bar{\mu}}{Pr})(C_i)_{x_j}$
k	=	thermal conductivity; fraction of the gird points put in the variably-spaced potion of the grid in the ξ_2 direction
KMAX	=	number of grid points in the ξ_3 direction
Le	=	Lewis number, $\rho^*\bar{C_p}^*D_{ij}^*/\bar{k}^*$
LMAX	=	number of grid points in the ξ_2 direction
M	=	Mach number
m	=	molecular weight
m_{njk}	=	$\xi_{n,j}\xi_{n,k}$, where n = 2 or 3
n	=	iteration number
NS	=	total number of chemical species
P,p	=	static pressure
PA	=	pressure along 2-D/axisymmetric channel axis
PHI	=	circumferential angle, ϕ
Pr	=	Prandtl number
PW	=	wall pressure
PINF	=	freestream static pressure, p_∞
QW	=	total wall heat-transfer rate in Btu/ft ^{2}/sec
r	=	axis-normal distance measured from the channel axis for 2-D/axisymmetric internal flows
R	=	half-channel width for 2-D/axisymmetric internal flows
Re	=	Reynolds number, $(\rho^*V^*Rn^*)/\mu^*$
RHO	=	static density

RHOINF	=	freestream static density, ρ_∞
RN,Rn	=	nose radius
T	=	static temperature
TINF	=	freestream static temperature, T_∞
u	=	x-component of mass-averaged velocity
u_j	=	u, v and w for j = 1,2 and 3
U_j	=	contravariant velocities, $u_k \xi_{j,x_k}$
V	=	total mass-averaged velocity
v	=	y-component of mass-averaged velocity
w	=	z-component of mass-averaged velocity
X,x	=	coordinate along body axis
x_j	=	x, y and z for j = 1, 2 and 3
Y	=	y coordinate
Z	=	z coordinate
α	=	angle of attack
ε	=	M_∞ / Re_∞
ε_1	=	εLe
η	=	normalized coordinate along the ξ_2 direction such that $\eta = 0$ at the wall and $\eta = 1$ at the shock
$\Delta\eta_1$	=	$\Delta\eta$ value at the wall, which is the same as the physical grid size at the wall as a fraction of the local shock-standoff distance
ξ_1	=	marching or streamwise coordinate
ξ_2	=	coordinate measured from the body to the outer bow shock
ξ_3	=	coordinate measured from the windward pitch plane to the leeward pitch plane
ρ	=	mixture density
ρ_i	=	density of the i-th species
μ	=	mixture viscosity
μ_i	=	viscosity of the i-th species
τ	=	shear stress
ϕ	=	circumferential angle measured from the windward pitch plane
$\dot{\omega}_i$	=	production rate of the i-th species
Σ	=	summation over all species, i = 1,2,3,....,NS

Superscript

j	=	index in ξ_1 direction
n	=	index for iteration
T	=	vector or matrix transpose
*	=	dimensional quantity
-	=	mixture property

Subscript

i	=	represents i-th chemical species
in	=	channel inlet conditions
j,k,l	=	indicial notation representing 1, 2 and 3
s	=	shock quantity
w	=	wall quantity
,	=	represents partial derivative
∞	=	freestream quantity

Vector and Matrix Notation

Vector	=	bold lower-case character
Matrix	=	bold upper-case character
$\bullet$	=	vector dot product
$\times$	=	vector cross product

I. INTRODUCTION

1.1. Introduction and Background

Over the past several years the area of aerothermodynamic analysis of hypersonic reentry vehicles has seen a significant change in direction in concept as well as technology development. The main motivation for such a change has not only come from practical needs, but also because the overall field of computational fluid dynamics/chemistry has seen some significant new developments and improvements. All these developments in the basic aerothermodynamic technology, as well as in the applied fields, have been greatly influenced by the tremendous improvements in the existing computational facilities and computer technology. As a natural consequence of an improved understanding of the physics and the corresponding improvements in the computational technology, vehicle concepts which were improbable some years ago can now be developed at much lower risk levels. The bulk of these space-technology developments rely (either partially or in full) upon the technology development efforts of NASA. From the general trend of these technology developments, it is clear that NASA is being relied upon to not only help in the conceptual developments but also in the development of the computational capabilities to effectively study the related aerothermodynamic and aerothermochemical problems. A detailed overview of NASA's present aerothermodynamic program was recently published by Graves and Hunt (1985), and the corresponding research and technology issues were outlined by Howe (1985).

The 1986 State-of-Union address by President Reagan clearly stated the need for a new "Orient Express" (hypersonic transport), and laid the foundation for a National Aero-Space Plane (NASP) technology development program. The NASP technology effort involves major developments in almost all areas of hypersonic transport, leading to an experimental vehicle in the near future. However, the development of a reliable propulsion system and an accurate prediction of the related 3-D inlet approach flowfield, is one of the most critical tasks. Due to a lack of flight data and limited experimental capabilities, the development of NASP propulsion technology (as well as the airframe design) program, in its first three phases, has to heavily rely upon the CFD support

provided. Our involvement with NASP technology development (airframe as well as propulsion) contractors has shown a keen need for accurate, reliable and computationally efficient numerical schemes for predicting large angle-of-attack, supersonic/hypersonic external flows over realistic (3-D) NASP configurations.

The typical flight envelope for NASP-type vehicles extends over a wide range of low to high flight altitudes. At low altitudes the surrounding gas chemistry can be accurately modeled using a perfect-gas model. However, under high-altitude (low-density) conditions the characteristic reaction times are of the order of the characteristic flow times, and the reactions between the various gas species become important. Under such high-Mach-number and low-Reynolds-number conditions the air can no longer be accurately modeled as a perfect gas, and one needs to account for ionization/dissociation/recombination of the various gas species involved and their impact on the overall mixture properties. Under such conditions the thermochemical nature of the flow can be modeled by assuming either (a) chemical nonequilibrium (finite-rate chemically-reacting flow) or (b) local chemical equilibrium. Typically, the high-altitude regimes (35 km and above) are more accurately modeled as finite-rate chemically-reacting air, whereas the moderate altitude regimes (15-30 km) are close to equilibrium chemically-reacting air. (Of course, these are rough limits and may vary with the vehicle configuration involved.)

Apart from the importance of flow chemistry, the complex three-dimensional nature of NASP-type vehicles is also a very important consideration. In short, the need exists to develop three-dimensional numerical capabilities for predicting the perfect-gas, equilibrium-air and nonequilibrium-air flowfields around complex 3-D configurations. Since there are little flight data and no ground-testing facilities available to properly simulate the type of flight conditions being considered, the development and operational analysis of the aforementioned configurations will benefit significantly from any such three-dimensional numerical capabilities. Furthermore, because these numerical schemes are to be also used in the preliminary as well as advanced design stages, they need to be fast, efficient, robust and accurate. It is also worth noting that for most of the NASP-related configurations under study, most of the compression required for the afterbody propulsion system occurs over the forebody region. Thus, for the type of problems being addressed, an accurate prediction of the external flow over the vehicle forebody region is also very important for an accurate analysis of the associated hypersonic-propulsion systems.

In the preceding Phase I effort we have successfully demonstrated the development of a new three-dimensional PNS scheme for complex 3-D configurations. This PNS scheme is based on a completely new formulation, and (unlike the classical PNS schemes) this new scheme is unconditionally time-like in the subsonic as well as the supersonic flow regions. We have applied this scheme to realistic high-speed flows over simplified (axisymmetric or 2-D) models of the NASP-related inlet configurations (Lewis, 1986, and White, 1986). We have also analyzed these inlets under small angle-of-attack (5 deg or less) conditions, and have covered a Mach range of 3 to 25 with the same scheme along with various gas models. With these unique characteristics, our PNS scheme is ideally suited for modification to study supersonic/hypersonic external flows over complex NASP-like geometries.

The Phase I work was, however, of a exploratory nature (representing a 'demonstration of concept') and needed to be further extended to study more realistic conditions. In this follow-on Phase II effort we successfully accomplished the following following tasks as proposed; viz.,

(i)   Extension to 3-D nonequilibrium-air flows.
(ii) Further development and improvement of the solution scheme.
(iii) Grid-generation and related considerations.
(iv) Application to realistic NASP-type configurations.
(v)   Extensions to 2-D/axisymmetric internal flows.
(vi) Reports, Documents and Deliverables.

1.2. Objectives and Scope of the Phase II Effort

The following six tasks were proposed and accomplished in this Phase II effort.

(1)   Extend the three-dimensional PNS scheme of Phase I to study nonequilibrium-air flows around complex three-dimensional configurations representative of realistic NASP configuration concepts. Furthermore, study and incorporate various ways of reducing computing times without sacrificing solution accuracy.

(2)   Further develop and extend the 3-D PNS scheme developed in Phase I to improve solution accuracy and efficiency. Consider different ways of minimizing crossflow smoothing effects and conduct crossflow grid-refinement studies. Furthermore,

restructure the solution scheme to make it more vectorizable and, thus, substantially reduce overall computing times.

(3) Improve the grid-generation scheme developed under the Phase I effort to handle more complicated geometry shapes such as wings, fins, etc. Improve the shock-prediction scheme of Phase I to reduce possible grid-twisting effects. Furthermore, develop an automated parabolic grid-generation approach for simpler geometries and minimize user interaction. Study the parabolic, elliptic, hyperbolic and hybrid grid-generation schemes, evaluate their usage potential and choose the best option(s).

(4) Apply the final three-dimensional PNS scheme to realistic NASP-type geometries under some typical flight conditions, and evaluate the accuracy and efficiency characteristics of the solution scheme. Study the effects of perfect-gas, equilibrium-air and nonequilibrium-air gas models on the flowfield. Also evaluate the grid-generation capabilities of the final 3-D PNS scheme.

(5) Develop a 2-D/axisymmetric PNS scheme for internal flows with perfect-gas, equilibrium-air and nonequilibrium-air gas models, by extending the axisymmetric PNS scheme of Bhutta and Lewis (1985a,b). Furthermore, run some simple test cases to evaluate the accuracy and applicability of the proposed internal-flow PNS scheme.

(6) Provide monthly progress reports during the Phase II effort. At the end of the Phase II effort provide NASA with a final report covering the mathematical details and results of the Phase II work.

The time schedule originally proposed for the completion of these Phase II tasks is summarized below.

Task	Time in months from May 1988 to May 1990							
	1-3	4-6	7-9	9-12	13-15	16-18	19-21	22-24
3-D, Neq. PNS code	X	X	X	X				
Improv. 3-D scheme	X	X	X	X				
Adv. grid gener.			X	X	X	X	X	X
Applic. to NASP					X	X	X	X
2-D/Axi. int. flow			X	X	X	X	X	X
Report/doc., deliv.					X	X	X	X

Time schedule for the Phase II effort

It should be noted that, although this Phase II work did represent a substantial effort, we accomplished all the task efforts in accordance with the time-schedule originally proposed.

II. GOVERNING EQUATIONS

2.1. Coordinate System

The coordinate system used for the present 3-D PNS scheme is a general curvilinear coordinate system (ξ_1, ξ_2, ξ_3) shown in Fig. 1. Also, a body-fixed orthogonal (Cartesian) coordinate system is chosen such that the origin of the Cartesian coordinate system is at the tip of the blunt nose, and the x-axis is aligned with the axis of the body. The z-axis is chosen as pointing downward such that the windward surface of the vehicle is on the positive z-axis side (see Fig. 1). For convenience of notation we will also refer to the x coordinate as x_1, the y coordinate as x_2 and the z coordinate as x_3.

The ξ_1 coordinate is along the body and is also the marching direction. The ξ_2 coordinate stretches from the body to the outer bow shock and lies in an axis-normal plane. The ξ_3 coordinate is measured in the crossflow direction from the windward pitch plane. In general, it is assumed that the (x,y,z) space is uniquely transformable to the (ξ_1, ξ_2, ξ_3) space through relations of the form

$$\xi_j = \xi_j (x,y,z) \tag{2.1}$$

The uniqueness property is automatically satisfied as long as coordinate lines of the same family do not cross, and it is important that the inverse transform of Eq. (2.1) is definable. Suppose we denote the marching step at which we seek the solution as 'j + 1' and the previous step as 'j', then the transformation of Eq. (2.1) is chosen such that the physical (x,y,z) grid between 'j' and 'j + 1' steps transforms to a rectangle in the computational (ξ_1, ξ_2, ξ_3) plane. The body surface corresponds to the $\xi_2 = 0$ curve, whereas the outer bow shock corresponds to $\xi_2 = $ LMAX curve (LMAX being the number of grid points in the ξ_2 coordinate direction). In the windward pitch plane $\xi_3 = 0$, and in the leeward pitch plane $\xi_3 = $ KMAX, where KMAX is the number of circumferential grid points. Also, $\xi_1 = 0$ at the j-th step and $\xi_1 = 1$ at the j + 1 step. Thus, at each marching step, every grid cell in the x-y-z space between the j and the j + 1 step is transformed into a unit cube in the ξ_1, ξ_2, ξ_3 plane with $\Delta\xi_1 = \Delta\xi_2 = \Delta\xi_3 = 1$ (see Fig. 2).

The transformation given by Eq. (2.1) is generally difficult to obtain. However, if we assume for the present that the (x,y,z) grid at the $j+1$ step were known (subsequent sections will discuss this in more detail), then the metric derivatives for the inverse transform

$$x_j = x_j (\xi_1, \xi_2, \xi_3) \tag{2.2}$$

can be easily obtained numerically. At each grid point, this information about the inverse-transform metrics is used to determine the transformation Jacobians (J) and the metric derivatives (ξ_{j,x_i}) for the transformation given by Eq. (2.1).

2.2. Governing Equations

The full Navier-Stokes equations governing the three-dimensional flow problem can be written in a nondimensional form as (see Appendix A)

$$(e_j - \varepsilon g_j)_{,x_j} = p \tag{2.3}$$

We choose our unknowns to be the density (ρ), the density-velocity products (ρu, ρv and ρw), the density-temperature product (ρT) and the pressure (p). Thus our vector of unknowns is

$$q = [\rho, \ \rho u, \ \rho v, \ \rho w, \ \rho T, \ p]^T \tag{2.4}$$

Following the approach of Viviand (1974) and Peyret and Viviand (1975), it can be shown that Eq. (2.3) can be transformed into the general curvilinear coordinate system (ξ_j), i.e.,

$$(f_j - \varepsilon s_j)_{,\xi_j} = h \tag{2.5}$$

It is assumed that in the freestream the gas mixture behaves like a perfect gas, and the nondimensionalization used in the above equations is shown in Appendix A.

Equation (2.5) is elliptic in ξ_1, ξ_2 and ξ_3 directions. If we neglect the viscous dissipation effects in the ξ_1 direction, we can combine Eqs. (2.5) and (2.3) in the following vectorial equation:

$$f_{j,\xi_j} - \varepsilon s_{2,\xi_2} - \varepsilon s_{3,\xi_3} = h \tag{2.6}$$

where the various components of this vectorial equations are defined in Appendix A.

These five equations representing the differential conservation of mass, momentum and energy are mathematically closed by using the equation of state for the particular gas model being used. This equation of state can be written in a general functional form as

$$f(\rho, T, p) = 0 \tag{2.7}$$

In the case of a perfect-gas model, the gas is assumed to be thermally as well as calorically perfect. The equation of state for this case is written in the simple algebraic form as

$$f(\rho, T, p) = \gamma p - \rho T = 0 \tag{2.8a}$$

In the case of an equilibrium-air gas model, the equation of state is written in the following functional form.

$$f(\rho, T, p) = \rho - \rho(p, T) = 0 \tag{2.8b}$$

Here the mixture density is a function of pressure and temperature and is available in the form of a table.

In this case of finite-rate chemically reacting air, the gas is assumed to be a mixture of perfect gases. The equation of state for such a reacting gas mixture is given by

$$f(\rho, T, p, C_i) = p - \rho T / \overline{m} = 0 \tag{2.8c}$$

where $\overline{m}$ is the nondimensional mixture molecular weight defined as

$$\overline{m} = \gamma_\infty \overline{m}^* / \overline{m}_\infty^* \tag{2.9}$$

The mixture thermodynamic properties (such as $\overline{m}$, $\overline{k}$, $\overline{C}_p$, $\overline{\mu}$, Pr, etc.) require a knowledge of the species concentrations (C_i) which are obtained from the species conservation equations. In the Cartesian coordinate system, the three-dimensional species conservation equation can be written as (Bird et al., 1960)

$$\rho u_j C_{i,x_j} + (J_i)_{i,x_j} = \dot{\omega}_i \tag{2.10}$$

These equations are first transformed into the (ξ_1, ξ_2, ξ_3) coordinate system, and the resulting equations are parabolized by neglecting diffusion effects in the ξ_1 and ξ_3 directions. The final parabolized species conservation equations are written as

$$[(\rho U_j /J)C_i]_{,\xi_j} - \varepsilon_1 [(\bar{\mu} m_{kk} /J Pr)C_{i,\xi_2}]_{,\xi_2} = \dot{\omega}_i \tag{2.11}$$

where $i = 1,2,3,...,(NS-1)$

The system of equations represented by Eqs. (2.6), (2.7c) and (2.11) is closed through a knowledge of the thermodynamic and transport properties of the mixture; namely, $\overline{C}_p$, $\overline{k}$, $\overline{m}$, $\bar{\mu}$, Pr, and Le.

III. NUMERICAL SOLUTION SCHEME

This chapter discusses in detail the procedure used to numerically solve the governing 3-D PNS equations for external flows.

3.1. Delta-Form of the Governing Equations

In this 'delta formulation' we solve for the changes in the flowfield variables from one iteration to the next. The approach used is separately discussed for perfect-gas, equilibrium-air and nonequilibrium-air gas models.

3.1.1. Perfect-Gas Model

Let us denote the iteration level by the index 'n', so that the iteration at which we seek the solution is represented by the superscript 'n+1', and the previous iteration (the solution to which is known) is represented by the superscript 'n'. Thus, for the 'n+1' iteration at the 'j+1' marching step we can write Eq. (2.6) as

$$f_{j,\zeta_j}^{j+1,\,n+1} - \varepsilon s_{2,\zeta_2}^{j+1,\,n+1} - \varepsilon s_{3,\zeta_3}^{j+1,\,n+1} = h^{j+1,\,n+1} \tag{3.1}$$

If we assume that the solution at the 'n+1' level is close to the solution at the n-th iteration, we can use a first-order Taylor series expansion around the previous iteration to write

$$
\begin{aligned}
f_j^{j+1,\,n+1} &\simeq f_j^{j+1,\,n} + A_j^n \cdot \Delta q^{n+1} \\
s_2^{j+1,\,n+1} &\simeq s_2^{j+1,\,n} + M_2^n \cdot \Delta q^{n+1} \\
s_3^{j+1,\,n+1} &\simeq s_3^{j+1,\,n} + M_3^n \cdot \Delta q^{n+1} \\
h^{j+1,\,n+1} &\simeq h^{j+1,\,n} + A_0^n \cdot \Delta q^{n+1}
\end{aligned}
\tag{3.2}
$$

where

$$\Delta q^{n+1} = q^{j+1,\,n+1} - q^{j+1,\,n} \tag{3.3}$$

and the matrices A_0, M_2 and M_3 are called the jacobian matrices (not to be confused with the transformation Jacobian matrix). The forms of these matrices are given in Appendix

B. It should be noted that in evaluating the jacobian matrices and doing the Taylor series expansion around the n-th iteration, we only consider the flowfield variables as the unknowns. Although the grid also changes from one iteration to the next, it is assumed that these changes are small and do not contribute to the jacobian matrices.

Thus, we see that by expanding the solution around the n-th iteration and using two-point streamwise differencing, we can write Eq. (3.1) as

$$
(A_1/\Delta\xi_1 - A_0)^n \cdot \Delta q^{n+1} - [(A_2^n - \varepsilon M_2^n) \cdot \Delta q^{n+1}]_{,\xi_2} - [(A_3^n - \varepsilon M_3^n) \cdot \Delta q^{n+1}]_{,\xi_3}
$$
$$
= -\omega[f_{,\xi_j} - \varepsilon s_{2,\xi_2} - \varepsilon s_{3,\xi_3} - h]^{j+1, n} = g^{j+1, n} \qquad (3.4)
$$

where ω is an under-relaxation factor which has values between 0 and 1, and it has been found to be very helpful in obtaining converged solutions for complex flowfields (Bhutta and Lewis, 1988a-b and 1989a-b). Typically, we use $\omega \leq 0.5$ for complicated flowfield calculations, and $\omega = 1$ for simple flowfield calculations.

Equation (3.1) is elliptic in the ξ_2 and ξ_3 directions so that for second-order accuracy we use central-differenced approximations for all ξ_2 and ξ_3 derivatives. However, the use of central-differenced schemes is typically associated with solution oscillations (Bhutta and Lewis, 1985a-d; Kaul and Chaussee, 1983; Shanks et al., 1979; and Schiff and Steger, 1979). This oscillatory behavior becomes more pronounced if the local velocities are small, so that the diagonal terms of the jacobian matrices also become relatively small. In order to damp these solution oscillations, it is necessary to add some additional higher-order diffusion terms to Eq. (3.1). In our earlier work (Bhutta and Lewis, 1985a-d, and Bhutta et al., 1985a) we had developed a second-order accurate fully implicit smoothing approach which is accurate and simple to use. In the present formulation we have extended this smoothing approach to a fourth-order accuracy. It is shown in Appendix C that by extending the basic approach of Bhutta and Lewis (1985a-d) and Bhutta et al. (1985), we can write Eq. (3.1) as

$$
f_{,\xi_j}^{j+1, n+1} = \varepsilon(s_{2,\xi_2} + s_{3,\xi_3})^{j+1, n+1} + h^{j+1, n+1} + \pi_1(q)(\Delta\xi_2)^4/16 + \pi_2(q)(\Delta\xi_3)^4/16 \qquad (3.5)
$$

where the form of the vectors π_1 and π_2 is chosen as

$$
\pi_1(q) = -(A_1/\Delta\xi_1 - A_0) \cdot \frac{\partial^4 q}{\partial\xi_2^4} - [(A_2 - \varepsilon M_2) \cdot \frac{\partial^4 q}{\partial\xi_2^4}]_{,\xi_2} - [(A_3 - \varepsilon M_3) \cdot \frac{\partial^4 q}{\partial\xi_2^4}]_{,\xi_3} \qquad (3.6a)
$$

$$
\pi_2(q) = -(A_1/\Delta\xi_1 - A_0) \cdot \frac{\partial^4 q}{\partial\xi_3^4} - [(A_2 - \varepsilon M_2) \cdot \frac{\partial^4 q}{\partial\xi_3^4}]_{,\xi_2} - [(A_3 - \varepsilon M_3) \cdot \frac{\partial^4 q}{\partial\xi_3^4}]_{,\xi_3} \qquad (3.6b)
$$

III. NUMERICAL SOLUTION SCHEME

It has been shown in Appendix C that (to fourth-order accuracy) we can rewrite Eq. (3.5) in terms of an intermediate solution χ^{j+1} as

$$[f_j(\chi^{j+1})]_{,\xi_j} = \varepsilon[s_2(\chi^{j+1})]_{,\xi_2} + \varepsilon[s_3(\chi^{j+1})]_{,\xi_3} + h(\chi^{j+1}) + O(\Delta\xi_2)^4 + O(\Delta\xi_3)^4 \qquad (3.7)$$

The actual solution that we seek at the j + 1 step is related to this intermediate solution by

$$(\chi_1)^{j+1} = \chi^{j+1} - \chi_{,\xi_3\xi_3\xi_3\xi_3}\Delta\xi_3^4/16 \qquad (3.8a)$$

$$q^{j+1} = (\chi_1)^{j+1} - (\chi_1)_{,\xi_2\xi_2\xi_2\xi_2}\Delta\xi_2^4/16 \qquad (3.8b)$$

An important advantage of this formulation is that the crossflow smoothing effects [Eqs. (3.8a)] and the axis-normal smoothing effects [Eqs. (3.8b)] can be separately identified. Furthermore, the way these smoothing operations affect the individual flowfield variables can also be clearly seen. Being able to separate these smoothing effects, permits us to further enhance its accuracy by restricting the axis-normal smoothing effects to only the pressure field. Thus, Eqs. (3.8) are rewritten as

$$(\chi_1)^{j+1} = \chi^{j+1} - \chi_{,\xi_3\xi_3\xi_3\xi_3}\Delta\xi_3^4/16 \qquad (3.9a)$$

$$q^{j+1} = (\chi_1)^{j+1} - [0,0,0,0,0,(\chi_{16})_{,\xi_2\xi_2\xi_2\xi_2}]^T\Delta\xi_2^4/16 \qquad (3.9b)$$

where χ_{16} is the sixth element of the vector χ_1 . In this manner, the axis-normal smoothing effects do not degrade the wall heat-transfer and skin-friction predictions.

In our PNS scheme, first-order backward-differenced approximations are used to approximate the streamwise convective flux derivatives (f_{1,ξ_1}). It has been shown by Bhutta and Lewis (1985a-d) and Bhutta et al. (1985a) that for the iterative process of Eq. (3.1), this first-order streamwise differencing is conservative in the limit of convergence. This is not only important from a storage point of view, but it also gives the present scheme a significantly improved capability for treating strong compression discontinuities. However, such a first-order accurate finite-difference representation has no inherent mechanism to check or suppress the onset of streamwise numerical oscillations. The numerical filtering provided by this first-order backward-differenced approximation is proportional to the streamwise stepsize. As the streamwise step size decreases, the numerics becomes more and more sensitive to the high frequency (small wave length) streamwise oscillations. In order to suppress such streamwise oscillations and, thus, enhance the small step-size capability of the our PNS scheme, small amounts

III. NUMERICAL SOLUTION SCHEME

of second-order streamwise numerical dissipation effects are added to the governing equations in order to damp and control the growth of any streamwise solution oscillation. This second-order streamwise damping approach is discussed in detail in Appendix D. However, briefly speaking, this approach uses the basic PNS approximation that for such parabolic flows the second-order streamwise derivatives are much smaller than the first-order streamwise derivatives ($\frac{\partial^2}{\partial \xi_1^2} < < \frac{\partial}{\partial \xi_1}$). For such a case, suppose we want to suppress a numerical oscillation (of constant vector amplitude) in the streamwise convective flux derivatives (f_{1,ξ_1}). It can be shown that for a constant stepsize case (see Appendix D) the vector amplitude of such an oscillation can be approximated as $\frac{1}{2} f_{1,\xi_1 \xi_1} \Delta \xi_1$. Based on this simple damping model, we choose the streamwise diffusion effects to be of the form

$$f_{1,\xi_1} \cong (f_{1,\xi_1})_b - \omega f_{1,\xi_1 \xi_1} \Delta \xi_1 \qquad (3.10)$$

where the subscript 'b' represents first-order backward-differenced approximation. The appropriate values of ω are between 0 and 1, and its form is chosen such that $\omega \rightarrow 1$ as $\Delta \xi_1 \rightarrow 0$ and $\omega \rightarrow 0$ when $\Delta \xi_1$ is adequately large. Thus, the numerical accuracy of a large step-size solution is not compromised.

For this perfect-gas model the mixture viscosity was obtained using the Sutherland formula (White, 1974), and the specific-heat ratio was assumed to be a constant (1.4 for air). The mixture Prandtl number was also assumed fixed (0.72 for air), and the mixture thermal conductivity was obtained from the definition of mixture Prandtl number.

3.1.2. Equilibrium-Air Gas Model

The numerical scheme used for equilibrium-air flows is essentially the same as for the case perfect-gas case, except that the mixture thermodynamic and transport properties are provided in the form of a table. The dependant variables for these tabular data are chosen to be pressure and temperature. The thermodynamic properties involve the mixture enthalpy, h(p,T), and mixture density, ρ(p,T), data and are based on the tabular data of Miner et al. (1971). The transport properties involve the mixture viscosity data, μ(p,T), the mixture thermal conductivity data, k(p,T), and the Prandtl number data, Pr(p,T). The viscosity and thermal conductivity data are based on the data developed by Peng and Pindroh (1962). The Prandtl number data were developed using this viscosity and thermal conductivity data and the mixture specific-heat data obtained by numerically differentiating the aforementioned enthalpy data of Miner et al. (1971). The equilibrium-air thermodynamic and transport property table used in this study covers

the temperature range of 10-15000 Kelvin and the pressure range of 0.0025-15.849 atmospheres. The pressure range of the thermodynamic property data of Miner et al. (1971) is from 0.000025 atmospheres to 39810.72 atmospheres; however, the reduced limits of the current table are due to transport property data of Peng and Pindroh (1962). The original transport property data of Peng and Pindroh (1962) are in terms of a table of density and temperature. When these data were rearranged in terms of pressure and temperature, it was observed that outside the limits of 0.0025-15.849 atmospheres, the available data did not completely cover the temperature range of 10-15000 Kelvin. Since a direct extrapolation of these data in terms of pressures may not be accurate, the current table was limited to this pressure and temperature range. It should be noted that this range adequately covers most of the flight regime in which the equilibrium-air effects may be important.

3.1.3. Nonequilibrium-Air Gas Model

The overall nonequilibrium PNS problem represented by Eqs. (2.6), (2.7c) and (2.11) is well-posed. However, the number of unknowns involved is very large (i.e., ρ, ρu, ρv, ρw, ρT, p, $\overline{C}_p$, $\overline{k}$, $\overline{m}$, $\overline{\mu}$, Pr, C_1, C_2, C_3,...,C_{NS}). A simultaneous solution of these quantities would be beyond the practical limits of present computational facilities, except perhaps, future supercomputers. Even so, the solution of a practical problem would be very expensive and time consuming. However, for many practical problems, the coupling between the fluid mechanics (ρ, ρu, ρv, ρw, ρT and p) and the chemistry ($\overline{C}_p$, $\overline{m}$, $\overline{k}$, $\overline{\mu}$, Pr, C_1, C_2,...,C_{NS}) is not very strong. With this idea in the mind, we can decouple the overall nonequilibrium PNS problem into (a) a fluid mechanics problem and (b) a chemistry problem.

The fluid mechanics problem is represented by Eqs. (2.6) and (2.7c) where the chemistry is assumed as known. The chemistry problem involves the solution of Eqs. (2.11) and the determination of the transport properties of the mixture, where the fluid mechanics are assumed as known. The coupling between the fluid mechanics and the chemistry is treated in an iterative manner. Thus, for each iteration at a given marching step we first solve the fluid mechanics problem, and then we solve the chemistry problem based on the solution to the fluid mechanics problem. With this updated chemistry, the fluid mechanics problem is solved once again, and the cycle is repeated until acceptable convergence is achieved. In this manner, in the limit of convergence, we have a fully iterated solution which completely accounts for the coupling between the fluid mechanics and the chemistry of the flowfield.

(a) Solution of the Fluid Mechanics Problem : In general, the solution of the fluid mechanics problem is very similar to the solution approach used for perfect-gas and equilibrium-air flows, except for some additional nonequilibrium terms appearing in the energy equation. As shown in Appendix A, these additional nonequilibrium terms are appropriately included in the definition of h and the corresponding jacobian matrix A_0 [Eqs. (3.1) and (3.2)].

(b) Solution of the Chemistry Problem : Using the solution of the fluid mechanics problem [Eqs. (3.4) and (3.8)], first the transport properties of the seven-species air system are determined. This information is then used to evaluate the production rates ($\dot{\omega}_i$) for the various species involved. For the chemistry problem, we use a seven species (O, O_2, N, N_2, NO, NO^+, and e^-) gas model to represent the finite-rate chemically-reacting air mixture. The thermodynamic properties of these species are obtained from the thermodynamic data of Browne (1962a-c). The diffusion model used in this seven-species model is limited to binary diffusion, with the binary diffusion coefficient for each gas species defined by a Lewis number of 1.4.

The gas-phase reactions considered in this seven-species air system correspond to the model used by Blottner et al. (1971) and Miner and Lewis (1975), and use the reaction-rate data proposed by Bortner (1963). The viscosities of O, O_2, N, N_2, NO, NO^+, and e^- are computed from the curve-fit relations used by Blottner et al. (1971), and the thermal conductivities of these species are estimated with the Eucken semi-empirical formula. After the viscosities and thermal conductivities of the individual species have been estimated, the viscosity and thermal conductivity of the mixture are calculated using Wilke's semi-empirical relations. A complete description of the reactions, reactions rates and viscosity data for this seven-species nonequilibrium-air gas model is given in Tables 1 thru 3.

In treating the species conservation equations in such a decoupled manner, special consideration needs to be given to the treatment of the species production terms. It is known that a full linearization of these production terms results in an unstable solution under typical flight conditions. For this reason it is necessary to split the overall production term into two parts (Blottner et al., 1971, and Miner and Lewis, 1975).

$$(\frac{\dot{\omega}_i}{\rho}) = \dot{\omega}_i^0 - \dot{\omega}_i^1 C_i \qquad (3.11)$$

where the respective forms of $\dot{\omega}_i^0$ and $\dot{\omega}_i^1$ have been derived in Appendix E, and are based on the work of Blottner et al. (1971) and Miner and Lewis (1975). As was noted by Blottner et al. (1971) (and it has also been our experience), writing the species production terms in terms of species concentrations adds to the stability of the solution. In the subsequent numerical formulation of the related species conservation equations, the $\dot{\omega}_i^0$ contribution acts as a source term in the right-hand side, while the $\dot{\omega}_i^1$ term appears as a diagonal contribution on the implicit (left-hand) side. This separation balances both sides of the equation, and results in a stable solution. Both these components of the species production term are functions of the species concentrations, local density and the local temperature. The calculations of these production terms involves several exponential and logarithmic operations to be performed for each species. Typically, the number of these operations increases at a rate much greater than the square of the total number of species. For a complex chemical system where there is a large number of species involved, a substantial part of the total computing time can easily be spent in doing these calculations.

In our nonequilibrium teflon-air PNS scheme we took a new approach of partially linearizing the production terms, where the production terms are still separated into left-hand side and a right-hand side contributions. However, these components are then linearized based on the mixture density and temperature information from the previous marching step. On the other hand, the species concentrations appearing in these production terms are only linearized around the previous iteration.

$$(\dot{\omega}_i^0)^{j+1,n+1} = \dot{\omega}_i^0(\rho^j, T^j, C_i^{j+1,n}) \tag{3.12a}$$

$$(\dot{\omega}_i^1)^{j+1,n+1} = \dot{\omega}_i^1(\rho^j, T^j, C_i^{j+1,n}) \tag{3.12b}$$

Since this linearization is only partial and is done on quantities which indeed change very slowly (especially in the PNS afterbody region), the errors introduced are very small. However, the computing-time efficiency achieved is substantial. Again, it should be noted that in this approach solution accuracy is maintained, because the linearization involves terms which do change very slowly (such as density and temperature) from one step to the other, and than again the linearization is only partial.

With the species production terms written as in Eqs. (3.11) and (3.12), using a two-point backward-difference formula for the ξ_1 derivative and central-differenced approximations for the ξ_2 and ξ_3 derivatives, we can write the parabolized species conservation equations [Eq. (3.13)] in the following scalar tridiagonal form.

$$a_{k,\ell}(C_i)_{k,\ell-1} + b_{k,\ell}(C_i)_{k,\ell} + c_{k,\ell}(C_i)_{k,\ell+1} + [(\rho U_3 / J)C_i]_{,\xi_3} = d^*_{k,\ell} \quad (3.13)$$

where the coefficients a, b, c and d · are functions of the flowfield variables, the transport properties of the gas mixture. The species production terms are included in the coefficients b and d ·.

3.2. Predictor-Corrector Solution Scheme

Under large angle of attack conditions strong crossflow separated regions may develop on the leeward side. Under these conditions, solution coupling in the crossflow direction is very important. If these coupling effects are not properly considered during the iterative solution, they can cause severe convergence difficulties. In order to address that problem of crossflow coupling we have developed a new predictor-corrector approach. This predictor-corrector scheme is divided into three different parts; namely, (a) the predictor step, (b) the shock solution and (c) the corrector step. The following discussion summarizes the details of these solution steps.

Using a two-point streamwise differencing and central-differenced approximations in the ξ_2 and ξ_3 directions, the final differenced equations corresponding to Eq. (3.4) can be written in the following block-pentadiagonal form.

$$[D \cdot \Delta\chi_{k-1,\ell}] + [A \cdot \Delta\chi_{k,\ell-1}] + [B \cdot \Delta\chi_{k,\ell}] + [C \cdot \Delta\chi_{k,\ell+1}] + [E \cdot \Delta\chi_{k+1,\ell}]$$
$$(3.13)$$
$$= -[f_{i,\xi_i} - \varepsilon s_{2,\xi_2} - \varepsilon s_{3,\xi_3} - h]^{j+1,n} = g^{j+1,n}$$

3.2.1. Predictor Step

In the predictor step we first neglect the implicit crossflow coupling effects in favor of the body-normal coupling effects. With this assumption the governing equations for the predictor step become

$$[A \cdot \Delta\chi^*_{k,\ell-1}] + [B \cdot \Delta\chi^*_{k,\ell}] + [C \cdot \Delta\chi^*_{k,\ell+1}] = g^n \quad (3.14)$$

These equations are inverted from the body to the shock to develop a recursive relationship between the solution at each successive grid point in the body-normal direction. These recursive relations have the form

$$\Delta\chi^{*}_{k,\ell} = -R_{k,\ell} \cdot \Delta\chi^{*}_{k,\ell+1} + r^{n}_{k,\ell} \qquad \text{where} \quad \begin{aligned} k &= 1,..,KMAX \\ \ell &= 1,..,LMAX-1 \end{aligned} \qquad (3.15)$$

3.2.2. Crossflow-Coupled Shock Solution

The crossflow-coupled shock-fitting scheme is discussed in detail in the following section. Briefly speaking, using the recursive relation from the predictor step at $\ell = (LMAX-1)$ location, the Rankine-Hugoniot shock-crossing equations are solved to obtain the solution at the shock. This shock solution is than used to solve the corrector step.

3.2.3. Corrector Step

Just like the shock-point solution, the solution in the corrector step uses the recursive relations from the predictor step to eliminate the $(k,\ell-1)$ contributions in the difference molecule. Then using the fact that the solution at the $(k,\ell+1)$ point is known, one can reduce the Eqs. (3.13) to only a coupled system in the crossflow direction. This crossflow corrector solution can be written as

$$D \cdot \Delta\chi_{k-1,\ell} + (B - AR_{k,\ell}) \cdot \Delta\chi_{k,\ell} + E \cdot \Delta\chi_{k+1,\ell}$$

$$\cong (g^{n} - A \cdot r^{n}_{k,\ell-1}) - C \cdot \Delta\chi_{k,\ell+1} \qquad (3.16)$$

where it is assumed that

$$\Delta\chi_{k,\ell-1} \cong \Delta\chi^{*}_{k,\ell-1} = -R_{k,\ell-1} \cdot \Delta\chi^{*}_{k,\ell} + r^{n}_{k,\ell-1}$$

$$\cong -R_{k,\ell-1} \cdot \Delta\chi_{k,\ell} + r^{n}_{k,\ell-1} \qquad (3.17)$$

This implicit crossflow solution is obtained using plane-of-symmetry boundary conditions applied in the windward and leeward pitch planes. In this way the flowfield solution is marched from the shock to the body.

3.3. Pseudo-Unsteady Solution Algorithm

It should be noted that the right-hand side of Eq. (3.4) as well as the right-hand side of Eq. (3.13) is the governing differential equation corresponding to the fluid mechanics problem written at the n-th iteration level and goes to zero in the limit of convergence. As discussed by Bhutta and Lewis (1985a-d), under these conditions the exact form of the left-hand implicit terms is of no great consequence except that it affects the convergence path of the solution. With this idea in mind we do not update the Jacobian matrices beyond the first iteration; i.e., we assume that

$$A_0^n \simeq A_0^{n=1}$$
$$A_j^n \simeq A_j^{n=1}$$
$$M_2^n \simeq M_2^{n=1}$$
$$M_3^n \simeq M_3^{n=1}$$

(3.18)

Such a pseudo-unsteady approach has been discussed in depth by Bhutta and Lewis (1985a-d) and interested readers are referred to these references for further details. Using this pseudo unsteady approach we obtain the final differenced equations as

$$(A_1/\Delta\xi_1 - A_0)^{n=1} \cdot \Delta\chi^{n+1} + [(A_2 - \varepsilon M_2)^{n=1} \cdot \Delta\chi^{n+1}]_{,\xi_2} + [(A_3 - \varepsilon M_3)^{n=1} \cdot \Delta\chi^{n+1}]_{,\xi_3}$$

(3.19)

$$= -[f_{j,\xi_j} - \varepsilon s_{2,\xi_2} - \varepsilon s_{3,\xi_3} - h]^{j+1,\,n} = g^{j+1,\,n}$$

The converged limit of Eqs. (3.19) is the same as the converged limit of Eqs. (3.4). However, Eqs. (3.19) is considerably more efficient and faster to solve. With the present pseudo-unsteady approach the time for each iteration after the first iteration (n = 2,3,...) is only 10-15% of the time taken by the first iteration.

3.4. Boundary Conditions

The problem represented by the governing PNS equations is a split-boundary-value problem; i.e., the equations are hyperbolic-parabolic in the ξ_1 direction and elliptic in the ξ_2 and ξ_3 directions. Thus, in order to solve the problem completely we need initial conditions to be specified at the start of the marching procedure, boundary conditions to be specified at the wall and at the outer bow shock and boundary conditions to be specified in the windward and leeward pitch planes (for flows with a pitch-plane of symmetry).

3.4.1. Initial Conditions

The initial conditions to start the perfect-gas and equilibrium-air PNS solutions were obtained from a VSL blunt-body solution scheme for perfect-gas and equilibrium-air flows (Murray and Lewis, 1978; Thareja et al., 1983; and Thompson et al., 1983). Similarly, the initial conditions to start the nonequilibrium-air PNS Solutions were obtained from a VSL blunt-body scheme for nonequilibrium-air flows (Swaminathan et al., 1983). The quality of such VSL solutions has been discussed in great detail by Thompson et al. (1983) and Bhutta et al. (1985b). The VSL blunt-body solution is interpolated to obtain the starting solution at the initial data plane (IDP) for the 3-D PNS afterbody solution. We typically choose the starting location to be approximately 2-3 nose-radii downstream of the nose stagnation-point location.

3.4.2. Wall Boundary Conditions

The boundary conditions at the wall consist of six independent relations representing the nature of the gas mixture and the physical conditions at the wall. These conditions are:

(1) Equation of state of the gas: $f(\rho, p, T) = 0$

(2) No-slip condition for 'u' velocity component: $\rho u = 0$

(3) No slip condition for 'v' velocity component: $\rho v = 0$

(4) No slip condition for 'w' velocity component: $\rho w = 0$

(5) Specified wall temperature: $(\rho T) = \rho T_w$.

and

(6) Zero pressure derivative in the ξ_2 direction ($p_{,\xi_2} = 0$)

The first five boundary conditions are easy to visualize as they represent the actual physical conditions at the wall. The sixth boundary condition on the pressure derivative comes from a boundary-layer-type analysis performed at the wall. The above set of boundary conditions are well-posed and form a linearly independent set.

For the chemistry problem of the nonequilibrium PNS solution scheme represented by the species conservation equations [Eqs. (3.13)], the wall boundary conditions used consist of either (i) a fully-catalytic wall [$C_i = C_{i\infty}$], or (ii) a non-catalytic wall [$C_{i,\xi_2} = 0$]. In the current study, however, we have only used fully-catalytic wall boundary conditions.

3.4.3. Boundary Conditions at the Shock

The boundary conditions at the outer bow shock are, however, much more involved. This boundary condition involves a fully-implict and crossflow coupled shock-fitting approach, and the bow shock is predicted as the solution marches down the body. This fully-implict bow shock-fitting scheme will be discussed in detail in Chapter 4.

3.4.4. Circumferential Boundary Conditions

Presently, the proposed three-dimensional nonequilibrium PNS schemes can only treat flows with a pitch plane of symmetry; i.e, the vehicle geometry is symmetric with respect to the pitch plane and there is no yaw. For such a case the boundary conditions at the windward and leeward pitch planes consist of reflective or symmetric boundary conditions. The symmetric and reflective boundary conditions used in the present study are based on the second-order crossflow boundary conditions used by Kaul and Chaussee (1983) and Shanks et al. (1979).

3.5. Laminar and Transitional/Turbulent Flow Simulation

The present 3-D external flow PNS scheme includes capabilities for modeling laminar as well as transitional/turbulent flows. The discussion so far has involved laminar flow conditions; however, the two-layer turbulent eddy-viscosity model of Cebeci and Smith (Cebeci, 1970) has also been included along with the transitional model of Dhawan and Narasimha (1958). Appendix F includes a detailed discussion of this transitional/turbulent flow modeling.

The procedure used for determining the surface heat-transfer rate and surface skin-friction is discussed in detail in Appendix G. Furthermore, the surface integration of pressure and skin-friction to obtain the vehicle force and moment data is discussed in Appendix H.

IV. FULLY-IMPLICIT SHOCK-FITTING PROCEDURE

4.1. Development of the Shock-Fitting Equations

In this study we have developed a new fully-implicit and crossflow coupled shock-fitting scheme. In this scheme the bow shock location is iteratively predicted as the solution marches down the body. This chapter provides a brief but complete description of this shock-fitting approach. The important features of this bow shock-fitting approach are:

(a) The bow-shock shape location is predicted along with the flowfield solution and does not have to be specified a priori.

(b) Unlike earlier noniterative shock-propagation approaches (Kaul and Chaussee, 1983; Shanks et al., 1979; and Chaussee et al., 1981), the present shock-fitting scheme is fully iterative and treats the various gas models (perfect-gas or equilibrium-air or nonequilibrium-air) accurately and in a unified manner.

(c) Unlike earlier noniterative shock-propagation approaches (Kaul and Chaussee, 1983; Shanks et al., 1979; and Chaussee et al., 1981), the present approach does not assume the flowfield behind the shock to be inviscid. This can be quite important when strong flowfield gradients exist behind the shock, as may be the case in the nose-dominated region and in regions where the bow shock starts to interact with the imbedded shock waves (or compression waves) originating from the body.

(d) Unlike the iterative shock-fitting approaches of Helliwell et al. (1980) and Lubard and Helliwell (1973), the present shock fitting approach is not only for a general curvilinear coordinate system but also does not increase the matrix size of the block-tridiagonal solution between the body and the shock.

(e) Unlike any earlier iterative or noniterative bow shock-fitting scheme, the present shock-fitting scheme does not neglect the crossflow coupling effects at the shock. This results in accurate and smooth shock shapes even when there are strong crossflow variations of the conditions behind the shock. This can be especially important when dealing with complex 3-D configurations (which is one of the main objectives of this study) where the 3-D nature of the body can interact with the bow

shock and substantially distort it. Similar strong crossflow variations may also occur on simple configurations when pitched at large angles of attack.

In developing the present bow shock-fitting scheme we assume that from one iteration to the next the shock-points move along the ξ_2 grid line. This direction corresponds to the intersection of the $\xi_1 = \text{constant}$ and $\xi_2 = \text{constant}$ surfaces. This assumption allows us to reduce the size of unknowns to be solved, and the final solution has only one additional unknown at the shock which completely defines the spatial movement of the shock point. This smaller size of the unknowns is very important for a faster iterative solution and faster convergence characteristics of the overall implicit shock-prediction scheme. Furthermore, this simplification only represents a certain constraint on the direction in which the shock-point moves and has no affect on the accuracy of the shock-crossing equations.

Furthermore, in order to simplify the numerical solution, it is assumed that the metric derivatives $y_{,\xi_2}$ and $z_{,\xi_2}$ at the shock can be safely assumed as known from the previous iteration; i.e.,

$$
\begin{aligned}
(y_{,\xi_2})_s^{n+1} &\simeq (y_{,\xi_2})_s^n \\
(z_{,\xi_2})_s^{n+1} &\simeq (z_{,\xi_2})_s^n
\end{aligned}
\tag{4.1}
$$

This is also only a simplification and does not affect the accuracy of the final converged solution. For the case of nonequilibrium-air flows a frozen shock-crossing approximation is used.

Using the first of the aforementioned assumptions we denote the amount by which the shock point moves in the ξ_2 direction as Δ_s. In other words

$$
(\xi_2)_s^{n+1} \simeq (\xi_2)_s^n + (\Delta)_s^{n+1}
\tag{4.2}
$$

Thus the corresponding movement of the shock-point coordinates from one iteration to the next can be written as

$$
(x_j)_s^{n+1} \simeq (x_j)_s^n + (x_{j,\xi_2})_s^n (\Delta)_s^{n+1}
\tag{4.3}
$$

Furthermore, we define a set of six unknowns (α_i) such that

$$\alpha_1^{n+1} = (x_{,\xi_1})_s^{n+1}$$
$$\alpha_2^{n+1} = (y_{,\xi_1})_s^{n+1}$$
$$\alpha_3^{n+1} = (z_{,\xi_1})_s^{n+1} \tag{4.4}$$
$$\alpha_4^{n+1} = (y_{,\xi_3})_s^{n+1}$$
$$\alpha_5^{n+1} = (z_{,\xi_3})_s^{n+1}$$

Where it should be noted that these five unknowns are actually functions of a single unknown $(\Delta_s)^{n+1}$ such that

$$\alpha_1^{n+1} = \alpha_1^n + (x_{,\xi_2})_s^n \Delta_s^{n+1}$$
$$\alpha_2^{n+1} = \alpha_2^n + (y_{,\xi_2})_s^n \Delta_s^{n+1}$$
$$\alpha_3^{n+1} = \alpha_3^n + (z_{,\xi_2})_s^n \Delta_s^{n+1} \tag{4.5}$$
$$\alpha_4^{n+1} = \alpha_4^n + [(y_{,\xi_2})_s^n \Delta_s^{n+1}]_{,\xi_3}$$
$$\alpha_5^{n+1} = \alpha_5^n + [(z_{,\xi_2})_s^n \Delta_s^{n+1}]_{,\xi_3}$$

At this point we define three orthogonal vector directions $\mathbf{n}$, $\mathbf{t}$ and $\mathbf{s}$ at the shock surface (note that these are not unit vectors). The vector $\mathbf{n}$ is normal to the shock surface. The vector $\mathbf{t}$ is tangent to the shock surface and directed in the ξ_3 direction. The vector $\mathbf{s}$ is also tangent to the shock surface and orthogonal to vectors $\mathbf{n}$ and $\mathbf{t}$

It can be shown that these vectors can be written as

$$\mathbf{s} = \alpha_1(\alpha_4^2 + \alpha_5^2)\mathbf{i} + \alpha_5(\alpha_2\alpha_5 - \alpha_3\alpha_4)\mathbf{j} - \alpha_5(\alpha_2\alpha_5 - \alpha_3\alpha_4)\mathbf{k}$$
$$\mathbf{n} = (\alpha_2\alpha_5 - \alpha_3\alpha_4)\mathbf{i} - \alpha_1\alpha_5\mathbf{j} + \alpha_1\alpha_4\mathbf{k} \tag{4.6}$$
$$\mathbf{t} = \alpha_4\mathbf{i} + \alpha_5\mathbf{k}$$

Or

$$\mathbf{s} = [s_x(\alpha_1, \alpha_4, \alpha_5)]\mathbf{i} + [s_y(\alpha_2, \alpha_3, \alpha_4, \alpha_5)]\mathbf{j} + [s_z(\alpha_2, \alpha_3, \alpha_4, \alpha_5)]\mathbf{k}$$
$$\mathbf{n} = [n_x(\alpha_2, \alpha_3, \alpha_4, \alpha_5)]\mathbf{i} + [n_y(\alpha_1, \alpha_5)]\mathbf{j} + [n_z(\alpha_1, \alpha_4)]\mathbf{k} \tag{4.7}$$
$$\mathbf{t} = [t_y(\alpha_4)]\mathbf{j} + [t_z(\alpha_5)]\mathbf{k}$$

With such a definition of the shock-normal and shock-tangent vectors the velocity components normal and tangent to the shock surface can now be written as

$$V_s = (u_s s_x + v_s s_y + w_s s_z)/|\mathbf{s}|$$
$$V_n = (u_s n_x + v_s n_y + w_s n_z)/|\mathbf{n}| \tag{4.8}$$
$$V_t = (u_s t_x + v_s t_y + w_s t_z)/|\mathbf{t}|$$

where V_n, V_t and V_s are the velocity components in the **n**, **t** and **s** directions, respectively. Similarly we can also define the freestream velocity components $(V_n)_\infty$, $(V_t)_\infty$ and $(V_s)_\infty$.

Having defined the relevant velocity components for the purpose of writing the five Rankine-Hugoniot shock-crossing equations (representing the conservation of mass, momentum and energy), we note that we have actually seven unknowns at the shock. These seven unknowns are written in a vectorial form as

$$q_s = [\rho, \rho u, \rho v, \rho w, \rho T, p, \Delta]_s^T \qquad (4.9)$$

Thus we need two more equations to close the system of equations at the shock. One of these additional equations is the equation of state of the gas and the other equation is provided by applying the differential continuity of mass equation behind the shock. As we see no approximation other than the assumption of a Rankine-Hugoniot shock has been made. These equations are equally valid whether the conditions behind the shock are viscous or inviscid dominated or whether substantial flowfield gradients exist behind the shock.

The seven governing equations at the shock can now be written as

$$h + V^2/2 - (h_0)_\infty = 0 \qquad (4.10a)$$

$$\rho V_n - \rho_\infty (V_n)_\infty = 0 \qquad (4.10b)$$

$$\rho[V_t - (V_t)_\infty] = 0 \qquad (4.10c)$$

$$\rho[V_s - (V_s)_\infty] = 0 \qquad (4.10d)$$

$$p - p_\infty + \rho(V_n)^2 - \rho_\infty(V_n)^2_\infty = 0 \qquad (4.10e)$$

along with the equation of state written in the functional form

$$f(\rho, T, p, C_i) = 0 \qquad (4.10f)$$

and the differential continuity equation written as

$$(\rho U_i/J)_{,\xi_i} = 0 \qquad (4.10g)$$

Equations (4.10a) to (4.10f) are quite straight forward; however, the differential continuity equation [Eq. (4.10g)] needs some further elaboration. Noting the definition of contravariant velocity components (U_i), we can re-write this equation as

$$[a_{i,x_j}(\rho u_j)]_{,\xi_i} = 0 \qquad (4.10g)$$

where

$$
\begin{aligned}
a_{1x} &= (z_{,\xi_2}\alpha_4 - y_{,\xi_2}\alpha_5) \\
a_{1y} &= x_{,\xi_2}\alpha_5 \\
a_{1z} &= -x_{,\xi_2}\alpha_4 \\
a_{2x} &= (\alpha_2\alpha_5 - \alpha_3\alpha_4) \\
a_{2y} &= -\alpha_1\alpha_5 \qquad\qquad (4.11) \\
a_{2z} &= \alpha_1\alpha_4 \\
a_{3x} &= (y_{,\xi_2}\alpha_3 - z_{,\xi_2}\alpha_2) \\
a_{3y} &= (z_{,\xi_2}\alpha_1 - x_{,\xi_2}\alpha_3) \\
a_{3z} &= (x_{,\xi_2}\alpha_2 - y_{,\xi_2}\alpha_1)
\end{aligned}
$$

It should be noted that the dependance of all the quantities appearing in Eqs. (4.10a) to (4.10g) on the seven unknowns at the shock point (q_s) is now completely described. Thus we can write the seven equations [Eqs. (4.10a) thru (4.10g)] at the shock in the vectorial form

$$f_s^{n+1} = f_s(q_s^{n+1}) = 0 \qquad (4.12)$$

These equations can now be linearized around the previous iteration. Using central-differenced approximations for ξ_3 derivatives and backward-differenced approximations for ξ_1 and ξ_2 derivatives, we can rewrite these equations in the form

$$(A_s)_k^n \cdot (\Delta q_s)_{k-1}^{n+1} + (B_s^*)_k^n \cdot (\Delta q_s)_k^{n+1} + (C_s)_k^n \cdot (\Delta q_s)_{k+1}^{n+1}$$

$$(4.13)$$

$$+ \begin{bmatrix} (D_s)_k^n & 0 \\ 0 & 0 \end{bmatrix} \cdot \begin{bmatrix} \Delta q_{k,LMAX-1}^{n+1} \\ 0 \end{bmatrix} = (g_s^*)_k^n$$

where A_s, B_s^* and C_s are 7×7 matrices, g_s^* is a vector of length 7 and D_s is a 6×6 matrix. These equations represents the final set of equations to be solved at the shock point in conjunction with flowfield solution within the shock-layer.

4.2. Coupling of the Shock-Point Solution With the Inner Flowfield

As can be seen with from Eq. (4.13) the solution of the equations at the shock are coupled to the inner flowfield solution through $\Delta q_{k,LMAX-1}^{n+1}$. In order to finally solve this system of equations we note that Eq. (3.14) shows that the inner flowfield solution (from $\ell = 1,2,3..,LMAX-1$) is decoupled in the crossflow direction. Thus a forward substitution approach is used for all crossflow planes to develop the recursive relations

$$\Delta \chi_{k,\ell}^{n+1} = -R_{k,\ell} \cdot \Delta \chi_{k,\ell+1}^{n+1} + r_{k,\ell} \tag{4.14}$$

Now we note that based on our smoothing approach we can write to a second-order accuracy

$$\Delta q_{k,LMAX-1}^{n+1} \simeq \Delta \chi_{k,LMAX-1}^{n+1} \tag{4.15a}$$

$$\Delta q_{k,LMAX}^{n+1} \simeq \Delta \chi_{k,LMAX}^{n+1} \tag{4.15a}$$

The inner flowfield solution can now be related to the shock-point solution vector Δq_s^{n+1} through relations of the form

$$\Delta q_{k,LMAX-1}^{n+1} = -[R_{k,LMAX-1} \quad 0] \cdot (\Delta q_s)_k^{n+1} + r_{k,LMAX-1} \tag{4.16}$$

After substituting Eq. (4.16) into Eq. (4.13), we can reduce Eq. (4.13) to the form

$$A_k^n \cdot (\Delta q_s)_{k-1}^{n+1} + B_k^n \cdot (\Delta q_s)_k^{n+1} + C_k^n \cdot (\Delta q_s)_{k+1}^{n+1} = g_k^n \tag{4.17}$$

Equation (4.17) is now solved using appropriate reflective and symmetric boundary conditions in the leeward and windward pitch planes of symmetry. This solution gives simultaneously the Δq_s^{n+1} vectors at each shock point ($k = 1,2,3,...,KMAX$).

Using the shock point solution and the recursive relations of Eq. (4.14), we can obtain the intermediate solution vector $\Delta \chi^{n+1}$ for all interior points. The final smoothed solution at these interior points is than determined from Eqs. (3.8a) and (3.8b). The x, y and z coordinates of the new shock point locations are now determined using Eq. (4.3) and the grid is updated for the next iteration. This overall iterative process is repeated until the solution converges at all grid points, and then the solution moves on to the next marching step.

V. GRID GENERATION AND RELATED CONSIDERATIONS

Five grid-generation schemes for external flows were considered in this study; namely, (1) cylindrical grid generation, (2) parabolic grid generation, (3) body-normal grid generation, (4) a modified body-normal grid generation and (5) elliptic grid generation. The cylindrical grid-generation scheme is used for axisymmetric cross sections, while the other four grid-generation schemes can be used for nonaxisymmetric 3-D cross sections. The body-normal and modified-body-normal grid-generation schemes are used for predominantly convex cross sections, while the elliptic grid-generation scheme is for general 3-D cross sections. The following sections discuss the details of these two grid-generation schemes.

5.1. Cylindrical Grid-Generation Algorithm

A simple cylindrical grid-generation scheme has been incorporated in the code to generate the grids for simple geometries with axisymmetric cross sections, such as multiconic configurations. For such cylindrical grids the grid points between the body and the shock are generated using a simple algebraic grid-generation procedure. In this approach we define the grid-distribution function η such that it is 0 at the wall and goes to 1 at the shock. In fact the overall grid-distribution function is divided into a variably spaced grid near the wall and equally spaced grid near the shock; i.e.,

$$0 \leq \eta_L \leq \eta_{L_c} \quad \text{variable-spaced grid for } L \leq L_c$$
$$\eta_{L_c} \leq \eta_L \leq 0 \quad \text{equally-spaced grid for } L \geq L_c \tag{5.1}$$

where the break point (L_c) is defined as

$$L_c = k(LMAX) \tag{5.2}$$

The grid-distribution function η is defined by the relation

$$\Delta\eta_L = \Delta\eta_{L-1}[1 + \varepsilon_0\gamma_L] \tag{5.3}$$

where

$$\gamma_L = 1 - [2(L-2)/(L_c - 1) - 1]^2 \quad \text{for } L \le L_c$$
$$= 0 \quad \text{for } L \ge L_c \quad (5.4)$$

From Eqs. (5.2) thru (5.4) it can be seen that if 'k' and $\Delta\eta_1$ are specified, Eq. (5.3) becomes a recursive relation which only depends upon ε_0. Thus, by combining Eqs. (5.3) and (5.1), we obtain

$$\sum_{L=1}^{\text{LMAX}} \Delta\eta_L(\varepsilon_0) = 1 \quad (5.5)$$

Equation (5.5) is solved numerically to obtain the appropriate value of ε_0, and the final grid-distribution function is then generated as

$$\eta_L = \eta_{L-1} + \Delta\eta_L \quad (5.6)$$

where $\eta_1 = 0$ and L = 2,3,....,LMAX.

Since this cylindrical grid-generation scheme is very simple and allows a direct control on the grid generated, it is the best choice when considering geometries with axisymmetric cross sections. When using 50 points between the body and the shock (LMAX = 50), we typically choose k = 0.6 and $\Delta\eta_1 = 0.0001$.

5.2. Parabolic Grid-Generation Algorithm

In order to better model geometries with nonaxisymmetric cross sections, we have also incorporated a parabolic grid-generation scheme in our nonequilibrium 3-D PNS scheme. This grid-generation scheme is based on the work of Noack (1985), which was appropriately modified to suit our solution scheme. The parabolic grid-generation is a fast and efficient way of generating almost orthogonal grids in the near-body region. Actually, the differential equations solved are the same as those for a fully elliptic grid generation scheme; however, the number of iterations performed is very few.

In the parabolic grid-generation scheme of Noack (1985), the grid-generation equations used are based on the elliptic grid-generation equations. This transformation between the physical and computational space is governed by Laplace's equation. After inverting these equations, so that they represent the transformation from the computational to the physical space, we can write the grid-generation equations as

$$a_1 y_{\xi_2\xi_2} + a_2 y_{\xi_2\xi_3} + a_3 y_{\xi_3\xi_3} = 0$$
$$a_1 z_{\xi_2\xi_2} + a_2 z_{\xi_2\xi_3} + a_3 z_{\xi_3\xi_3} = 0 \tag{5.7}$$

where

$$
\begin{aligned}
a_1 &= y_{\xi_2}^2 + z_{\xi_2}^2 \\
a_2 &= -2(y_{\xi_2}z_{\xi_3} + y_{\xi_3}z_{\xi_2}) \\
a_3 &= y_{\xi_3}^2 + z_{\xi_3}^2
\end{aligned}
\tag{5.8}
$$

For the parabolic grid generation, the ξ_2 direction is chosen as the marching direction. If the index ℓ denotes the grid points in the ξ_2 direction, the parabolic formulation of the elliptic grid-generation equations [Eqs. (5.7)] is achieved by treating the grid points at $\ell + 1$ in a special manner. In the approach of Noack (1985), a simple algebraic technique to predict the grid at the $\ell + 1$ location. This predicted grid at the $\ell + 1$ location and the already calculated grid-point locations at the $\ell - 1$ location are then used to evaluate the coefficients in Eqs. (5.7). Similarly, the $y_{,\xi_2\xi_3}$ and the $z_{,\xi_2\xi_3}$ terms can be estimated and used as source terms on the right hand side of the equations. The resulting equations can be solved using a simple tridiagonal solution scheme in the ξ_3 direction.

As noted by Noack (1985), with a parabolic marching scheme it is not easy to satisfy the specified grid-point locations at the shock. This problem is also observed in the hyperbolic grid-generation schemes. In Noack's approach this problem is circumvented by using a weighting function which gradually changes the grid from a nearly orthogonal grid at the wall to an algebraic grid behind the shock. Furthermore, with this approach the computational grid smoothly blends into the specified grid-point locations at the shock. It is important to note that an important advantage of such a parabolic grid-generation scheme over a hyperbolic grid generation scheme is that the shock-point locations are specified by the user and not determined by the grid-generation scheme. This also provides the user with a better control on the grids generated. Our experience with such a grid-generation scheme has been very encouraging. We have observed that by using some care in specifying the shock points and by doing as many as 5 iterations on the parabolic grid-generation, good quality grids can be generated with reasonable ease.

5.3. Body-Normal Grid-Generation Algorithm

The body-normal grid generation scheme uses grid lines which are straight body normal in an axis-normal plane. A simple algebraic grid generation is then used to lo-

cate the grid points along these body-normal grid lines. This grid generation is faster then the parabolic grid generation scheme, while at the same time it does not have the problem of grid twisting. However, with this straight body-normal grid generation scheme, abrupt changes may occur around relatively sharp body corners due to the rapidly changing crossflow body slopes.

5.4. Modified Body-Normal Grid-Generation Algorithm

A modified body-normal grid generation scheme was developed specifically to address the grid-generation problems posed by bodies with relatively sharp corners in the cross-flow direction. In this case the grids generated are body normal everywhere except in the corner region where the grid slopes are gradually varied to provide a smoothly changing grid. For convex three-dimensional shapes, this grid-generation scheme provides a fast and efficient way of generating accurate and well-behaved grids.

5.5. Elliptic Grid-Generation Algorithm

The elliptic grid-generation scheme is based on the work of Sorenson and Steger (1978), Chaussee and Steger (1981) and Kaul and Chaussee (1984). In this approach, the elliptic grid between the body and the outer bow shock corresponds to the solution of the following elliptic partial differential equations.

$$
\begin{aligned}
ay_{\xi_3\xi_3} - 2by_{\xi_3\xi_2} + cy_{\xi_2\xi_2} &= -J^2 P \\
az_{\xi_3\xi_3} - 2bz_{\xi_3\xi_2} + cz_{\xi_2\xi_2} &= -J^2 Q
\end{aligned}
\tag{5.9}
$$

where

$$
\begin{aligned}
a &= y_{\xi_2}^2 + z_{\xi_2}^2 \\
b &= y_{\xi_2}y_{\xi_3} + z_{\xi_2}z_{\xi_3} \\
c &= y_{\xi_3}^2 + z_{\xi_3}^2 \\
J &= y_{\xi_2}z_{\xi_3} - y_{\xi_3}z_{\xi_2}
\end{aligned}
\tag{5.10}
$$

The functions P and Q in Eq. (5.9) control the grid clustering and and grid orthogonality. Numerically it is very difficult to exactly satisfy the user-specified grid-clustering distribution and also the orthogonality constraints of the elliptic grid (described by the P and Q functions inside the wall and shock region). In the present approach the P and Q functions at the wall and at the shock are based on imposing grid orthogonality con-

straints, while inside they are exponentially varied from their specified values at the wall to the specified values at the shock.

This exponential variation of the forcing functions P and Q works very well, except that the grid generated does not correspond to the grid-clustering finally required. However, one can use this grid and interpolate on it along ξ_3 = constant lines to get the desired clustering. Unlike the actual grid before interpolation, the final interpolated grid is not exactly orthogonal every where. However, it does ensure grid orthogonality at the body and the shock and also ensures that the grid lines thus generated will never cross. In short, the basic requirements for a good computational grid are satisfied.

Since the final grid is generated by interpolating on the elliptic grid in ξ_2 direction, the elliptic grid can be generated using fewer grid points in the ξ_2 direction. Furthermore, since exact orthogonality of the grid it not really needed, there is no additional advantage in driving the grid-iterations to complete convergence. Thus, we use a maximum of 30 equally-space ξ_2 grid points for the elliptic solution and limit the number of grid iterations to 25. Typically, in these iterations the grid coordinates are converged to within 0.01-0.1% of their local value and the residual norm has decreased by 3 orders of magnitude. In addition, in our scheme the full elliptic grid-generation is done only once at a marching step, which is during the first solution iteration. In subsequent solution iterations at a step, only the shock points move along ξ_3 = constant grid lines. Thus, during each iteration the elliptic grid between the body and the shock is not changed and only the grid points at the shock are adjusted to account for the shock motion. The required flowfield grid is generated by simply interpolating on this adjusted elliptic grid. This approach accounts for substantial computational savings, while retaining the powers of a full elliptic grid generation.

VI. MODIFICATIONS FOR 2-D/AXISYMMETRIC INTERNAL FLOWS

The coordinate system used in this 2-D/axisymmetric internal-flow PNS scheme is a general curvilinear coordinate system (ξ_1, ξ_2). The ξ_1 coordinate is along the channel axis and is also the marching direction. The ξ_2 coordinate stretches from the channel axis to the outer wall boundary, and lies in an axis-normal plane (see Fig. 3).

The flowfield unknowns are the density (ρ), the density-velocity products $(\rho u, \rho v$ and $\rho w)$, the density-temperature product (ρT) and the pressure (p). Here u, v and w are the velocity components in x, y and z directions, respectively. Although $v = 0$ for 1-plane 2-D/axisymmetric flows, it has been retained in the numerical formulation to simplify future extensions. The five equations representing the differential conservation of mass, momentum and energy are mathematically closed by using the equation of state for the gas. The gas models treated in this internal flow study consist of perfect-gas, equilibrium-air and nonequilibrium-air gas models.

The overall approach used is very similar to our 3-D PNS approach for external flows. Briefly speaking, after expanding the solution around the previous (n-th) iteration, using two-point streamwise differencing, and using central-differenced approximations for all ξ_2 derivatives, we can write these governing equations in a block-tridiagonal system of equations. This system of equations is then solved to obtain the solution changes between the previous (n-th) and the current (n+1) iterations. In order to damp the numerical solution oscillations caused by these central-differenced approximations, we use a fourth-order dissipation approach for the pressure field. In addition, a second-order streamwise dissipation model is also used to suppress any numerical oscillations caused by the use of small marching step sizes.

The boundary conditions along the channel axis consist of six independent relations representing the equation of state and the physical conditions along the channel axis. However, the flow along the channel axis is numerically complicated by the existance of a geometric singularity at the channel axis (r = 0, where r is the radial distance from the channel axis). This geometric singularity is primarily due to a singularity in the

transformation Jacobian (J) along the channel axis ($r = 0$). However, this is a removable singularity, and the effects of this geometric singularity can be removed by appropriately expanding the metric derivatives in the small region around the channel axis ($r = 0$). Analysis shows that along the channel axis these terms can be written as

$$
\begin{aligned}
J(r) &= -1/rr_{\xi_2} \\
\xi_{1,x}(r) &= 1 \\
\xi_{1,y}(r) &= 0 \\
\xi_{1,z}(r) &= 0 \\
\xi_{2,x}(r) &= r_{\xi_1}/r_{\xi_2} \\
\xi_{2,y}(r) &= 0 \\
\xi_{2,z}(r) &= 1/r_{\xi_2}
\end{aligned}
\tag{6.1}
$$

In the governing equations, these terms typically appear as either of the form $\xi_{1,x_j}/J$ (convective terms) or of the form $\xi_{2,x_i}\xi_{2,x_j}/J$ (thin-layer viscous terms). However, if these terms are evaluated as ratios rather than calculated individually, it is seen that all these metric ratios have actually a finite value of zero at $r = 0$. When used in the governing equations, these metric terms result in zero viscous effects and zero U_2 velocity along the channel axis, where U_2 is the contravariant velocity in the ξ_2 direction. Furthermore, these results are also consistent with the boundary conditions along the 2-D/axisymmetric channel axis.

The problem represented by the governing 2-D/axisymmetric PNS equations is also a split-boundary-value problem; i.e., the equations are hyperbolic-parabolic in the ξ_1 direction and elliptic in the ξ_2 direction. Thus, in order to solve the problem completely, we need initial conditions to be specified at the start of the marching procedure and boundary conditions to be specified along the channel axis and at the outer wall boundary (away from the channel axis).

The boundary conditions along the channel axis consist of simple reflective and symmetry boundary conditions. These boundary conditions imply that along the channel axis $\rho_{,\xi_2} = (\rho u)_{,\xi_2} = (\rho v) = (\rho w)_{,\xi_2} = (\rho T)_{,\xi_2} = p_{,\xi_2} = 0$. The outer wall boundary consists of isothermal, no-slip boundary conditions and assumes that the axis-normal pressure gradient at the wall is zero ($p_{,\xi_2} = 0$). When combined with the equation of state, these

wall-boundary conditions provide six mutually-coupled equations to be solved at the wall.

As far as the initial conditions to start the PNS internal-flow marching procedure are concerned, they need to be appropriately generated in an internally consistent manner. This internal consistency is important because flowfield inconsistencies may lead to numerical difficulties in obtaining a converged solution. This is especially true in the near-wall region. In the present case, the initial profiles for the various internal-flow calculations were generated assuming a slug-flow condition. In this case uniform inflow conditions were assumed everywhere except at the wall, where the wall density and wall-temperature were adjusted to account for the specified wall temperature.
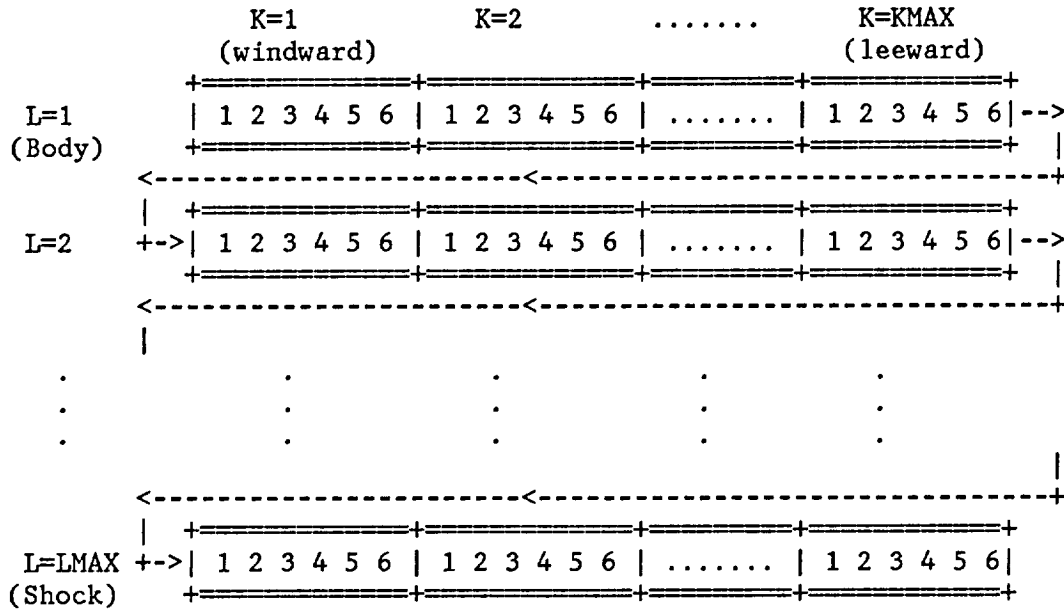
VII. VECTORIZATION STUDIES WITH THE 3-D PNS SCHEME

In this vectorization study, we have mainly emphasized a better management of the fast-core memory, appropriate re-structuring of the loop indicies to minimize the strides and memory-paging operations, and a re-formulation of the predictor-corrector solution scheme to make it more vectorizable. The present solution scheme involves a block-matrix solution approach, which is typical of most of the present-day implicit flowfield solvers. These block-matrix solvers represent efficient solution schemes for computers which predominantly perform scalar operations. Since the sizes of the block matrices involved are typically between 4 and 6 (depending upon the particular solution scheme), a direct implementation of these solution schemes on vector machines does not produce any significant operational improvement. Any significant speed-up of the corresponding vectorized operations requires the development of an entirely different storing and indexing strategy, which also has to take into account the non-recursive and vectorizable direction of operations.

Another problem with these block-matrix solvers is that they involve a large number of vector-matrix multiplications, matrix-matrix multiplications and inversions of the small block matrices. If the indexing strategy is not properly chosen, these simple operations may either require access to information which is not within the same memory bank or, even worse, may require the replacement of the current memory bank with new information from the core memory. Thus, several system I/O operations may be required to perform these simple operations. The problem gets more complicated when we consider the additional constraint that, with the current auto-vectorization features on IBM or Cray-like machines, only the inner most loops are vectorized. Thus, for best auto-vectorization results, most loop structures need to consist of either one big loop or a big loop nested inside a small outer loop.

7.1. Array Indexing and Memory Access Strategy

In our PNS formulation, the stored matrix elements require addressing indicies of the form (K,L,N,M), and the vector elements require addressing of the form (K,L,N). Here

K is the crossflow index, L is the axis-normal index, N is the row index and M is the column index. After careful consideration of the various options, we believe that the best possible strategy is to store the matrix elements as a double index (KLN,M) and the vector elements as a single index (KLN). When doing operations which are only recursive in the axis-normal (L) direction, the KLN index is defined as $KLN=(L-1)*KMAX*6 + (K-1)*6 + N$. The schematic description of this indexing strategy for storing vectors is shown below.
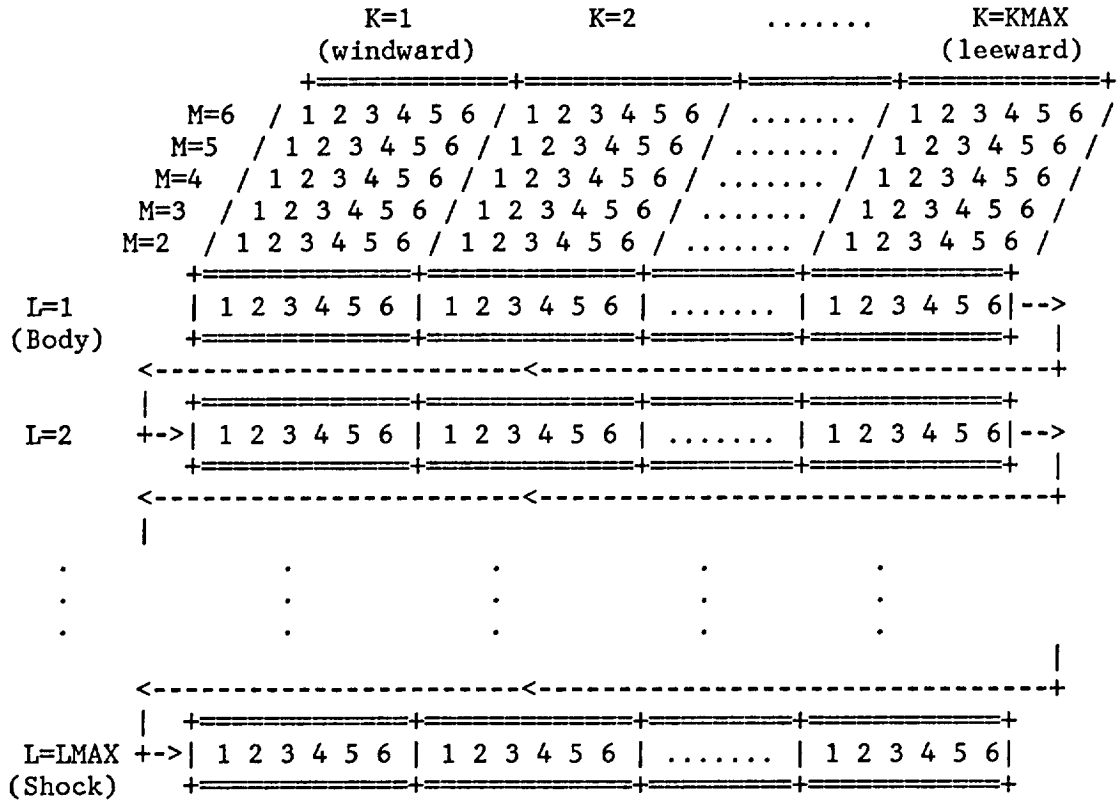
```
                 K=1              K=2        .......    K=KMAX
               (windward)                             (leeward)
            +============+============+========+============+
    L=1     | 1 2 3 4 5 6 | 1 2 3 4 5 6 | ....... | 1 2 3 4 5 6|-->
   (Body)   +============+============+========+============+    |
          <----------------------------<---------------------------+
          |   +============+============+========+============+
    L=2   +-->| 1 2 3 4 5 6 | 1 2 3 4 5 6 | ....... | 1 2 3 4 5 6|-->
              +============+============+========+============+    |
          <--------------------------<---------------------------+
          |

        .         .         .         .         .
        .         .         .         .         .
        .         .         .         .         .
                                                              |
          <----------------------------<---------------------------+
          |   +============+============+========+============+
  L=LMAX  +-->| 1 2 3 4 5 6 | 1 2 3 4 5 6 | ....... | 1 2 3 4 5 6|
  (Shock)     +============+============+========+============+

      Thus,  V(1),V(2),V(3),....,V(KLN),....,V(LMAX*KMAX*6)
             where KLN=[(L-1)*KMAX+K-1]*6 + N
```

Schematic description of the vector storage

On the other hand, when doing operations which are recursive in the crossflow (K) direction, the KLN index is defined as $KLN=(K-1)*LMAX*6 + (L-1)*6 + N$. Thus, for any given grid point (K,L) all the row elements occupy successive storage locations in the same memory bank, and are simultaneously available.

As far as the column elements (M) are concerned, their storage locations may vary with the computer at hand. For IBM-type computers where the storage is in column form, the present approach will be ideal because for any (K,L) location all the 36 matrix elements will be stored in 36 consecutive locations in the same memory bank, and will

be simultaneously available for operations. The schematic description of this indexing strategy for storing matrices is shown below.

```
                    K=1              K=2          .......       K=KMAX
                 (windward)                                   (leeward)
                 +===========+===========+=======+===========+
        M=6   / 1 2 3 4 5 6 / 1 2 3 4 5 6 / ....... / 1 2 3 4 5 6 /
        M=5   / 1 2 3 4 5 6 / 1 2 3 4 5 6 / ....... / 1 2 3 4 5 6 /
        M=4   / 1 2 3 4 5 6 / 1 2 3 4 5 6 / ....... / 1 2 3 4 5 6 /
        M=3   / 1 2 3 4 5 6 / 1 2 3 4 5 6 / ....... / 1 2 3 4 5 6 /
        M=2   / 1 2 3 4 5 6 / 1 2 3 4 5 6 / ....... / 1 2 3 4 5 6 /
              +===========+===========+=======+===========+
  L=1         | 1 2 3 4 5 6 | 1 2 3 4 5 6 | ....... | 1 2 3 4 5 6|-->
  (Body)      +===========+===========+=======+===========+    |
           <-----------------------<----------------------------+
           |  +===========+===========+=======+===========+
  L=2      +->| 1 2 3 4 5 6 | 1 2 3 4 5 6 | ....... | 1 2 3 4 5 6|-->
              +===========+===========+=======+===========+    |
           <--------------------<-------------------------------+
           |
           .          .         .          .        .
           .          .         .          .        .
           .          .         .          .        .
                                                                |
           <---------------------<-----------------------------+
           |  +===========+===========+=======+===========+
  L=LMAX +->| 1 2 3 4 5 6 | 1 2 3 4 5 6 | ....... | 1 2 3 4 5 6|
  (Shock)     +===========+===========+=======+===========+
```

Thus, A(1,M),A(2,M),A(3,M),....,A(KLN,M),....,A(LMAX*KMAX*6,M)
where KLN=[(L-1)*KMAX+K-1]*6 + N
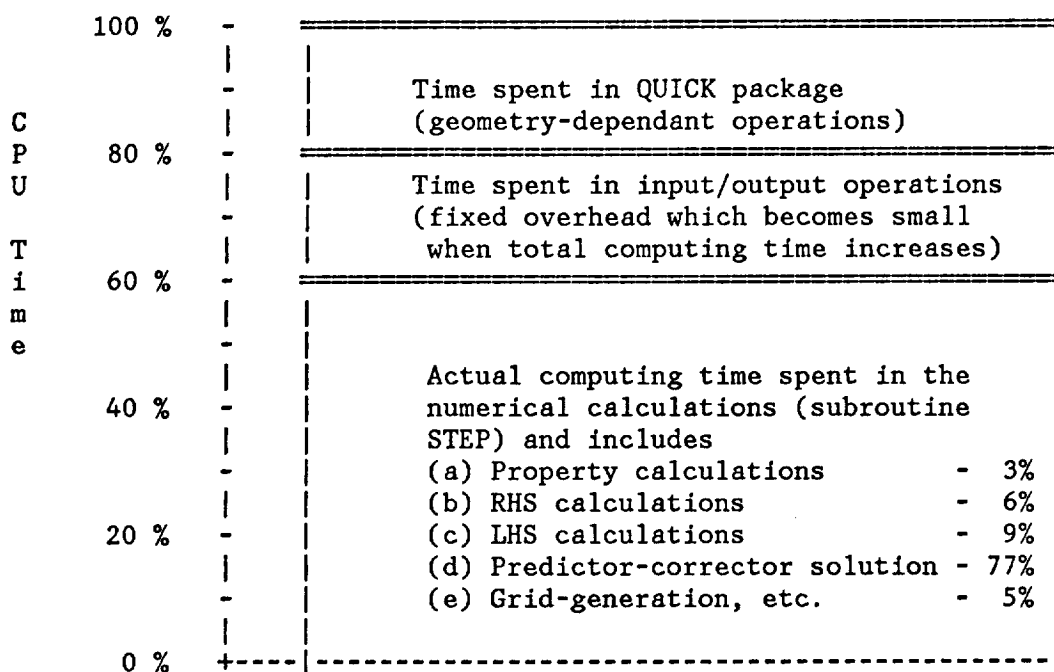
Schematic description of the matrix storage

On Cray-type machines where the storage is in row form, with the present approach each of the column elements will be stored at locations which are KLNMAX apart, where KLNMAX is the maximum dimension specified for the KLN index. On such Cray-like machines the memory banks are stored in a form analogous to a rotating table. Thus, one can choose the KLNMAX value to be such that the effective stride has a acceptable value, such as 1. Thus we believe that our storing strategy will be well suited for almost all IBM or Cray-like computers which support auto-vectorization. We have performed some sample vectorization tests on the NAS Cray-2 and Cray-Y/MP computer facility at the NASA Ames Research Center, CA, in which we tested the matrix-matrix multiplications, matrix-vector multiplications and matrix inversion algorithms using the proposed indexing strategy, and compared it with the corresponding approach using the classical nested-loop way of doing such operations. The results indicated that,

with the propsed indexing strategy, the simple matrix-matrix and matrix-vector multiplications performed 2-3 times faster, while the matrix inversion algorithm worked 15-16 times faster.

With this indexing strategy, apart from the aforementioned vector/matrix operations, various other load and store operations involved in our 3-D PNS code have also become more vectorizable. We have revised our 3-D perfect-gas and equilibrium-air PNS code to use this indexing strategy and loop restructuring.

7.2. Initial Timing Studies

Before making any vectorization changes, we did a timing study on our 3-D PNS code at a typical marching step using a 31x30 crossflow grid. The results showed that, at a marching step for the particular test case being considered, the QUICK geometry calculation took nearly 20% of the total time, the output and disk storing operations accounted for another 20% of the total time, and 60% of the time was spent in doing the actual numerical solution. A schematic description of the distribution of computing time spent in the PNS calculations is given below.

```
          100 %  -   =========================================================
                 |   |                                                       |
                 -   |   Time spent in QUICK package                         |
   C             |   |   (geometry-dependant operations)                     |
   P      80 %   -   =========================================================
   U             |   |   Time spent in input/output operations               |
                 -   |   (fixed overhead which becomes small                 |
   T             |   |    when total computing time increases)               |
   i      60 %   -   =========================================================
   m             |   |                                                       |
   e             -   |                                                       |
                 |   |   Actual computing time spent in the                  |
          40 %   -   |   numerical calculations (subroutine                  |
                 |   |   STEP) and includes                                  |
                 -   |   (a) Property calculations        -  3%              |
                 |   |   (b) RHS calculations             -  6%              |
          20 %   -   |   (c) LHS calculations             -  9%              |
                 |   |   (d) Predictor-corrector solution - 77%              |
                 -   |   (e) Grid-generation, etc.        -  5%              |
                 |   |                                                       |
           0 %   +---|-------------------------------------------------------|
```

Typical distribution of computing time spent at a marching step

The numerical solution is done by one controlling subroutine (STEP), so we have focussed our attention on vectorizing this subroutine. The subroutine STEP consists of five (5) distinct operations; namely, (i) turbulent viscosity calculations, (ii) evaluation of the explicit right-hand-side (RHS) terms, (iii) evaluation of the implicit left-hand-side (LHS) terms, (iv) the predictor-corrector solution and (v) grid generation and solution updating. As shown in the illustration obove, for the first iteration of the test case calculations, before any vectorization modifications, the turbulent viscosity and gas property calculations accounted for 3% of the time spent in subroutine STEP, the RHS calculations took 6% of the time, the LHS calculations took 9% of the time, the predictor-corrector solution took 77% of the time, and the grid-generation accounted for the remaining 5% of the time spent in subroutine STEP.

7.3. Vectorization and Restructuring Studies

In our vectorization studies we concentrated on modifying (a) the viscosity and gas property calculations, (b) the RHS calculations, (c) the LHS calculations, and (c) the predictor-corrector solution scheme. The results show that with our indexing strategy and loop re-structure, the time taken by the viscosity calculations was reduced by a factor of 2-3, the time taken by the RHS calculations was reduced by a factor of 6-7, and the time taken by the LHS calculations was reduced by a factor of 5-6. As far as the predictor-corrector solution scheme is concerned, typically, the predictor step and the subsequent corrector step take nearly equal amount of time. The results show that with the present modifications the time taken by the predictor step as well as the corrector step was reduced by a factor of 4-5. Finally, the results of this vectorization effort and the associated timing studies show that with our current code-reorganization and restructuring, the time taken by subroutine STEP has been reduced by a factor of 4-5. This means that the overall computing time for a particular 3-D calculation will also be reduced by nearly a factor of 4-5. For 2-D/axisymmetric calculations, however, the results show a factor of 2 reduction in the required computing time.

VIII. A SIMPLIFIED ANALYSIS FOR DEPARTURE

Unlike classical PNS treatments in the present approach the governing PNS equations are written in as a differential/algebraic system rather than a pure differential system. By a differential/algebraic system we mean a system of equations composed of several differential equations coupled together through an algebraic relation. In the present PNS formulation the differential equations governing the conservation of mass, momentum and energy are coupled together through the algebraic relation representing the equation of state. By studying a model differential/algebraic problem (see Appendix I) we have been able to show that unlike classical PNS treatments (Schiff and Steger, 1979; Shanks et al., 1979; Chaussee et al., 1981; and Vigneron et al., 1978) the present formulation is unconditionally time-like (Bhutta and Lewis, 1985c and 1985d). In order to further demonstrate this approach we also studied a simplified version of the governing PNS equations. The general outline and conclusions of this simplified eigenvalue analysis are briefly presented in the following discussion.

In order to simplify the required mathematics, let us restrict ourselves to

(a) two-dimensional perfect-gas flows, and
(b) an evenly spaced square grid such that $\xi_{1,x} = \xi_{2,z} = 1$ and $\xi_{1,z} = \xi_{2,x} = 0$

The simplification of a perfect gas is done with the understanding that even for the actual multi-component reacting-gas case the fluid is still assumed to be a mixture of perfect gases. Consequently the basic numerical scheme has to be at least stable for a single-species perfect-gas model. Furthermore, we choose to approximate the equation of state for a perfect gas by

$$\gamma p - \rho T + \theta(p_{,\xi_1} + p_{,\xi_2}) = 0 \tag{8.1}$$

where the coefficient 'θ' is chosen such that $\theta \simeq 0$, and for all practical purposes

$$\theta p_{,\xi_1} + \theta p_{,\zeta} + \gamma p - \rho T \simeq \gamma p - \rho T$$

It should be noted that the use of this coefficient θ is for the sole purpose of the following stability analysis, and not for the actual solution scheme. In other words, the actual solution corresponds to the use of $\theta = 0$. The reason for introducing this coefficient $'\theta'$ is that it makes the streamwise jacobian matrix nonsingular, so that one can perform certain matrix operations to simplify the stability analysis. Furthermore, there are no mathematical tools available to directly determine the character of differential/algebraic systems. The available mathematical tools are strictly for purely differential systems. Thus, by introducing the coefficient $'\theta'$ in Eq. (8.1) we are able to transform our differential/algebraic problem into a purely differential form, which can then be analyzed.

The choice of 'small enough θ' does not adversly affect the resulting conclusions. In other words we can take the limit $\theta \to 0$. This is indeed a heuristic approach, and the justification comes from the model differential/algebraic problem discussed in Appendix D. The use of $'\theta'$ in Eq. (8.1) corresponds to the use of the $'\varepsilon'$ term in Formulation II of the model problem. For this model problem it has been shown in Appendix D that the choice of $\varepsilon \to 0^+$ does not produce any singularity in the final solution. This fact has also been numerically demonstrated by the present authors in their earlier work (Bhutta and Lewis, 1985d).

With the equation of state given by Eq. (8.1), and after neglecting the viscous terms containing the contributions of w and $w_{,\xi_2}$, we can write the simplified PNS equations as

$$(A_1^n \cdot d)_{,\xi_1} + (A_2^n \cdot d)_{,\xi_2} - \varepsilon[M^n \cdot d]_{,\xi_2} - A_0^n \cdot d$$
$$= -[f_{1,\xi_1}^n + f_{2,\xi_2}^n - \varepsilon s_{,\xi_2}^n - h^n] \tag{8.2}$$

where

$$d = \Delta q^{n+1} \tag{8.3}$$

and A_1^n, A_2^n and M^n are the jacobian matrices.

If we assume that A_1^n, A_2^n and M^n do not change with ξ_1 and ξ_2 (a frozen coefficient analysis), we can write

$$A_1^f \cdot d_{,\xi_1} + A_2^f \cdot d_{,\xi_2} - B^f \cdot d_{,\xi_2\xi_2} + c = 0 \tag{8.4}$$

Although the above equation is a significantly simplified version of the original PNS equations, it is still difficult to study directly. As a further simplification, we choose to separately look at the viscous and inviscid limits of Eq. (8.4). We also note that as a minimum criterion of streamwise stability (which in this case, and for the class of PNS schemes based on the Schiff-Steger formulation, implies a marching-like character of the governing equations), the "simplified PNS equations" being studied have to be streamwise stable (i.e., marching-like in the streamwise direction) in the viscous as well as the inviscid limits. In the following sections we look into the streamwise stability (marching-like character) of the viscous and the inviscid limits of Eq. (8.4).

8.1. Inviscid Limit

The inviscid limit of Eq. (8.4) can be written as

$$d_{,\xi_1} + [A_1^{\Gamma^{-1}} A_2^f] \cdot d_{,\xi_2} + A_1^{\Gamma^{-1}} \cdot c = 0 \tag{8.5}$$

or

$$d_{,\xi_1} + N_1 \cdot d_{,\xi_2} + c = 0 \tag{8.6}$$

This equation is now in a form which can be easily studied. For Eq. (8.6) to be stable, the ξ_1 direction should be a valid marching direction. In other words, Eq. (8.6) has to be hyperbolic/parabolic or marching-like always. This condition is satisfied if the eigenvalues of N_1 are all real. If for simplicity we assume that $w << u$, then an eigenvalue analysis gives the eigenvalues of N_1 as (Bhutta and Lewis, 1985d)

$$\lambda_i = (1, w/u, w/u, w/u, w/u) \tag{8.7}$$

Thus, we see that all the eigenvalues of N_1 are unconditionally real. That is to say, the simplified PNS equations being studied are unconditionally marching-like in the inviscid limit and represent a stable marching scheme in the subsonic as well as the supersonic flow regions.

It is of interest to consider the case where (like conventional non-iterative PNS schemes) we do not uncouple the pressure terms. In such a case the form of A_1^f is similar to the one studied by Schiff and Steger (1979). The only difference is that we have ρT as the independent variable rather than 'e'. The A_1^f matrix for such a case is nonsingular and, thus, can be inverted. However, the eigenvalues of N_1 for such a case

(where we do not uncouple the pressure) turn out to be complex in the subsonic flow regions, and the marching scheme becomes unstable (not marching-like; i.e., elliptic) unless methods such as the sublayer approximations of Schiff and Steger (1979) or Vigneron et al. (1978) are used.

8.2. Viscous Limit

In the viscous limit, Eq. (8.4) simplifies to

$$\mathbf{d}_{,\xi_1} = [A_1^{\Gamma^{-1}} B^f] \cdot \mathbf{d}_{,\xi_2\xi_2} + A_1^{\Gamma^{-1}} \cdot \mathbf{c} \tag{8.8}$$

or

$$\mathbf{d}_{,\xi_1} = N_2 \cdot \mathbf{d}_{,\xi_2\xi_2} + \mathbf{c} \tag{8.9}$$

In this form, the stability analysis becomes much simpler. The criterion of a stable marching scheme requires that Eq. (8.9) should be parabolic. The parabolic character depends upon the eigenvalues of N_2, which should be real. Furthermore, in order to have positive diffusion effects in the ξ direction, these eigenvalues should also be positive. Thus, for the viscous limiting case to be stable, the eigenvalues of N_2 should be real and positive. An eigenvalue analysis of N_2 shows that the eigenvalues are (Bhutta and Lewis, 1985d)

$$\sigma_i = (0, 0, \varepsilon\mu/\mathrm{Pr}\rho u, \ 4\varepsilon\mu/3\rho u, \ \varepsilon\mu/\rho u) \tag{8.10}$$

Thus, the eigenvalues σ_i are always real; however, they are positive only if $u > 0$. That is to say, as long as no flow reversal occurs in the streamwise direction, the viscous limit of the simplified PNS equations is also unconditionally marching-like. Since flow reversal means axial separation, this streamwise stability requirement actually tells us that a "single-sweep" solution of these PNS equations can not be marched through regions of axial flow separation. Of course, this conclusion comes as no surprise and has been a well accepted fact in fluid mechanics for a long time. It may be of value to note that the viscous terms do not include any pressure terms and, thus, for the present scheme as well as the previous PNS schemes the viscous terms do not provide any speed-of-sound contribution to the eigenvalues of the viscous limit. The speed-of-sound contributions to these eigenvalues for the viscous limit can come only from the jacobian matrix corresponding to the streamwise convective terms. For the classical PNS

schemes (Schiff and Steger, 1979; Shanks et al., 1979; Chaussee et al., 1981; and Vigneron et al., 1978), this speed-of-sound contribution is the one which causes the problem of negative eigenvalues in the subsonic sublayer region. For the present PNS scheme, although the speed of sound does appear in the streamwise jacobian matrix ($A_i^\prime$), it does not contribute to the eigenvalues in the viscous limit.

IX. RESULTS AND DISCUSSION

A brief overview of the main features of the present PNS scheme is given in Appendix J along with a point-by-point comparison with classical non-iterative PNS schemes. In order to evaluate the applicability of this PNS scheme, in this study several external flow and internal flow calculations were done using perfect-gas, equilibrium-air and nonequilibrium-air gas models. The main results of these 3-D external flow and 2-D/axisymmetric internal flow calculations are discussed in the following sections.

9.1. 3-D External-Flow PNS Calculations

For these 3-D external-flow studies, we studied the 5-deg angle-of-attack flow around a sample lifting configuration at a Mach number of 20. The flight altitude for this test case was 125 kft, and the wall temperature was kept fixed at 2000 degrees Rankine. The freestream conditions for this case are given in Table 4, and the vehicle geometry is shown in Fig. 4. This model geometry was developed using the QUICK geometry package (Vachris and Yeager, 1974). It consists of a spherically blunt elliptical cross section with a flat bottom. This vehicle has a nose radius of 0.1 inch and has a total length of 50 Rn. The foremost nose-afterbody tangent point for this geometry is at 0.778 Rn, and the side surface has a compression corner between 20-25 Rn. The wall temperature for these calculations was fixed at 2000 °R, and only fully laminar flow conditions were considered. For nonequilibrium-air calculations, only fully-catalytic wall boundary conditions were used.

9.1.1. Grid-Generation Results

In order to better model the geometry and the flowfield around it, in this Case 1 study we have looked at the use of (a) a parabolic grid generation, (b) a body normal grid generation, (c) a modified body-normal grid generation and (d) an elliptic grid generation. The modified body-normal grid-generation scheme was used in the Case 1c calculations, the body-normal grid-generation scheme was used in Case 1d and the parabolic grid-generation scheme was used in Case 1e. In order to make a realistic comparison, the crossflow grid distribution used at the surface in all cases was the same.

Some sample grids generated at x = 30 Rn by using these schemes are shown in Figs. 5 thru 9. The grid generated using the parabolic grid-generation scheme is shown in Fig. 5, the body-normal grid is shown in Fig. 6 and the modified body-normal grid is shown in Fig. 7. As can be seen from these grids, for the case considered, all the grid generation schemes work reasonably well. There are, however, some important differences in the final grids generated. The parabolic grid shown in Fig. 5 shows a small amount of grid twisting developing around the lower body corner. This twist has started to develop even after efforts were made to match the crossflow grid distribution at the body and the shock. Furthermore, if the crossflow grid in the corner region was made any finer, there would be a substantial increase in grid distortion. The corresponding body-normal grid given in Fig. 6 shows that although the grid twisting is eliminated, due to the rapidly changing body slopes around the corner region, the crossflow grid distribution away from the body is not good. The modified body-normal grid in Fig. 7 shows that the grid-twisting and the crossflow grid-spacing problems of the parabolic and the body-normal grids have been adequately resolved.

Although the modified body-normal and the parabolic grids shown look similar, the important difference is that farther down the body length the parabolic grids become excessively distorted while the modified body-normal grids are still well behaved. The computing times given in Table 5 show yet another important difference in the effects of these grids. These computing times show that the calculations with the body-normal and the modified body-normal grid generation schemes take nearly 15-20% less time than the corresponding calculations using the parabolic grid generation scheme. Thus we see that our modified body-normal grid-generation scheme not only provides better quality grids for such geometries, but it is also faster and more efficient.

Figure 8 shows the elliptic grid for the geometry and flowfield conditions of the perfect-gas Case 1. The elliptic grid shown in Fig. 8 was generated at an axial location of 28 Rn, and used 31 crossflow planes and 30 points between the body and the shock. The wall boundary points were generated using equally spaced ξ_3 (crossflow) arclength, whereas the corresponding boundary points at the shock were located using body-normal lines from the grid points on the body. The initial guess on the elliptic grid was generated by joining the corresponding grid points at the body and at the shock by straight lines; in short a body-normal grid. Consequently, just like the body-normal grid of Fig. 7, the initial crossflow grid spacing around the side corner was much to large. This choice was made deliberately to see how the elliptic grid generation improves the grid distribution. Figure 9 shows the $\xi_3 =$ constant grid lines for this case and shows that,

compared to a straight body-normal grid, the elliptic grid-generation scheme does indeed improve the crossflow grid spacing in the near-wall region.

9.1.2. Perfect-Gas and Equilibrium-Air Flowfield Predictions

Several types of calculations were done to study these cases, which are summarized in Table 5. Cases 1a thru 1e are for a perfect-gas model, while Case 2 is for an equilibrium-air gas model. Case 1a corresponds to a 51x30 grid with fourth-order smoothing and was done using the modified body-normal grid-generation scheme. Case 1b corresponds to a 31x30 grid with fourth-order smoothing effects, while Case 1c corresponds to a 31x30 grid with second-order smoothing effects. Cases 1d and 1e are for 31x30 grids using body-normal and parabolic grid-generation schemes, respectively. Except for the equilibrium-air gas model used, the grid generation and smoothing used in Case 2 is the same as the one used for Case 1b. In all these grids, the grid-spacing near the wall was kept at 0.01% of the local shock-standoff distance. It should be noted that only the Case 1a calculations were carried over the entire body length, whereas, the calculations for Cases 1b thru 1e and Case 2 calculations were done for only the first 30 nose radii of the body length.

The results of the Case 1a (perfect-gas) calculation are shown in Figs. 10 thru 16. The grid detail around the corner region of the geometry at x = 30 Rn is shown in Fig. 10. The perfect-gas pressure contour plots at x = 20 Rn, x = 30 Rn, x = 40 Rn and x = 50 Rn along the body are shown in Figs. 11 thru 14, respectively. These figures clearly show a strong embedded shock around the lower corner surface which is quite developed by x = 30 Rn. By x = 40 Rn this embedded shock starts to interact and impinge on the bow shock, and in the process pushes the bow shock outwards along the corner region. The embedded shock wave is still clearly visible in these contour plots. By x = 50 Rn the embedded shock has mostly coalesced with the bow shock; however, the shock surface is still quite distorted because of the rapidly changing body geometry (especially the corner region) and the resulting strong interaction with the embedded shock wave. It is important to note that despite the large changes and the strong interaction encountered at the bow sock, the shock shape predicted is smooth and the solution converges quickly. This is indeed a credit to the new fully-implicit and crossflow-coupled shock-fitting scheme used. The corresponding temperature and density contours at x = 30 Rn are shown in Figs. 15 and 16, respectively.

The results of the Case 2 (equilibrium-air) calculation are shown in Figs. 17 thru 19. This Case 2 calculation uses a 31x30 grid along with the fourth-order smoothing formulation. The crossflow pressure contours for this equilibrium-air case at x = 30 Rn are shown in in Fig. 17. The corresponding temperature contours at x = 30 Rn are shown in Fig 18, and the density contours are shown Fig. 19.

9.1.3. Nonequilibrium-Air Flowfield Predictions

The crossflow pressure contours for the nonequilibrium-air Case 3a calculation at x = 20Rn, x = 30Rn, x = 40Rn and x = 50Rn are shown in Figs. 20 thru 23, respectively. Just like the perfect-gas case, the effects of the 7.5 deg compression turn at x = 25Rn (and at $\phi = 90°$) are clearly visible. The embedded compression wave can be seen to move toward the bow shock, interact with the bow shock and push it outwards. It can be seen that despite the strong gradients in the flowfield, the predicted flowfield solution is quite well behaved. As can be seen from these figures, a strong embedded shock is clearly developed by x = 30Rn and impinges on the outer bow shock by x = 40Rn. By x = 50Rn the embedded shock and the bow shock have almost coallessed in the vicinity of the corner region; whereas, away from the corner region there is still some weak evidence of the embedded shock wave.

The axial distribution of the surface pressure along the windward ($\phi = 0°$) and the leeward ($\phi = 180°$) pitch planes are shown in Fig. 24, and the corresponding crossflow distribution of the wall pressure at the body end (x = 50 Rn) is shown in Fig. 25. These figures include the predictions of both Case 3a (51x30 grid) and Case 3b (31x30 grid) calculations. These results show that the wall pressure is equally well predicted with the coarse (Case 3b) grid. Along the windward side the surface pressure is almost constant and sharply rises as we approach the the side corner ($\phi = 90°$). The flow then rapidly expands around this corner region, goes through some over expansion and then recompresses slightly as we approach the leeward pitch plane. The corresponding crossflow distribution of the shock-standoff distance at the body end is shown in Fig. 26, and shows the rapid thinning of the shock layer around the corner region. Again, there is no noticable difference between the predictions of the fine (Case 1) and coarse (Case 2) crossflow grids.

The axial distributions of the wall heat-transfer rate along the windward and leeward pitch planes are shown in Fig. 27, and the corresponding crossflow distribution at the body end is shown in Fig. 28. Figure 27 shows that along the body the predictions of

the fine crossflow grid (Case 3a) and the coarse crossflow grid (Case 3b) are in very good agreement with each other. The maximum differences are around the $x = 25$ Rn location, where the fine grid (Case 3a) predictions are about 10% higher than the corresponding coarse grid (Case 3b) predictions. However, in the afterbody region these predictions become even closer. Figure 28 shows the crossflow distribution of heat-transfer rate at the body end, and shows that the Case 3a and Case 3b predictions are almost identical every where except on the leeside where the coarse grid (Case 3b) predictions are about 5% lower. The corresponding crossflow distribution of the streamwise skin-friction coefficient is shown in Fig. 29. As expected, the skin-friction predictions follow the same trend as the aforementioned predictions of the surface heat-transfer.

The predicted species concentration distributions for the Case 3a (51×30 grid) calculations are shown in Figs. 30 thru 39. The crossflow contour plots of the predicted electron number density ($1/cm^3$) at $x = 20Rn$, $x = 30Rn$, $x = 40Rn$ and $x = 50Rn$ locations are shown in Figs. 30 thru 33, respectively. These results show that the predicted electron-density distribution (as well as the related species mass-fractions) is smooth and well behaved, and the gradients have also been captured quite well. This is reflective of the quality of the present 3-D nonequilibrium PNS solution scheme. Another important feature seen from these figures is the fact that, as the lower body corner becomes more pronounced, the dissociation and ionization levels in the vicinity of this lower corner decrease. This is consistent with the strong convection effects away from this corner region, which tends to move the dissociated and ionized species away from the corner toward the leeward and windward sides. This is a good example of the flowfield chemistry being strongly influenced by the three-dimensional nature of the vehicle geometry.

The corresponding crossflow contours of the species mass-fractions at the the body end are shown in Figs. 34 thru 39. The species mass-fractions of O and O_2 are shown in Figs. 34 and 35, whereas the N and N_2 mass-fractions are shown in Figs. 36 and 37. Figures 38 and 39 show the predicted mass-fractions of NO and NO^+ at the body end. In all cases the predicted mass-fraction distributions are smooth and well behaved

9.1.4. Gas Model Effects

The Case 1a (perfect-gas), Case 2 (equilibrium-air) and Case 3b (nonequilibrium-air) calculations in this study use the same computational grid and the same numerical scheme, and differ only in the gas model used. Thus, these numerical calculations rep-

resent a good data base to study the effects of the using different gas models when studying such complex 3-D configurations.

The axial and crossflow distributions of the various flowfield quantities obtained using perfect-gas, equilibrium-air and nonequilibrium-air gas models are shown in Figs. 40 thru 45. carried out only up to $x = 30$ Rn, whereas the nonequilibrium-air calculations extend up to the body end ($x = 50$ Rn).

The axial distribution of surface pressure is shown in Fig. 40, while the corresponding crossflow distribution at $x = 30$ Rn is shown in Fig. 41. These results show that, in general, the present nonequilibrium-air predictions are bounded on the upper side by the perfect-gas predictions and on the lower side by the equilibrium-air predictions. Even so, the nonequilibrium surface-pressure predictions are much closer to the corresponding perfect-gas predictions than the equilibrium-air predictions.

The crossflow distribution of the shock-standoff distance at $x = 30$ Rn is compared in Fig. 42. These results show that under these flowfield conditions the nonequilibrium shock-standoff distance along the windward and leeward sides is in close agreement with the perfect-gas prediction, which is much larger than the corresponding equilibrium-air prediction. However, in the corner region the predicted nonequilibrium shock-standoff distance is much closer to the corresponding equilibrium-air value. In general, the nonequilibrium predictions of the shock-standoff distance are bounded on the upper side by the perfect-gas predictions and on the lower side by the equilibrium-air predictions.

The effects of perfect-gas, equilibrium-air and nonequilibrium-air gas models on the surface heat-transfer rate are shown in Figs. 43 and 44. The axial distributions of the surface heat-transfer rate are compared in Fig. 43, whereas the corresponding crossflow distributions at $x = 30$ Rn are compared in Fig. 44. These results show that the predictions of the three gas models are within 5% of each other. Again it is seen that, in general, the nonequilibrium predictions are bounded by the corresponding perfect-gas and equilibrium-air predictions. The crossflow distribution of the streamwise skin-friction coefficient at $x = 30$ Rn is shown in Fig. 45 and follows the same trend as the predictions of the surface heat-transfer rate.

IX. RESULTS AND DISCUSSION   51

9.1.5. Effects of Higher-Order Smoothing

The effects of second-order and fourth-order smoothing were studied using the Case 1b and Case 1c calculations. The only difference between these two cases is that Case 1b uses our recent fourth-order accurate smoothing formulation, whereas the Case 1c uses our previous (Bhutta and Lewis, 1985a-d) second-order accurate formulation. Figures 46 and 47 show some sample results of these calculations. The axial distributions of wall heat-transfer are shown in Fig. 46, and the corresponding crossflow distributions at $x = 30$ Rn are compared in Fig. 47. These figures show that the predictions using the second-order and fourth-order formulations are in excellent agreement. The maximum differences in the heat-transfer rates are of the order of 1% or less. Thus, for all practical purposes, in this particular case the predictions of the fourth-order and second-order formulation are the same. However, there is an important difference in the computing times required for these calculations. The computing times given in Table 5 show that the calculations with fourth-order formulation took 5 min and 11 sec on IBM 3090 (model 200VF), while the similar calculations with the second-order formulation took 6 min and 11 sec. Thus, although the converged results did not change, with the fourth-order formulation the solution converged at a faster rate and resulted in a 20% reduction in the overall computing time required.

9.1.6. Small Marching Step-Size Capabilities

Figure 48 shows some sample wall heat-transfer results showing the small step-size capabilities of the current PNS scheme. These results are for the Mach 19.2 flow over a 6-deg sphere cone at a flight altitude of 120 kft. The nose radius (Rn) for these calculations was 0.05 inch and the gas model used was equilibrium chemically-reacting air. The vehicle geometry was 1000 Rn (50 inches) long and solutions were done with 10 Rn, 5 Rn, 2.5 Rn, 1 Rn, 0.25 Rn and 0.1 Rn step sizes, respectively. Figure 48 shows that there are negligible (if any) differences in the numerical predictions of the various step sizes. It should be noted that the form of streamwise damping used in these calculations was such that the solutions with 10 Rn, 5 Rn and 2.5 Rn step sizes had effectively no streamwise numerical dissipation effects.

The PNS calculations shown in Fig. 48 used 50 points between the body and the shock. The solutions with 10 Rn, 5 Rn, 2.5 Rn, 1 Rn, 0.25 Rn and 0.1 Rn step sizes took 11 sec, 17 sec, 28 sec, 58 sec, 204 sec and 493 sec on the Cray Y-MP, respectively. The

corresponding number of axial marching steps required for these calculations were 135, 227, 420, 1009, 3985 and 9955, respectively.

9.1.7. Computing Times

The computing times for the Case 1, Case 2 and Case 3 calculations are shown in Table 5. These computing times show that, after accounting for the differences in grid sizes, the present nonequilibrium computing times are only a factor of 2-3 more than the corresponding perfect-gas or equilibrium-air computing times. Thus, despite the complex three-dimensional geometry being modeled and the numerical complexity of these nonequilibrium-air calculations, the overall computing times are quite reasonable and certainly very affordable.

9.2. 2-D/Axisymmetric Internal-Flow PNS Calculations

Sample 2-D internal-flow calculations were done using three (3) different cases (Cases 4, 5 and 6). Two sets of initial conditions were considered, as shown in Table 6. The first set of initial conditions was estimated from the computed results of Mach = 25 perfect-gas flow over a 5°-10° ramp-inlet configuration at an altitude of 150 kft. The resulting inflow conditions at the inlet consisted of Mach = 6.7 flow at a pressure of 142.2 psf and a peak inlet temperature of 5332.89° Rankine. The inlet Reynolds number for this case is 2.33×10^5. The next set of inlet conditions correspond to a Mach 10 inlet flow at a pressure of 50 psf and a temperature of 500° Rankine, and the corresponding inlet Reynolds number is 1.76×10^6. In all these internal-flow tests, only fully laminar flow conditions were considered.

9.2.1. Case 4 Calculations

The Case 4 configuration (see Fig. 49) consists of a 50 ft long 2-D channel with a 2 ft wide inlet (half channel width = R = 1 ft) and a 4° compression surface located 5 ft from the channel enterance. At 13 ft from the channel inlet, this 4° compression surface becomes horizontal, and the subsequent channel remains straight. The locations of these compression and expansion corners have been designed using inviscid ($y = 1.4$) calculations to provide wave cancellation and, consequently, a shock-free exit flow. These Case 4 calculations were done using the Mach 6.7 inlet conditions, and the wall temperature was kept fixed at 2000° Rankine.

These Case 4 calculations were done using (a) a perfect-gas model (Case 4a), (b) an equilibrium-air gas model (Case 4b), and (c) a nonequilibrium-air gas model (Case 4c). In all cases 150 grid points were used across the channel half-height, and the maximum axial step size was 0.25 R (where R = 1 ft is the half channel height). The axis-normal grid distribution was very fine near the wall, and it was gradually made coarse toward the centerline.

Figures 50 thru 52 show the pressure contours for these Case 4 calculations. The pressure contours for x = 0.11 R to x = 15.77 R are shown in Fig. 50, the pressure contours for x = 15.77 R to x = 32.02 R are shown in Fig. 51, and the pressure contours for x = 32.02 R to x = 50 R are shown in Fig. 52. These figures show that the present perfect-gas, equilibrium-air and nonequilibrium-air results are smooth and well behaved. The shock-wave structure agrees very well with the inviscid predictions, except that exact wave cancellation does not occur in the viscous case. This is because, in the viscous case, the embedded shock wave is not a line discontinuity, rather it has a finite thickness. However, after the expansion corner, there are only a few weak shocks which dissipate quickly and the subsequent exit flow tends to become uniform and free of shocks. It is interesting to note that, compared to the inviscid calculations, the predicted exit pressure distribution has a significant viscous-induced component (approximately 30% larger). Furthermore, the use of equilibrium-air as well as nonequilibrium-air gas models has a significant effect on the embedded shock structure and the exit pressure. The equilibrium-air gas model predicts a 20% lower exit pressure than the perfect-gas model, and the nonequilibrium-air gas model predicts a 37% lower exit pressure. both equilibrium-air and nonequilibrium-air gas models predict that the shock waves travel further downstream than the perfect-gas case and, thus it takes much longer for the embedded shocks to dissipate. In general the equilibrium-air and nonequilibrium-air predictions are in good agreement with each other, and predicted pressures are substantially lower than the perfect-gas case.

The pressure profiles at x = 7.5 R and x = 11.5 R are compared in Fig. 53. This figure also shows that the embedded shocks have been captured quite well. It is interesting to note that the equilibrium-air and nonequilibrium-air gas models predict much sharper embedded shocks. Since the streamwise as well as the axis-normal grids for all cases are practically the same, this difference is primarily due to the gas model. It is possible that the sharpness of the embedded shocks can be further improved by either a larger number of axis-normal grid points or a better distribution of the the grid points available. So far, our studies have shown 150 points to be quite adequate in resolving flowfield gradients;

IX. RESULTS AND DISCUSSION   54

however, in subsequent studies we will also study the effects of using finner axis-normal grids.

Axial distribution of the pressure along the channel axis is shown in Fig 54, and the axial distribution of the pressure along the channel wall is shown in Fig. 55. These results also show that the pressure distributions predicted by the equilibrium-air and nonequilibrium-air gas models differ by less than 10%; however, they are substantially lower (20-40% lower) than the corresponding perfect-gas predictions. The consistently good agreement between the equilibrium-air and nonequilibrium-air calculations indicate that for this Reynolds number (2.33×10^5/ft) the flow is close to equilibrium. This is important because the present uncoupled nonequilibrium solution scheme becomes numerically stiff (difficult to solve) under equilibrium or near-equilibrium conditions, and this case may be a borderline case. This is also substantiated by the next set of calculations (Cases 5 and 6), which are for a higher Reynolds number condition (1.76×10^6/ft) and, thus, even closer to equilibrium.

The Cray-Y/MP computing times for these case 4 calculations are shown in Table 7. The perfect-gas (Case 4a), equilibrium-air (Case 4b) and nonequilibrium-air (Case 4c) calculations took 212, 226 and 227 marching steps and required 59, 105 and 268 sec, respectively. It should be noted that the current internal flow code is an un-optimized research code, and we expect these computing times to be significantly improved with further code restructuring and vectorization.

9.2.2. Case 5 Calculations

The Case 5 configuration (see Fig. 56) consists of a 50 ft long 2-D channel with a 2 ft wide inlet (half channel width = R = 1 ft) and a 2° compression surface located 5 ft from the channel enterance. At 18.57 ft from the channel inlet, this 4° compression surface becomes horizontal, and the subsequent channel remains straight. Like Case 4, the locations of these compression and expansion corners were also designed using inviscid ($\gamma = 1.4$) calculations to provide wave cancellation and, consequently, a shock-free exit flow. These Case 5 calculations were done using the Mach 10 inlet conditions, and the wall temperature was kept fixed at 1000° Rankine.

These Case 5 calculations were done using (a) a perfect-gas model (Case 5a) and (b) an equilibrium-air gas model (Case 5b). Compared to Case 5, in this case the Reynolds number is higher (1.76×10^6/ft). Consequently, the flow is even closer to equilibrium and,

thus, the nonequilibrium-air calculations suffer from convergence problems resulting from the numerical stiffness of the <u>uncoupled</u> species conservation equations. For these cases 150 grid points were used across the channel half-height, and the maximum axial step size was 0.1 R.

Axial distribution of the pressure along the channel axis is shown in Fig 57, and the axial distribution of the pressure along the channel wall is shown in Fig. 58. These results also show that the pressure distributions predicted by the perfect-gas and equilibrium-air are almost identical. It should be noted that in this case the wall temperature is 1000° Rankine and the peak flowfield temperatures are 2500°-3500° Rankine. These are relatively low temperatures and, thus, the corresponding gas-model effects on the pressure distribution are quite small. However, for higher flowfield temperatures the gas models effects could be larger.

One of the purposes of this higher Reynolds number case was to reduce the amount of viscous induced pressure and thus provide potentially better agreement with the inviscid calculations. Indeed the results show that the viscous exit pressure is only 10% higher than the inviscid predictions. Furthermore, the predicted embedded shock structure is also in very good agreement with the inviscid predictions.

The Cray-Y/MP computing times for these Case 5 calculations are shown in Table 7. The perfect-gas (Case 5a) and equilibrium-air (Case 5b) calculations took 526 marching steps and required 146 and 223 sec, respectively. These differences in the computing times for the perfect-gas and equilibrium-air calculations are primarily due to the larger number of iterations required by the equilibrium-air calculations at each marching step (20-25 iterations for the equilibrium-air calculations compared to the 10-15 iterations for perfect-gas calculations).

9.2.3. Case 6 Calculations

The Case 6 configuration (see Fig. 59) consists of a 100 ft long 2-D channel with a 2 ft wide inlet (half channel width = R = 1 ft) and a sustained 0.5° compression surface located 5 ft from the channel enterance. This configuration was chosen to investigate the effects of sustained compression. These Case 6 calculations were also done using the Mach 10 inlet conditions, and the wall temperature was kept fixed at 1000° Rankine.

These Case 6 calculations were done using (a) a perfect-gas model (Case 6a) and (b) an equilibrium-air gas model (Case 6b). Just like the Case 5 calculations, in this case the Reynolds number is higher (1.76×10^6/ft); consequently, the flow is close to equilibrium and numerical stiffness problems occur in the nonequilibrium-air calculations. In this case 150 grid points were used across the channel half-height, and the maximum axial step size was 0.1 R.

Axial distribution of the pressure along the channel axis is shown in Fig. 60, and the axial distribution of the pressure along the channel wall is shown in Fig. 61. These results also show that the pressure distributions predicted by the perfect-gas and equilibrium-air are almost identical, and are in very good agreement with the inviscid predictions. Again, since the flowfield temperatures are relatively low (2500°-3500° Rankine), the corresponding real-gas effects on the pressure distribution are quite small. However, at higher wall and flowfield temperatures the gas models effects could be larger. It should be noted that in this case the flowfield between the inlet and the exit goes through a strong and sustained compression, resulting in exit pressures which are approximately 10 times the inlet pressure. This sustained compression is equally well predicted by the inviscid and viscous calculations; however, unlike the inviscid predictions, the viscous effects result in a quicker dissipation of embedded shocks. Thus, after nearly 50 ft along the channel, the viscous calculations predict a continuous compression rather than the discontinuous pressure rise due to embedded shocks.

The Cray-Y/MP computing times for these Case 6 calculations are shown in Table 7. The perfect-gas (Case 6a) and equilibrium-air (Case 6b) calculations took 1011 and 962 marching steps and required 343 and 380 sec, respectively. In this case the perfect-gas and equilibrium-air calculations typically required the same number of iterations at each step and, consequently, the final computing times differed by only 10-15%.

X. CONCLUSIONS

A new 3-D PNS scheme has been developed to study three-dimensional hypersonic flows over complex 3-D configurations. This PNS scheme has been used to study the flow around a three-dimensional lifting configuration at an angle of attack of 5 deg and a Mach number of 20. In addition, it has also been demonstrated that this basic PNS scheme can also be extended to study 2-D/axisymmetric supersonic/hypersonic internal flows. These external-flow and internal-flow PNS schemes can treat perfect-gas, equilibrium-air and nonequilibrium-air gas models in a consistent and unified manner. The results of these studies substantiate the following comments:

(1)   Based on the axisymmetric PNS scheme of Bhutta and Lewis (1985a-b) a new three-dimensional PNS scheme has been developed for perfect-gas, equilibrium-air and nonequilibrium-air external flows. This three-dimensional PNS scheme is unconditionally time-like in the subsonic as well as the supersonic flow regions and does not require the use of any sublayer approximation. Furthermore, the scheme permits very fine grids to be used in the near-wall region for improving solution accuracy.

(2)   This PNS scheme uses a fourth-order accurate smoothing approach which is an extension of the earlier second-order approach of Bhutta and Lewis (1985a-b). In this approach the crossflow smoothing effects are applied to all variables; however, the smoothing effects in the axis-normal direction are limited only to the pressure field. This results in accurate wall heat-transfer and skin-friction predictions even with coarse grids in the axis-normal direction.

(3)   A new predictor-corrector solution scheme has been developed to treat the strong crossflow coupling effects in and around the crossflow separated regions. This predictor-corrector scheme involves the same amount of operations as an Approximate Factorization scheme; however, it retains a stronger coupling between the crossflow and body-normal directions.

(4)   At the shock a new fully-implicit shock-prediction scheme has been developed and used for 3-D external flows. This scheme uses a general curvilinear coordinate

system and predicts the correct shock location without having to make any approximation about the viscous or inviscid nature of the flow behind the shock. Furthermore, this shock-fitting solution is fully coupled in the crossflow direction, results in smooth and accurate shock-shapes, and has very good stability and convergence characteristics.

(5) It is shown that with a pseudo-unsteady algorithm, the present fully-iterative three-dimensional results can be obtained accurately and efficiently without any significant computing-time penalty. Furthermore, due to the enhanced solution accuracy, much larger marching steps can be used which substantially reduces the final computing times.

(6) Cylindrical, parabolic, body-normal and elliptic grid-generation schemes have been successfully incorporated in the present 3-D PNS scheme to efficiently and accurately model a wide class of complex three-dimensional configurations. It is shown that for lifting configurations with generally convex cross-sections, the body-normal grid generation scheme produces very good grids which are smoothly behaved. For general 3-D cross sections the present elliptic grid generation scheme represents a powerful yet economical means of generating the required computational grids.

(7) The results of the three-dimensional test cases considered show that substantial three-dimensional crossflow effects exist in the predicted flowfields. Even in regions where the body surface looks like a two-dimensional or an axisymmetric surface, there are considerable three-dimensional effects from the neighboring flow regions. Thus, simple quasi 2-D or axisymmetric approximations for these flowfield regions are inadequate, and the overall flowfield is best predicted using an appropriate three-dimensional solution scheme.

(8) Due to the strongly three-dimensional nature of the flowfields around complex lifting configurations, a localized grid refinement at the expense of the neighboring regions may not be an appropriate approach. In such cases the solution inaccuracies in the neighboring regions do exert a strong influence on the local solution accuracy. Thus, for such flowfield calculations a more uniform grid refinement is a better and safer solution strategy.

X. CONCLUSIONS

(9) Studies with different types of gas models show that for complex configurations, the type of gas model used has a substantial effect on the important flowfield quantities; such as, the wall pressures, the shock-standoff distances, wall heat-transfer and skin-friction predictions, etc.

(10) Results of the 2-D/axisymmetric internal-flow calculations show that the basic PNS scheme developed for external flows is also applicable to internal flow conditions. Test case results for some simple 2-D cases show that the viscous internal-flow PNS predictions are in excellent agreement with classical 2-D inviscid techniques.

APPENDIX A. DERIVATION OF THE 3-D FULL PNS EQUATIONS

The general motion of viscous compressible fluids is described by the well known full Navier-Stokes (NS) equations (Bird et al., 1960, and White, 1974). If we assume (a) Newtonian fluid behavior, (b) Stokes' Hypothesis, and (c) no body forces, we can write the three-dimensional NS equations as

$$(\rho u)_{,x} + (\rho v)_{,y} + (\rho w)_{,z} = 0 \tag{A.1}$$

$$(\rho u^2 + p)_{,x} + (\rho vu)_{,y} + (\rho wu)_{,z} = a_1 \tag{A.2}$$

$$(\rho uv)_{,x} + (\rho v^2 + p)_{,y} + (\rho wv)_{,z} = a_2 \tag{A.3}$$

$$(\rho uw)_{,x} + (\rho vw)_{,y} + (\rho w^2 + p)_{,z} = a_3 \tag{A.4}$$

$$(\rho u\Phi)_{,x} + (\rho v\Phi)_{,y} + (\rho w\Phi)_{,z} = a_4 \tag{A.5}$$

where

$$a_1 = [2\bar{\mu}u_{,x} - (2\bar{\mu}/3)\nabla \cdot V]_{,x} + [\bar{\mu}(u_{,y} + v_{,x})]_{,y} + [\bar{\mu}(u_{,z} + w_{,x})]_{,z} \tag{A.6}$$

$$a_2 = [2\bar{\mu}v_{,y} - (2\bar{\mu}/3)\nabla \cdot V]_{,y} + [\bar{\mu}(v_{,x} + u_{,y})]_{,x} + [\bar{\mu}(v_{,z} + w_{,y})]_{,z} \tag{A.7}$$

$$a_3 = [2\bar{\mu}w_{,z} - (2\bar{\mu}/3)\nabla \cdot V]_{,z} + [\bar{\mu}(w_{,x} + u_{,z})]_{,x} + [\bar{\mu}(w_{,y} + v_{,z})]_{,y} \tag{A.8}$$

and

$$a_4 = \nabla \cdot (k\nabla T) + \nabla \cdot (v \cdot \tau) + a_5 \tag{A.9}$$

Here τ is the stress tensor for a Newtonian fluid, and is defined as (White, 1974)

$$\tau_{ij} = \bar{\mu}[u_{i,x_j} + u_{j,x_i} - (2/3)\delta_{ij}u_{k,x_k}] \tag{A.11}$$

where $u_1 = u$, $u_2 = v$, $u_3 = w$, $x_1 = x$, $x_2 = y$ and $x_3 = z$.

Equation (A.1) corresponds to the conservation of mass, and Eqs. (A.2-A.4) correspond to the conservation of momentum in the x, y and z directions, respectively. Equation (A.5) corresponds to the conservation of energy, and these equations [Eqs. (A.1)-(A.5)] are closed through the use of equation-of-state for the gas mixture written in the functional form

$$f(\rho,T,P,C_i) = 0 \qquad (A.12)$$

The form of 'Φ', 'a $_s$' and the functional form of the equation of state depends upon the gas model being used; such as, perfect-gas, equilibrium-air or nonequilibrium-air gas model. For a perfect gas model these quantities are defined as

$$\Phi = C_p T + 0.5V^2 \qquad (A.13a)$$

$$a_5 = 0 \qquad (A.14a)$$

$$f(\rho,T,P,C_i) = (\gamma_\infty p - \rho T) = 0 \qquad (A.15a)$$

For an equilibrium-air gas model these quantities are defined as

$$\Phi = h(p,T) + 0.5V^2 \qquad (A.13b)$$

$$a_5 = 0 \qquad (A.14b)$$

$$f(\rho,T,P,C_i) = [\gamma_\infty p/\rho T - Z^*(p,T)] = 0 \qquad (A.15b)$$

For nonequilibrium flows these quantities are defined as

$$\Phi = \overline{C}_p T + 0.5V^2 \qquad (A.13c)$$

$$a_5 = \Sigma(\frac{\varepsilon_1 \overline{\mu}}{Pr}(Cp)_i \nabla T \cdot \nabla C_i - h_i \dot{\omega}_i) + \rho T v \cdot \nabla \overline{C}_p \qquad (A.14c)$$

$$f(\rho,T,P,C_i) = (\overline{m}p - \rho T) = 0 \qquad (A.15c)$$

The above equations have been written in a nondimensional form, and the nondimensionalization scheme used is

$$u_i = u_i^*/a_\infty^*; \quad \rho = \rho^*/\rho_\infty^*; \quad T = T^*/T_\infty^*; \quad p = p^*/(\rho_\infty^* a_\infty^{*2}); \\ \mu = \mu^*/\mu_\infty^*; \quad k = k^*/k_\infty^*; \quad \overline{m} = \gamma_\infty \overline{m}^*/m_\infty^*; \quad x_i = x_i^*/Rn^* \qquad (A.16)$$

Equations (A.1)-(A.5) and Eq. (A.12) can be combined together and written in the following vectorial form:

$$e_{1,x} + e_{2,y} + e_{3,z} = \varepsilon(g_{1,x} + g_{2,y} + g_{3,z}) + p \tag{A.17}$$

Using indicial notation we can write Eq.(A.17) as

$$(e^j - \varepsilon g^j)_{,x_j} = p \tag{A.18}$$

Or

$$k^j_{,x_j} = p \tag{A.19}$$

Now consider the general coordinate transformation

$$\xi_j = \xi_j(x_k) \tag{A.20}$$

where the orientation of our general curvilinear coordinate system is such that ξ_1 is measured along the body, ξ_2 is measured from the body to the outer bow shock, and ξ_3 is the crossflow direction. Thus, derivatives in the transformed space are related to the derivatives in the physical space by

$$( )_{,\xi_k} = x_{j,\xi_k}( )_{,x_j} \tag{A.21}$$

If 'J' represents the determinant of the Transformation-Jacobian for Eq. (A.20); i.e.,

$$J = Det[(\xi_1, \xi_2, \xi_3)/(x_1, x_2, x_3)] \tag{A.22}$$

we can write Eq. (A.19) as

$$(1/J)(\xi_{j,x_k})(k_{k,\xi_j}) = (1/J)p \tag{A.23}$$

Equation (A.23) can be further expanded as

$$[(1/J)(\xi_{j,x_k})k_k]_{,\xi_j} - k_k[(1/J)(\xi_{j,x_k})]_{,\xi_j} = (1/J)p \tag{A.24}$$

Viviand (1974) has shown that the Jacobian satisfies the identity

$$J_{,\alpha} = J(\xi_{j,\alpha})_{,\xi_j} \tag{A.25}$$

where 'α' is an arbitrary quantity. Equation (A.25) can be used to obtain

$$J_{,x_k} = J(\xi_{j,x_k})_{,\xi_j} \qquad (A.26)$$

At the same time the chain rule of differentiation gives

$$J_{,x_k} = (\xi_{j,x_k})J_{,\xi_j} \qquad (A.27)$$

Thus, we can see that by combining Eqs. (A.26) and (A.27) we can obtain yet another identity

$$(\xi_{j,x_k})_{,\xi_j} - (1/J)(\xi_{j,x_k})J_{,\xi_j} = 0 \qquad (A.28)$$

The chain rule of differentiation also gives

$$[(1/J)\xi_{j,x_k}]_{,\xi_j} = (1/J)[(\xi_{j,x_k})_{,\xi_j} - (1/J)(\xi_{j,x_k})J_{,\xi_j}] \qquad (A.29)$$

Thus, from Eqs. (A.28) and (A.29) we obtain

$$[(1/J)\xi_{j,x_k}]_{,\xi_j} = 0 \qquad (A.30)$$

Substituting Eq. (A.30) in Eq. (A.24), we see that the NS equations in a general curvilinear coordinate system can be written as

$$[(1/J)\xi_{j,x_k}k_k]_{,\xi_j} = (1/J)p \qquad (A.31)$$

If we use the notation

$$f_j = (1/J)\xi_{j,x_k}e_k \qquad (A.32)$$

$$s_j = (1/J)\xi_{j,x_k}g_k \qquad (A.33)$$

$$h = (1/J)p \qquad (A.34)$$

we can write the NS equations in a general curvilinear coordinate system as

$$f_{j,\xi_j} = \varepsilon s_{j,\xi_j} + h \qquad (A.35)$$

In order to parabolize Eq. (A.35) we neglect all streamwise diffusion effects. With this assumption, the three-dimensional parabolized Navier-Stokes (PNS) equations in a general curvilinear coordinate system become

$$f_{j,\xi_j} = \varepsilon(s_{2,\xi_2} + s_{3,\xi_3}) + h \qquad (A.36)$$

where

$$\mathbf{f_j} = (1/J) \begin{bmatrix} \rho U_j \\ \rho u U_j + \xi_{j,x} p \\ \rho v U_j + \xi_{j,y} p \\ \rho w U_j + \xi_{j,z} p \\ \Phi \rho U_j \\ 0 \end{bmatrix} \qquad (A.37)$$

$$\mathbf{s_n} = (\bar{\mu}/J) \begin{bmatrix} 0 \\ m_{nkk} u_{,\xi_2} + 0.5(m_{n1j} u_{j,\xi_2}) \\ m_{nkk} v_{,\xi_2} + 0.5(m_{n2j} u_{j,\xi_2}) \\ m_{nkk} w_{,\xi_2} + 0.5(m_{n3j} u_{j,\xi_2}) \\ \{m_{nkk} T_{,\xi_2} \bar{C}_p/Pr + m_{nkk} u_j u_{j,\xi_2} \\ (1/3) m_{njk} u_j u_{k,\xi_2} \} \\ 0 \end{bmatrix} \qquad (n = 2,3) \qquad (A.38)$$

and

$$\mathbf{h} = [0, \ 0, \ 0, \ h_4, \ f - f(\rho,T,P,C_i)]^T \qquad (A.39)$$

The metric product $'m_{njk}'$ is defined as

$$m_{njk} = \xi_{n,j} \xi_{n,k} \qquad (A.40)$$

where n takes the values 2 and 3, respectively. The word 'full' PNS equations is used to distinguish from the corresponding 'thin-layer' PNS equations, which are obtained by neglecting both the streamwise (ξ_1) and the crossflow (ξ_3) viscous effects.

For perfect-gas and equilibrium-air flows $h_4 = 0$, while for nonequilibrium flows

$$h_4 = (1/J)\{\Sigma[\frac{\varepsilon_1 m_{nkk} \bar{\mu}}{Pr} T_{,\xi_2}(Cp)_i C_{i,\xi_2} - h_i \dot{\omega}_i] + \rho T U_j \bar{C}_{p,\xi_j}\} \qquad (A.41)$$

APPENDIX B. EXPRESSIONS FOR THE JACOBIAN MATRICES

The three-dimensional parabolized Navier-Stokes (PNS) equations for a general gas flow in a general curvilinear coordinate system, at the $j+1$ marching step and at the $n+1$ iteration level, can be written in the following vectorial form:

$$f_{j,\zeta_j}^{j+1,n+1} = \varepsilon(s_{2,\xi_2} + s_{3,\xi_3})^{j+1,n+1} + h^{j+1,n+1} \tag{B.1}$$

Using a first-order Taylor series expansion around the previous iteration, we can write

$$f_j^{j+1,n+1} \simeq f_j^{j+1,n} + A_1^{j+1,n} \cdot \Delta q^{n+1}$$
$$s_n^{j+1,n+1} \simeq s_n^{j+1,n} + M_n^{j+1,n} \cdot \Delta q^{n+1} \tag{B.2}$$
$$h^{j+1,n+1} \simeq h^{j+1,n} + A_0^{j+1,n} \cdot \Delta q^{n+1}$$

where

$$\Delta q^{n+1} = q^{j+1,n+1} - q^{j+1,n} \tag{B.3}$$

The matrices A_0, A_j and M are called the jacobian matrices, and have the following form:

$$A_j = (1/J)\begin{bmatrix}
0 & \xi_{j,x} & \xi_{j,y} & \xi_{j,z} & 0 & 0 \\
-uU_j & \xi_{j,x}u + U_j & \xi_{j,y}u & \xi_{j,z}u & 0 & \xi_{j,x} \\
-vU_j & \xi_{j,x}v & \xi_{j,y}v + U_j & \xi_{j,z}v & 0 & \xi_{j,y} \\
-wU_j & \xi_{j,x}w & \xi_{j,y}w & \xi_{j,z}w + U_j & 0 & \xi_{j,z} \\
-\Phi U_j & \xi_{j,x}\Phi + uU_j & \xi_{j,y}\Phi + vU_j & \xi_{j,z}\Phi + wU_j & U_j & 0 \\
0 & 0 & 0 & 0 & 0 & 0
\end{bmatrix} \tag{B.4}$$

$$M_n = (\bar{\mu}/J)\begin{bmatrix}
0 & 0 & 0 & 0 & 0 & 0 \\
M_{n21} & M_{n22} & M_{n23} & M_{n24} & 0 & 0 \\
M_{n31} & M_{n32} & M_{n33} & M_{n34} & 0 & 0 \\
M_{n41} & M_{n42} & M_{n43} & M_{n44} & 0 & 0 \\
M_{n51} & M_{n52} & M_{n53} & M_{n54} & M_{n55} & 0 \\
0 & 0 & 0 & 0 & 0 & 0
\end{bmatrix} \tag{B.7}$$

$$A_0 = \begin{bmatrix} 0 & 0 & 0 & 0 & 0 & 0 \\ 0 & 0 & 0 & 0 & 0 & 0 \\ 0 & 0 & 0 & 0 & 0 & 0 \\ 0 & 0 & 0 & 0 & 0 & 0 \\ a_{51} & a_{52} & a_{53} & a_{54} & a_{55} & 0 \\ f_{,\rho} & 0 & 0 & 0 & f_{,\rho T} & f_{,p} \end{bmatrix}$$ (B.8)

where the definition of Φ depends upon the gas model used. For a perfect-gas model

$$\Phi = C_p T + 0.5V^2$$ (B.9a)

For an equilibrium-air gas model

$$\Phi = h(p,T) + 0.5V^2$$ (B.9b)

and for a nonequilibrium gas model

$$\Phi = \overline{C}_p T + 0.5V^2$$ (B.9c)

The elements of the viscous jacobian matrix are

$$M_{n21} = - m_{nkk}(u/\rho)_{,\xi_2} + (1/3)m_{n1j}(u_j/\rho)_{,\xi_2}$$ (B.10)

$$M_{n22} = (1/3)[(3m_{nkk} + m_{n11})(1/\rho)_{,\xi_2}]$$ (B.11)

$$M_{n23} = (1/3)m_{n12}(1/\rho)_{,\xi_2}$$ (B.12)

$$M_{n24} = (1/3)m_{n13}(1/\rho)_{,\xi_2}$$ (B.13)

$$M_{n31} = - m_{nkk}(v/\rho)_{,\xi_2} + (1/3)m_{n2j}(u_j/\rho)_{,\xi_2}$$ (B.14)

$$M_{n32} = (1/3)m_{n21}(1/\rho)_{,\xi_2}$$ (B.15)

$$M_{n33} = (1/3)[(3m_{nkk} + m_{n22})(1/\rho)_{,\xi_2}]$$ (B.16)

$$M_{n34} = (1/3)m_{n23}(1/\rho)_{,\xi_2}$$ (B.17)

$$M_{n41} = - m_{nkk}(w/\rho)_{,\xi_2} + (1/3)m_{n3j}(u_j/\rho)_{,\xi_2}$$ (B.18)

$$M_{n42} = (1/3)m_{n31}(1/\rho)_{,\xi_2}$$ (B.19)

$$M_{n43} = (1/3)m_{n32}(1/\rho)_{,\xi_2} \tag{B.20}$$

$$M_{n44} = (1/3)[(3m_{nkk} + m_{n33})(1/\rho)_{,\xi_2}] \tag{B.21}$$

$$M_{n51} = -(T/\rho)_{,\xi_2}\overline{C}_p/Pr - m_{nkk}(V^2/\rho)_{,\xi_2} - 2m_{njk}u_j(u_k/\rho)_{,\xi_2}/3 \tag{B.22}$$

$$M_{n52} = m_{nkk}(u/\rho)_{,\xi_2} + m_{n1j}(u_j/\rho)_{,\xi_2}/3 \tag{B.23}$$

$$M_{n53} = m_{nkk}(v/\rho)_{,\xi_2} + m_{n2j}(u_j/\rho)_{,\xi_2}/3 \tag{B.24}$$

$$M_{n54} = m_{nkk}(w/\rho)_{,\xi_2} + m_{n3j}(u_{j/\rho})_{,\xi_2}/3 \tag{B.25}$$

$$M_{n55} = m_{nkk}(1/\rho)_{,\xi_2}\overline{C}_p/Pr \tag{B.26}$$

The elements a_{51} thru a_{55} of the jacobian matrix A_0 are equal to zero for perfect-gas and equilibrium-air flows, whereas for nonequilibrium flows these coefficients are of the form

$$
\begin{aligned}
a_{51} = (1/J)\{(\varepsilon_1\bar{\mu}m_{nkk}/Pr)[(-T/\rho)_{,\xi_2}\Sigma(Cp)_iC_{i,\xi_2} \\
- (TT_{,\xi_2}/\rho)\Sigma(Cp)_i'C_{i,\xi_2}] - \Sigma[(h_i-Th_i')(\dot{\omega}_i/\rho) \\
-Th_i(\dot{\omega}_i/\rho)'] - TU_k\overline{C}_{p,\zeta_k}\}
\end{aligned}
\tag{B.27}
$$

$$a_{52} = (1/J)T\xi_{k,x}\overline{C}_{p,\zeta_k} \tag{B.28}$$

$$a_{53} = (1/J)T\xi_{k,y}\overline{C}_{p,\zeta_k} \tag{B.29}$$

$$a_{54} = (1/J)T\xi_{k,z}\overline{C}_{p,\zeta_k} \tag{B.30}$$

and

$$
\begin{aligned}
a_{55} = (1/J)\{(\varepsilon_1\bar{\mu}\,m_{nkk}/Pr)[(1/\rho)_{,\xi_2}\Sigma(Cp)_iC_{i,\xi_2} \\
+ (T_{,\xi_2}/\rho)\Sigma(Cp)_i'C_{i,\xi_2}] - \Sigma(h_i\dot{\omega}_i/\rho)' + U_k\overline{C}_{p,\zeta_k}\}
\end{aligned}
\tag{B.31}
$$

In these equations the total derivative of a quantity with respect to temperature is denoted by ( )'. The expression for $(\dot{\omega}_i/\rho)'$ is given in Appendix E, and the corresponding values for h_i' and $(Cp)_i'$ are obtained using central-differenced approximations and the tabular data of h_i and $(Cp)_i$.

APPENDIX C. FOURTH-ORDER ACCURATE SMOOTHING TERMS

The governing three-dimensional PNS equations are elliptic in the ξ_2 and ξ_3 directions so that we use central-differenced approximations for all ξ_2 and ξ_3 derivatives. However, as was also noted by Schiff and Steger (1979), the use of central-differenced schemes is typically associated with solution oscillations. This oscillatory behavior becomes more pronounced if the local velocities are small, so that the diagonal terms of the jacobian matrices become relatively small also. In order to damp these solution oscillations, it is necessary to add some additional higher-order diffusion terms to the governing PNS equations.

The search for an appropriate form of the higher-order diffusion-like terms which would permit a simple yet a fully consistent and fully implicit treatment, was very tedious and involved. The use of central-difference formulas for ξ_2 and ξ_3 derivatives makes the solution of the PNS equations second-order accurate, that is to say the leading truncation error is $O(\Delta\xi_2^2, \Delta\xi_3^2)$. Thus, if we were to add $O(\Delta\xi_2^4)$ and $O(\Delta\xi_3^4)$ diffusion-like terms to the right-hand side of governing equations, we would not affect the formal second-order accuracy of the difference scheme in the ξ_2 and ξ_3 directions. The governing equations can thus be written as

$$\mathbf{f}_{i,\xi_j}^{j+1} = \varepsilon(s_{2,\xi_2} + s_{3,\xi_3})^{j+1} + \mathbf{h}^{j+1} + [\pi_1(q^{j+1})](\Delta\xi_2)^4/16 + [\pi_2(q^{j+1})](\Delta\xi_3)^4/16 \quad (C.1)$$

The proper choice of smoothing terms was actually based on a trial and error procedure. To start with, an explicit relation relating the smoothed (q) and unsmoothed (χ) variables was chosen such that it included some second-order diffusion effects. A backtracking approach was used to obtain the corresponding smoothing terms that needed to be added to the governing equations to produce the desired result. Once these smoothing terms in the governing equations were obtained, the order of each of these terms was analyzed and lower order terms were eliminated. Then, the governing equations with the modified smoothing terms were analyzed to see the impact of these changes on the final relationship between the smoothed and unsmoothed variables. After several iterations of this trial and error procedure, we were able to find a proper choice of these smoothing terms such that not only a second-order accuracy was re-

tained, but a simple and explicit transformation between the unsmoothed and smoothed variables was also retained.

By choosing the form of the vector π to be

$$\pi_1(\mathbf{q}) = -(\mathbf{A}_1/\Delta\xi_1 - \mathbf{A}_0) \cdot \frac{\partial^4 \mathbf{q}}{\partial\xi_2^4} - [(\mathbf{A}_2 - \varepsilon\mathbf{M}_2) \cdot \frac{\partial^4 \mathbf{q}}{\partial\xi_2^4}]_{,\xi_2} - [(\mathbf{A}_3 - \varepsilon\mathbf{M}_3) \cdot \frac{\partial^4 \mathbf{q}}{\partial\xi_2^4}]_{,\xi_3} \quad (C.2a)$$

$$\pi_2(\mathbf{q}) = -(\mathbf{A}_1/\Delta\xi_1 - \mathbf{A}_0) \cdot \frac{\partial^4 \mathbf{q}}{\partial\xi_3^4} - [(\mathbf{A}_2 - \varepsilon\mathbf{M}_2) \cdot \frac{\partial^4 \mathbf{q}}{\partial\xi_3^4}]_{,\xi_2} - [(\mathbf{A}_3 - \varepsilon\mathbf{M}_3) \cdot \frac{\partial^4 \mathbf{q}}{\partial\xi_3^4}]_{,\xi_3} \quad (C.2b)$$

one can re-write Eq. (C.1) as

$$
\begin{aligned}
[\mathbf{f}_j + \mathbf{A}_j \cdot (\frac{\partial^4 \mathbf{q}}{\partial\xi_2^4} \Delta\xi_2^4/16 + \frac{\partial^4 \mathbf{q}}{\partial\xi_3^4} \Delta\xi_3^4/16)]_{,\xi_j}^{j+1} \\
= \varepsilon[\mathbf{s}_2 + \mathbf{M}_2 \cdot (\frac{\partial^4 \mathbf{q}}{\partial\xi_2^4} \Delta\xi_2^4/16 + \frac{\partial^4 \mathbf{q}}{\partial\xi_3^4} \Delta\xi_3^4/16)]_{,\xi_2}^{j+1} \\
+ \varepsilon[\mathbf{s}_3 + \mathbf{M}_3 \cdot (\frac{\partial^4 \mathbf{q}}{\partial\xi_2^4} \Delta\xi_2^4/16 + \frac{\partial^4 \mathbf{q}}{\partial\xi_3^4} \Delta\xi_3^4/16)]_{,\xi_3}^{j+1} \\
+ [\mathbf{h} + \mathbf{A}_0 \cdot (\frac{\partial^4 \mathbf{q}}{\partial\xi_2^4} \Delta\xi_2^4/16 + \frac{\partial^4 \mathbf{q}}{\partial\xi_3^4} \Delta\xi_3^4/16)]^{j+1} + O(\Delta\xi_2^4, \Delta\xi_3^4)
\end{aligned}
\quad (C.3)
$$

Now, let us define a new intermediate quantity χ^{j+1} as

$$\chi^{j+1} = \mathbf{q}^{j+1} + \frac{\partial^4 \mathbf{q}}{\partial\xi_2^4} \Delta\xi_2^4/16 + \frac{\partial^4 \mathbf{q}}{\partial\xi_3^4} \Delta\xi_3^4/16 \quad (C.4)$$

So that

$$\chi^{j+1} - \mathbf{q}^{j+1} = \frac{\partial^4 \mathbf{q}}{\partial\xi_2^4} \Delta\xi_2^4/16 + \frac{\partial^4 \mathbf{q}}{\partial\xi_3^4} \Delta\xi_3^4/16 = O(\Delta\xi_2^4, \Delta\xi_3^4) \quad (C.5)$$

and

$$(\chi^{j+1} - \mathbf{q}^{j+1})^2 = O(\Delta\xi_2^8, \Delta\xi_3^8, \Delta\xi_2^4\Delta\xi_3^4) \quad (C.6)$$

Using Eqs. (C.5) and (C.6) it can be shown that to fourth-order accuracy we can also write Eq. (C.4) as

$$\mathbf{q}^{j+1} = \chi^{j+1} - \chi_{,\xi_2\xi_2\xi_2\xi_2}\Delta\xi_2^4/16 - \chi_{,\xi_3\xi_3\xi_3\xi_3}\Delta\xi_3^4/16 \quad (C.7)$$

Now consider the Taylor series expansion of vector $f_j(\chi^{j+1})$ around q^{j+1}, i.e.,

$$f_j(\chi^{j+1}) = f_j(q^{j+1}) + [f_{j,q}]^{j+1} \cdot (\chi^{j+1} - q^{j+1})$$
$$+ [f_{j,qq}]^{j+1} \cdot (\chi^{j+1} - q^{j+1})^2 + \ldots \ldots \qquad (C.8)$$
$$\simeq f_j(q^{j+1}) + A_j \cdot (q_{,\xi_2\xi_2\xi_2\xi_2}\Delta\xi_2^4/16 + q_{,\xi_3\xi_3\xi_3\xi_3}\Delta\xi_3^4/16)$$

Thus, to fourth-order accuracy we can write the above expression as

$$f_j(\chi^{j+1}) \simeq f_j(q^{j+1}) + A_j \cdot (q_{,\xi_2\xi_2\xi_2\xi_2}\Delta\xi_2^4/16 + q_{,\xi_3\xi_3\xi_3\xi_3}\Delta\xi_3^4/16) \qquad (C.9)$$

Similar expansions can be obtained for s and h so that to fourth-order accuracy in $\Delta\xi_2$ we can rewrite Eq. (C.3) in terms of an intermediate solution χ^{j+1} as

$$[f_j(\chi^{j+1})]_{,\xi_j} = \varepsilon[s_2(\chi^{j+1})]_{,\xi_2} + \varepsilon[s_3(\chi^{j+1})]_{,\xi_3} + h(\chi^{j+1}) + O(\Delta\xi_2^4, \Delta\xi_3^4) \qquad (C.10)$$

The actual solution that we seek at the $j+1$ step is related to this intermediate solution by Eq. (C.5). If we use ℓ to denote the grid points in the ξ_2 direction (i.e., $\ell = 1,2,3...$ LMAX) and use k to denote the grid points in the ξ_3 direction (i.e., $k = 1,2,3...$ KMAX), we can further express q^{j+1} in terms of the intermediate solution χ^{j+1} as

$$(\chi_1)^{j+1} = \chi^{j+1} - \chi_{,\xi_3\xi_3\xi_3\xi_3}\Delta\xi_3^4/16 \qquad (C.11a)$$

$$q^{j+1} = (\chi_1)^{j+1} - (\chi_1)_{,\xi_2\xi_2\xi_2\xi_2}\Delta\xi_2^4/16 \qquad (C.11b)$$

Thus, we see that in order to introduce a fourth-order accurate fully implicit smoothing, we solve a block-tridiagonal system of equations [Eq. (C.10)] which is identical in form to the differenced form of the original PNS equations. However, this solution is just an intermediate solution (χ^{j+1}), and the final smoothed solution (q^{j+1}) can be explicitly obtained by using Eq. (C.11). It should be noted that computationally this procedure is no more involved than the original (unsmoothed) differenced form of the PNS equations. Furthermore, another important feature of the present fourth-order smoothing is that the additional diffusion terms are proportional to $\Delta\xi_2^4$ and $\Delta\xi_3^4$, so that the magnitude of the aforementioned smoothing automatically decreases with a decreasing ξ_2 and ξ_3 grid size, while still successfully damping out the numerical solution oscillations. Also, despite its final simple form, the present smoothing approach is more accurate and performs considerably better than the conventional smoothing approaches of Schiff and Steger (1979) and Shanks et al. (1979).

An important advantage of this formulation is that the crossflow smoothing effects [Eqs. (C.11a)] and the axis-normal smoothing effects [Eqs. (C.11b)] can be separately identified. Furthermore, the way these smoothing operations affect the individual flowfield variables can also be clearly seen. Being able to separate these smoothing effects, permits us to further enhance its accuracy by restricting the axis-normal smoothing effects to only the pressure field. Thus, Eqs. (C.11) are rewritten as

$$(\chi_1)^{j+1} = \chi^{j+1} - \chi_{,\,\xi_3\xi_3\xi_3\xi_3}\Delta\xi_3^4/16 \tag{C.12a}$$

$$\mathbf{q}^{j+1} = (\chi_1)^{j+1} - [0,0,0,0,0,(\chi_{16})_{,\,\xi_2\xi_2\xi_2\xi_2}]^T\Delta\xi_2^4/16 \tag{C.12b}$$

where χ_{16} is the sixth element of the vector χ_1 . In this manner, the axis-normal smoothing effects do not degrade the wall heat-transfer and skin-friction predictions.

APPENDIX D. SECOND-ORDER ACCURATE STREAMWISE DAMPING

In the present PNS scheme, first-order backward-differenced approximations are used to approximate the streamwise convective flux derivatives (f_{1,ξ_1}). Such a first-order accurate finite-difference representation has no inherent mechanism to check or suppress the onset of streamwise numerical oscillations. The numerical filtering provided by this first-order backward-differenced approximation is proportional to the streamwise stepsize. As the streamwise step size decreases, the numerics becomes more and more sensitive to the high frequency (small wave length) streamwise oscillations. Thus, in order to damp and suppress the growth of any streamwise solution oscillation, small amounts of second-order streamwise numerical dissipation effects are added to the first-order accurate streamwise convective derivatives such that in the limit of $\Delta\xi_1 \to 0$ the streamwise convective derivatives are continuous.

This approach is based on a very simple damping model. Suppose we denote the numerically evaluated streamwise flux derivatives as f_{1,ξ_1}^* and the corresponding exact value as f_{1,ξ_1}. Let us assume that the numerically evaluated convective flux derivatives have developed an oscillation $[\varepsilon(\xi_1)]$ of constant vector amplitude ε_0 (see Fig. D.1). In other words

$$f_{1,\xi_1}^* = f_{1,\xi_1} + \varepsilon(\xi_1) \tag{D.1}$$

The basic PNS approximation for parabolic flows says that for such flows the second-order streamwise derivatives (such as $f_{1,\xi_1\xi_1}$) are negligible. Thus, by differentiating Eq. (D.1), we can write

$$f_{1,\xi_1\xi_1}^* = f_{1,\xi_1\xi_1} + \varepsilon_{,\xi_1} \cong \varepsilon_{,\xi_1} \cong 2\varepsilon_0/\Delta\xi_1 \tag{D.2}$$

Using Eq. (D.2), we can now estimate and correct for the effects of the numerical oscillation as

$$(f_{1,\xi_1})^{j+1} = (f_{1,\xi_1}^*)^{j+1} - \varepsilon_0 \cong (f_{1,\xi_1}^*)^{j+1} - \frac{1}{2}f_{1,\xi_1\xi_1}^*\Delta\xi_1 \tag{D.3}$$

Based on this simple damping model, we choose the streamwise diffusion effects to be of the form

$$(f_{1,\xi_1})^{j+1} \cong (f_{1,\xi_1})_b^{j+1} - \omega f_{1,\xi_1\xi_1}\Delta\xi_1 \qquad (D.4)$$

where the subscript 'b' represents first-order backward-differenced approximation. The second-order derivative to be used in Eq. (D.4) is estimated using one-sided backward-differenced approximation

$$f_{1,\xi_1\xi_1} \cong [(f_{1,\xi_1})_b^{j+1} - (f_{1,\xi_1})^j]/\Delta\xi_1 \qquad (D.5)$$

The appropriate values of ω appearing in the above damping model are between 0 and 1. The lower limit of $\omega = 0$ is quite evident as it corresponds to the damping-free limit. The upper limit of $\omega \to 1$ corresponds to the limiting case of a vanishingly small step size ($\Delta\xi_1 \to 0$) and the requirement that the streamwise flux derivatives at the 'j' and 'j+1' steps are continuous; i.e., $(f_{1,\xi_1})^{j+1} \to (f_{1,\xi_1})^j$. In the present approach, a simple linear model is used for ω such that $\omega \to 1$ as $\Delta\xi_1 \to 0$ and $\omega \to 0$ when $\Delta\xi_1$ is adequately large. Thus, the numerical accuracy of a large step-size solution is not compromised.

Figures D.2 and D.3 show sample results of some numerical tests that were done using the aforementioned scheme. These results are for the Mach 19.2 flow over a 6-deg sphere cone at a flight altitude of 120 kft. The nose radius (Rn) for these calculations was 0.05 inch and the gas model used was equilibrium chemically-reacting air. The vehicle geometry was 1000 Rn (50 inches) long and solutions were done with 10 Rn, 5 Rn, 2.5 Rn, 1 Rn, 0.25 Rn and 0.1 Rn step sizes, respectively. Figure D.2 shows the wall-pressure distribution, whereas the wall heat-transfer distribution is shown in Fig. D.3. These results show that there are negligible (if any) differences in the numerical predictions of the various step sizes. It should be noted that the form of streamwise damping used in these calculations was such that the solutions with 10 Rn, 5 Rn and 2.5 Rn step sizes had effectively no streamwise numerical dissipation effects.

The equilibrium-air PNS calculations shown in Figs. D.2 and D.3 used 50 points between the body and the shock. The solutions with 10 Rn, 5 Rn, 2.5 Rn, 1 Rn, 0.25 Rn and 0.1 Rn step sizes took equivalent of 11 sec, 17 sec, 28 sec, 58 sec, 204 sec and 493 sec, respectively, on a Cray-Y/MP class machine. The corresponding number of axial marching steps required for these calculations were 135, 227, 420, 1009, 3985 and 9955, respectively.
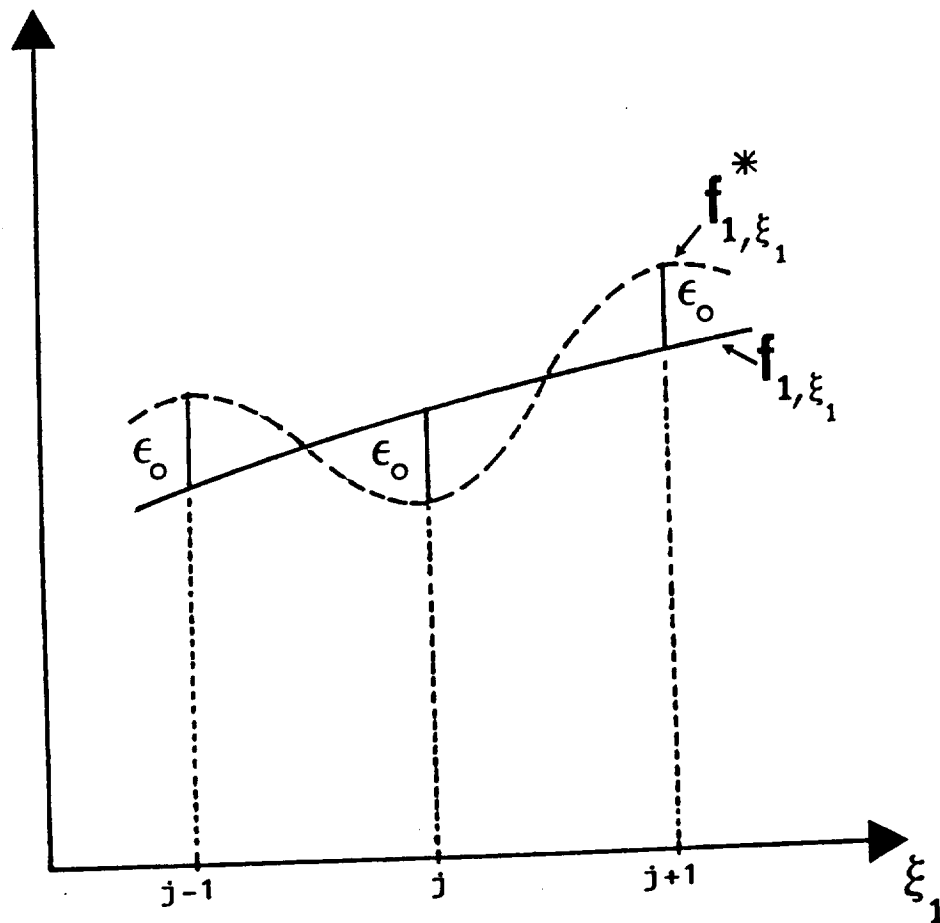
Fig. D.1. Schematic description of a typical streamwise oscillation in the streamwise convective flux derivatives.

Appendix D. SECOND-ORDER ACCURATE STREAMWISE DAMPING
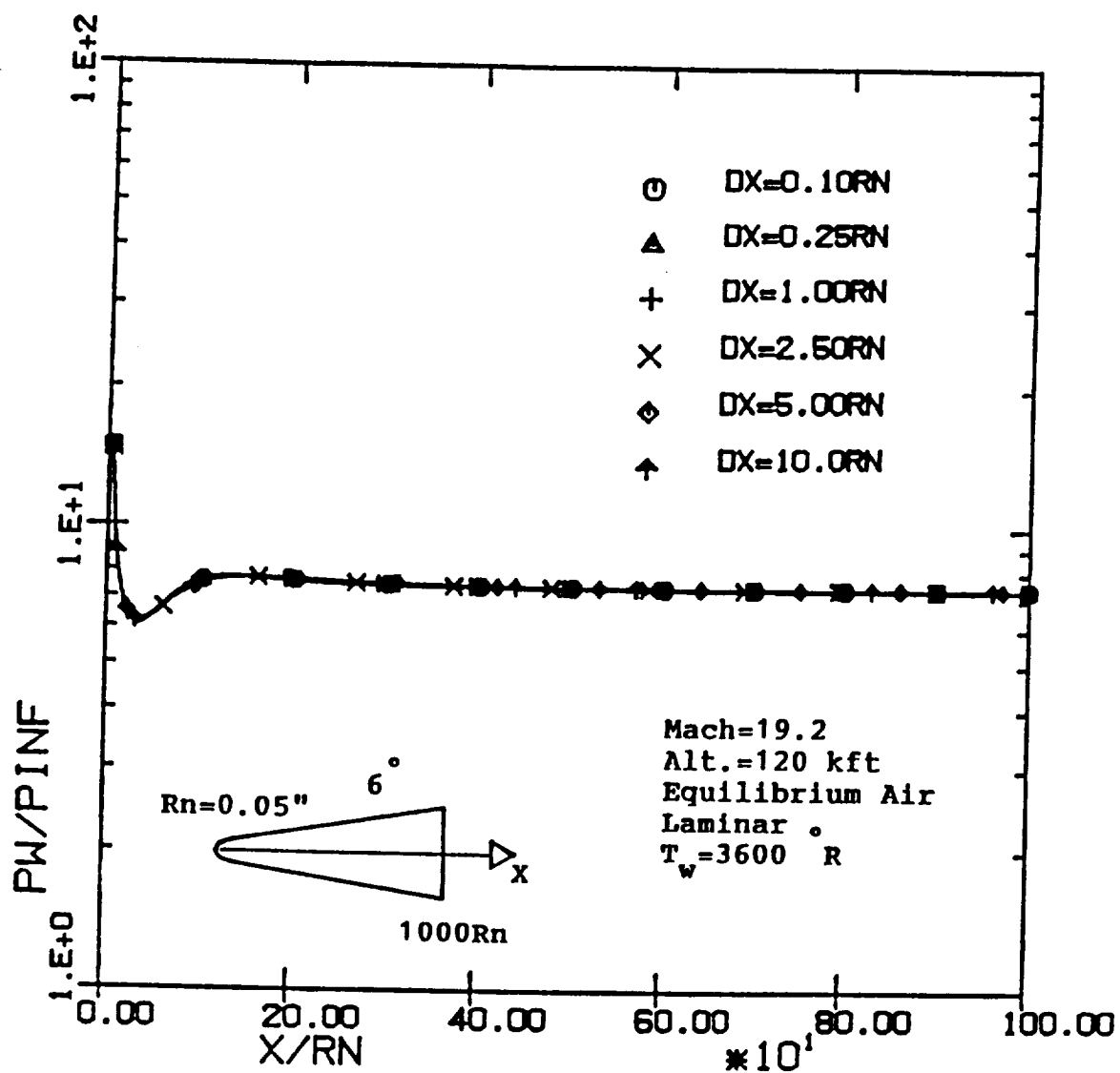
Fig. D.2. Axial distribution of wall pressure with an equilibrium-
air gas model.
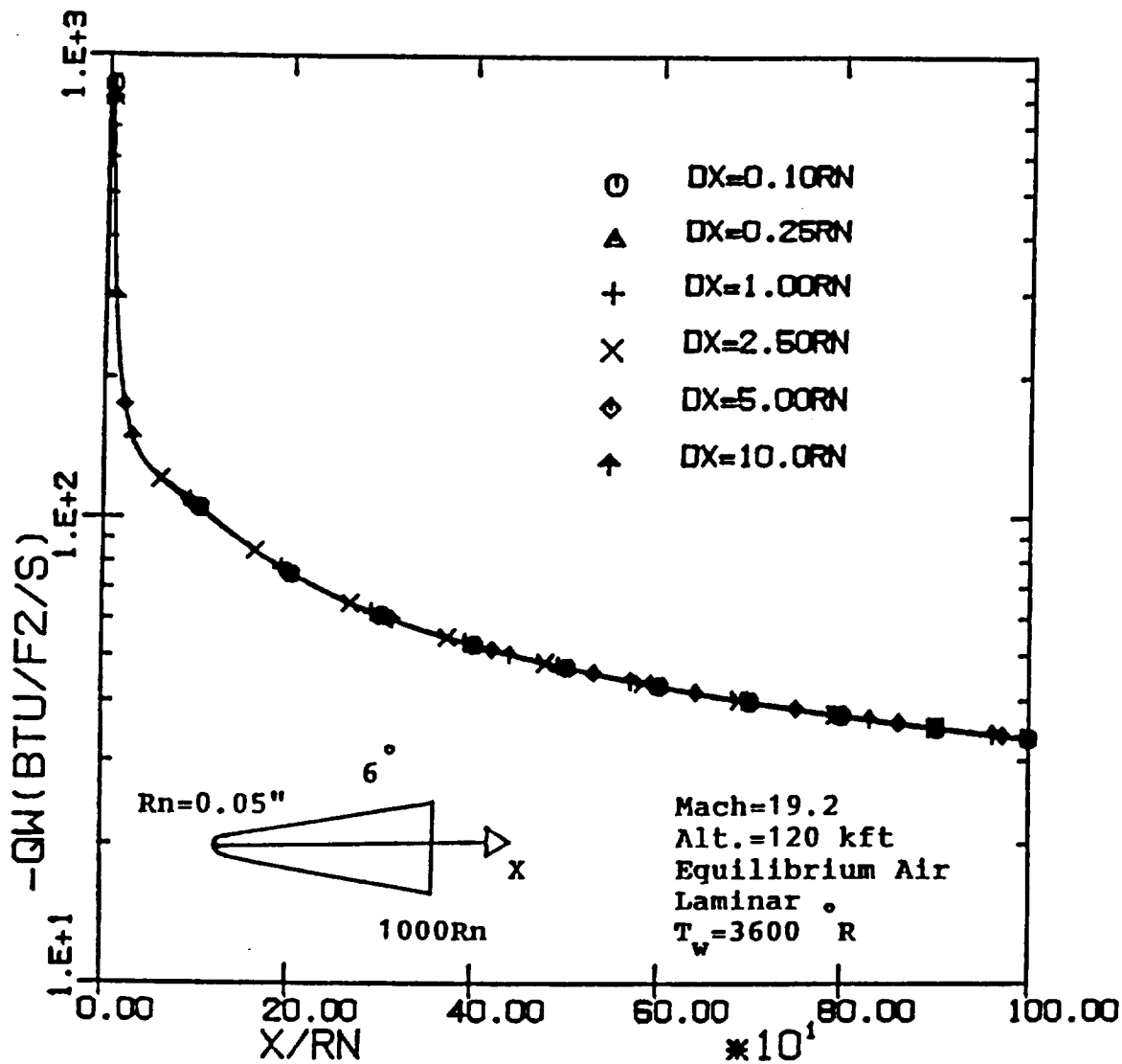
Fig. D.3. Axial distribution of wall heat-transfer rate with an
equilibrium-air gas model.

APPENDIX E. EXPRESSIONS FOR THE SPECIES PRODUCTION TERMS

The stoichiometric relations for a multicomponent gas with NS distinct chemical species and NR simultaneous chemical reactions can be expressed as

$$\sum_{i=1}^{NJ} \alpha_{ri} X_i \underset{k_{br}}{\overset{k_{fr}}{=}} \sum_{i=1}^{NJ} \beta_{ri} X_i \quad r = 1, ..., NR \tag{E.1}$$

The quantities X_i represent the chemical species and catalytic bodies and α_{ri}, β_{ri} are the stoichiometric coefficients of the reaction 'r'. Thus the summation limit NJ is equal to the number of species NS plus the number of catalytic bodies NZ.

The rates at which the forward and backward reactions occur are specified by the forward and backward rate constants which can be expressed by the equations

$$k_{f_r} = T_k^{C_{2r}} \, e^{(C_{0_r} - \frac{C_{1_r}}{T_k})} \tag{E.2a}$$

and

$$k_{b_r} = T_k^{D_{2r}} \, e^{(D_{0_r} - \frac{D_{1_r}}{T_k})} \tag{E.2b}$$

The net rate of production per unit volume of the i-th species during the chemical reactions is written as

$$\frac{\dot{\omega_i}}{\rho} = M_i \sum_{r=1}^{NR} (\beta_{ri} - \alpha_{ri})(L_{f_r} - L_{b_r}) \tag{E.3}$$

where

$$\alpha_r = \sum_{j=1}^{NJ} \alpha_{rj} - 1 \tag{E.4a}$$

$$\beta_r = \sum_{j=1}^{NJ} \beta_{rj} - 1 \tag{E.4b}$$

$$L_{f_r} = k_{f_r} \bar{\rho}^{\bar{\alpha}_r} \prod_{j=1}^{NJ} (\gamma_j)^{\alpha_{rj}} \tag{E.5a}$$

$$L_{b_r} = k_{b_r} \bar{\rho}^{\bar{\beta}_r} \prod_{j=1}^{NJ} (\gamma_j)^{\beta_{rj}} \tag{E.5b}$$

where $\bar{\rho}$ is the mixture density in gm/cm^3.

For the NS species, the molar concentrations γ_j, are given by the expression

$$\gamma_j = \frac{C_j}{M_j} \tag{E.6a}$$

For the catalytic third bodies the γ_j are given by the following expression

$$\gamma_j = \sum_{i=1}^{NS} Z_{(j-NS),i} \, \gamma_i, \qquad j = (NS + 1, \ldots, NJ) \tag{E.6b}$$

where $Z_{(j-NS),i}$ is the catalytic third body efficiency relative to argon, and depends upon the reaction being considered.

The production term can be rewritten so that the species concentration appears as one of the unknowns, and the rate of production terms are given by the expression

$$\frac{\dot{\omega}_i}{\rho} = \dot{\omega}_i^0 - \dot{\omega}_i^1 C_i \tag{E.7}$$

where

$$\dot{\omega}_i^0 = M_i \sum_{r=1}^{NR} (\Gamma_{ri}^+ L_{f_r} + \Gamma_{ri}^- L_{b_r}) \tag{E.8a}$$

$$\dot{\omega}_i^1 = \sum_{r=1}^{NR} [\Gamma_{ri}^+ (\frac{L_{b_r}}{\gamma_i}) + \Gamma_{ri}^- (\frac{L_{f_r}}{\gamma_i})]$$

(E.8b)

$$\Gamma_{ri}^+ = (\beta_{ri} - \alpha_{ri}) \quad \text{if} \quad (\beta_{ri} - \alpha_{ri}) > 0$$
$$= \quad 0 \quad \text{if} \quad (\beta_{ri} - \alpha_{ri}) \leq 0$$

(E.9a)

$$\Gamma_{ri}^- = (\beta_{ri} - \alpha_{ri}) \quad \text{if} \quad (\beta_{ri} - \alpha_{ri}) < 0$$
$$= \quad 0 \quad \text{if} \quad (\beta_{ri} - \alpha_{ri}) \geq 0$$

(E.9b)

The derivative of $\dfrac{\dot{\omega}_i}{\rho}$ with respect to temperature is given as

$$\left(\frac{\dot{\omega}_i}{\rho} \right)_{,T_k} = \frac{M_i}{T_k} \sum_{r=1}^{NR} (\beta_{ri} - \alpha_{ri}) [(C_{2_r} + \frac{C_{1_r}}{T_k} - \alpha_r) L_{f_r} - (D_{2_r} + \frac{D_{1_r}}{T_k} - \beta_r) L_{b_r}]$$

(E.10)

where T_k is the local temperature in degrees Kelvin.

APPENDIX F. TRANSITIONAL/TURBULENT FLOW MODELING

In turbulent flow calculations, one must relate Reynolds stress terms to the mean flow quantities in order to mathematically close the problem. The simplest approach is a two-layer eddy-viscosity model consisting of an inner law based upon Prandtl's mixing-length concept (Adams, 1972) and an outer law based on the Clauser-Klebanoff (Clauser, 1954) expressions. This model (introduced originally by Cebeci, 1970) assumes that the inner law is applicable from the wall outward to the location where the eddy-viscosity given by the inner law is equal to that of the outer law. The outer law is then assumed applicable for the remainder of the viscous layer. It is noted that the eddy-viscosity degenerates to approximately zero in the inviscid portion of the shock layer. This two-layer eddy-viscosity approach has been used in the present nonequilibrium PNS formulation.

In order to calculate the inner eddy-viscosity (μ_{in}) distribution, Adams (1972) extended Prandtl's mixing-length concept for two-dimensional flows to three-dimensional flows. In this approach it is assumed that the eddy-viscosity is a scalar function independent of the coordinate directions and can be written as

$$\mu_{in} = \rho \ell^2 |\omega| \tag{F.1}$$

where ω is the local vorticity vector and $|\omega|$ is its magnitude. The mixing length ℓ is evaluated by the following expression

$$\ell = \kappa n[1 - \exp(n^+/26)] \tag{F.2}$$

where

$$n^+ = \rho u^* n/\mu \tag{F.3}$$

Here, the von Karman constant (κ) is equal to 0.4, n is the distance measure from the wall boundary and the friction velocity u^* is defined as

$$u^* = [\mu_w(|\omega|)_w/\rho]^{0.5} \tag{F.4}$$

For the outer region, the outer eddy-viscosity (μ_o) is approximated by the Clauser-Klebanoff expression

$$\mu_o = 0.0168\rho u_e \delta^* \gamma_{int} \qquad (F.5)$$

In this expression, the incompressible displacement thickness (δ^*) is defined as

$$\delta^* = \int_0^n (1 - \frac{u}{u_e})dn \qquad (F.6)$$

where δ is the local boudary layer thickness. For the present cold-wall cases this boundary-layer thickness is calculated using an enthalpy model. In this enthalpy model it is assumed that appropriate value of δ to be used is equal to the value of normal co-ordinate 'n' where

$$\frac{[\bar{h}_0 - \bar{h}_w]}{[(\bar{h}_0)_\infty - \bar{h}_w]} = 0.995 \qquad (F.7)$$

where the subscrip '0' represents total conditions. The intermittency factor (γ_{int}) appearing in Eq. (F.5) is defined as

$$\gamma_{int} = \frac{1}{[1 + 5.5(n/\delta)^6]} \qquad (F.8)$$

The turbulent Prandtl number and Lewis number are assumed to be 0.9 and 1.0, respectively.

The distance between transition onset at x_{tr} and the beginning of fully turbulent flow further downstream at x_T is called the transition zone. The transition model used in the present formulation is based on the model proposed by Dhawan and Narasimha (1958). In this model, continuous transition is effected by defining a streamwise transition intermittency factor (γ_{tr}) which modifies the composite eddy viscosity (μ_{turb}) over the transition region ($x_T - x_{tr}$). The factor γ_{tr} is initially set to zero and is evaluated when the $x \geq x_{tr}$. In the region $x \geq x_{tr}$, the streamwise intermittency factor (γ_{tr}) is evaluated using the the following relation

$$\gamma_{tr} = [1 - \exp(-0.412\bar{x}^2)] \leq 1 \qquad (F.9)$$

where γ_{tr} has a maximum value of 1 and

$$\bar{x} = 2.96(x - x_{tr})/x_{tr} \qquad (F.10)$$

The various coefficients and parameters used in this model are based on numerical tests and comparisons with experimental data.

APPENDIX G. WALL HEAT-TRANSFER RATE AND SHEAR STRESSES

Let us define the normal, streamwise and tangential vectors to a $\xi_2 =$ constant surface as **n**, **s** and **t**, respectively. These vector directions are schematically shown in Fig. G.1, and can be expressed in terms of metric derivatives as

$$
\begin{aligned}
\mathbf{n} &= (y_{,\xi_1}z_{,\xi_3} - z_{,\xi_1}y_{,\xi_3})\mathbf{i} - x_{,\xi_1}z_{,\xi_3}\mathbf{j} + x_{,\xi_1}yz_{,\xi_3}\mathbf{k} \\
\mathbf{s} &= x_{,\xi_1}\quad \mathbf{i} + y_{,\xi_3}\ \mathbf{j} + zy_{,\xi_3}\ \mathbf{k} \qquad\qquad (G.1) \\
\mathbf{t} &= \quad\qquad \mathbf{i}\quad y_{,\xi_3}\ \mathbf{j} + zy_{,\xi_3}\ \mathbf{k}
\end{aligned}
$$

where **i**, **j** and **k** are unit vectors in the x, y and z coordinate directions, respectively.

The directional derivative of any quantity 'ϕ' in the direction of **n** is given as

$$
\phi_{,n} = \frac{\mathbf{n}}{|\mathbf{n}|}\bullet\nabla\phi = \frac{n_k}{|\mathbf{n}|}\phi_{,x_k} = \frac{n_k\xi_{j,x_k}}{|\mathbf{n}|}\phi_{,\xi_j} \qquad (G.2)
$$

where n_1, n_2 and n_3 are the components of vector **n** in the x, y and z directions, respectively. The required ξ_1 and ξ_2 derivatives at the wall can be calculated using one-sided difference approximations, while the ξ_3 derivatives can be calculated using central-difference approximation. Accuracy of the derivatives in the ξ_2 direction can be enhanced by using higher-order (three-point or more) difference formulas. In calculating these coordinate derivatives, it should be noted that the computational grid is equally spaced in terms of the ξ_1, ξ_2 and ξ_3 coordinates.

The component of wall heat-transfer due to conduction ($\dot{Q}_{cond}$), and the component of wall heat transfer due to species diffusion ($\dot{Q}_{diff}$) are defined as follows.

$$
\dot{Q}_{cond} = -k(\frac{\partial T}{\partial n})_w \qquad (G.3)
$$

$$
\dot{Q}_{diff} = -\sum_{i=1}^{NS}[\frac{\mu Le}{Pr}h_{iw}\frac{\partial C_i}{\partial n}]_w \qquad (G.4)
$$

The total wall heat-transfer rate ($\dot{Q}_{tot}$) at the wall is a sum of these two contributions.
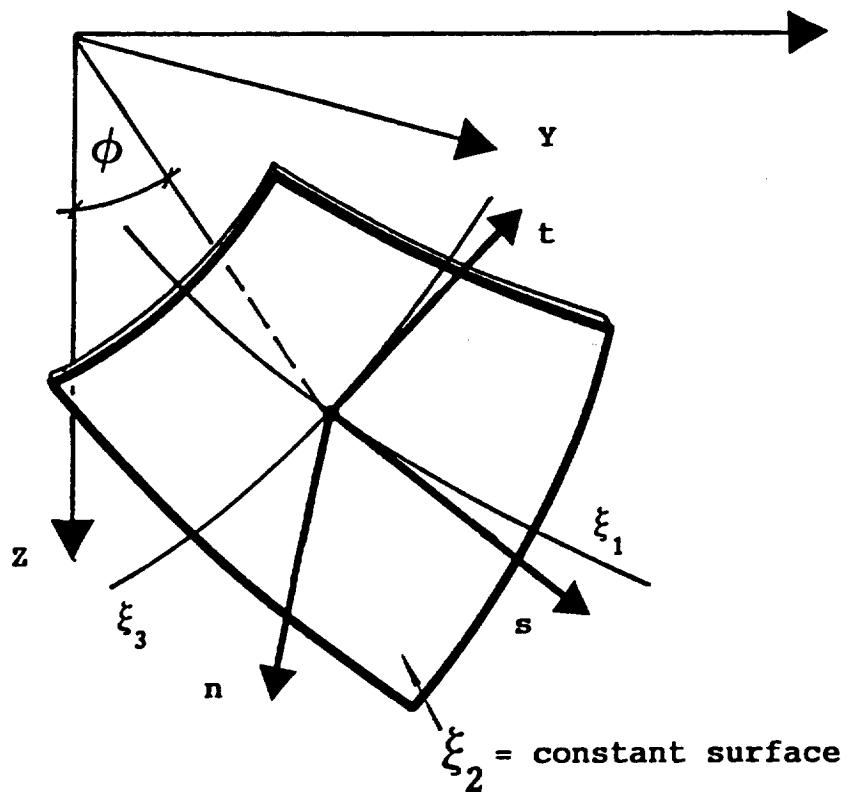
Fig. G.1. Schematic description of the normal and tangential vectors for a ξ_2=constant surface.

APPENDIX H. AERODYNAMIC FORCES AND MOMENTS

Let us define the normal, streamwise and tangential vectors to a $\xi_2 =$ constant surface as n, s and t, respectively. These vector directions can be expressed in terms of metric derivatives as

$$
\begin{aligned}
\mathbf{n} &= (y_{,\xi_1}z_{,\xi_3} - z_{,\xi_1}y_{,\xi_3})\mathbf{i} - x_{,\xi_1}z_{,\xi_3}\mathbf{j} + x_{,\xi_1}yz_{,\xi_3}\mathbf{k} \\
\mathbf{s} &= x_{,\xi_1} \quad \mathbf{i} + y_{,\xi_3}\ \mathbf{j} + zy_{,\xi_3}\ \mathbf{k} \\
\mathbf{t} &= \quad\quad \mathbf{i} \quad y_{,\xi_3}\ \mathbf{j} + zy_{,\xi_3}\ \mathbf{k}
\end{aligned}
\tag{H.1}
$$

where i, j and k are unit vectors in the x, y and z coordinate directions, respectively.

With the n, s and t directions defined as above, we can write the components of the force vector due to pressure (Δf_p), due streamwise skin-friction (Δf_s) and due to cross-flow skin-friction (Δf_t) as

$$
\Delta f_p = -\int_0^{\Delta A_s} (p - p_\infty)\frac{\mathbf{n}}{|\mathbf{n}|}\, dA
\tag{H.2}
$$

$$
\Delta f_s = \int_0^{\Delta A_s} \tau_s \frac{\mathbf{s}}{|\mathbf{s}|}\, dA
\tag{H.3}
$$

and

$$
\Delta f_t = \int_0^{\Delta A_s} \tau_t \frac{\mathbf{t}}{|\mathbf{t}|}\, dA
\tag{H.4}
$$

where τ_s is the streamwise wall-shear stress, τ_t is the crossflow wall-shear stress and ΔA_s is the surface area of the body between the current and previous marching steps. Similarly we can define the component of the moment vector as

$$
\Delta m_t = \int_0^{\Delta A_s} (\mathbf{r}\times\Delta f_p + \mathbf{r}\times\Delta f_s + \mathbf{r}\times\Delta f_t)\, dA
\tag{H.5}
$$

where r is the local position vector defined as

$$r = xi + yj + k \tag{H.6}$$

If j represents the previous marching step and j + 1 represents the current marching step, the total force vector (f) and the total moment vector (m) at the current step become

$$
\begin{aligned}
f^{j+1} &= f^j + \Delta f_p + \Delta f_s + \Delta f_t \\
m^{j+1} &= m^j + \Delta m_p + \Delta m_s + \Delta m_t
\end{aligned} \tag{H.7}
$$

Once the force and moment vectors are known, the force and moment coefficients can be obtained. Figure H.1 shows a schematic description of the positive direction of the force and moment coefficients relative to the Cartesian coordinate. The axial-force coefficient (C_A), the normal-force coefficient (C_N) and the pitching-moment coefficient (C_M) become

$$C_A = \frac{f_x}{(q_\infty A_c)} \tag{H.8}$$

$$C_N = -\frac{f_z}{(q_\infty A_c)} \tag{H.9}$$

and

$$C_M = -\frac{m_y}{(q_\infty A_c x)} \tag{H.10}$$

where f_x and f_z are the x and z components of f^{i+1}, m_y is the y component of m^{i+1}, A_c is the local cross-sectional area, and q_∞ is the freestream dynamic pressure. From Fig. H.1 it can also be seen that the lift coefficient (C_L) and the drag coefficient (C_D) can now be expressed as

$$
\begin{aligned}
C_D &= C_A \cos\alpha + C_N \sin\alpha \\
C_L &= -C_A \sin\alpha + C_N \cos\alpha
\end{aligned} \tag{H.11}
$$
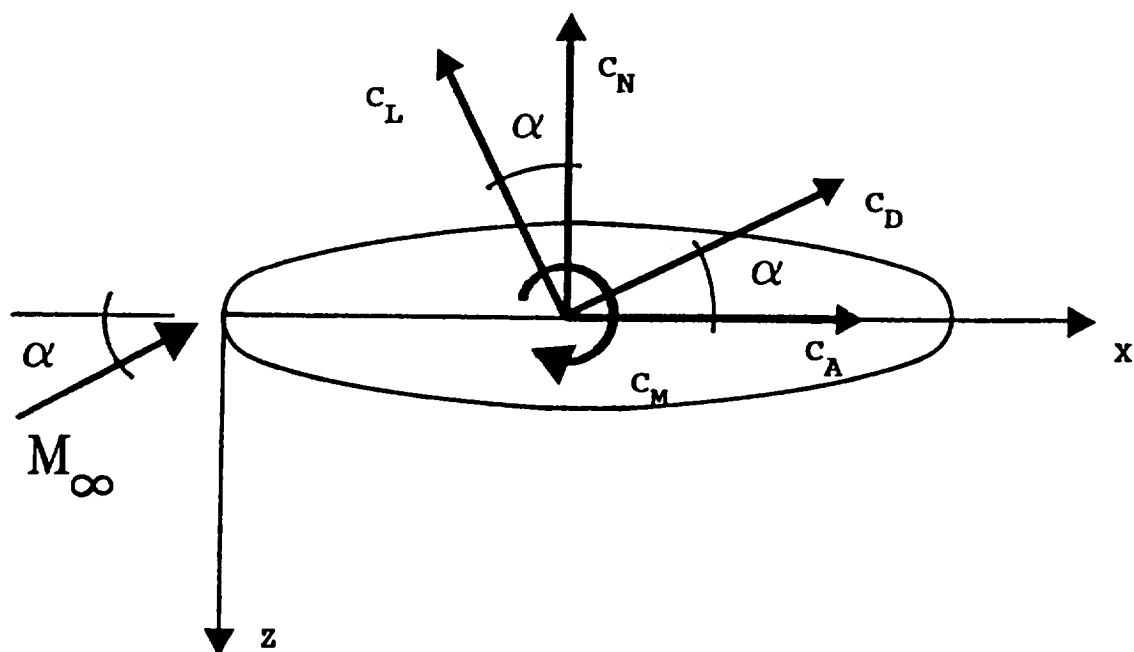
Fig. H.1. Schematic description of the positive directions for the force and moment coefficients.

APPENDIX I. A MODEL DIFFERENTIAL/ALGEBRAIC MARCHING PROBLEM

The system of equations represented by the governing PNS equations is not a pure differential system, it consists of five partial differential equations coupled through a sixth equation which is a purely algebraic relation. In the present treatment this set of governing equations is referred to as a 'differential/algebraic system'. The most important view point to be presented in this section is that the character classification of a differential/algebraic system is significantly different from the classical character classification of purely differential systems. In other words a purely differential system has a certain character; i.e., it is either elliptic or time-like or mixed. By 'time-like' we mean that a differential system is either hyperbolic or parabolic or mixed hyperbolic-parabolic. However, as long as the differential system is time-like, the numerical solution can be marched in the time-like direction. On the other hand, if the differential system is elliptic in character, marching-like numerical solutions are invalid.

The case of the differential/algebraic systems is, however, quite different. For such differential/algebraic systems the overall character of the system may depend upon the way in which the problem is formulated. That is to say, it may be possible to have a differential/algebraic system as elliptic or conditionally elliptic if one formulates the problem in one way, and have it unconditionally marching-like if one formulates the problem in another way. This idea is new and has given rise to a fair amount of controversy. Nonetheless, it may be analytically demonstrated on a model mixed-type system.

Consider the following system involving 3 unknowns, ϕ_1, ϕ_2 and ϕ_3; i.e.,

$$\phi_{1,x} - \phi_{2,y} = 0$$
$$\phi_{2,x} - \phi_{1,y} + 2\phi_{2,y} + \phi_{3,y} = 0 \qquad (I.1)$$
$$a^2\phi_1 - \phi_3 = 0$$

with initial condition specified at $x = 0$ and boundary conditions specified at $y = 0$ and at $y = 1$. Suppose we consider the following initial and boundary conditions:

$$\phi_3(0,y) = a^2\phi_1(0,y)$$
$$\phi_1(0,y) = \phi_2(0,y) = y \qquad (I.2)$$

$$\phi_3(x,0) = a^2\phi_1(x,0)$$
$$\phi_{1,y}(x,0) = \phi_{2,y}(x,0) = 1 \tag{I.3}$$

and

$$\phi_3(x,1) = a^2\phi_1(x,1)$$
$$\phi_1(x,1) = 1 + x$$
$$\phi_2(x,1) = 1 - (a^2 + 1)x \tag{I.4}$$

The solution to Eqs. (I.1) for these boundary conditions [Eqs. (I.2), (I.3) and (I.4)] is (Bhutta and Lewis, 1985d)

$$\phi_1(x,y) = y + x$$
$$\phi_2(x,y) = y - (a^2 + 1)x \tag{I.5}$$
$$\phi_3(x,y) = a^2(y + x)$$

The above model problem resembles the inviscid limit of the governing PNS equations. The model problem involves only first-order derivatives in the two spatial coordinate directions to simulate the convective derivatives of the inviscid limit of the PNS equations. The third equation of this model problem is an algebraic relation, and is used to simulate the role of the algebraic equation of state in the PNS equations. Just like the equation of state in the governing PNS equations, the algebraic relation of the model problem appears not only as a relation to be satisfied within the solution domain, but it also appears in the initial conditions and the boundary conditions. The variable ϕ_3 of the model problem plays a similar role as played by pressure in the governing PNS equations. Now consider the following two different formulations of the model problem.

I.1. Formulation I

In this approach we can substitute the third equation of Eq. (I.1) into the second equation and obtain

$$\phi_{1,x} - \phi_{2,y} = 0$$
$$\phi_{2,x} + (a^2 - 1)\phi_{1,y} + 2\phi_{2,y} = 0 \tag{I.6}$$

Or we may simply write

$$\boldsymbol{\varphi}_x + \mathbf{A} \cdot \boldsymbol{\varphi}_y = 0 \tag{I.7}$$

where

$$\varphi = [\phi_1, \ \phi_2]^T \tag{I.8}$$

and the eigenvalues of **A** are

$$\lambda_1 = 1 + (2 - a^2)^{0.5}$$
$$\lambda_2 = 1 - (2 - a^2)^{0.5} \tag{I.9}$$

It is shown by Bhutta and Lewis (1985d) that we can write Eq. (I.7) as

$$\psi_{1,x} + \lambda_1 \psi_{1,y} = 0$$
$$\psi_{2,x} + \lambda_2 \psi_{2,y} = 0 \tag{I.10}$$

where

$$\phi_1 = \psi_1 + \psi_2$$
$$\phi_2 = -\lambda_1 \psi_1 - \lambda_2 \psi_2 \tag{I.11}$$

Thus, we see that Eqs. (I.10), and equivalently Eqs. (I.6), are time-like if λ_1 and λ_2 are real ($a^2 \leq 2$). When λ_1 and λ_2 are not real ($a^2 > 2$), Eqs. (I.6) and (I.10) are elliptic in nature. In other words, a marching-like solution of Eqs. (I.6) will be valid only if $a^2 \leq 2$. Furthermore, it has been shown by Bhutta and Lewis (1985d) that for $a^2 \leq 2$ the analytic solution to Eqs. (I.6) can be found, and it is the same as given by Eqs. (I.5).

I.2. Formulation II

From the earlier discussion on Formulation I of the model problem, we see that the variable 'a' of the model problem is like the speed of sound in the governing PNS equations. That is to say, in the classical PNS schemes where the speed of sound appears in the eigenvalues through the pressure terms and the accompanying equation of state (Schiff and Steger, 1979, and Shanks et al., 1979), in the model problem the variable 'a' appears in the eigenvalues through the variable ϕ_3 and the corresponding algebraic relation. Now, for this model problem, if we can devise another formulation such that the variable 'a' no longer contributes to the eigenvalues of the system, it may provide us with a key to attempt a similar treatment of the governing PNS equations. Such a re-formulation of the model problem is mathematically possible, and it will be called Formulation II.

In the aforementioned Formulation I, the overall differential/algebraic system was reduced to a pure differential system. In Formulation II we attempt to solve directly the actual differential/algebraic system [Eq. (I.1)], and look at the character of the resulting system. At first glance it does not seem likely to be able to do that. However, it is possible to do such an analysis if one looks at Eq. (I.1) as the limiting case of a small-perturbation problem. Such an approach is valid as long as the small-perturbation problem being considered allows us to take this limit without any singular behavior.

For this purpose, consider the following problem (were $\varepsilon \geq 0$)

$$\phi_{1,x} - \phi_{2,y} = 0$$
$$\phi_{2,x} - \phi_{1,y} + 2\phi_{2,y} + \phi_{3,y} = 0 \tag{I.12}$$
$$\varepsilon\phi_{3,x} = a^2\phi_1 - \phi_3$$

with

$$\phi_1(0,y) = y$$
$$\phi_2(0,y) = y \tag{I.13}$$
$$\phi_3(0,y) = a^2 y$$

$$\phi_{1,y}(x,0) = 1$$
$$\phi_{2,y}(x,0) = 1 \tag{I.14}$$
$$\varepsilon\phi_{3,x}(x,0) = a^2\phi_1(x,0) - \phi_3(x,0)$$

and

$$\phi_1(x,1) = 1 + x$$
$$\phi_2(x,1) = 1 - (a^2 + 1)x \tag{I.15}$$
$$\varepsilon\phi_{3,x}(x,1) = a^2\phi_1(x,1) - \phi_3(x,1)$$

Thus, the small perturbation problem being presented has the correct initial conditions, and the boundary conditions at $y = 0$ and $y = 1$ are consistent with the governing equations [Eqs. (I.12)].

The complete solution of this problem is given by Bhutta and Lewis (1985d). However, briefly speaking, Eqs. (I.12) can be written as

$$\varphi_x + A \cdot \varphi_y - (1/\varepsilon)B \cdot \varphi = 0 \tag{I.16}$$

The eigenvalues of A are

$$\lambda_1 = 1 + \sqrt{2}$$
$$\lambda_2 = 1 - \sqrt{2} \tag{I.17}$$
$$\lambda_3 = 0$$

It is shown by Bhutta and Lewis (1985d) that we can write Eqs. (I.16) as

$$\psi_{1,x} + \lambda_1\psi_{1,y} - \lambda_2(f/\varepsilon) = 0$$
$$\psi_{2,x} + \lambda_2\psi_{2,y} + \lambda_1(f/\varepsilon) = 0 \tag{I.18}$$
$$\psi_{3,x} - (\lambda_1 - \lambda_2)(f/\varepsilon) = 0$$

where

$$f = [a^2(\psi_1 + \psi_2) + (a^2 - 1)\psi_3]/(\lambda_1 - \lambda_2) \tag{I.19}$$

and

$$\phi_1 = \psi_1 + \psi_2 + \psi_3$$
$$\phi_2 = -\lambda_1\psi_1 - \lambda_2\psi_2 \tag{I.20}$$
$$\phi_3 = \psi_3$$

Since λ_1 and λ_2 are real [see Eqs. (I.17)], we can see that Eqs. (I.18) are unconditionally time-like, and a marching-type numerical solution of Eqs. (I.18) will be unconditionally valid.

In order to answer the question, "How does the small perturbation problem of Eqs. (I.12) relate to the original problem of Eqs. (I.1)?", we can see that under the limiting condition

$$\varepsilon \to 0^+ \tag{I.21}$$

Eqs. (I.12) reduce to Eqs. (I.1), and the boundary conditions given by Eqs. (I.14) and (I.15) reduce to the actual boundary conditions given by Eqs. (I.3) and (I.4). The initial conditions are the same anyway.

A question arises --- "Is it valid to take the limit of Eqs. (I.18)?", or in other words "Does Eqs. (I.18) behave singularly because of the $1/\varepsilon$ factor?" To answer this question, the third equation of this system [Eqs. (I.18)] shows that for all ε

$$f/\varepsilon = \psi_{3,x}/(\lambda_1 - \lambda_2) \tag{I.22}$$

In other words, Eq. (I.22) indicates that 'f/ε' is always defined, if $\psi_{3,x}$ is defined for $\varepsilon \geq 0$.

The demonstration that $\psi_{3,x}$ is bounded for $\varepsilon \geq 0$ [i.e., Eqs. (I.18) is not singular when $\varepsilon \rightarrow 0^+$], comes from the actual analytic solution of Eqs. (I.18). It is shown by Bhutta and Lewis (1985d) that the analytic solution to Eqs. (I.18) and (I.20) is

$$\phi_1(x,y) = y + x$$
$$\phi_2(x,y) = y - (a^2 + 1)x \qquad (I.23)$$
$$\phi_3(x,y) = a^2(y + x) - a^2\varepsilon[1 - \exp(-x/\varepsilon)]$$

where

$$\varepsilon \geq 0 \qquad (I.24)$$

It should be noted that we are marching in the x direction, so that our x is always positive and increasing. Thus, we see that with $\varepsilon \rightarrow 0^+$, Eqs. (I.22) does not appear to be singular [or, equivalently Eqs. (I.22) does not appear to be singular] and, furthermore, this solution seems to be valid even for $\varepsilon = 0$ (Bhutta and Lewis, 1985d). Also, we see that with $\varepsilon \rightarrow 0^+$, the solution to our hypothetical small perturbation problem appears to correctly approach the solution to our actual model problem; i.e.,

$$\phi_1(x,y) = y + x$$
$$\phi_2(x,y) = y - (a^2 + 1)x \qquad (I.25)$$
$$\phi_3(x,y) \rightarrow a^2(y + x)$$

The aforementioned mathematical exercise is only used to present the conclusion --- There exist a class of 'differential/algebraic' system-of-equations where it is possible to have a conditionally time-like behavior if one formulates the problem in one way, and it is also possible to have the same problem as unconditionally time-like if one formulates the problem in a slightly different manner.

The model problem [Eqs. (I.1)] presented herein, bears considerable similarity to the inviscid limit of the governing PNS equations. The classical treatments of these PNS equations (Schiff and Steger, 1979; Vigneron et al., 1978; Shanks et al., 1979; etc.) correspond to the Formulation I presented earlier, which was conditionally time-like. The present scheme, however, follows the approach of Formulation II, which had an unconditionally time-like character.

I.3. Numerical Solution of the Model Problem

The key point to be understood before attempting a solution of the model problem is that this model problem does not have an asymptotic limit; i.e., the solution grows as one marches on. Also, for this problem the equations governing the propagation of errors are the same as the governing equations. Consequently, the errors also convect and grow as the solution marches away from the initial conditions. This in itself is not a big problem because if the problem were only limited to this, the solution and associated errors grow at comparable rates and the relative error (which is actually the important quantity) does not change much. However, the problem with truncation errors is that these errors not only convect and grow (as dictated by the governing equations), but at each step the cause for the generation of numerical errors remains there and keeps on adding to the existing errors. Thus, the net effect of this is that the growth of truncation errors is faster than the actual growth of the solution itself, and if one does not control these errors they can (and will) become large enough to start affecting the solution.

It is important to note that the solution in the y-coordinate direction is not only the initial source of truncation errors, but also the subsequent reason for their increased rate of growth (because at each step it adds to the existing error). Thus, it should be clear that the growth of these truncation errors is actually governed by the number of times the y-solution (and associated truncation errors) are committed. In other words, the errors will grow more rapidly if one takes smaller steps and, thus, commits a larger number of times the y-solution and the associated errors. This could be wrongfully interpreted as a step-size (departure) problem, but the fact remains that the step-size has nothing to do with the actual cause of the problem which is simply the inaccuracies in doing the numerical solution.

A clear advantage of an analytic solution of the problem (if possible) is that it does not suffer from solution inaccuracies and presents the true picture. Furthermore, when using numerical solutions to either validate or contradict analytic analysis, it is essential that either the numerical truncation errors be eliminated or controlled before one can focus on anything else as the potential source of any problems with the numerical solution.

In the following sections we will consider two different approaches to the numerical solution of Eqs. (I.1). The first approach will use an explicit Lax method (Anderson et al., 1984), and will focus on controlling the growth of errors at a marching step. In the

second approach we will use an implict bidiagonal scheme and will focus on the elimination of truncation errors. Thus, by controlling/eliminating the truncation errors, we will obtain numerical solutions which will truely reflect the character of the governing equations and not the effects of numerical inaccuracies.

The explicit Lax method has been used for the $\varepsilon = 0$ case only, while the bidiagonal implicit method has been used for zero and nonzero values of ε. The main thrust of our numerical study is the bidiagonal implicit scheme because it is the most accurate. On the other hand, the explicit Lax method (although less accurate) is also interesting because the solution procedure is identical to the one used for a classical two-dimensional wave propagation problem, and the stability constraint obtained is comparable to the classical CFL condition.

I.3.1. Explicit Lax Method

This approach is modeled after the Lax method for solving a linear first-order hyperbolic set of equations (Anderson et al., 1984, pp. 78). In this method the x-derivatives are forward differenced, so that the y-derivatives become explicitly known from the previous marching step. At the same time the solution values at the previous marching step are averaged, which is an $O(\Delta y^2)$ approximation. The idea for this approach is that by avoiding the implicit solution in the y-direction we substantially reduce and limit the generation of numerical truncation errors. Furthermore, in this case an eigenvalue analysis can be performed on the error-propagation equations to obtain a constraint condition which theoretically limits the growth of errors. Since numerically at each step we still cause a truncation error (however small), the actual errors still grow in magnitude, but this growth is extremely small if we maintain the stability constraint.

The important thing to note about this method is that for a given step size in the y-direction (Δy), there is only an upper bound on the marching step size (Δx) and not a lower bound which would have implied the classical departure-like behavior. As for the upper bound on the marching step-size, a similar analysis of the wave equations also gives an upper bound, which is the classical CFL condition (Anderson et al., 1984, pp. 78). Thus, this upper bound on the marching step-size is consistent with the classical treatments of true marching problems.

If we denote the x-direction by the superscript 'i' and the y-direction by the superscript 'j', the Eqs. (I.1) take the form

$$\begin{bmatrix} 1 & 0 & 0 \\ 0 & 1 & 0 \\ -a^2 & 0 & 1 \end{bmatrix} \begin{bmatrix} \phi_1 \\ \phi_2 \\ \phi_3 \end{bmatrix}^{i+1,j} = (1/2)(\begin{bmatrix} \phi_1 \\ \phi_2 \\ 0 \end{bmatrix}^{i,j+1}_{i,j} + \begin{bmatrix} \phi_1 \\ \phi_2 \\ 0 \end{bmatrix}^{i,j-1})$$

$$-\Delta x \begin{bmatrix} 0 & -1 & 0 \\ -1 & 2 & 1 \\ 0 & 0 & 0 \end{bmatrix} \begin{bmatrix} \phi_1 \\ \phi_2 \\ \phi_3 \end{bmatrix}_{,y} \qquad (I.26)$$

where we have used forward-differenced approximations for the x-derivatives and an averaging of the solution at the previous (i-th) marching step. Furthermore, we make use of the fact that the solution at the previous (i-th) marching step is correctly known and satisfies the following algebraic relations (which come from the governing equations applied at the i-th step):

$$\phi_3^{i,j+1} = a^2\phi_1^{i,j+1}$$
$$\phi_3^{i,j-1} = a^2\phi_1^{i,j-1} \qquad (I.27)$$

Thus, the Eqs. (I.26) reduce to simply the following

$$\begin{bmatrix} \phi_1 \\ \phi_2 \end{bmatrix}^{i+1,j} = (1/2)(\begin{bmatrix} \phi_1 \\ \phi_2 \end{bmatrix}^{i,j+1} + \begin{bmatrix} \phi_1 \\ \phi_2 \end{bmatrix}^{i,j-1})$$

$$- (k/2)\begin{bmatrix} 0 & -1 \\ (a^2-1) & 2 \end{bmatrix}(\begin{bmatrix} \phi_1 \\ \phi_2 \end{bmatrix}^{i,j+1} - \begin{bmatrix} \phi_1 \\ \phi_2 \end{bmatrix}^{i,j-1}) \qquad (I.28)$$

and

$$\phi_3^{i+1,j} = a^2\phi_1^{i+1,j} \qquad (I.29)$$

where $k = (\Delta x/\Delta y)$. The numerical solution of the above system is simple as all the quantities on the right-hand side of Eqs. (I.28) are known from the previous step and the values of $\phi_1^{i+1,j}$ and $\phi_2^{i+1,j}$ can than be explicitly obtained. Once $\phi_1^{i+1,j}$ is known, the value of $\phi_3^{i+1,j}$ is obtained from Eq. (I.29).

Suppose we denote the errors in ϕ_1 and ϕ_2 by E_1 and E_2, respectively. An error analysis of Eqs. (I.28) can be performed if we assume these errors to be of the form

$$E_1^{i+1} = e_1^{i+1} \exp[-iky]$$
$$E_1^{i+1} = e_1^{i+1} \exp[-iky] \qquad (I.30)$$

and look at the amplification of the amplitudes of these errors (i.e., e_1 and e_2) as we march in the x direction (Anderson et al., 1984, pp. 78). A Fourier analysis of the error equations can now be performed and shows that error amplitudes will not grow if

$$|k^2(c^2 + d^2) + dk| < 1 \tag{I.31}$$

where

$$(c + id) = 1 + (2 - a^2)^{0.5} \tag{I.32}$$

Further simplification shows that the constraint of Eq. (I.31) reduces to the following constraint on $k = \Delta x/\Delta y$; i.e.,

$$|k - k_0| < [k_0^2 + 1/(c^2 + d^2)]^{0.5} \tag{I.33}$$

where

$$k_0 = -d/[2(c^2 + d^2)] \tag{I.34}$$

This constraint condition gives an upper bound on the choice of 'k' (k_{max}) or, equivalently, an upper bound on Δx for a given choice of Δy.

Figures I.1 to I.3 show the results obtained with the aforementioned explicit algorithm. These results are for a choice of $a^2 = 10$ which corresponds to $k_{max} = 0.2$. Two cases have been considered. Case 1 uses $\Delta y = 0.1$ and $\Delta x = 0.001$ ($k = 0.01$), and Case 2 is for a choice of $\Delta y = 0.05$ and $\Delta x = 0.001$ ($k = 0.02$). In other words, Case 1 uses 11 grid points in the y direction and 5000 marching steps in the x direction, while Case 2 uses 21 grid points in the y direction and 5000 marching steps in the x direction. Figures I.1, I.2 and I.3 show the ϕ_1, ϕ_2 and ϕ_3 solution at $y = 0$, respectively. For both cases the solution was carried out until $x = 5.0$, at which location the maximum error in both solutions was of the order of 10^{-29}. For these cases the truncation errors at the first marching station were of the order of 10^{-31}-10^{-32}. Figure I.4 shows the effect of violating the stability constraint (for this case) of $k_{max} = 0.2$. It shows solutions for $\Delta y = 0.1$ and for Δx values of 0.001, 0.005, 0.01, 0.02 and 0.1 (11 grid points in the y direction and 5000, 1000, 500, 250 and 50 steps, respectively, in the x direction). These values correspond to k values of 0.01, 0.05, 0.1, 0.2 and 1.0, respectively. It can be seen that for large values of k (> 0.2) the maximum errors start to increase quite rapidly.

I.3.2. Bidiagonal Implicit Method

The idea behind this approach is to eliminate the numerical truncation errors resulting from the floating-point roundoff (especially during the division operations). Multiplication by whole numbers and addition/subtraction operations do not contribute to the roundoff errors as much as the division operation by numbers with decimal fraction parts. Thus, the most desirable case would be to either have no division operations or at worst have division by whole numbers such as 2, 4, 5, etc. (because division operations for such numbers can be done exactly for almost all cases). One way of achieveing this would be to (if possible) do as much of the algebra by hand as possible (such as matrix inversions, multiplications, etc.) and adjust the various solution parameters such as to have either no divisions or divisions by numbers such as 2, 4, 5, etc. Fortunately, in the case of this model problem this is possible to do. In order to do so in the following discussion we will focus on the case of $a^2 = 3$ and for $k = \Delta x / \Delta y = 0.5$. The choice of these variables is solely based on the algebra simplification they introduce, and this makes the following analysis simple.

For the purely differential problem of Eqs. (I.12), we note that if we use one-sided (forward) difference operators for the y-derivatives, the solution at a given marching step can be integrated downwards from the specified boundary conditions at the $y = 1$ boundary toward the $y = 0$ boundary, where the solution can be obtained using the implicit boundary conditions of Eqs. (I.14). This method would in general be $O(\Delta y)$ accurate; however, it will be exact for solutions having a linear behavior in y-direction. With such forward-difference approximations for the y-derivatives and backward-difference approximations for the x-derivatives, Eqs. (I.12) take the following form (for $a^2 = 3$ and $\Delta x = 0.5 \Delta y$):

$$\begin{bmatrix} 2 & 1 & 0 \\ 1 & 0 & 1 \\ -3 & -1 & (1+\alpha) \end{bmatrix} \begin{bmatrix} \phi_1 \\ \phi_2 \\ \phi_3 \end{bmatrix}^{i+1,j} = \begin{bmatrix} 0 & 1 & 0 \\ 1 & -2 & -1 \\ 0 & 0 & 0 \end{bmatrix} \begin{bmatrix} \phi_1 \\ \phi_2 \\ \phi_3 \end{bmatrix}^{i+1,j+1} + \begin{bmatrix} 2 & 0 & 0 \\ 0 & 2 & 0 \\ 0 & 0 & \alpha \end{bmatrix} \begin{bmatrix} \phi_1 \\ \phi_2 \\ \phi_3 \end{bmatrix}^{i,j} \quad (I.35)$$

where $\alpha = \varepsilon / \Delta x$. These equations are further simplified by doing the associated matrix inversion and using the information that

$$(1 + \alpha) \phi_3^{i+1,j+1} = 3\phi_1^{i+1,j+1} + \alpha \phi_3^{i,j+1} \quad (I.36)$$

The use of Eq. (I.36) is correct because the solution progresses in the decreasing 'j' direction (decreasing y), so that while solving for the solution at $(i+1,j)$ grid point the

solution at $(i+1,j+1)$ grid point has already been obtained and satisfies Eqs. (I.35) applied at the $(i+1,j+1)$ grid point. In other words, Eq. (I.36) is simply the last equation of Eqs. (I.35) when applied at the $(i+1,j+1)$ grid point. At the $y=1$ boundary, Eq. (I.36) is simply the differenced form of the boundary condition on ϕ_3 [see Eqs. (I.14)].

With the abovementioned operations the solution at $(i+1,j)$ grid point can be written as

$$\phi_1^{i+1,j} = \phi_1^{i+1,j+1} + k_1(\phi_2^{i+1,j+1} - \phi_2^{i,j}) + k_2(\phi_3^{i,j+1} - \alpha\phi_3^{i,j}) \qquad (I.37)$$

$$\phi_2^{i+1,j} = -k_3\phi_1^{i+1,j+1} + \phi_2^{i+1,j+1} + 2(\phi_1^{i,j} + \phi_2^{i,j}) - k_4(3\phi_1^{i+1,j} - \phi_3^{i,j} + \phi_3^{i,j+1}) \quad (I.38)$$

$$\phi_3^{i+1,j} = k_5\phi_1^{i+1,j} + k_4\phi_3^{i,j} \qquad (I.39)$$

where

$$
\begin{aligned}
k_1 &= 2(1+\alpha)/(2-\alpha) \\
k_2 &= \alpha/(2-\alpha) \\
k_3 &= (2-\alpha)/(1+\alpha) \\
k_4 &= \alpha(1+\alpha) \\
k_5 &= 3/(1+\alpha)
\end{aligned}
\qquad (I.40)
$$

The values of these coefficients (k_1, k_2, k_3, k_4 and k_5) for $\alpha = 0$, 1 and 3 ($\varepsilon = 0$, Δx and $2\Delta x$, respectively) are given in Table I.1. As can be seen from this table, for $\alpha = 0$ the coefficients are whole numbers and no division operations are involved while for $\alpha = 1$ and 3 only division by 2 and 4 is involved which introduces minimal errors (if any). Solutions were obtained with different grids for the cases of $\alpha = 0$ and 1. Figures I.5 to I.7 show the solutions for the $\alpha = 0$ case, while Figs. I.8 to I.11 show the solutions for the $\alpha = 1$ case.

Figures I.5, I.6 and I.7 show the solutions for ϕ_1, ϕ_2 and ϕ_3 at $y = 0$ for the case of $\alpha = 0$. Solutions were obtained with Δx values of 0.0025, 0.005, 0.01, 0.025, 0.05 and 0.10 (corresponding to 6, 11, 21, 51, 101 and 201 grid points in the y-direction and 4000, 2000, 1000, 400, 200 and 100 steps, respectively, in the x direction). In each case the solution was marched from $x = 0$ to $x = 10$, and the numerical results showed that for all these cases the solution error was exactly zero at all stages of marching. This is indeed to be expected, because the exact solutions are bilinear space functions [Eqs. (I.5)], and for such bilinear functions one-sided differences in the x and y directions are mathematically exact. It is important to note that these solutions have been obtained by putting $\alpha = 0$

in the differenced form of Eqs. (I.12). No singular behavior or associated numerical difficulty was encountered in doing so, and the solution was the exact bilinear solution to the differential-algebraic system of Eqs. (I.1). This confirms the earlier conclusion that the Eqs. (I.1) are the true limiting case of Eqs. (I.12) with $\varepsilon = 0$, and that this limit is valid and can be taken without any singular behavior.

The solutions ϕ_1, ϕ_2 and ϕ_3 at $y = 0$ and for $\alpha = 1$ are shown in Figs. I.8, I.9 and I.10, respectively. Solutions are presented for Δx values of 0.10, 0.025 and 0.01, corresponding to Δy values of 0.2, 0.05, and 0.02, respectively (corresponding to 6×100, 21×400 and 51×1000 grid points, respectively). The results show that the solutions for ϕ_1 and ϕ_2 are exact, while the solution for ϕ_3 is not exact. However, it can be seen from Fig. I.10 that with decreasing Δx the numerical solution of ϕ_3 starts approaching the exact solution. This behavior is explained by the fact that the actual solution of ϕ_3 for $\varepsilon > 0$ has a non-linear exponential behavior in the x direction, which can not be properly modeled by a simple backward-differenced approximation of the $\phi_{3,x}$ term. However, this modeling improves as the marching step size (Δx) is decreased, and this is exactly the behavior shown by the numerical results for ϕ_3. The analysis presented in Section I.2 had shown that the solution of ϕ_1 and ϕ_2 for nonzero values of α (or equivalently ε) were composed of bilinear space functions. The numerical solutions of these variables do give the exact bilinear space variations and, thus, confirm the analytic solution of Eqs. (I.12) obtained in Section I.3. Figure I.11 shows the percentage error in the solution of ϕ_3 for the three different step-size distributions that were tried. This clearly shows the improvement in accuracy obtained by a decreasing sequence of marching step sizes.

It is worth pointing out that we also attempted a solution of the aforementioned $\alpha = 0$ case in which we numerically inverted the matrices rather than using the afore-mentioned coefficients (k_1 to k_5). In principal there should have been no difference in these two treatments; however, such was not the case. We tried the case with $\Delta x = 0.01$ and found that solution suffered from truncation errors which grew in magnitude as the number of marching steps increased, and after a couple of hundred steps these errors significantly degenerated the solution accuracy. Again, the only difference between this calculation and the similar calculation using Eqs. (I.37-I.39) was the numerical accuracy of the solution, and had nothing to do with the character of the governing equations which remain time-like.

I.3.3. Concluding Remarks on the Numerical Solution

Based on the results of this study following conclusion have been drawn.

(a) The results of this numerical study confirm the analysis of Bhutta-Lewis model problem. These results show that the solution of the Bhutta-Lewis model problem can be properly and accurately marched, provided one controls or eliminates the numerical errors and maintains solution accuracy.

(b) The numerical results confirm that the model differential-algebraic problem is the true limiting case of a purely differential system with an unconditional time-like character. This limit can even be taken numerically without any singular behavior, and this limiting solution is the correct solution to the model differential-algebraic problem.

(c) For marching problems which do not have an asymptotic limit, it is important to control the growth and generation of truncation errors. These truncation errors not only convect and grow in the same way as the actual solution, but in addition to this new truncation errors are also generated at each marching step. Consequently, the rate of growth of these errors may be more than the rate of growth of the actual solution. Thus, after a sufficient number of marching steps, these errors may become large enough to substantially degenerate the solution. In other words, in case of an inaccurate numerical algorithm the smaller the marching step-size, the larger the number of times we have to do an inaccurate solution in the y direction and, thus, the larger the number of times we cause the numerical errors to generate. This behavior could wrongfully be thought of as a problem caused by the small step-size; whereas, the small marching step has nothing to do with the problem except that by doing so the numerical inaccuracies start affecting the solution much sooner. The real solution to these problems lies not in the step-size manipulation, but in improving our solution accuracy and limiting or eliminating associated numerical truncation errors.

Table I.1. Coefficients of the Bidiagonal Implicit Scheme

$\alpha = \varepsilon/\Delta x$	Coefficients of the Bidiagonal Scheme				
	k_1	k_2	k_3	k_4	k_5
0	1	0	2	0	3
1	4	1	1/2	1/2	3/2
3	-8	-3	-1/4	3/4	3/4

o   CASE 1   ($\Delta y=0.10$, $\Delta x=0.001$, k=0.01, $a^2=10$, $\varepsilon=0$)
Δ   CASE 2   ($\Delta y=0.05$, $\Delta x=0.001$, k=0.02, $a^2=10$, $\varepsilon=0$)
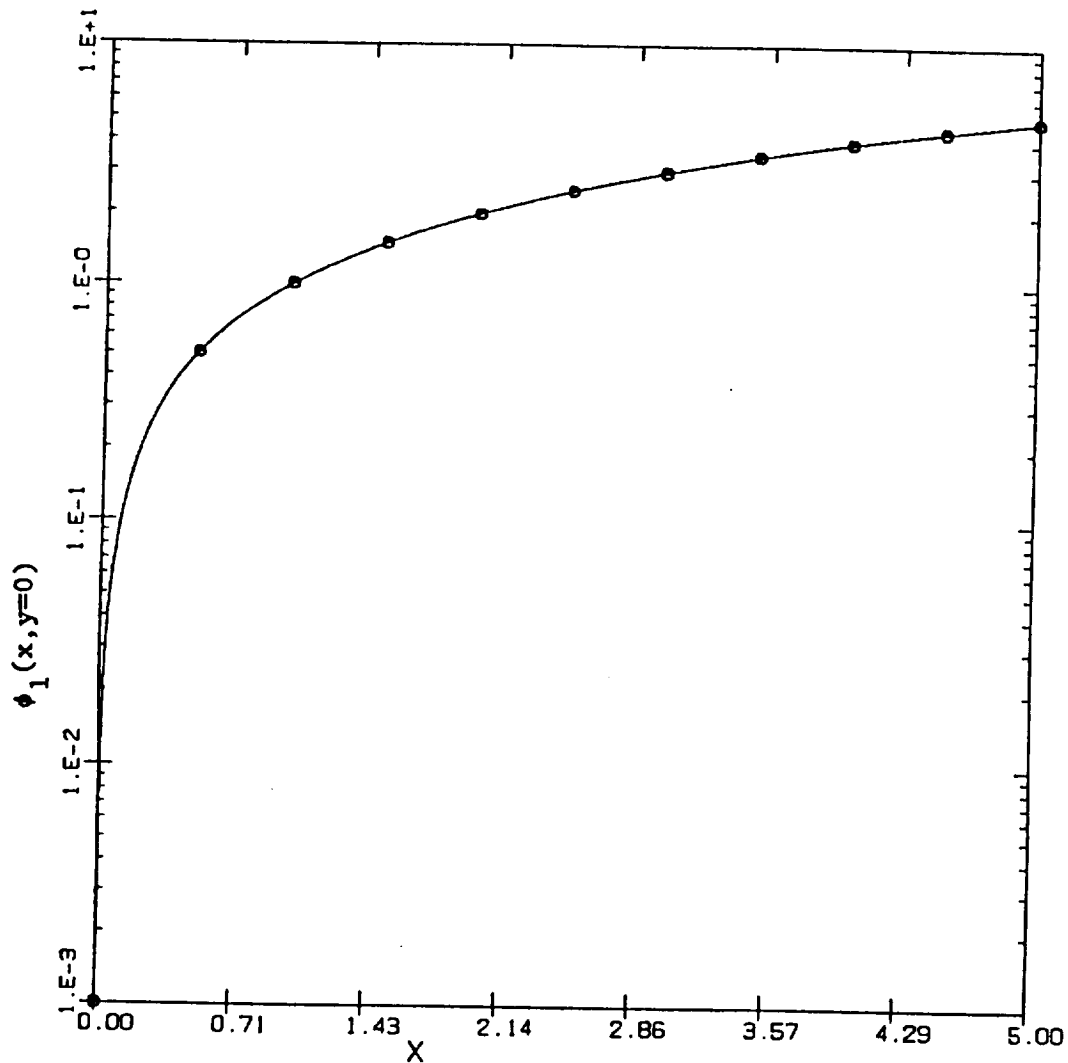
Fig. I.1.   Solution for $\phi_1(x,y=0)$ with the Lax method for the case
of $a^2=10$ and $\varepsilon=0$

o CASE 1 (Δy=0.10, Δx=0.001, k=0.01, a^2=10, ε=0)
Λ CASE 2 (Δy=0.05, Δx=0.001, k=0.02, a^2=10, ε=0)
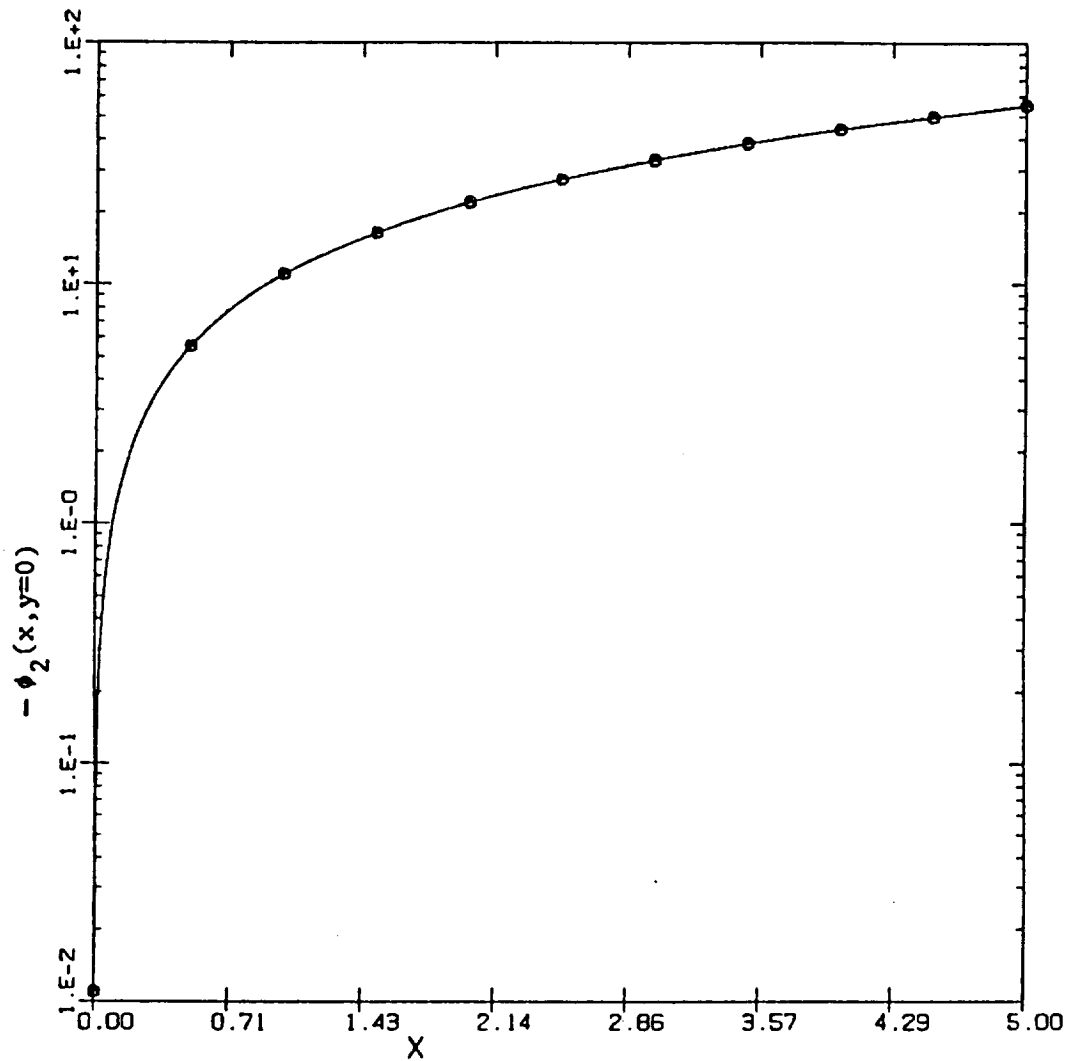
Fig. I.2. Solution for ϕ_2(x,y=0) with the Lax method for the case of a^2=10 and ε=0

o CASE 1   ($\Delta y=0.10$, $\Delta x=0.001$, $k=0.01$, $a^2=10$, $\varepsilon=0$)
Δ CASE 2   ($\Delta y=0.05$, $\Delta x=0.001$, $k=0.02$, $a^2=10$, $\varepsilon=0$)
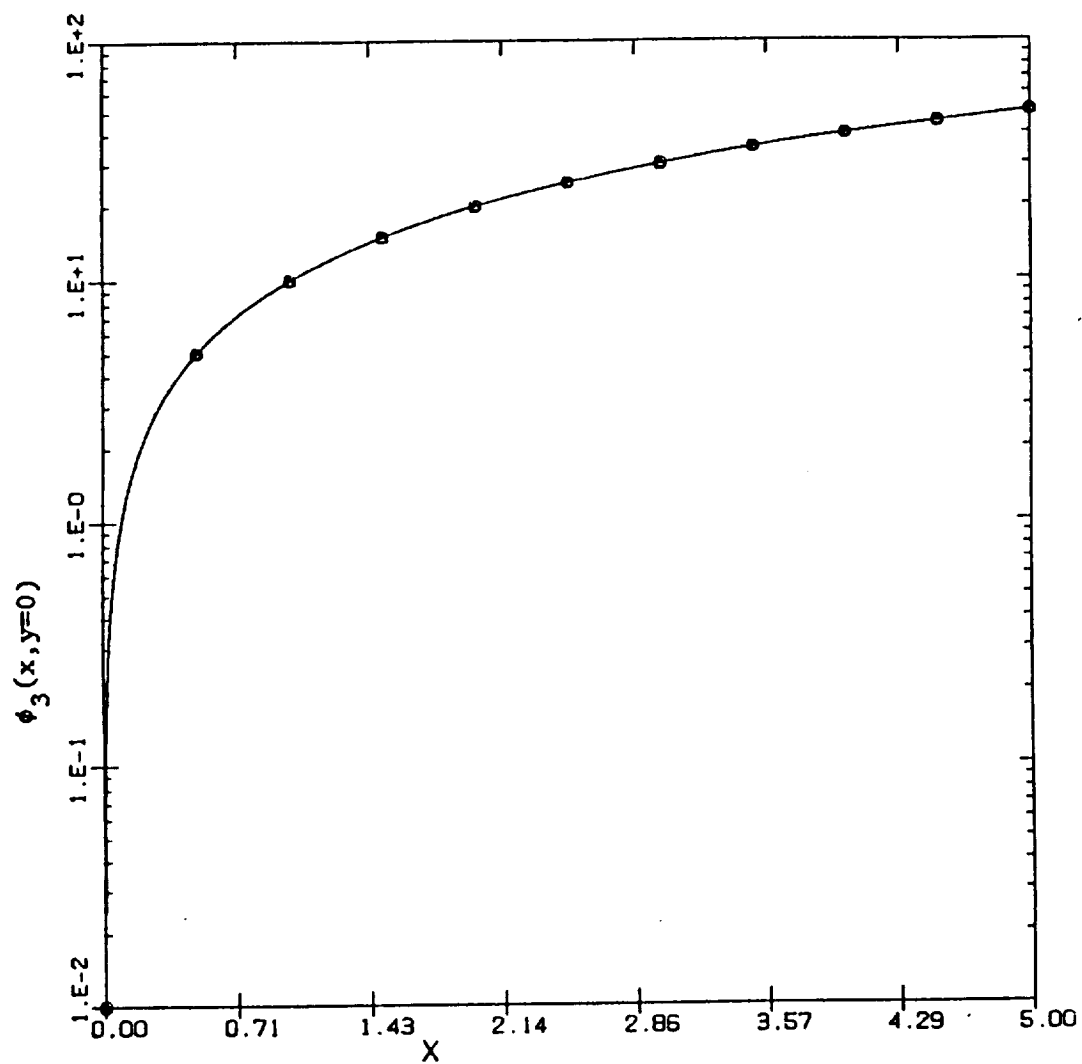
Fig. I.3. Solution for $\phi_3(x,y=0)$ with the Lax method for the case of $a^2=10$ and $\varepsilon=0$

○	k=0.01	(Δy=0.10, Δx=0.001, a^2=10, ε=0)
△	k=0.05	(Δy=0.10, Δx=0.005, a^2=10, ε=0)
+	k=0.10	(Δy=0.10, Δx=0.010, a^2=10, ε=0)
×	k=0.20	(Δy=0.10, Δx=0.020, a^2=10, ε=0)
◇	k=1.00	(Δy=0.10, Δx=0.100, a^2=10, ε=0)

Explicit Lax Method

$$\left[k_{max} \cong 0.2\right]$$
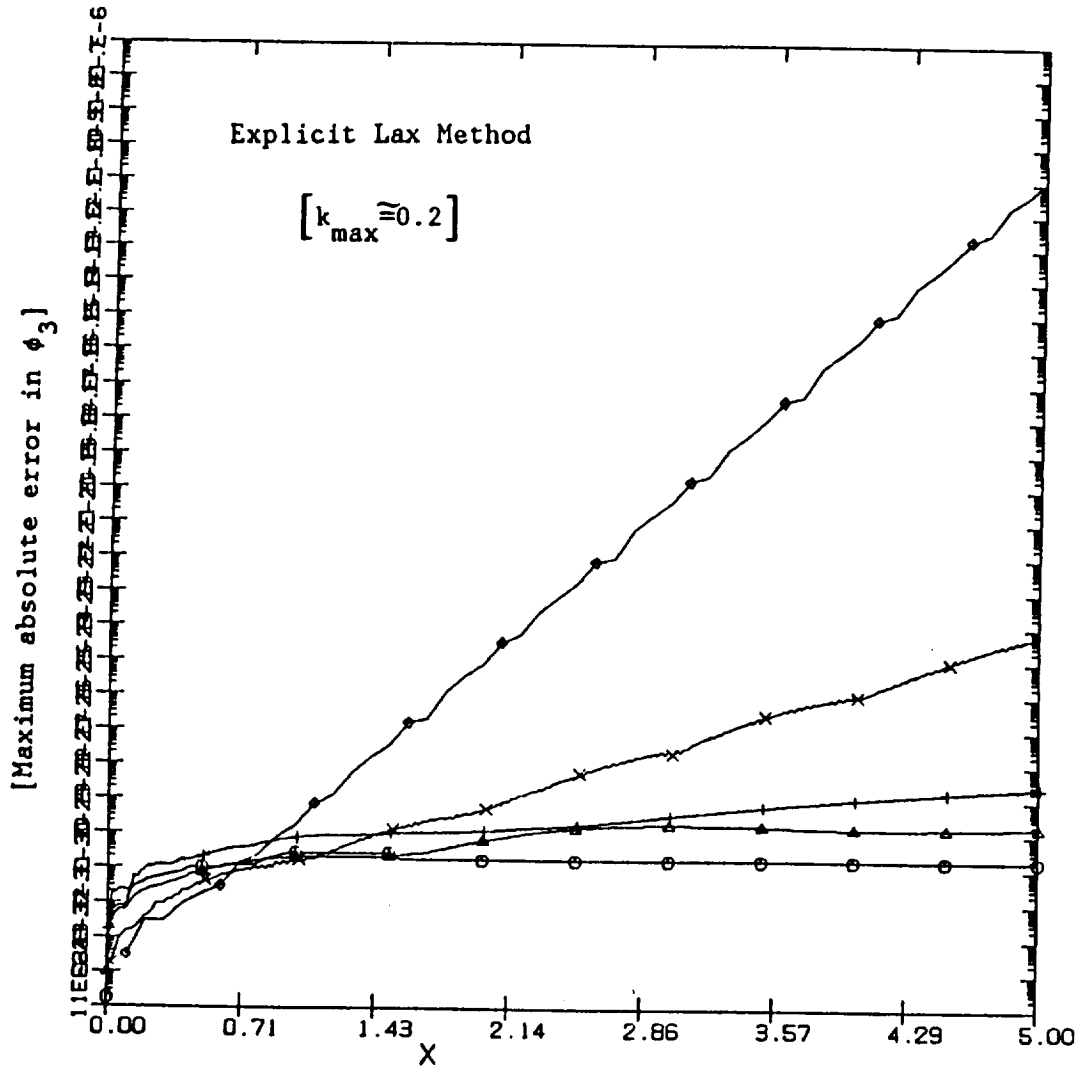
Fig. I.4. Effect of increasing the ratio k=Δx/Δy on the maximum absolute error in ϕ_3.

o $\Delta x=0.0025$ $(\Delta y=0.0050$, $k=0.50$, $\varepsilon=0$, $a^2=3)$
$\triangle$ $\Delta x=0.0050$ $(\Delta y=0.0100$, $k=0.50$, $\varepsilon=0$, $a^2=3)$
+ $\Delta x=0.0100$ $(\Delta y=0.0200$, $k=0.50$, $\varepsilon=0$, $a^2=3)$
$\times$ $\Delta x=0.0250$ $(\Delta y=0.0500$, $k=0.50$, $\varepsilon=0$, $a^2=3)$
$\diamond$ $\Delta x=0.0500$ $(\Delta y=0.1000$, $k=0.50$, $\varepsilon=0$, $a^2=3)$
ϕ $\Delta x=0.1000$ $(\Delta y=0.2000$, $k=0.50$, $\varepsilon=0$, $a^2=3)$

Fig. I.5. Solution for $\phi_1(x,y=0)$ with the bidiagonal implicit method
for of $a^2=3$ and $\varepsilon=0$ $(\alpha=0)$

o $\Delta x=0.0025$ $(\Delta y=0.0050,\ k=0.50,\ \varepsilon=0,\ a^2=3)$
$\triangle$ $\Delta x=0.0050$ $(\Delta y=0.0100,\ k=0.50,\ \varepsilon=0,\ a^2=3)$
+ $\Delta x=0.0100$ $(\Delta y=0.0200,\ k=0.50,\ \varepsilon=0,\ a^2=3)$
× $\Delta x=0.0250$ $(\Delta y=0.0500,\ k=0.50,\ \varepsilon=0,\ a^2=3)$
$\Diamond$ $\Delta x=0.0500$ $(\Delta y=0.1000,\ k=0.50,\ \varepsilon=0,\ a^2=3)$
$\triangle$ $\Delta x=0.1000$ $(\Delta y=0.2000,\ k=0.50,\ \varepsilon=0,\ a^2=3)$

Fig. I.6.   Solution for $\phi_2(x,y=0)$ with the bidiagonal implicit method
for of $a^2=3$ and $\varepsilon=0$ $(\alpha=0)$

o $\Delta x=0.0025$ $(\Delta y=0.0050,\ k=0.50,\ \varepsilon=0,\ a^2=3)$
Δ $\Delta x=0.0050$ $(\Delta y=0.0100,\ k=0.50,\ \varepsilon=0,\ a^2=3)$
+ $\Delta x=0.0100$ $(\Delta y=0.0200,\ k=0.50,\ \varepsilon=0,\ a^2=3)$
x· $\Delta x=0.0250$ $(\Delta y=0.0500,\ k=0.50,\ \varepsilon=0,\ a^2=3)$
$\Diamond$ $\Delta x=0.0500$ $(\Delta y=0.1000,\ k=0.50,\ \varepsilon=0,\ a^2=3)$
$\triangle$ $\Delta x=0.1000$ $(\Delta y=0.2000,\ k=0.50,\ \varepsilon=0,\ a^2=3)$
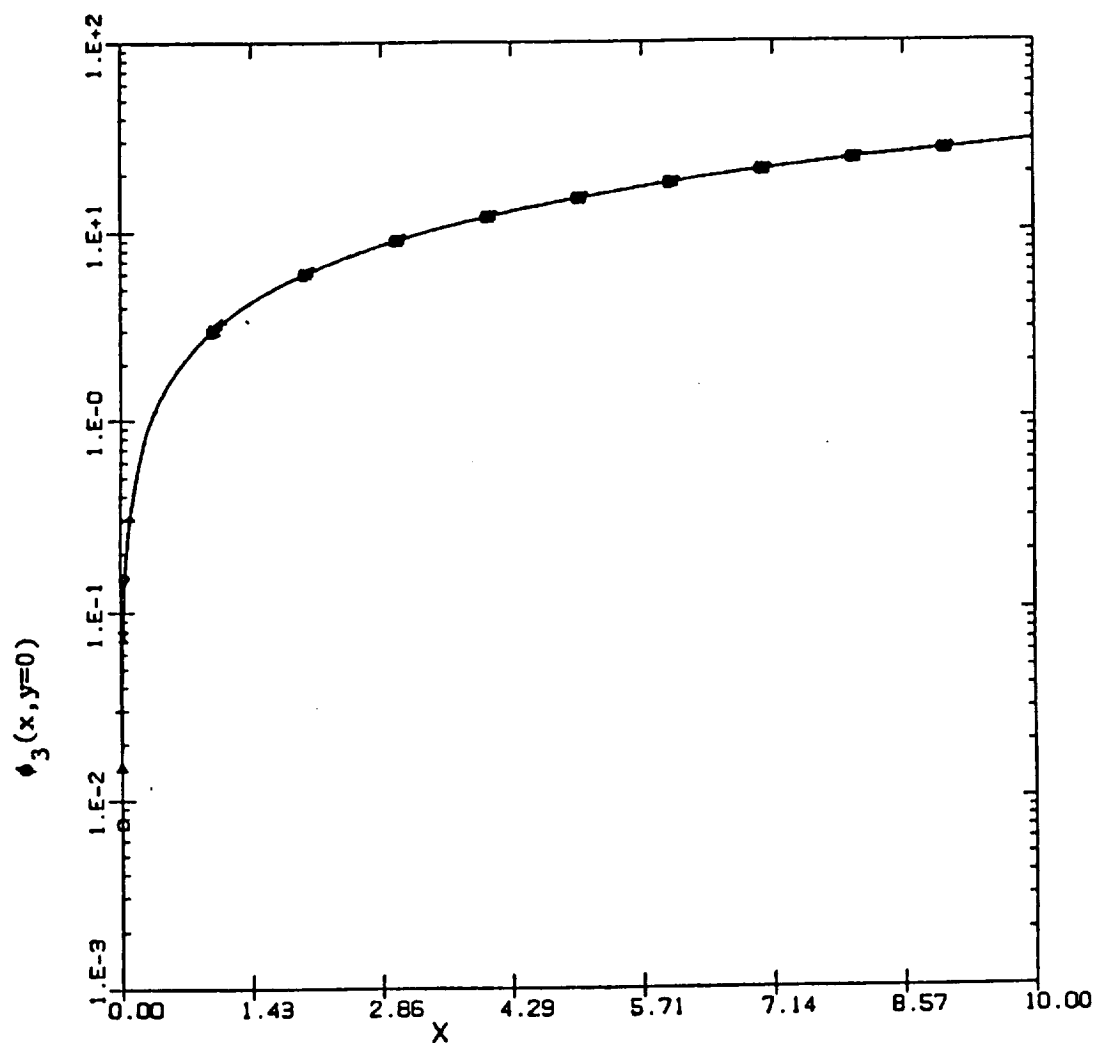
Fig. I.7.   Solution for $\phi_3(x,y=0)$ with the bidiagonal implicit method
for of $a^2=3$ and $\varepsilon=0$ ($\alpha=0$)

○   Δx=0.010   (Δy=0.02, k=0.50, ε=Δx, a^2=3)
Λ   Δx=0.025   (Δy=0.05, k=0.50, ε=Δx, a^2=3)
+   Δx=0.100   (Δy=0.20, k=0.50, ε=Δx, a^2=3)

Fig. I.8.   Solution for ϕ_1(x,y=0) with the bidiagonal implicit method
for of a^2=3 and ε=Δx (α=1)

Fig. I.9. Solution for $\phi_2(x,y=0)$ with the bidiagonal implicit method for of $a^2=3$ and $\varepsilon=\Delta x$ ($\alpha=1$)

o Δx=0.010   (Δy=0.02, k=0.50, $\epsilon=\Delta x$, a^2=3)
Δ Δx=0.025   (Δy=0.05, k=0.50, $\epsilon=\Delta x$, a^2=3)
+ Δx=0.100   (Δy=0.20, k=0.50, $\epsilon=\Delta x$, a^2=3)

Fig. I.10.   Solution for ϕ_3(x,y=0) with the bidiagonal implicit method for of a^2=3 and $\epsilon=\Delta x$ (α=1)

o $\Delta x=0.010$ ($\Delta y=0.02$, $k=0.50$, $\varepsilon=\Delta x$, $a^2=3$)
Δ $\Delta x=0.025$ ($\Delta y=0.05$, $k=0.50$, $\varepsilon=\Delta x$, $a^2=3$)
+ $\Delta x=0.100$ ($\Delta y=0.20$, $k=0.50$, $\varepsilon=\Delta x$, $a^2=3$)
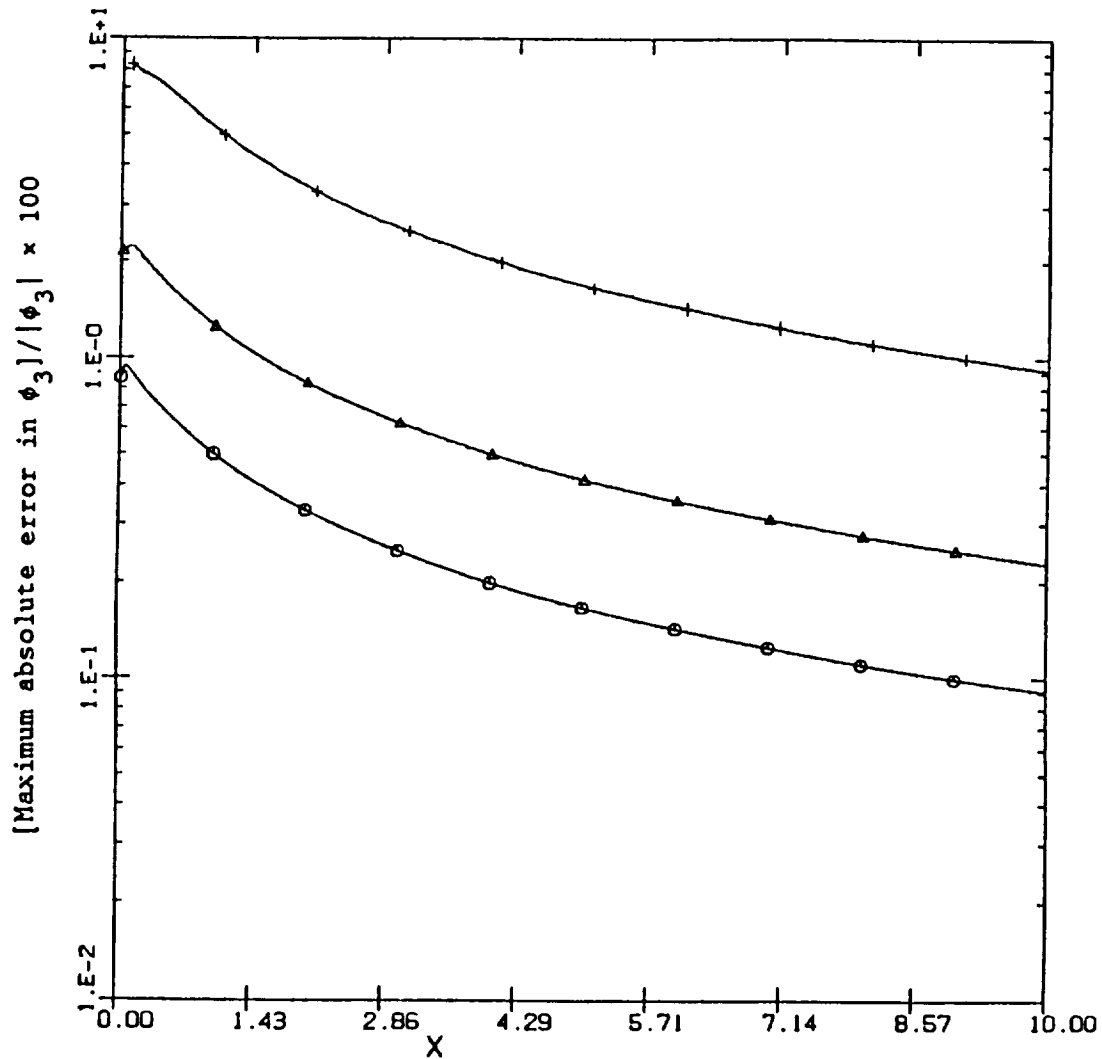
Fig. I.11. Improvement in the solution of ϕ_3 by decreasing the
marching step size ($\Delta=x$) for $a^2=3$ and $\varepsilon=\Delta x$
($\alpha=1$) and using the bidiagonal implicit method

APPENDIX J. SOME IMPORTANT ASPECTS OF PRESENT 3-D PNS SCHEME

J.1. Distinction from Classical PNS Approaches

Our 3-D PNS scheme is very different from any available PNS scheme, not only in terms of the enhanced solution accuracy it offers, but even the basic formulation is based on a completely new and inovative approach. It is important to mention that the original development of our PNS scheme (Bhutta and Lewis, 1985a-d) was motivated to address several numerical accuracy and instability problems suffered by existing PNS methodology. Before developing our own PNS approach to answer these problems (without making substantial approximations) we had extensively used many of the classical PNS solution schemes (Shanks et al., 1979; Helliwell et al., 1980; Lubard and Helliwell, 1973). The following table gives a good overview of the differences between our 3-D PNS scheme and the classical noniterative PNS approaches (Schiff and Steger, 1979; Shanks et al., 1979; Kaul and Chaussee, 1983; Vigneron et al., 1978; etc.).

Our PNS Scheme	Classical Noniterative PNS Approaches
Solution Scheme	
(1) Solves a differential/algebraic system of equations.	Solve a purely differential system of equations.
(2) Fully conservative solution in the limit of convergence so that two-point streamwise differencing is adequate and the memory requirement is less.	Nonconservative errors need to be compensated by using special three-point streamwise operators, requiring larger computer memory.
Accuracy	
(3) Involve a fully-iterative solution scheme.	Involve a noniterative solution which is only the first guess of the true

solution.

(4) Satisfies global as well as differential conservation of mass, momentum and energy to within a user-specified accuracy.

Typically have large global conservation errors.

(5) The solution scheme has a fully-implicit pressure treatment and does predict possible axial separation across strong compression discontinuities.

Due to the pressure approximations caused by the use of sublayer approximation, the numerical solution can march through axially separated regions without indicating any separation-like behavior.

Character of Equations

(6) Unconditional time-like (hyperbolic/parabolic) character and does not require any sublayer-type approximation.

Conditionally time-like character and requires the use of a sublayer-type approximation to render the equations time-like in the sublayer region (Schiff and Steger, 1979, and Vigneron et al., 1978).

Treatment of Shock Boundary

(7) Fully-implicit shock prediction which is fully iterative in nature and coupled in the crossflow direction.

Involve various shock prediction schemes which are not iterated (Shanks et al., 1982, and Kaul and Chaussee, 1983).

(8) Does not require the assumption of inviscid flow behind the shock.

Noniterative implict shock treatments typically assume that the flow behind the shock is inviscid so that certain characteristic-type relations can be used to close the system. This is clearly a deficient approach in the nose-dominated region as well as in regions of bow-shock interaction.

(9) Does not involve any arbitrary solution parameters to be provided by the user.

Involve a number of arbitrary solution parameters which have to be specified by the user and can have substantial impact on the numerical solution generated.

Grid-Refinement Capabilities

(10) Good grid-refinement character-istics and very fine grids can be used in the near-wall region.

Use of fine grids in the near-wall region typically cause solution instabilities.

Low-Reynolds-Number Flows

(11) Because of the inherent time-like character, our PNS scheme can accurately treat high-Mach-number and low-Reynolds-number flows where the subsonic sublayer spans over as much as 50-60% of the computational domain.

Under low-Reynolds-number conditions sublayer region becomes large and the sublayer approximation becomes inadequate to suppress instabilities.

Computing Times

(12) Our 3-D PNS scheme uses a pseudo-unsteady approach (along with its ability to take larger marching steps) to provide accurate results with overall computing times which are comparable to or less than the noniterative PNS schemes.

The use of Approximate Factorization scheme and the restriction of small marching steps results in fairly large overall computing times.

J.2. Validation and Comparison with Experimental Data

Over the years we have and also others have compared the predictions of our PNS scheme with available flight as well as experimental data. Although such data have been limited in access and availability, the indications have been that the agreement has been very good. Data available in the open literature have been typically for relatively low Mach number conditions (of the order of Mach 10), and even then not all data are for

"clean" conditions that can be correctly simulated. Many times even if the data are "clean" there are uncertainties associated with the correct determination of freestream conditions and related unsteady freestream effects. This suggests that the experimental data for code-validation purposes has to be carefully selected to make sure all effects are accounted for, in order to correctly simulate the test conditions. Figures J.1 and J.2 show some results comparing the predictions of our PNS scheme with some good and reliable experimental data.

Figure J.1 shows the wall-pressure distribution for flow over a 10.5/7 deg spherically blunt bicone configuration. The Mach number for this test was 6, and a perfect-gas model was used for the numerical predictions. The experimental data were obtained in the AEDC wind tunnel and have been taken form an AEDC report (AEDC-TR-80-14). The agreement between the predicted and measured wall pressures is excellent.

Figure J.2 shows the predicted wall heat-transfer rates for the conditions of the Cleary test cases (Cleary, 1969). The Cleary tests were conducted for several bluntness ratios of a 15 deg cone. The results are shown for the largest bluntness ratio (nose radius of 1.1 inch) under zero angle-of-attack conditions. This case was chosen because the experimental data indicated the onset of transition to turbulent conditions for smaller bluntness ratios and, also, at larger angles of attack. Figure J.2 shows the results of the predictions for three different freestream total-pressure conditions (400psi, 1200psi and 1800psi). The numerical solutions assumed an isothermal wall at 540 Rankine and a perfect-gas model along with fully-laminar flow conditions. The numerical results shown in Fig. J.2 include the VSL solution for the blunt-body region as well as the PNS afterbody solution. The PNS IDP data were generated at an axial location fo 4.5 nose radii. These results clearly show the excellent agreement between the predicted and experimental wall heat-transfer rates.

The aforementioned results show that our PNS scheme does indeed produce accurate aerothermodynamic predictions under hypersonic flow conditions. These code-validation results fully support the accuracy, efficiency and stability claims of our PNS scheme.
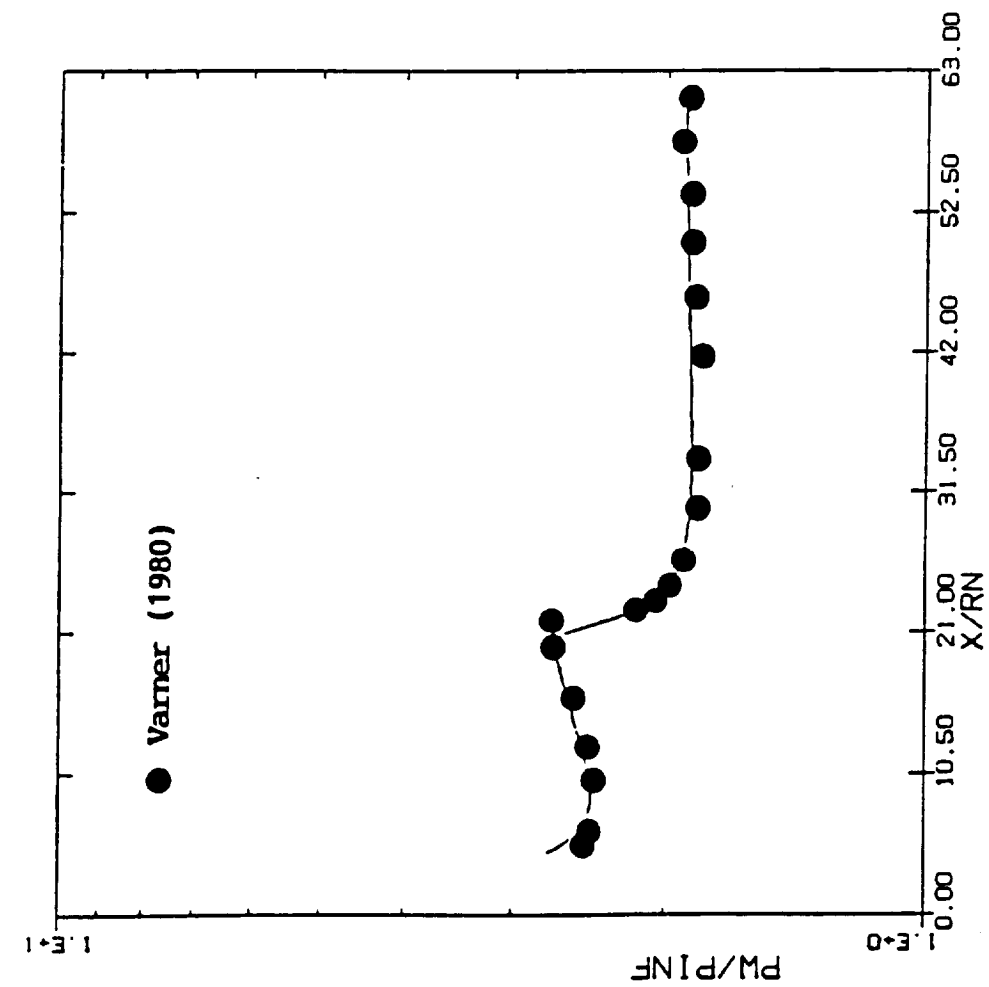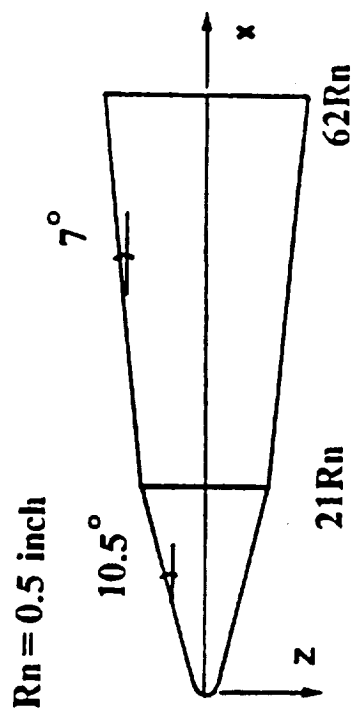
Fig. J.1. Comparison of predicted and experimental wall-pressure distributions
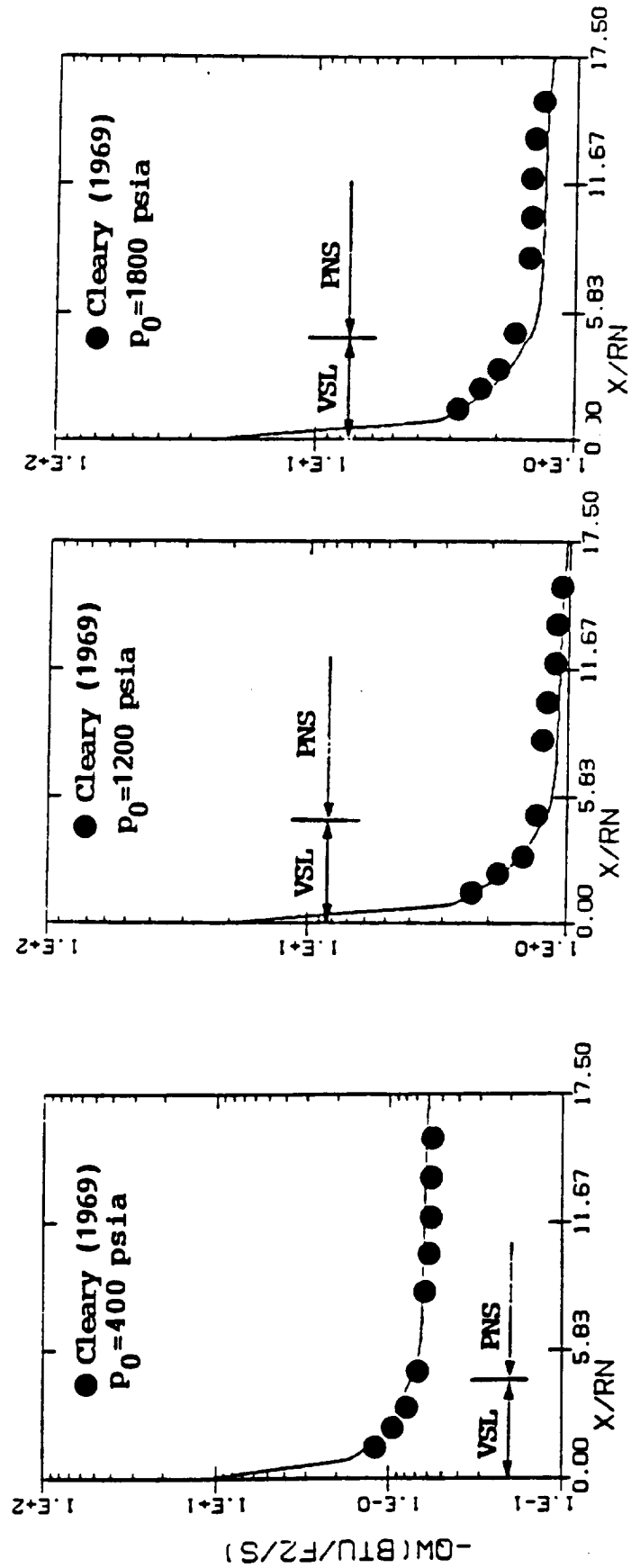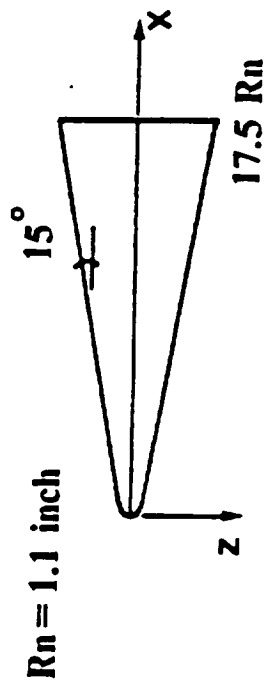
Fig. J.2. Comparison of predicted and experimental wall heat-transfer rates

REFERENCES

Adams, J.C., (1972) "Analysis of the Three-Dimensional Compressible Turbulent Boundary Layer on a Sharp Cone at Incidence in Supersonic and Hypersonic Flow," AEDC-TR-72-66, von Karman Gas Dynamics Facility, Arnold Engineering Development Center, June 1972.

Bhutta, B.A., and Lewis, C.H., (1985a) "Low Reynolds Number Flows Past Complex Multiconic Geometries," AIAA Paper No. 85-0362, Jan. 1985.

Bhutta, B.A. and Lewis, C.H., (1985b) "An Implicit Parabolized Navier-Stokes Scheme for High-Altitude Reentry Flows," AIAA Paper No. 85-0036, Jan. 1985.

Bhutta, B.A., and Lewis, C.H., (1985c) "Prediction of Three-Dimensional Hypersonic Reentry Flows Using a PNS Scheme," AIAA Paper No. 85-1604, July 1985. Also see Journal of Spacecraft and Rockets, Vol. 26, Jan.-Feb. 1989, pp. 4-13.

Bhutta, B.A., and Lewis C.H., (1985d) "Parabolized Navier-Stokes Predictions of High-Altitude Reentry Flowfields," VRA-TR-85-02, VRA, Inc., Blacksburg, VA, April 1985.

Bhutta, B.A., and Lewis, C.H., (1988a) "Three-Dimensional Hypersonic Nonequilibrium Flows at Large Angles of Attack," AIAA Paper No. 88-2568, June 1988. Also see Journal of Spacecraft and Rockets, Vol. 26, May-June 1989, pp. 158-166.

Bhutta, B.A., and Lewis, C.H., (1988b) "PNS Predictions of Three-Dimensional Hypersonic Flows with Strong Crossflow Effects," AIAA Paper No. 88-2696, June 1988.

Bhutta, B.A., and Lewis, C.H., (1989a) "Large Angle-of-Attack Viscous Hypersonic Flows Over Complex Lifting Configurations," AIAA Paper No. 89-0269, Jan. 1989.

Bhutta, B.A., and Lewis, C.H., (1989b) "Prediction of Nonequilibrium Viscous Hypersonic Flows Over Lifting Configurations," AIAA Paper No. 89-1696, June 1989.

Bhutta, B.A., Lewis, C.H. and Kautz II, F.A., (1985a) "A Fast Fully-Iterative Parabolized Navier-Stokes Scheme for Chemically-Reacting Reentry Flows," AIAA Paper No. 85-0926, June 1985.

Bhutta, B.A., Kautz II, F.A., and Lewis, C.H., (1985b) "Influence of Aerodynamic Prediction Methodology on Performance Evaluation of Reentry Vehicle Configurations", Journal of Spacecraft and Rockets, Vol. 22, Sept.-Oct. 1985, pp. 541-547.

Bird, R.B., Stewart, W.E. and Lightfoot, E.N., (1960) Transport Phenomena, John Wiley and Sons, Inc., New York, NY, 1960.

Blottner, F.G., Johnson, M., and Ellis, M., (1971) "Chemically Reacting Viscous Flow Program for Multi-Component Gas Mixtures," Report No. SC-RR-70-754, Sandia Laboratories, Albuquerque, NM, Dec. 1971.

Bortner, M.H., (1963) "Chemical Kinetics in a Re-entry Flow Field," General Electric TIS R63SD63, August 1963.

Browne, W.G., (1962a) "Thermodynamic Properties of Some Atoms and Atomic Ions," MSD Engineering Physics TM2, General Electric Co., Philadelphia, PA, 1962.

Browne, W.G., (1962b) "Thermodynamic Properties of Some Diatomic and Linear Polyatomic Molecules," MSD Engineering Physics TM3, General Electric Co., Philadelphia, PA, 1962.

Browne, W.G., (1962c) "Thermodynamic Properties of Some Diatomic and Diatomic Ions at High Temperatures," MSD Advanced Aerospace Physics TM8, General Electric Co., Philadelphia, PA, 1962.

Cebeci, T., (1970) "Behavior of Turbulent Flows near a Porous Wall with Pressure Gradient," AIAA Journal, Vol. 8, Dec. 1970, pp. 2152-2156.

Chaussee, D.S., and Steger, J.L., (1981) "Three Dimensional Viscous Flowfield Program; Part 2; A Curvilinear Grid and Body Generation Program for Generalized Configurations (Interim Report)," Flow Simulations, Inc., Ca, March 1981.

Chaussee, D.S., Patterson, J.L., Kutler, P., Pulliam, T.H., and Steger, J.L., (1981) "A Numerical Simulation for Hypersonic Viscous Flows Over Arbitrary Geometries at High Angle of Attack," AIAA Paper No. 81-0050, Jan. 1981.

Clauser, F.H., (1954) "Turbulent Boundary Layers in Adverse Pressure Gradients," Journal of Aeronautical Science, Vol. 21, Feb. 1954, pp. 91-108.

Cleary, J.W., (1969) "Effects of Angle of Attack and Bluntness on Laminar Heating-Rate Distribution of a 15° Cone at a Mach Number of 10.6," NASA TN D-5450, October 1969.

Dhawan, S., and Narasimha, R., (1958) "Some Properties of Boundary-Layer Flow During the Transition from Laminar to Turbulent Motion," Journal of Fluid Mechanics, Vol. 3, Jan. 1958, pp. 418-436.

Graves Jr., R.A., and Hunt, L.H., (1985) "NASA's Hypersonic Fluid and Thermal Physics Program (Aerothermodynamics)," AIAA Paper No. 85-0922, June 1985.

Helliwell, W.S., Dickinson, R.P., and Lubard, S.C., (1980) "Viscous Flows Over Arbitrary Geometries at High Angle of Attack," AIAA Paper No. 80-0064, Jan. 1980.

Howe, J.T., (1985) "Introductory Aerothermodynamics of Advanced Space Transportation Systems," Journal of Spacecraft and Rocket, Vol. 22, Jan.-Feb. 1985, pp. 19-26.

Kaul, U.K., and Chaussee, D.S., (1983) "AFWAL Parabolized Navier-Stokes Coded: 1983 AFWAL/NASA Merged Baseline Version", AFWAL-TR-83-3118, Flight Dynamics Laboratory, AF Wright Aeronautical Laboratories, Wright-Patterson AFB, OH, Oct. 1983.

Kaul, U.K., and Chaussee, D.S., (1984) "A Comparative Study of the Parabolized Navier-Stokes (PNS) Code Using Various Grid Generation Techniques," AIAA Paper No. 84-0459, Jan. 1984.

REFERENCES

Lewis, C.H., (1986) "Blunt Body, Viscous Shock Layer and PNS Codes at VRA," Paper presented at the First National Aerospace Plane Technology Symposium, NASA Langley Research Center, Hampton, Va, May 1986.

Lubard, S.C., and Helliwell, W.S., (1973) "Calculation of the Flow on a Cone at High Angle of Attack," Report No. RDA-TR-150, R & D Associates, Santa Monica, CA, Feb. 1973.

Miner, E.W. and Lewis, C.H., (1975) "Hypersonic Ionizing Air Viscous Shock-Layer Flows Over Nonanalytic Blunt Bodies," NASA CR-2550, May 1975.

Miner, E.W., Anderson, E.C., and Lewis, C.H., (1971) "A Computer Program for Two-Dimensional and Axisymmetric Nonreacting Perfect Gas and Equilibrium Chemically Reacting Laminar Transitional and/or Turbulent Boundary Layer Flows," Virginia Polytechnic Institute and State University, Blacksburg, VA, VPI-E-71-8, May 1971.

Murray, A.L., and Lewis, C.H., (1978) "Hypersonic Three-Dimensional Viscous Shock-Layer Flows Over Sphere-Cones at High Altitudes and High Angles of Attack, VPI&SU AERO-078, Virginia Polytechnic Institute and State University, Blacksburg, VA, January 1978.

Noack, R.W., (1985) "Inviscid Flow Field Analysis of Maneuvering Hypersonic Vehicles Using the SCM Formulation and Parabolic Grid Generation," AIAA Paper No. 85-1682, July 1985.

Peng, T.C., and Pindroh, A.L., (1962) "An Improved Calculation of Gas Properties at High Temperature Air," Boeing Report D2-11722, Aerospace Division, The Boeing Co., Seattle, WA, 1962.

Peyert, R. and Viviand, H., (1975) "Computations of Viscous Compressible Flows Based on the Navier-Stokes Equations," AGARD-AG-212, 1975.

Schiff, L.B. and Steger, J.L., (1979) "Numerical Simulation of Steady Supersonic Viscous Flows," AIAA Paper No. 79-0130, Jan. 1979.

Shanks, S.P., Srinivasan, G.R. and Nicolet, W.E., (1979) "AFWAL Parabolized Navier-Stokes Code: Formulation and User's-Manual, " AFWAL-TR-823034, Air Force Flight Dynamics Laboratory, Wright Patterson AFB, OH, June 1979.

Sorenson, R.L., and Steger, J.L., (1978) "Simplified Clustering of Nonorthogonal Grids Generated by Elliptic Partial Differential Equations," NASA TM-73252, 1978.

Swaminathan, S., Kim, M.D. and Lewis, C.H., (1983) "Nonequilibrium Viscous Shock-Layer Flows Over Blunt Sphere-Cones at Angle of Attack," Journal of Spacecraft and Rockets, Vol. 20, July-August 1983, pp. 331-338.

Thareja, R.R., Szema, K.Y., and Lewis, C.H., (1983) "Chemical Equilibrium Laminar or Turbulent Three-Dimensional Viscous Shock-Layer Flows," Journal of Spacecraft and Rockets, Vol. 20, No. 5, Sept. 1983, pp. 454-460.

Thompson, R.A., Lewis, C.H., and Kautz, II, F.A., (1983) "Comparison Techniques for Predicting 3-D Viscous Flows Over Ablated Shapes," AIAA Paper 8-0345, Jan. 1983.

REFERENCES   123

Vachris, A., and Yeager, L., (1974) "QUICK-GEOMETRY User's Manual," Grumman Aerospace/Aerodynamic Section Technical Data Report No. 393-74-1, 1974.

Vigneron, Y.C., Rakich, J.V., and Tannehill, J.C., (1978) "Calculations of Supersonic Viscous Flows over Delta Wings with Sharp Subsonic Leading Edges," AIAA Paper No. 78-1137, July 1978.

Viviand, H., (1974) "Conservative Forms of Gas Dynamics Equations," La Recherche Aerospatiale, No. 1, Jan.-Feb. 1974, pp. 65-68.

White, F.M., (1974) Viscous Fluid Flow, McGraw-Hill Book Co., 1974.

White, M., (1986) "Hypersonic Flowfield Calculation for a Generic Inlet/Forebody," Paper presented at the First National Aerospace Plane Technology Symposium, NASA Langley Research Center, Hampton, Va, May 1986.

REFERENCES

124

Table 1. Gas-phase reactions and catalytic
third-body efficiency matrix

Species	Catalytic Third Bodies			
	M1	M2	M3	e-
O	25	1	20	0
O2	9	1	1	0
NO	1	1	20	0
N	1	0	20	0
NO+	0	0	0	1
N2	2	2	1	0

Reaction (1) :   O2 + M1 = 2O + M1
Reaction (2) :   N2 + M2 = 2N + M2
Reaction (3) :   N2 + N = 2N + N
Reaction (4) :   NO + M3 = N + O + M3
Reaction (5) :   NO + O = N + O2
Reaction (6) :   N2 + O = N + NO
Reaction (7) :   N + O = e- + NO+

Table 2. Reaction rate data for the reacting-air mixture

R	(a) EXP(COR)	(a) C1R	(a) C2R	(b) EXP(DOR)	(b) D1R	(b) D2R
1	0.361E+19	59400.00	-1.00	0.301E+16	0.00	-0.50
2	0.192E+18	113100.00	-0.50	0.109E+17	0.00	-0.50
3	0.415E+23	113100.00	-1.50	0.232E+22	0.00	-1.50
4	0.397E+21	75600.00	-1.50	0.101E+21	0.00	-1.50
5	0.318E+10	19700.00	1.00	0.963E+12	3600.00	0.50
6	0.675E+14	37500.00	0.00	0.150E+14	0.00	0.00
7	0.903E+10	32400.00	0.50	0.180E+20	0.00	-1.00

(a) Forward Reaction Rate $= k_{fr} = [EXP(COR)] \ [(TK)^{**}C2R] \ EXP(-C1R/TK)$
where TK is the temperature in degree Kelvin.
(b) Backward Reaction Rate $= k_{br} = [EXP(DOR)] \ [(TK)^{**}D2R] \ EXP(-D1R/TK)$
where TK is the temperature in degree Kelvin.

Table 3. Curve-fit coefficients for the species viscosities

Species	A_i (a)	B_i (a)	C_i (a)
O	0.20022000E-01	0.43094000E+00	-0.11246000E+02
O2	0.38271000E-01	0.21076000E-01	-0.95986000E+01
NO	0.42501000E-01	-0.18874000E-01	-0.96197000E+01
N	0.85863000E-02	0.64630000E+00	-0.12581000E+02
NO+	0.42501000E-01	-0.18874000E-01	-0.96197000E+01
N2	0.48349000E-01	-0.22485000E-01	-0.99827000E+01

(a) Species viscosity $= \mathrm{Ln}\,[\mu_i\,(\mathrm{gm/cm\text{-}sec})] = C_i + (A_i \mathrm{Ln}T_k + B_i)\mathrm{Ln}T_k$
where T_k is the temperature in degree Kelvin.

127

Table 4. Freestream conditions 3-D external-flow
          calculations (Cases 1, 2 and 3)

Quantity	
Mach number	20.000
Altitude (kft)	125.000
Reynolds number	5.313E+3
Pressure (lb/ft^2)	7.760E+0
Density $(slug/ft^3)$	1.017E-5
Temperature (R)	442.727
Velocity (ft/sec)	2.067E+4
Angle of attack (deg)	5.000
Wall temperature (R)	2000.000
Wall boundary condition	Fully-Catalytic

Table 5. Case parameters and computing times for 3-D external-flow calculations (Cases 1, 2 and 3)

Case	x/Rn From-to	(a) Grid Used N1xN2xN3	(b) IBM-3090 (m:s)	(c) Cray-(Y/MP) (m:s)	(d) Type of Grid	(e) Gas Model Used	Order of Smoothing
Case 1a	0.8-50	46x30x51	11:07	3:27	MBN	PG	4-th
Case 1b	0.8-30	36x30x31	5:11	1:36	MBN	PG	4-th
Case 1c	0.8-30	36x30x31	6:13	1:56	MBN	PG	2-nd
Case 1d	0.8-30	36x30x31	6:11	1:55	BN	PG	2-nd
Case 1e	0.8-30	36x30x31	7:17	2:15	PB	PG	2-nd
Case 2	0.8-30	36x30x31	5:57	1:51	MBN	EQ	4-th
Case 3a	0.8-50	46x30x51	24:30	7:38	MBN	NEQ	4-th
Case 3b	0.8-50	46x30x31	15:00	4:40	MBN	NEQ	4-th

(a) N1, N2 and N3 represent the number of grid points in the streamwise, axis-normal and crossflow directions.

(b) Estimated computing times on IBM 3090 (model 200VF) with VS-compiler and scalar LEVEL=3 optimization.

(c) Actual computing times on Cray-Y/MP with CFT77 compiler and auto vectorization.

(d) MBN, BN and PB represent the modified body-normal, the body-normal and the parabolic grid-generation schemes.

(e) PG, EQ and NEQ represent perfect-gas, equilibrium-air and nonequilibrium-air gas models.

Table 6. Freestream conditions 2-D internal-flow
calculations (Cases 4, 5 and 6)

Quantity		Case 4	Cases 5-6
Mach number		6.70	10.00
Reynolds number	(1/ft)	2.33E+5	1.76E+6
Pressure	(lb/ft^2)	142.20	50.00
Temperature	(R)	5332.89	500.00
Wall temperature	(R)	2000.00	1000.00
Flow conditions		Laminar	Laminar

Table 7. Case parameters and computing times for internal-flow
calculations (Cases 4, 5 and 6)

Case	(a) Gas Model	x/R From-to	(b) Grid N1 x N2	(c) Cray-Y/MP (sec)
Case 4a	PG	0.0-50.0	212 x 150	59
Case 4b	EQ	0.0-50.0	226 x 150	105
Case 4c	NEQ	0.0-50.0	217 x 150	268
Case 5a	PG	0.0-50.0	526 x 150	146
Case 5b	EQ	0.0-50.0	526 x 150	223
Case 6a	PG	0.0-100.0	1011 x 150	343
Case 6b	EQ	0.0-100.0	962 x 150	380

(a) PG=perfect-gas, EQ=equilibrium-air and NEQ=nonequilibrium-
air gas models.
(b) N1 and N2 represent the number of grid points in the
streamwise and axis-normal directions.
(c) Actual computing times on Cray-Y/MP with CFT77
compiler and auto-vectorization.
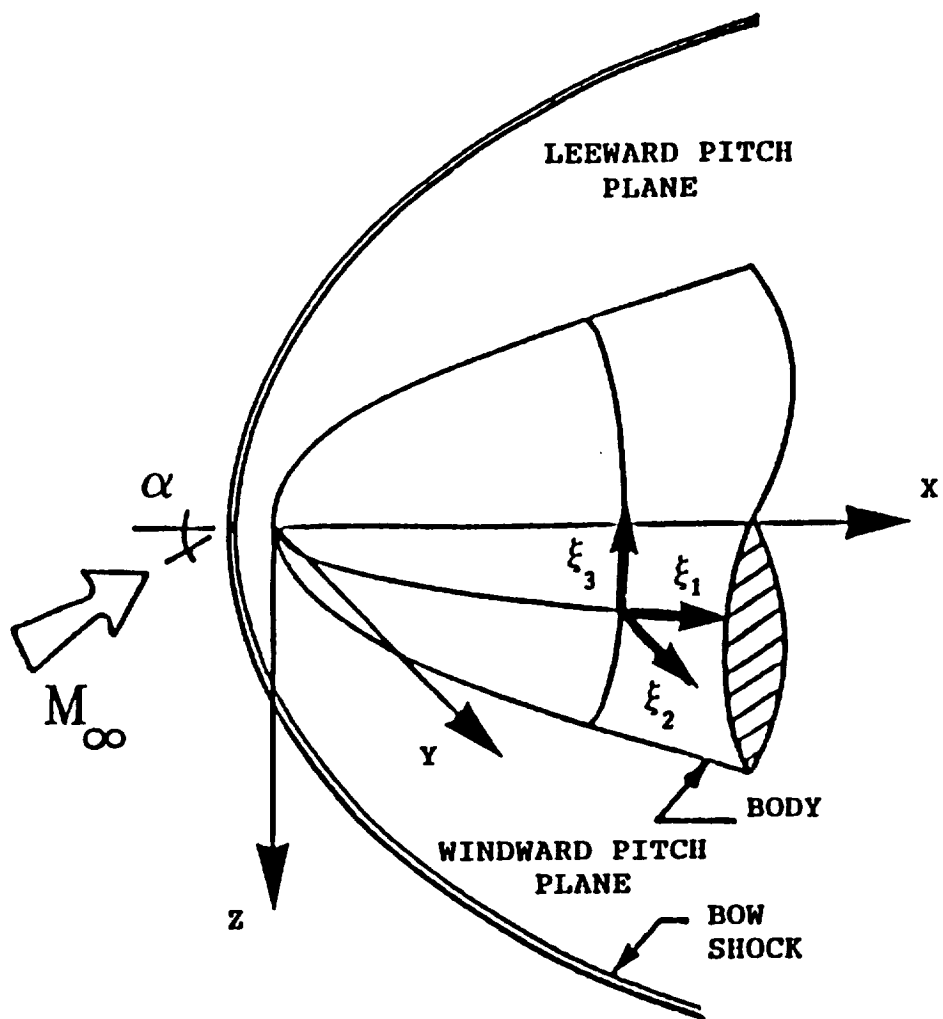
Fig. 1. Coordinate system for 3-D external flows

x-y-z Space
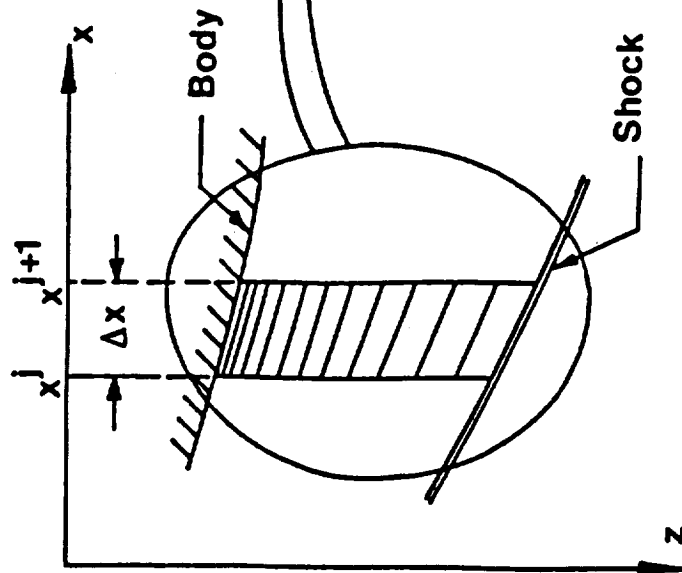
ξ_1-ξ_2-ξ_3 Space
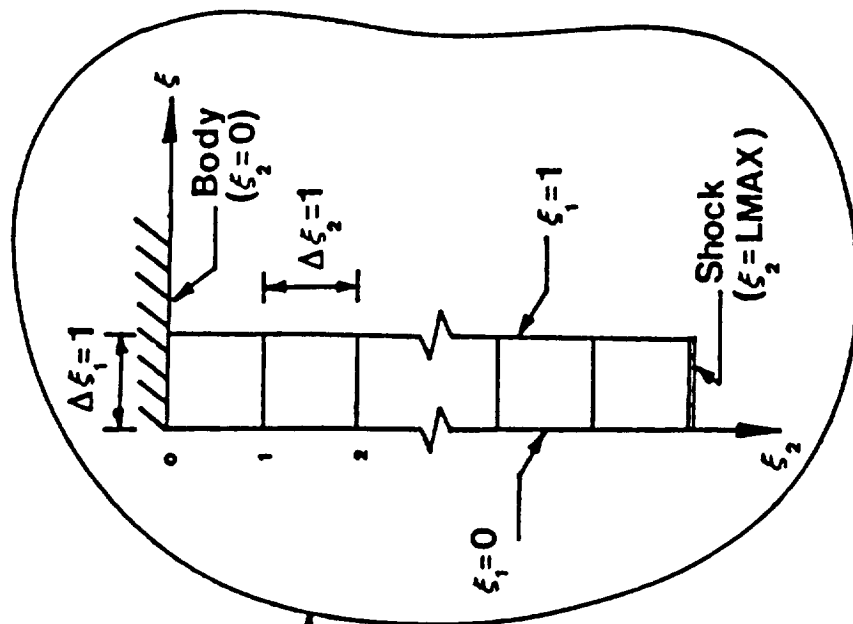
Fig. 2. Coordinate transformation
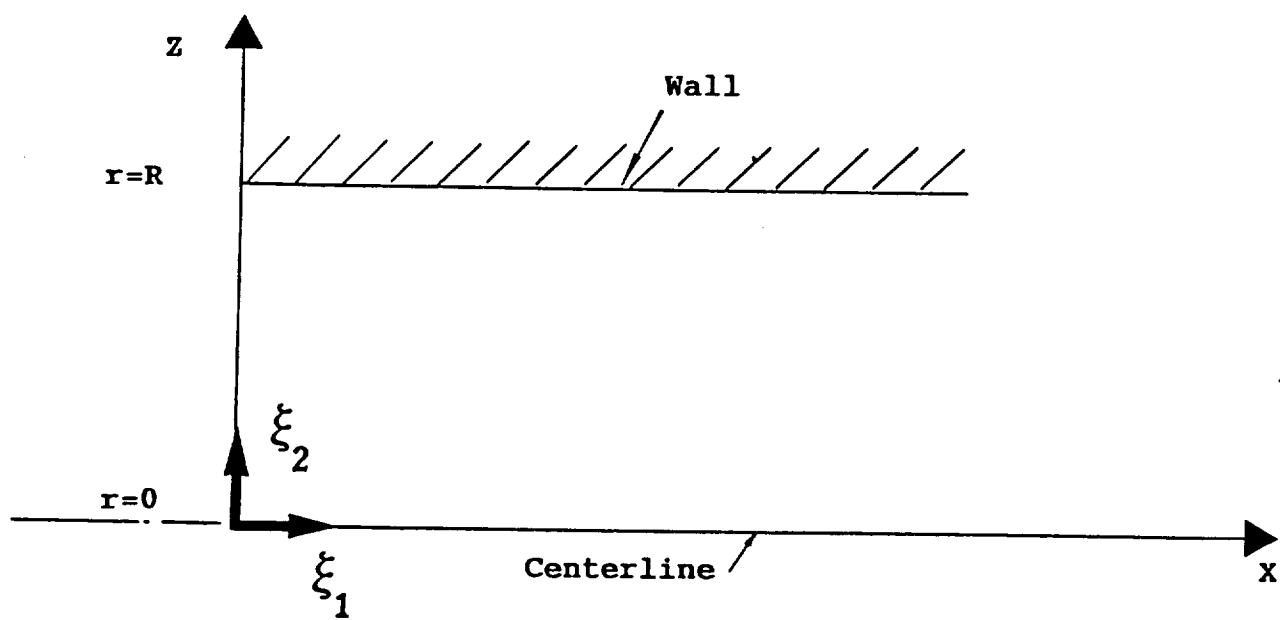
Fig. 3. Coordinate system for 2-D/axisymmetric internal flows

SIDE VIEW

Rn=0.1 inch   ~5°

50Rn

x

z

TOP VIEW

50Rn

~7°

~15°

y

x
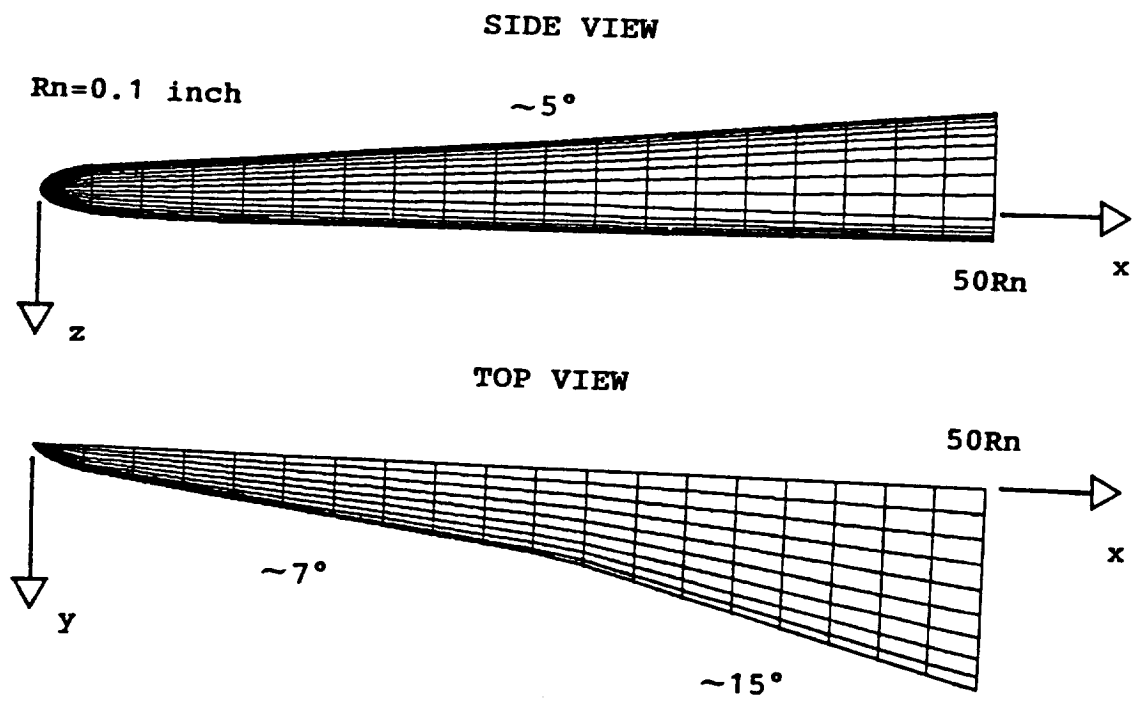
Fig. 4. Vehicle geometry for Cases 1, 2 and 3

PARABOLIC
GRID

Alt.=125kft
Mach=20
5-deg angle
   of attack
Perfect-gas

Case 1e

(31x30 grid)

x=30Rn
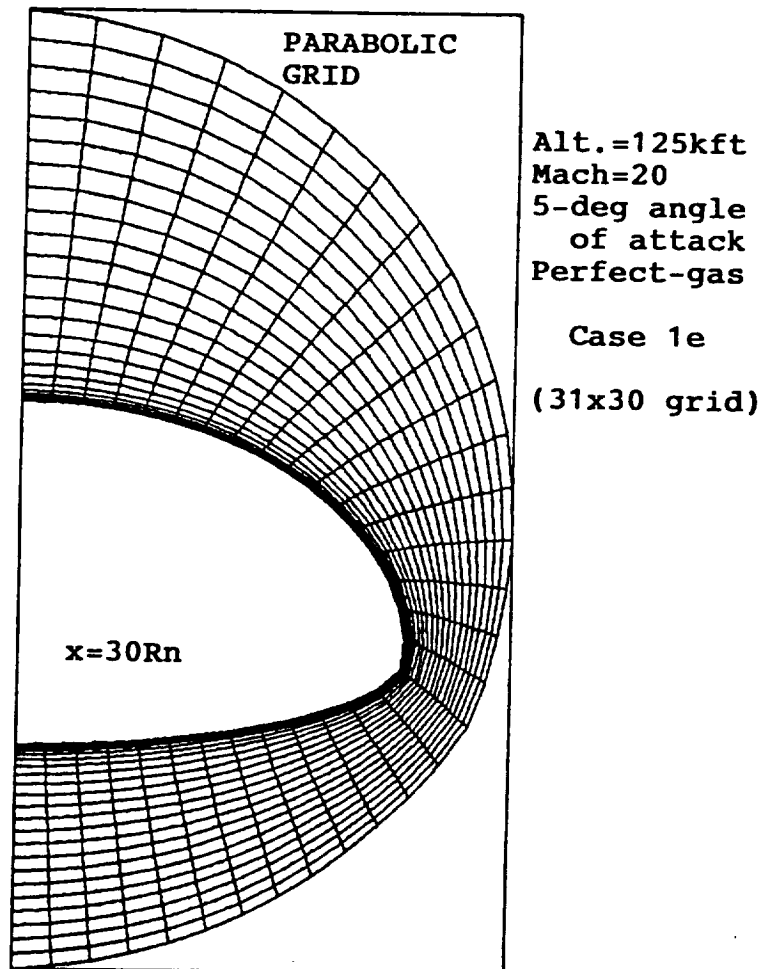
Fig. 5. Results of the parabolic grid-generation scheme for Case 1

BODY-NORMAL
GRID

Alt.=125kft
Mach=20
5-deg angle
   of attack
Perfect-gas

Case 1d

(31x30 grid)

x=30Rn
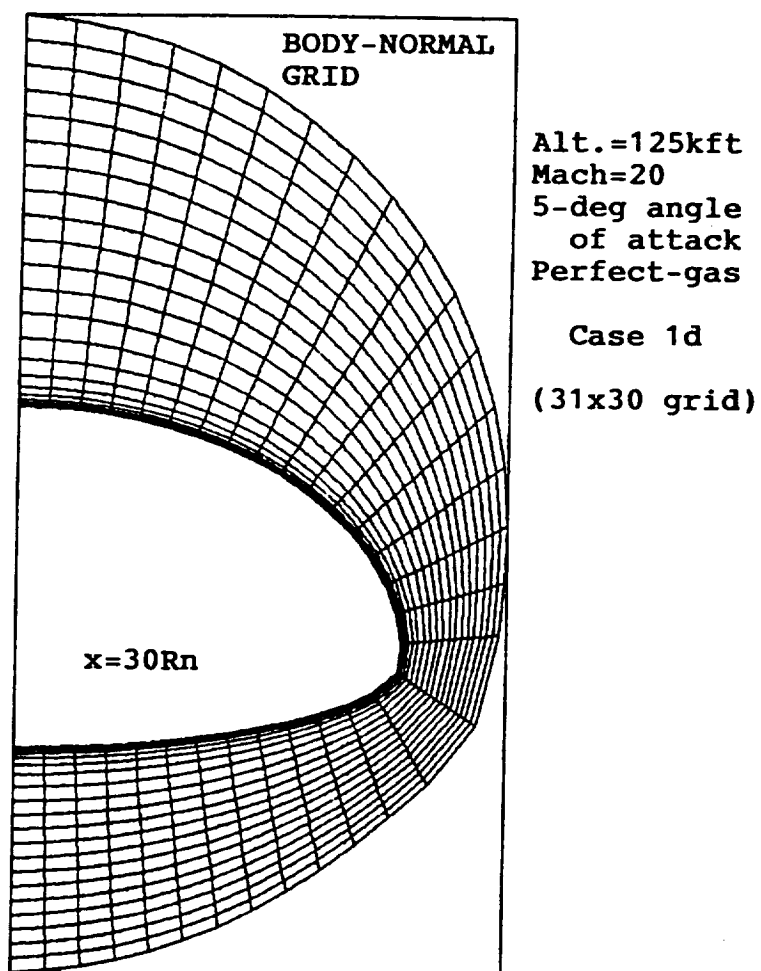
Fig. 6.   Results of the body-normal grid-generation scheme for Case 1
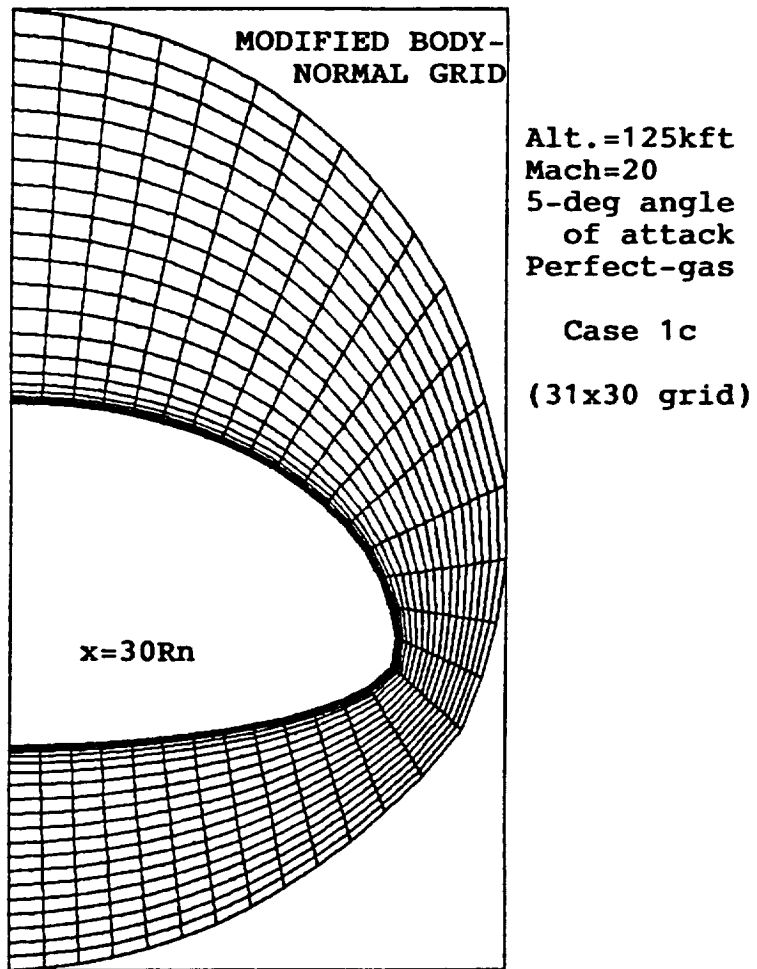
Fig. 7. Results of the modified body-normal grid-generation scheme for Case 1
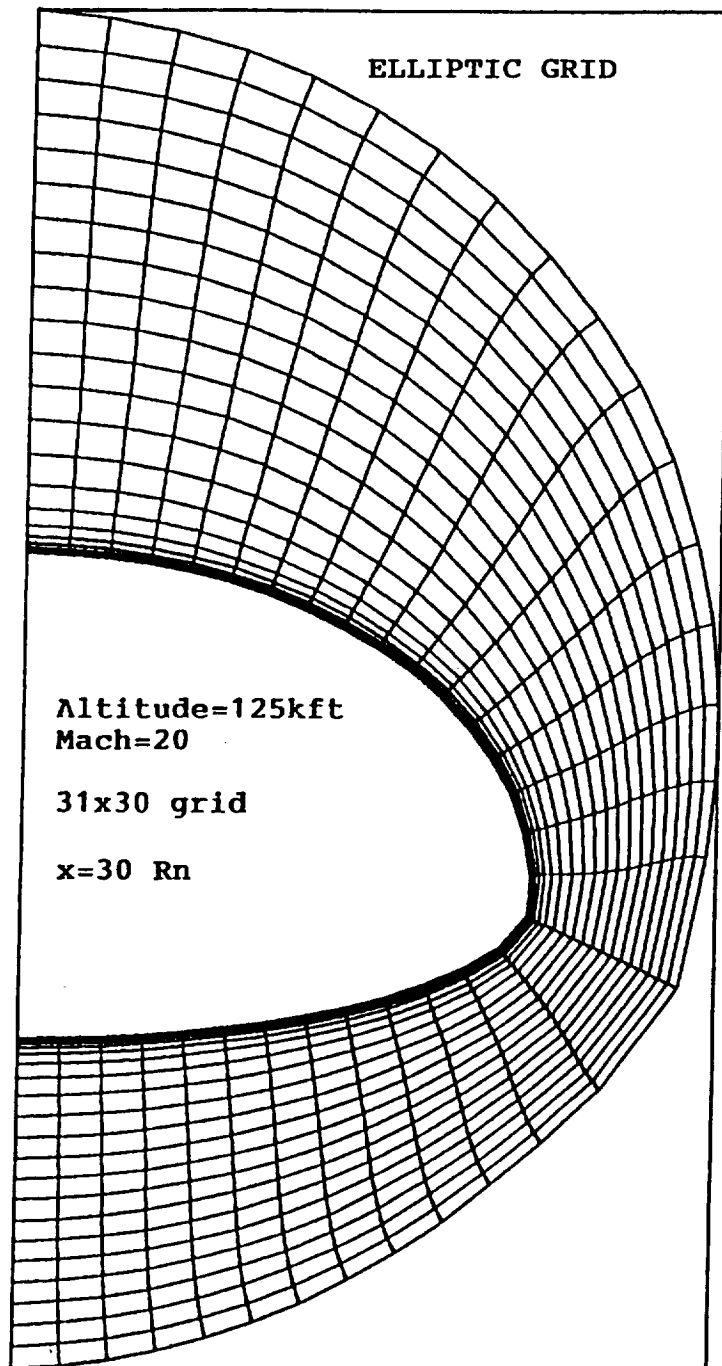
Fig. 8. Results of the elliptic grid-generation scheme for Case 1

ELLIPTIC GRID

Altitude=125kft
Mach=20
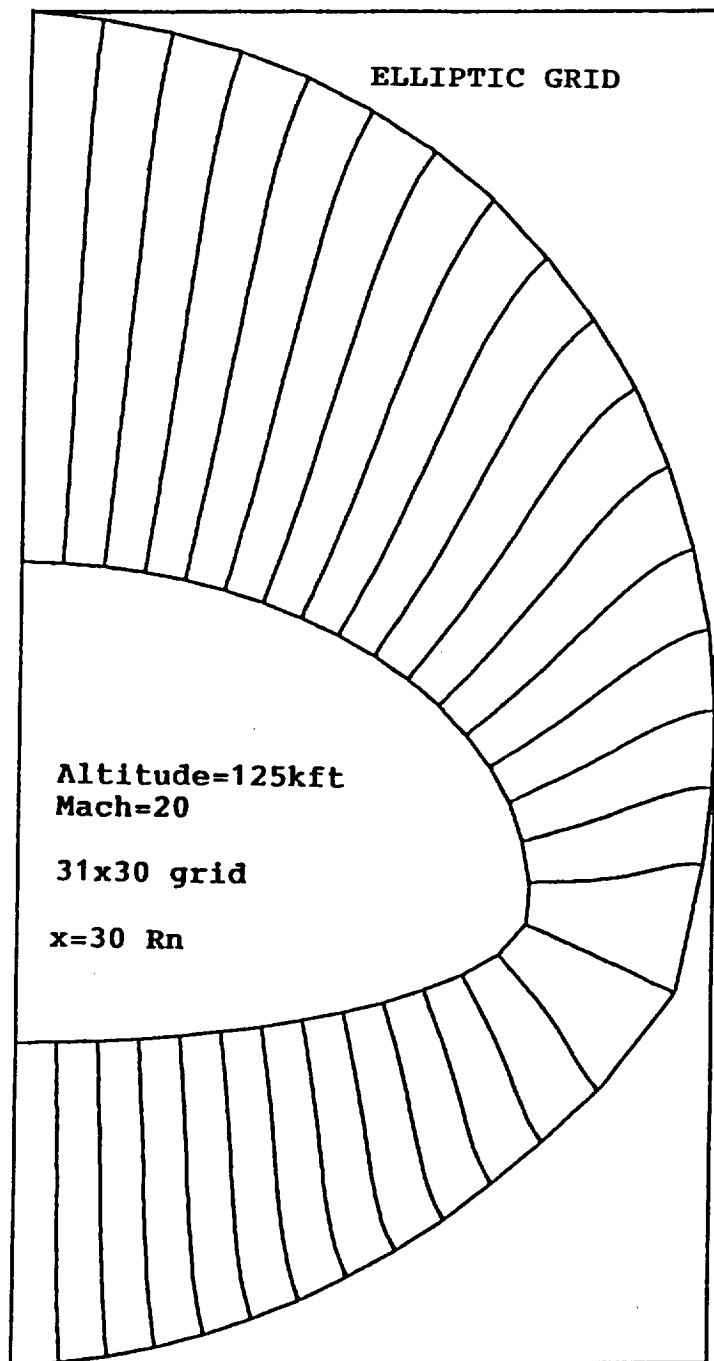
31x30 grid

x=30 Rn

Fig. 9. The body-normal grid lines for the elliptic grid

x=30Rn

k=32

Alt.=125kft
Mach=20
5-deg angle
  of attack
Perfect-gas

Case 1a

(51x30 grid)

L=1

L=30

k=
22
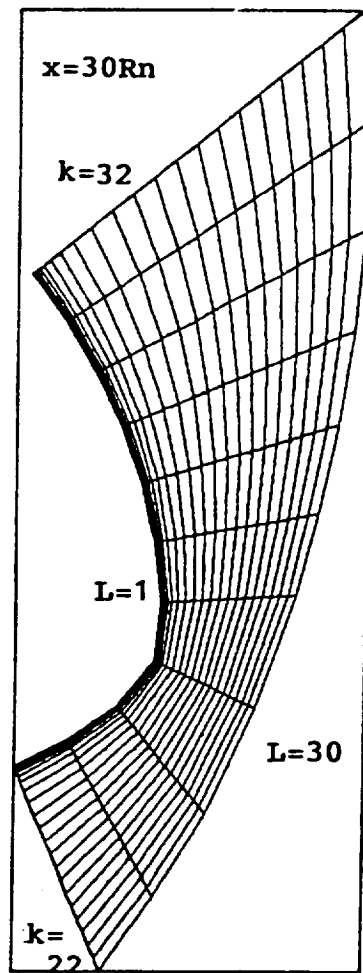
Fig. 10. Grid detail in the corner region for Case 1a at x = 30 Rn

(P/PINF)

x=20Rn

Alt.=125kft
Mach=20
5-deg angle
    of attack
Perfect-gas

Case 1a

(51x30 grid)

3.57

9.95—

7.02
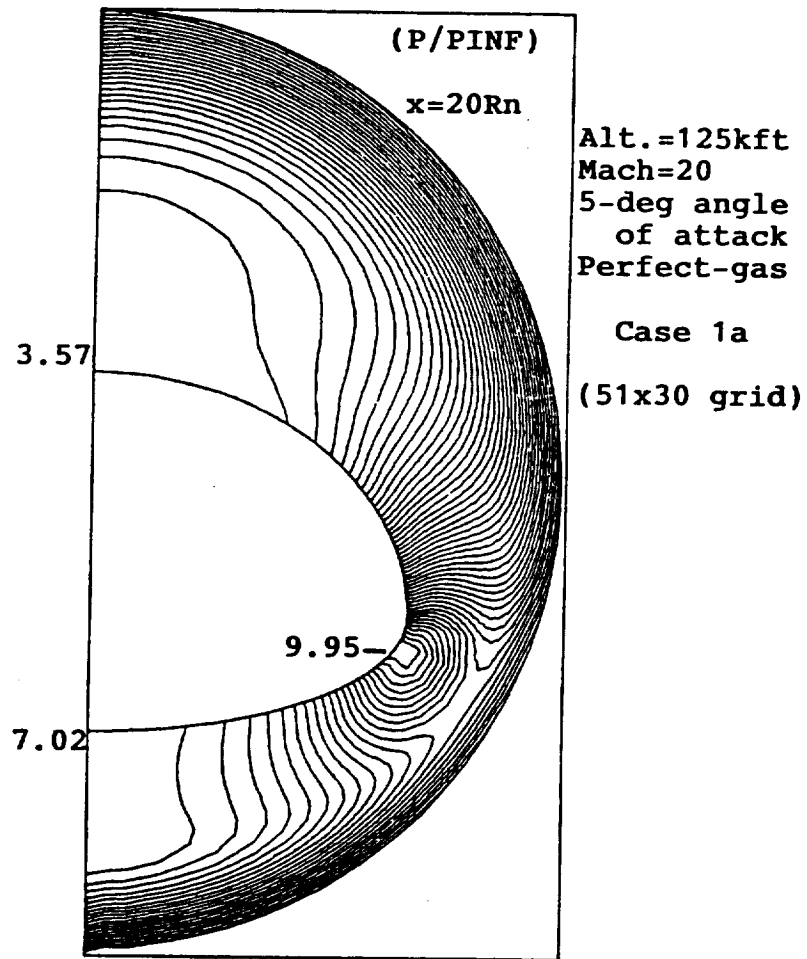
Fig. 11. Crossflow pressure contours for Case 1a at x = 20 Rn

(P/PINF)

x=30Rn

Alt.=125kft
Mach=20
5-deg angle
    of attack
Perfect-gas

Case 1a

(51x30 grid)

3.34

41.9

7.34
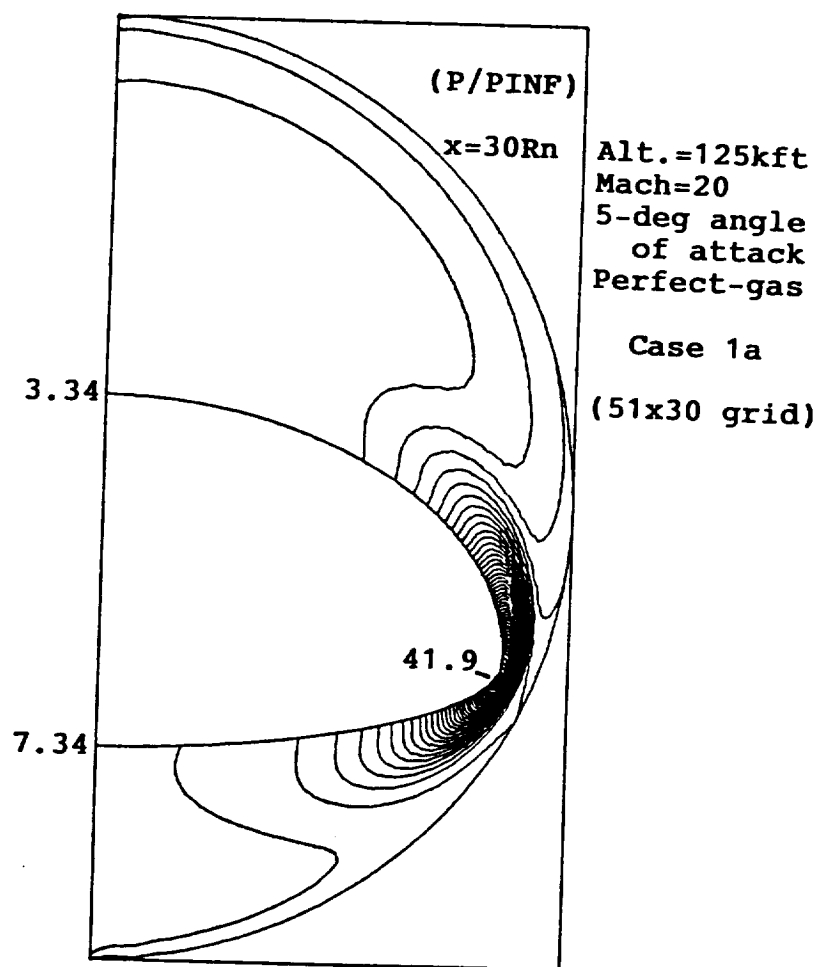
Fig. 12. Crossflow pressure contours for Case 1a at x = 30 Rn
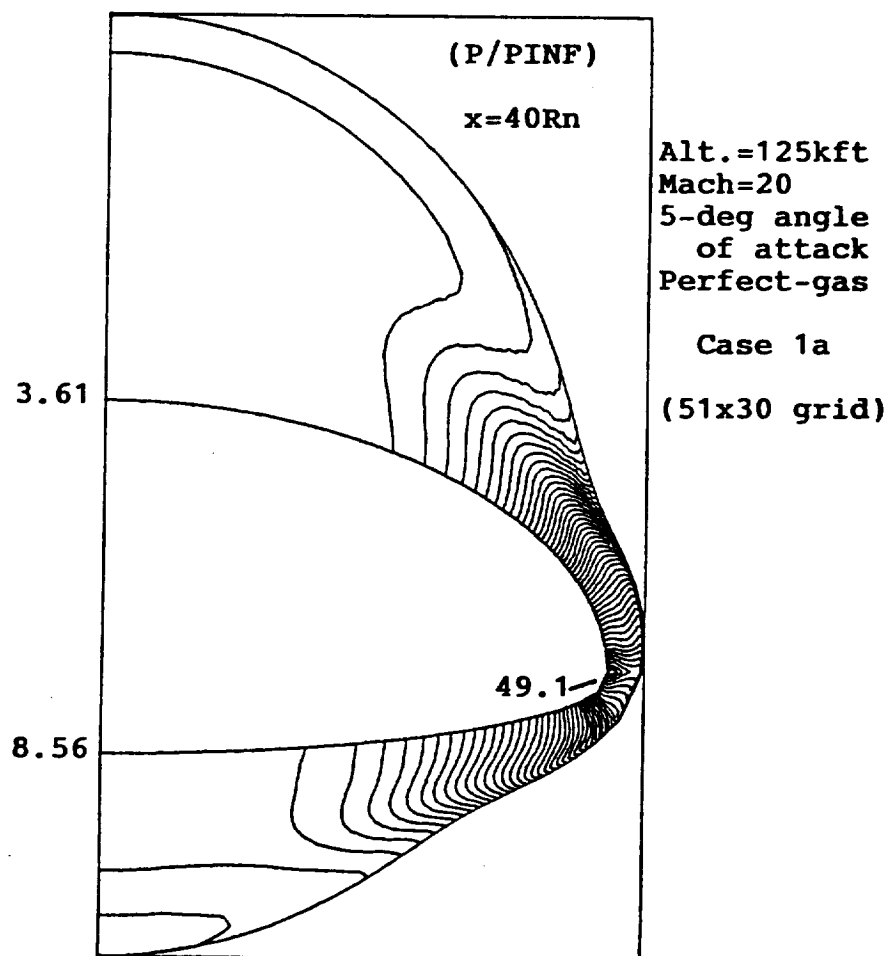
Fig. 13. Crossflow pressure contours for Case 1a at x = 40 Rn
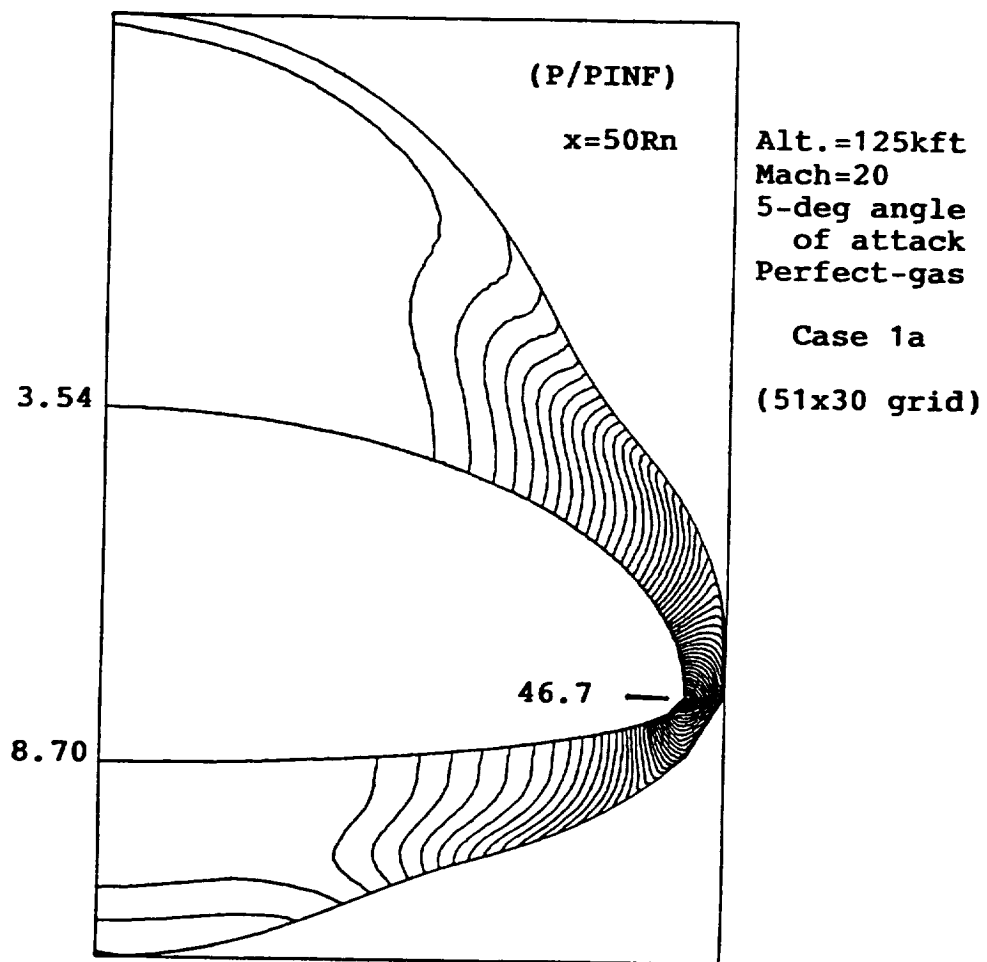
Fig. 14. Crossflow pressure contours for Case 1a at x = 50 Rn
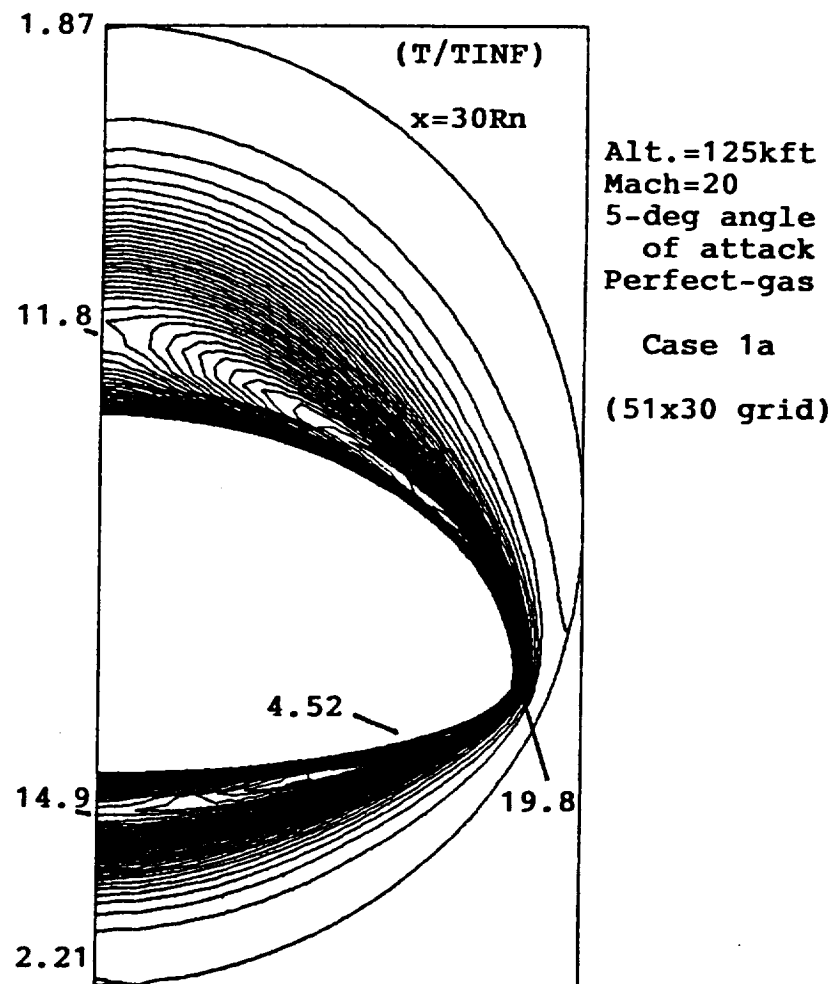
Fig. 15. Crossflow temperature contours for Case 1a at x = 30 Rn
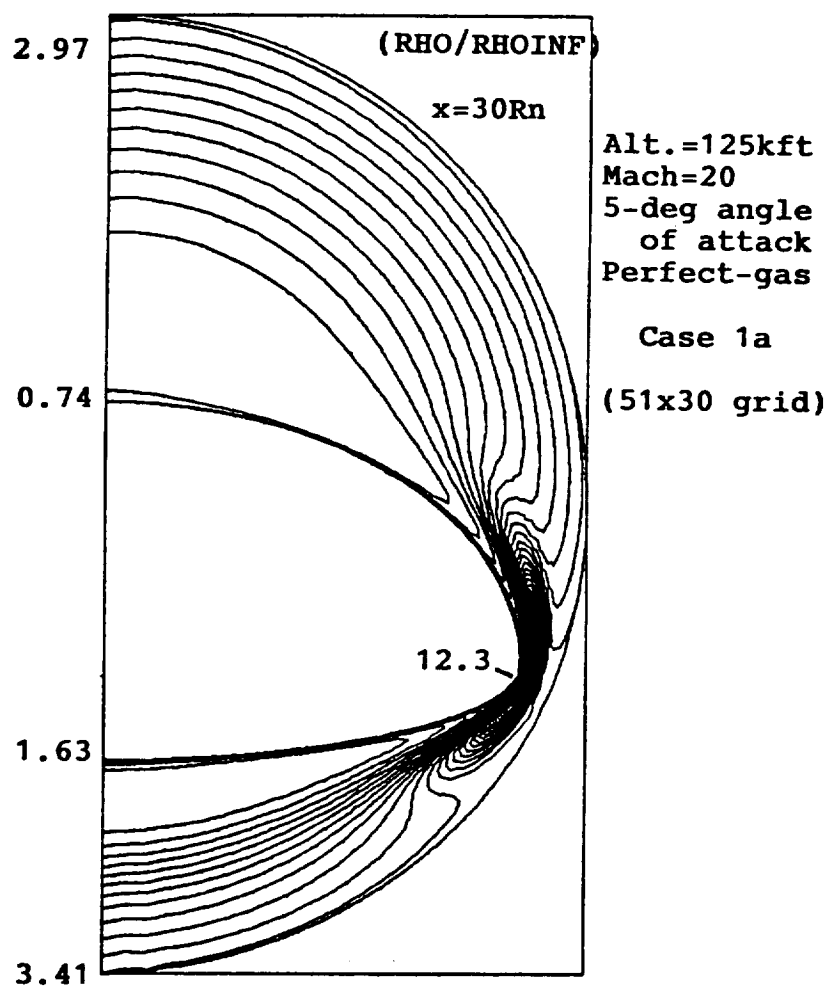
Fig. 16. Crossflow density contours for Case 1a at x = 30 Rn
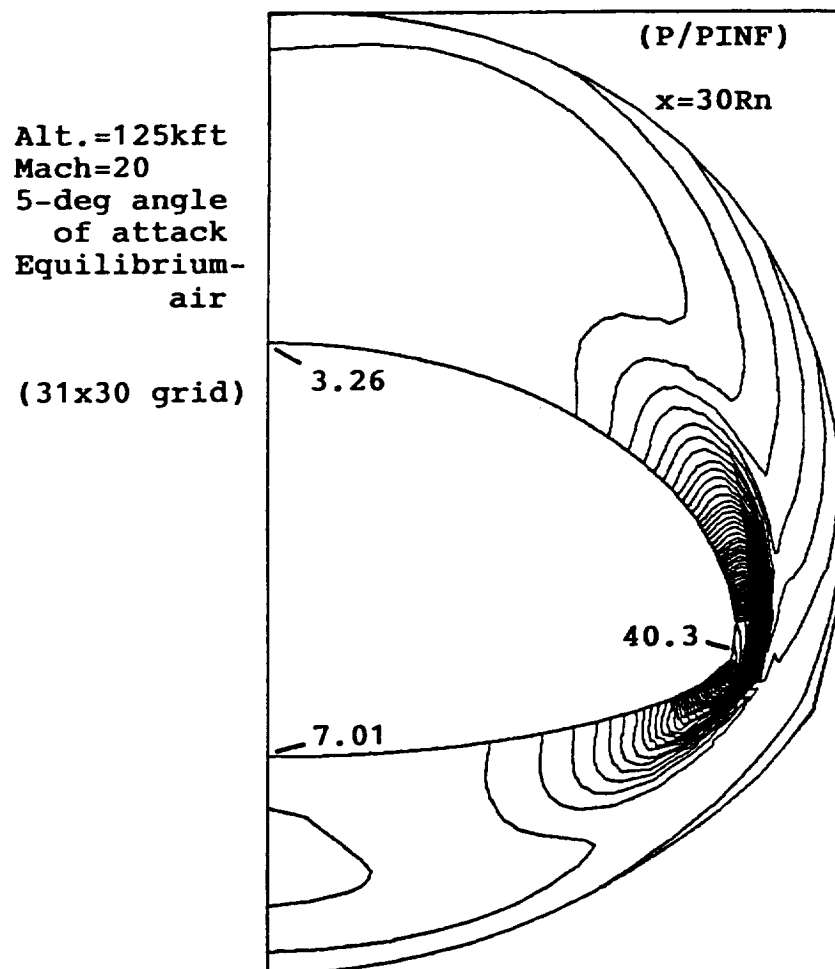
Fig. 17. Crossflow pressure contours for Case 2 at x = 30 Rn
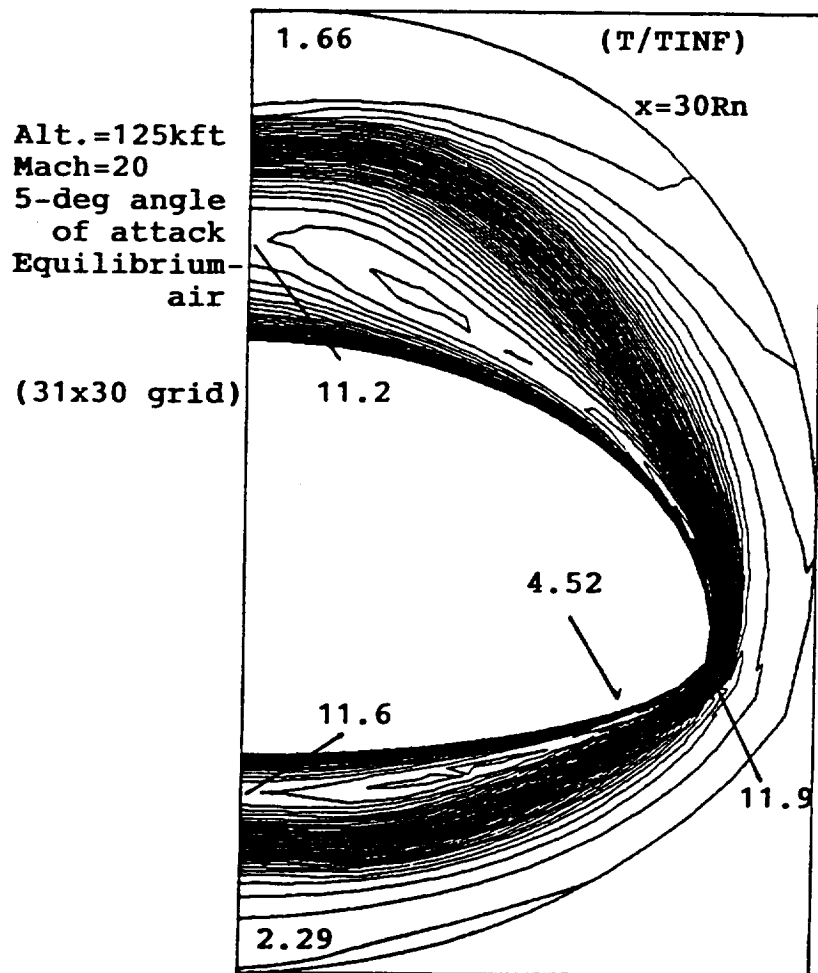
Fig. 18. Crossflow temperature contours for Case 2 at x = 30 Rn

Fig. 19. Crossflow density contours for Case 2 at x = 30 Rn

Figure content labels:

P/PINF

x=20Rn

Alt.=125kft
Mach=20
5° angle of
    attack
Nonequilibrium
    air

51x30 grid

3.78

8.68

7.20
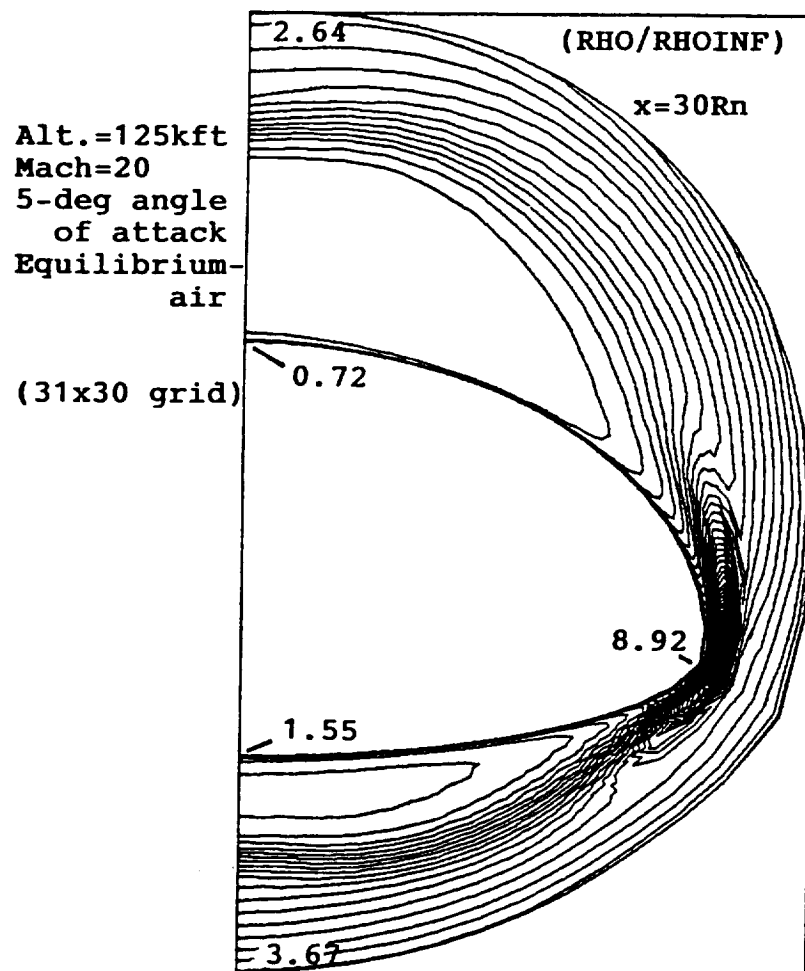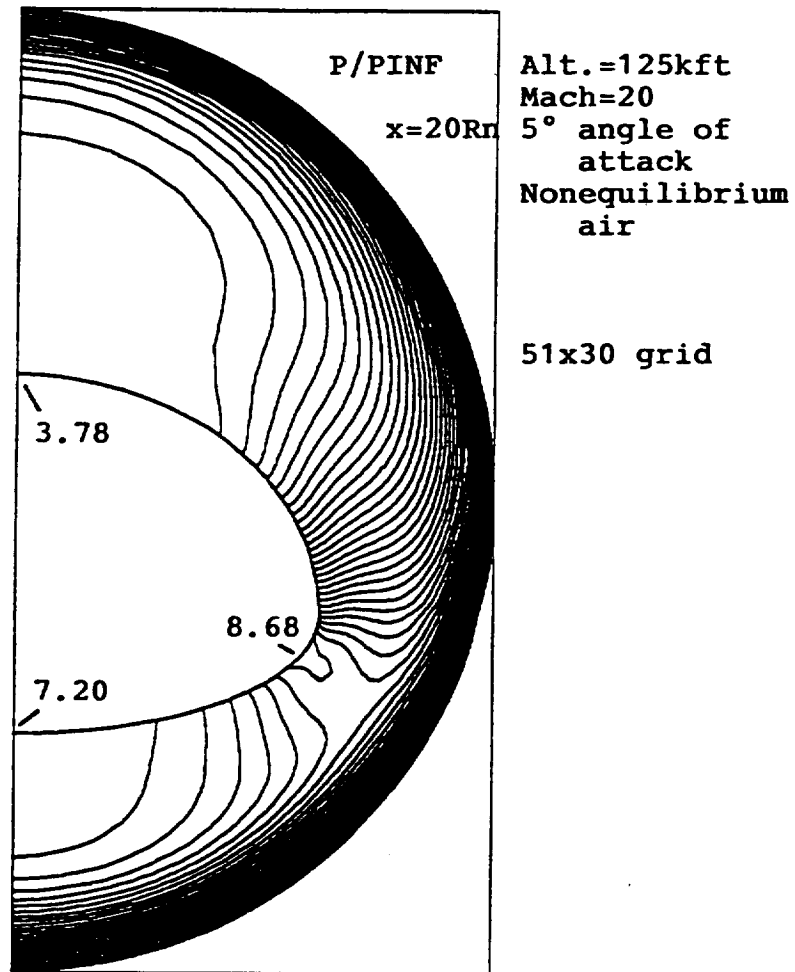
Fig. 20. Crossflow pressure contours for Case 3a at x = 20Rn

P/PINF

x=30Rn

Alt.=125kft
Mach=20
5° angle of
    attack
Nonequilibrium
    air

51x30 grid

3.48

39.8

7.00
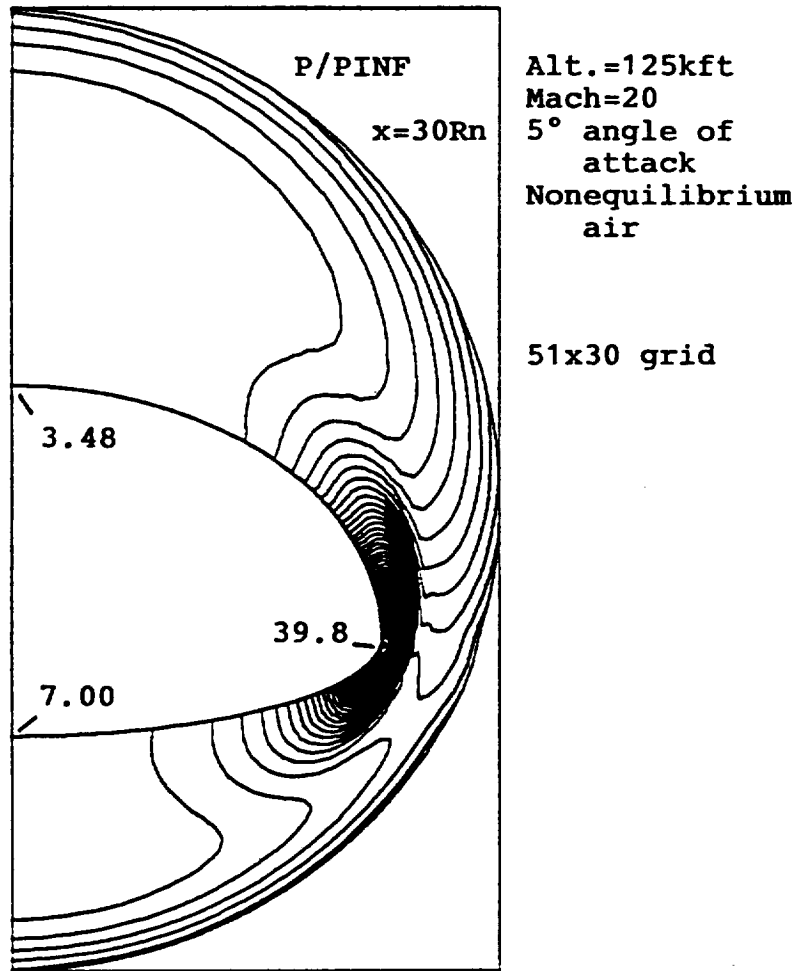
Fig. 21. Crossflow pressure contours for Case 3a at x = 30Rn

P/PINF

x=40 Rn

Alt.=125kft
Mach=20
5° angle of
    attack
Nonequilibrium
    air

51x30 grid

3.58

7.72

41.2
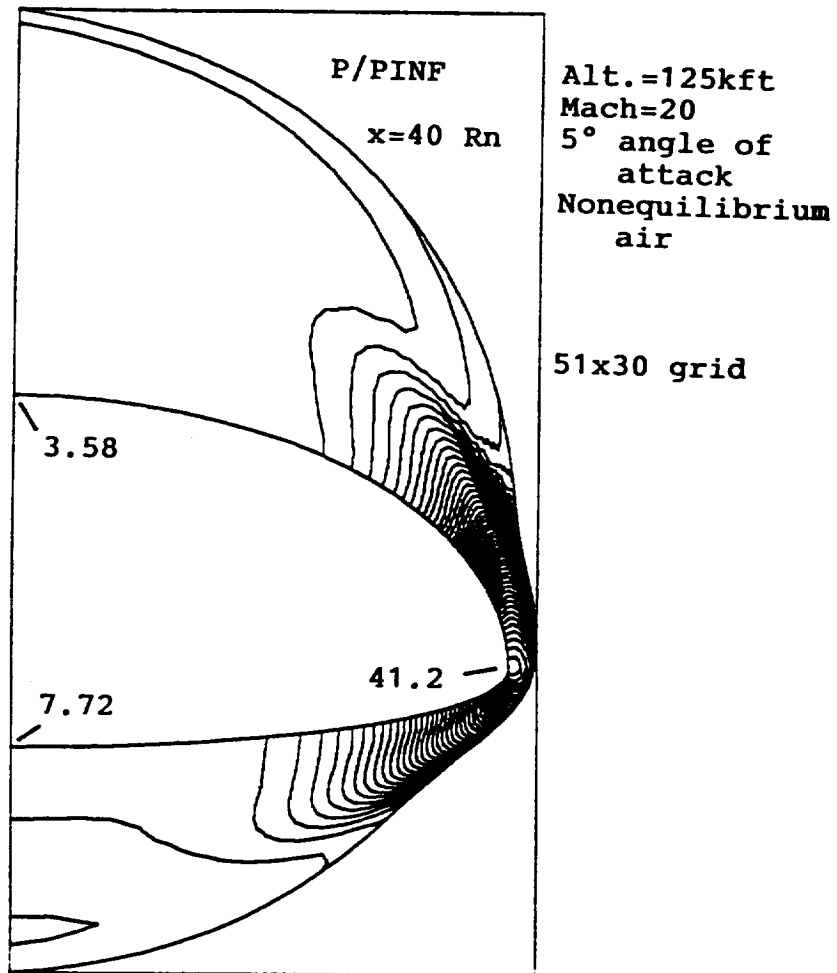
Fig. 22. Crossflow pressure contours for Case 3a at x = 40Rn
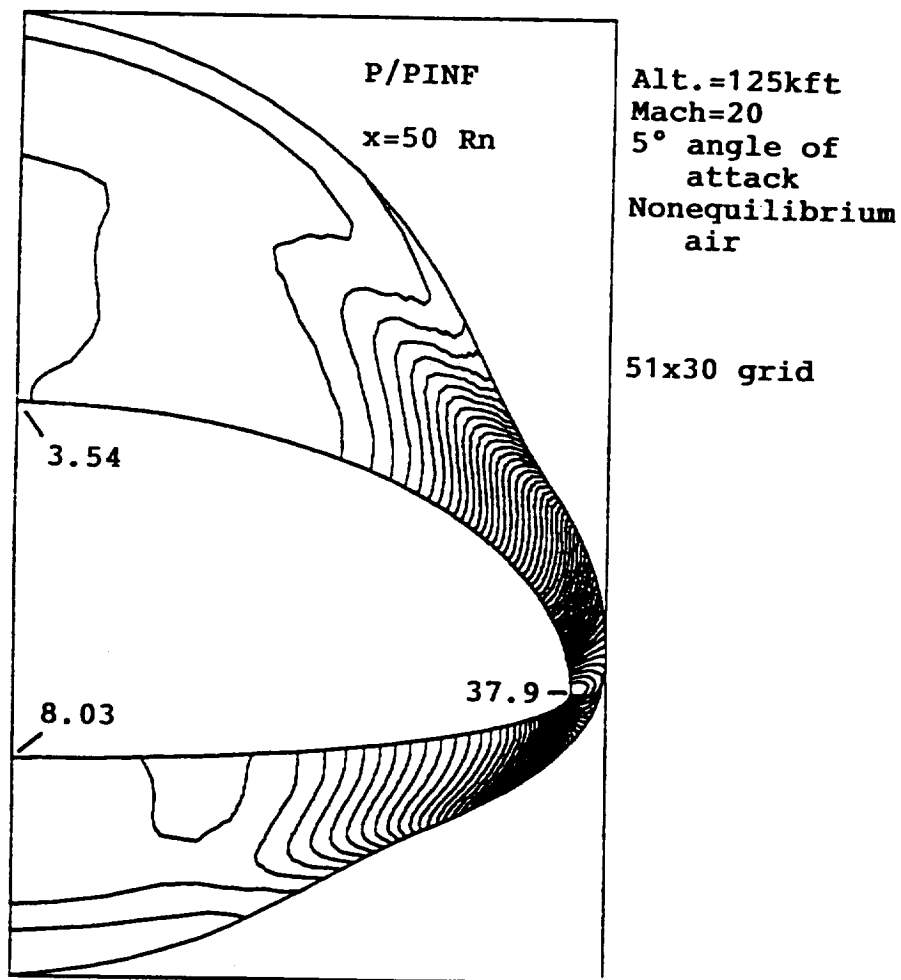
Fig. 23. Crossflow pressure contours for Case 3a at x = 50Rn
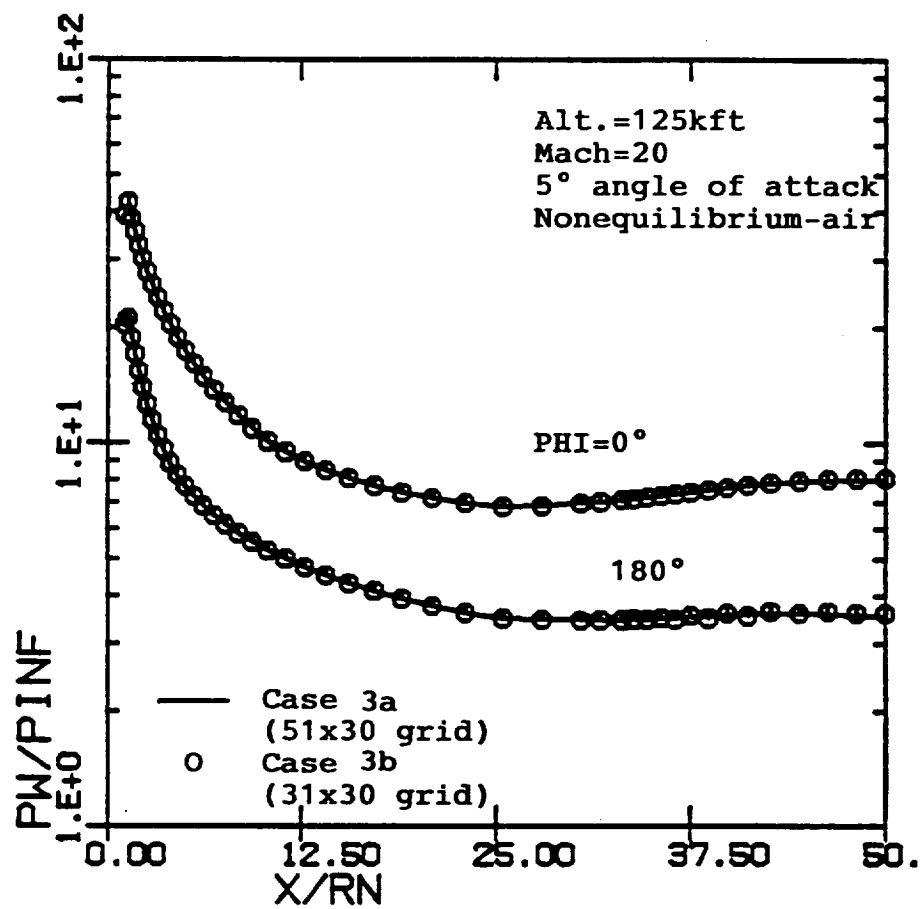
Fig. 24. Axial distribution of surface pressure for Case 3
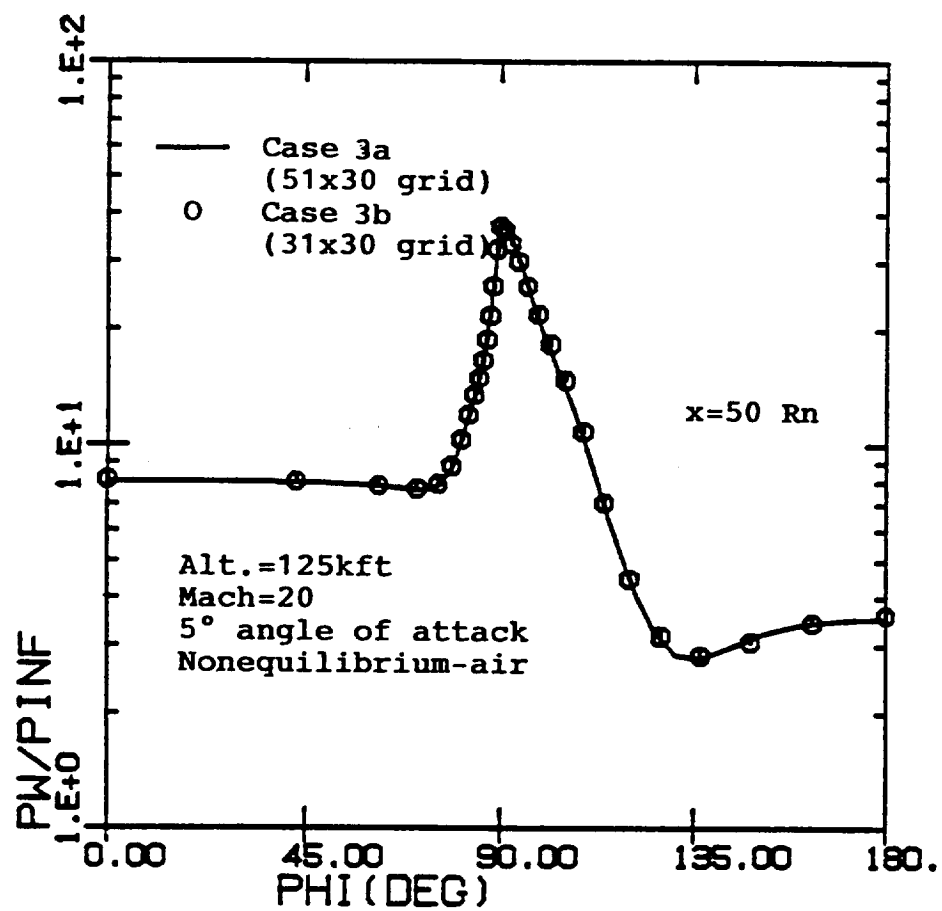
Fig. 25. Crossflow distribution of surface pressure for Case 3 at x = 50Rn
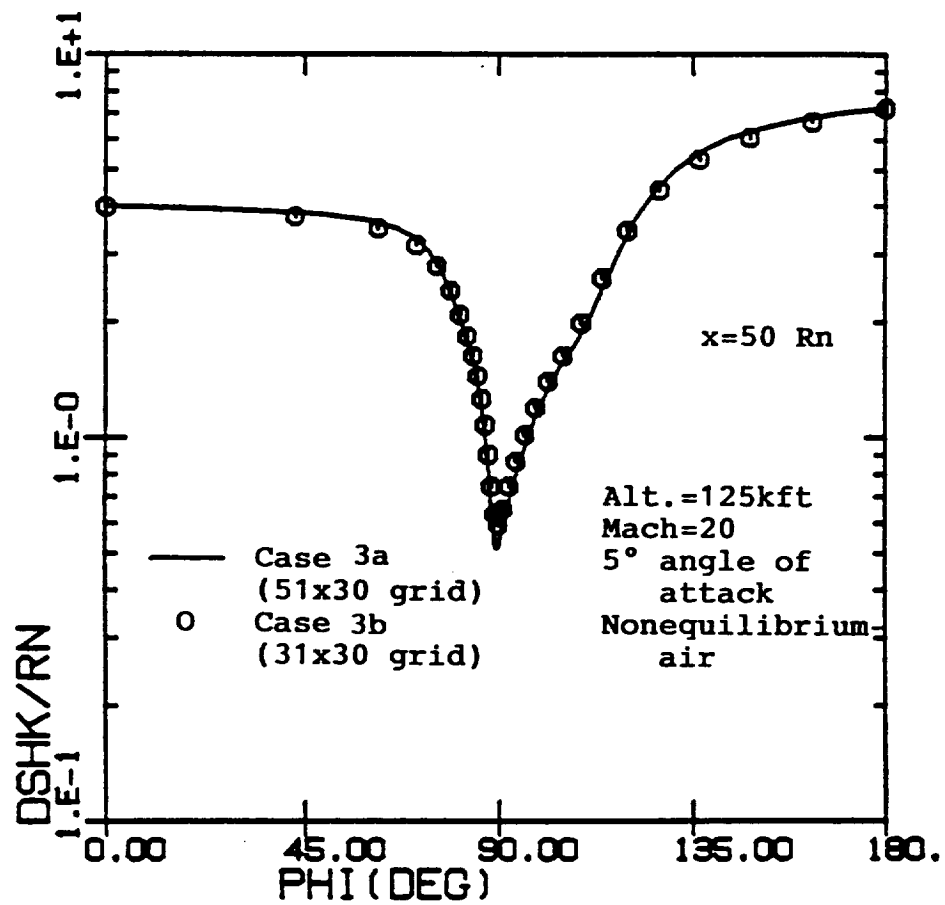
Fig. 26. Crossflow distribution of shock-standoff distance for Case 3 at x = 50Rn
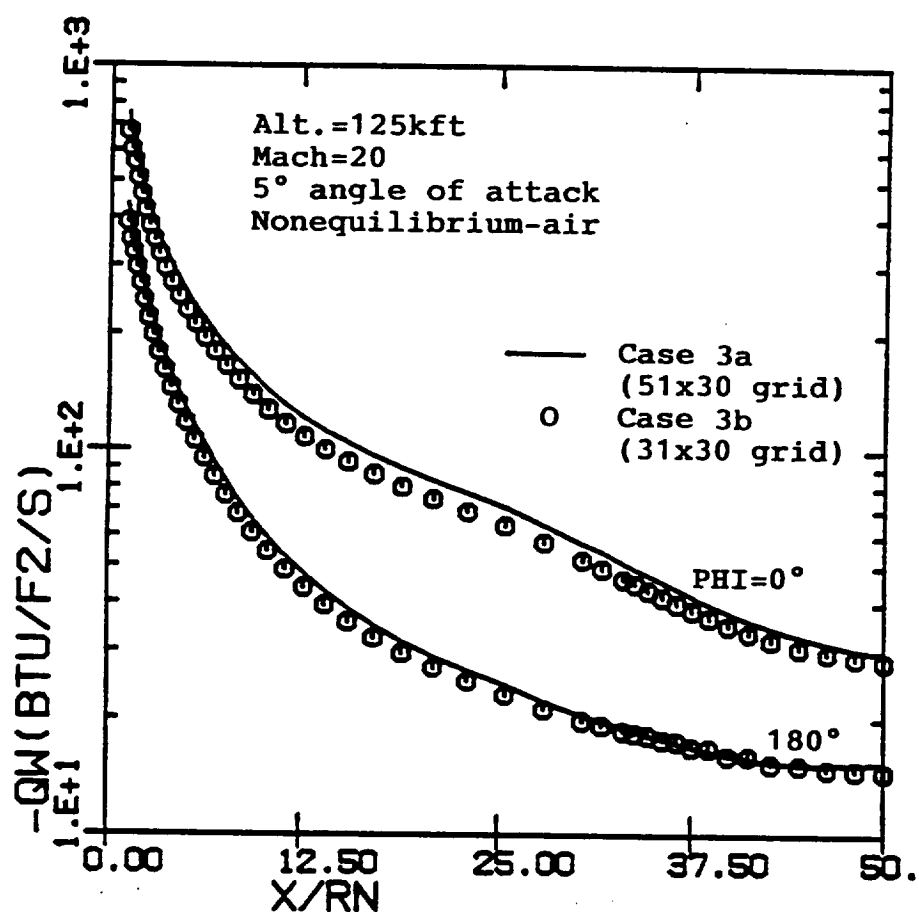
Fig. 27. Axial distribution of surface heat-transfer rate for Case 3
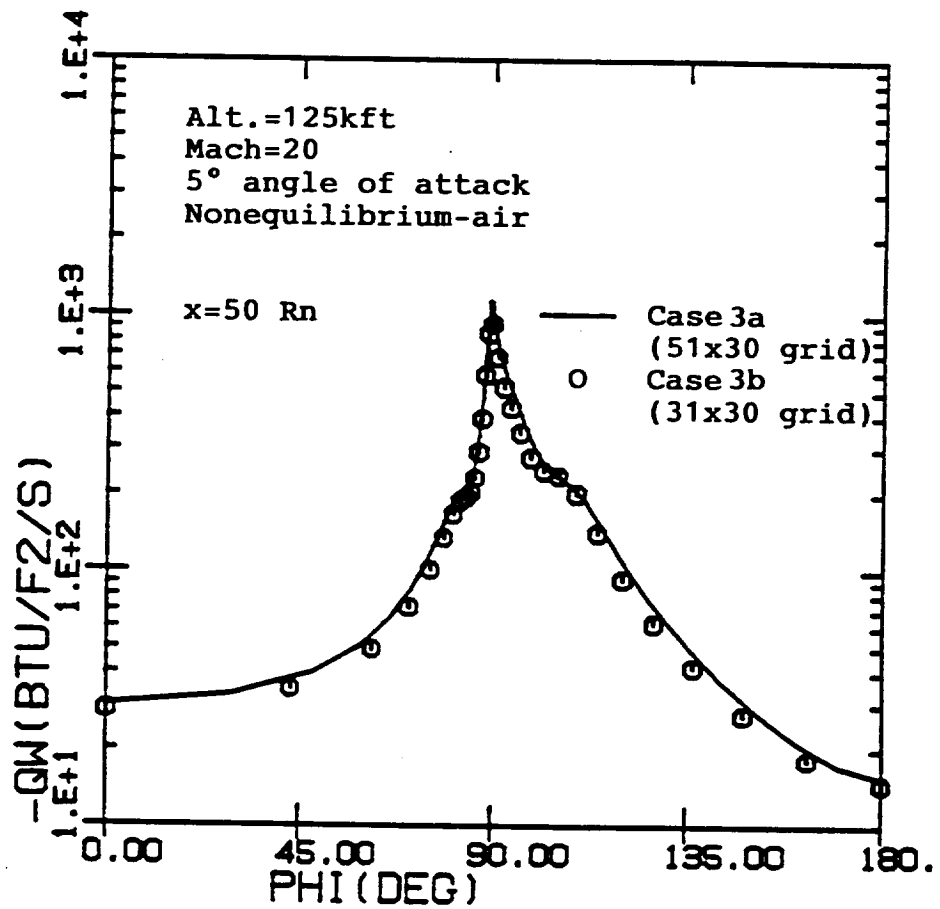
Fig. 28. Crossflow distribution of surface heat-transfer rate for for Case 3 at x = 50 Rn
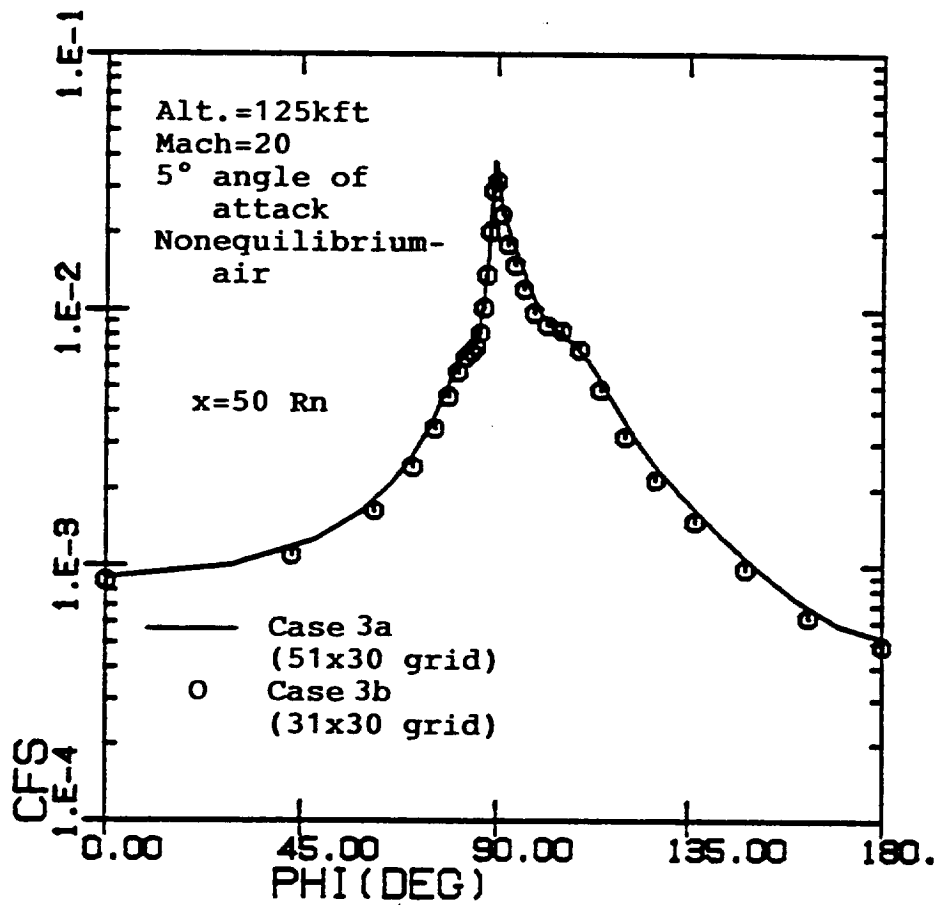
Fig. 29. Crossflow distribution of skin-friction for Case 3 at x = 50 Rn
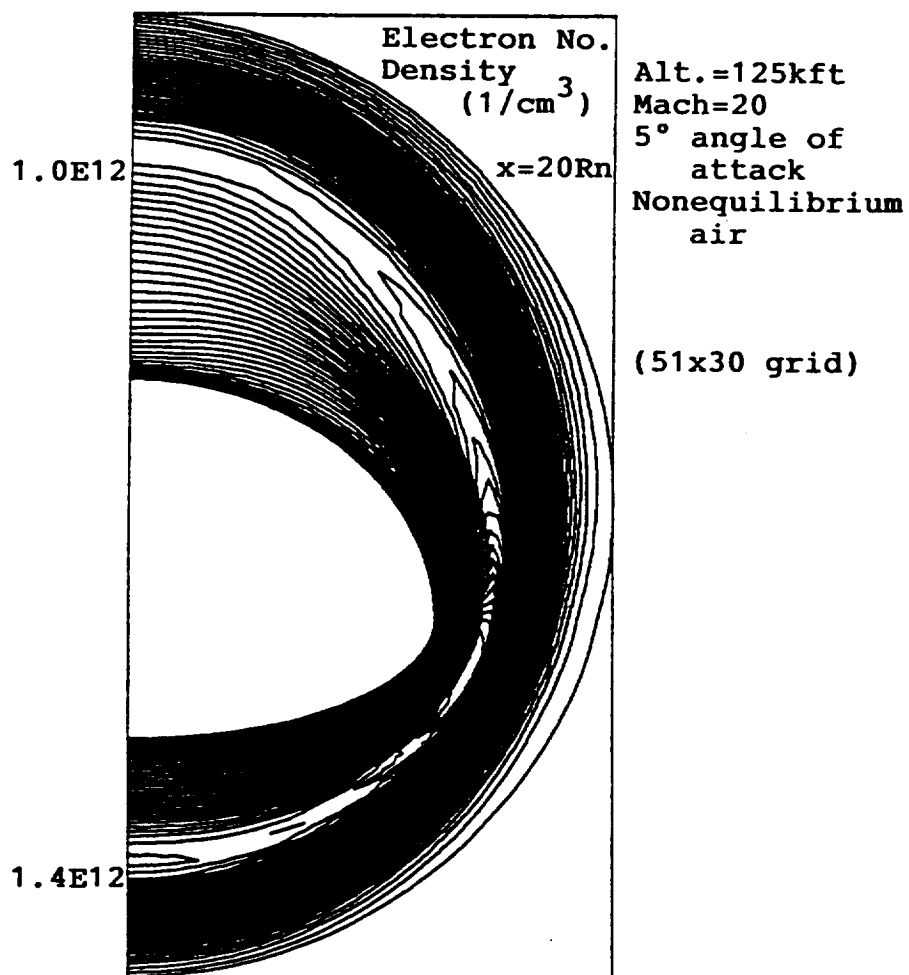
Fig. 30. Crossflow contours of electron number density for Case 3a at x = 20 Rn
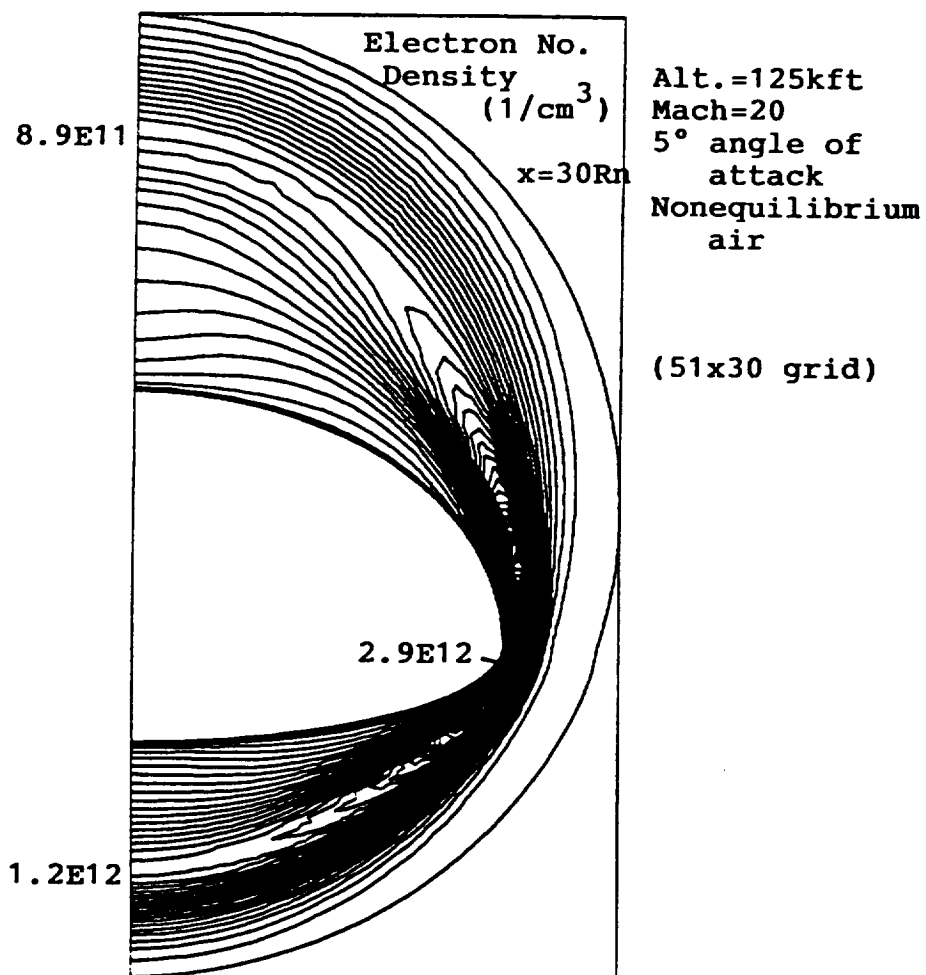
Fig. 31. Crossflow contours of electron number density for Case 3a at x = 30Rn
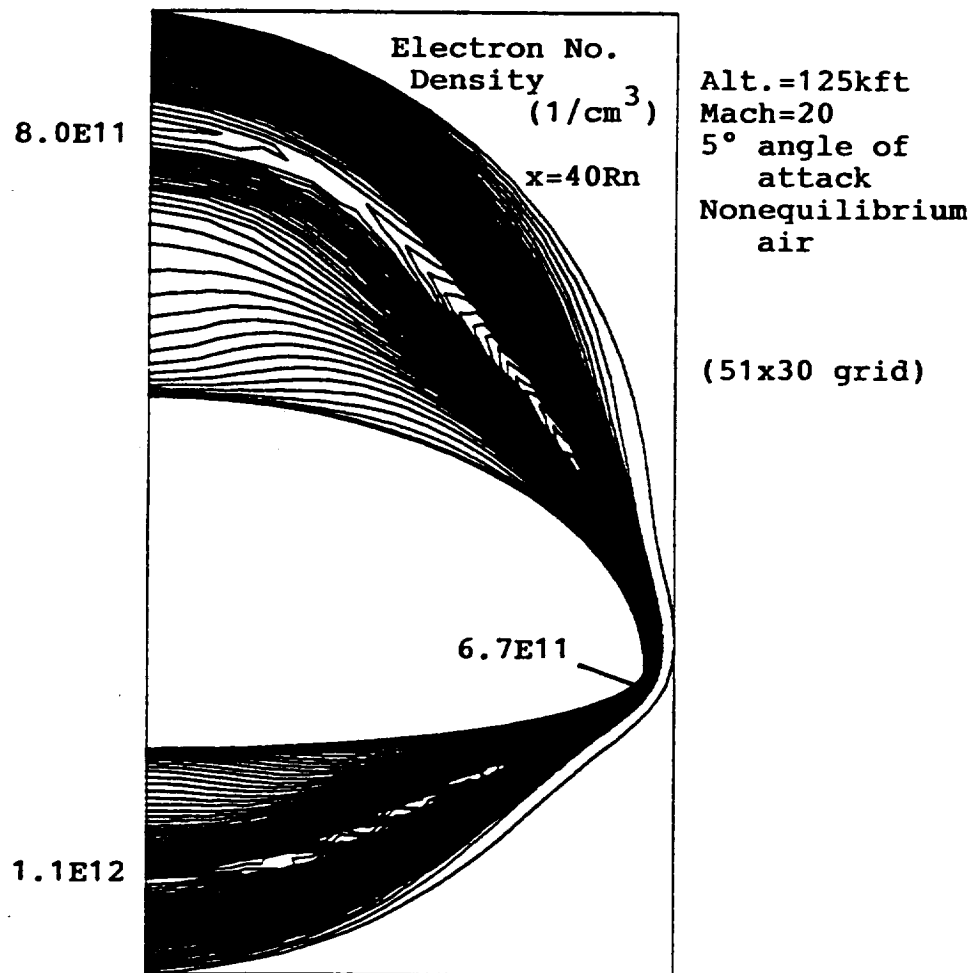
Fig. 32. Crossflow contours of electron number density for Case 3a at x = 40Rn
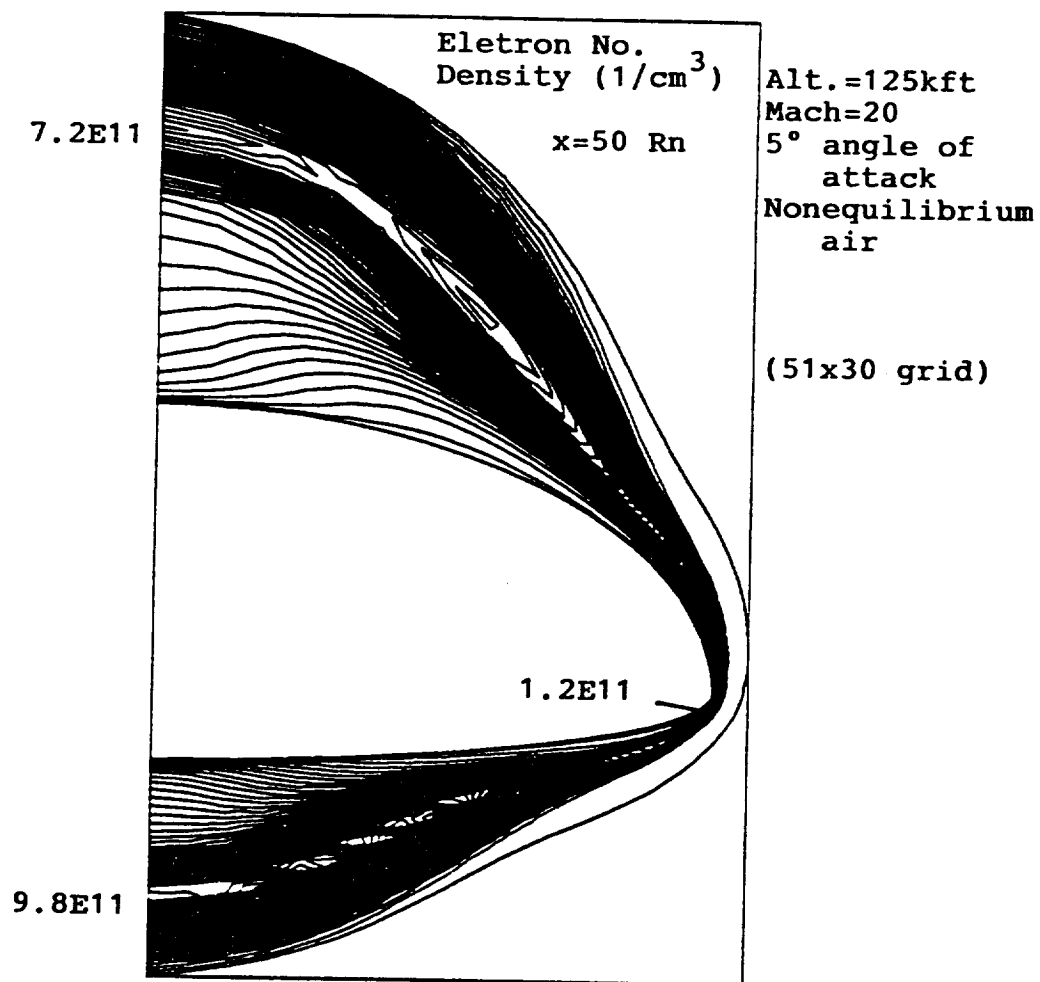
Fig. 33. Crossflow contours of electron number density for Case 3a at x = 50Rn
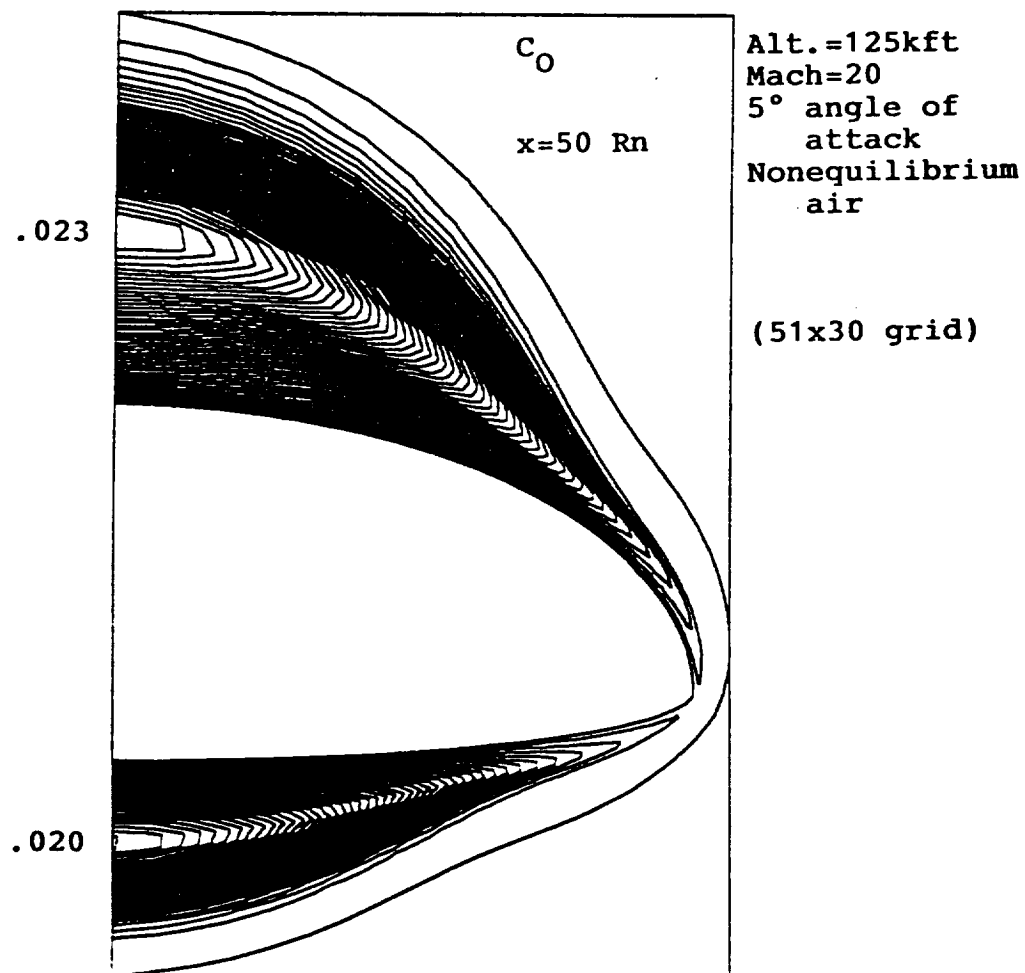
Fig. 34. Crossflow contours of O concentration for Case 3a at x = 50Rn
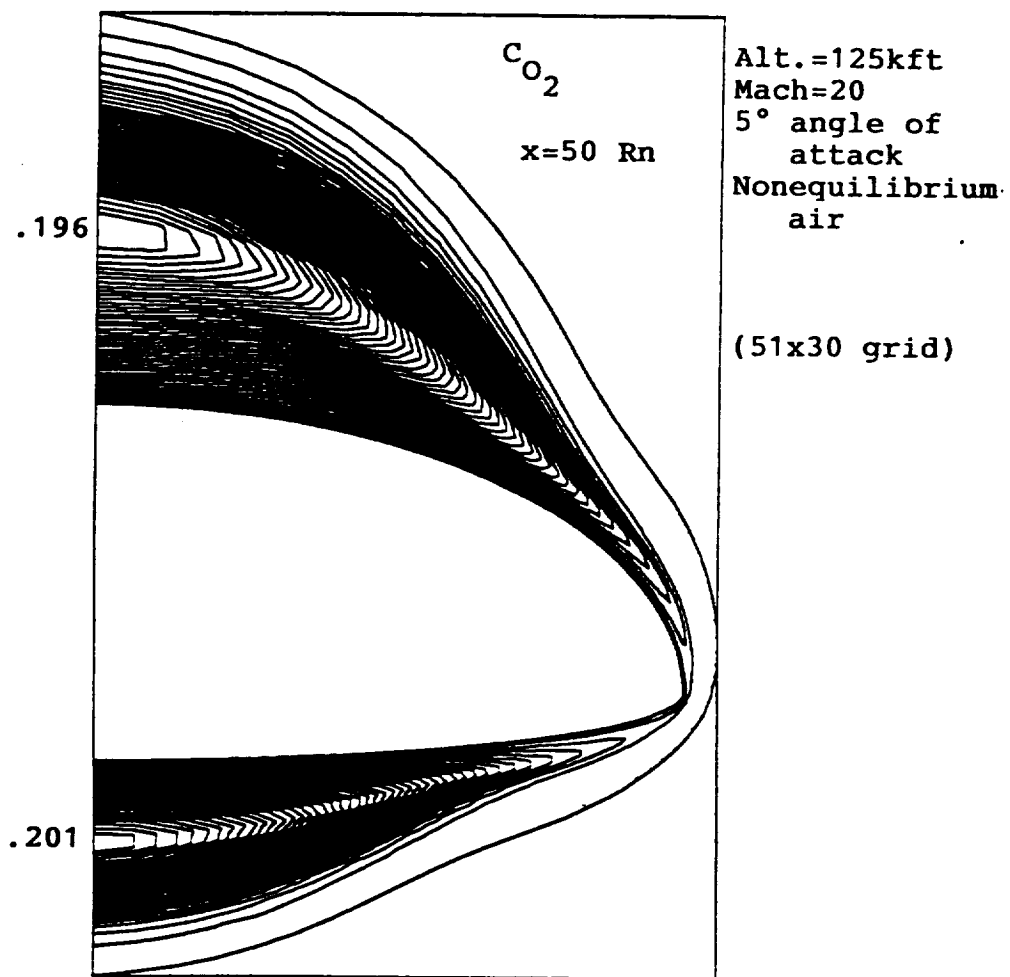
Fig. 35. Crossflow contours of O_2 concentration for Case 3a at $x = 50Rn$

5.7E-5

C_N

x=50 Rn

Alt.=125kft
Mach=20
5° angle of
    attack
Nonequilibrium
    air

(51x30 grid)

2.5E-5
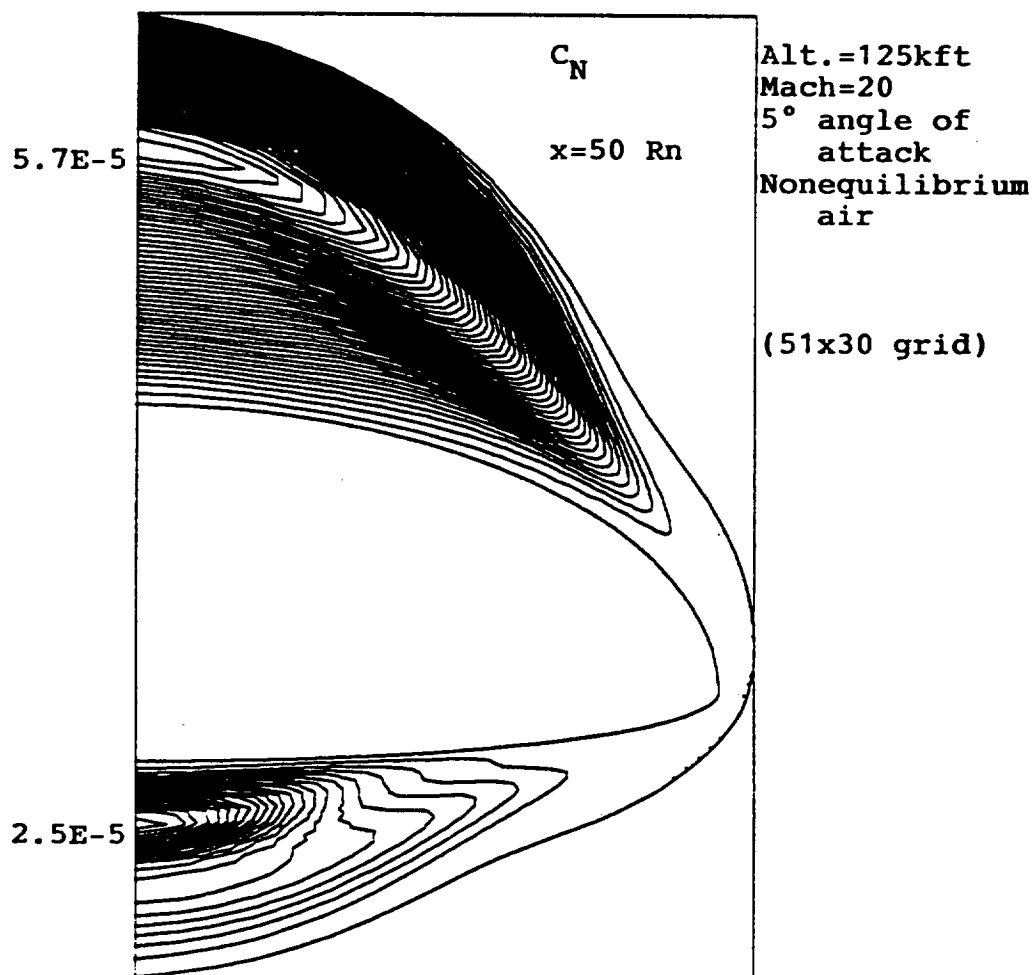
Fig. 36. Crossflow contours of N concentration for Case 3a at x = 50Rn
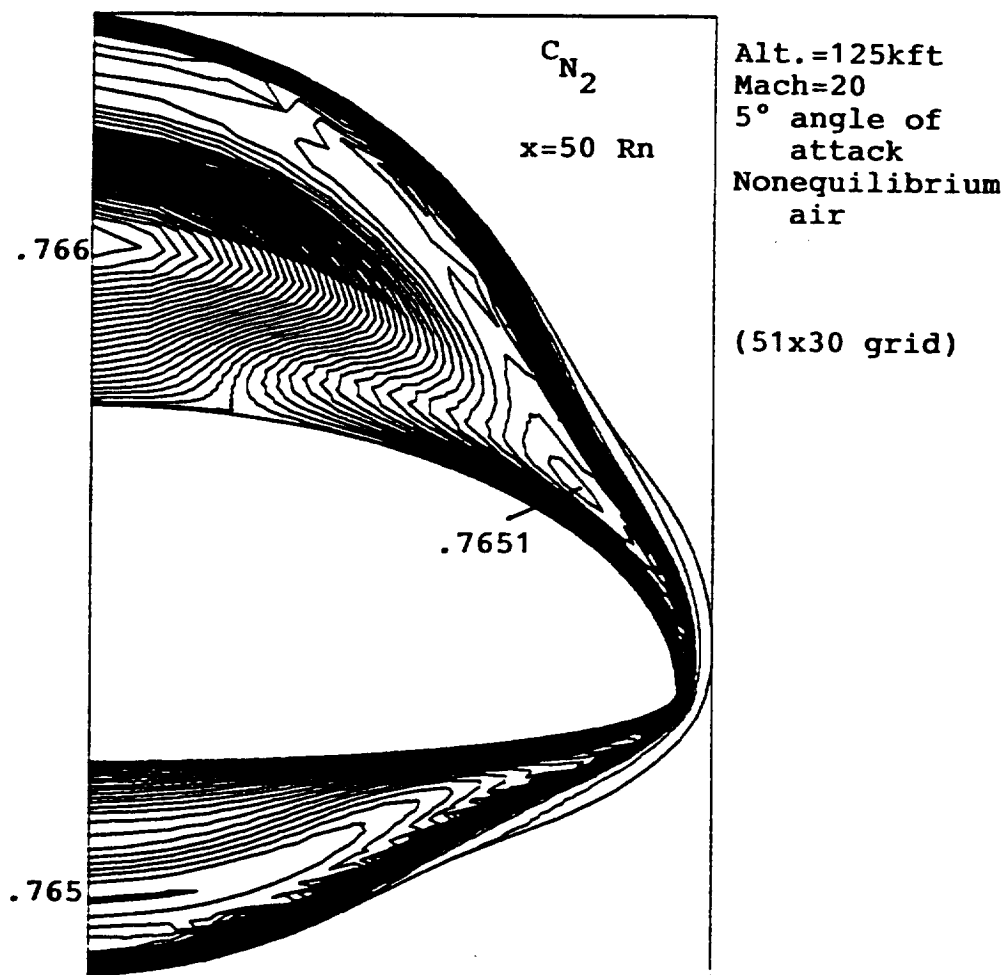
Fig. 37. Crossflow contours of N_2 concentration for Case 3a at $x = 50Rn$
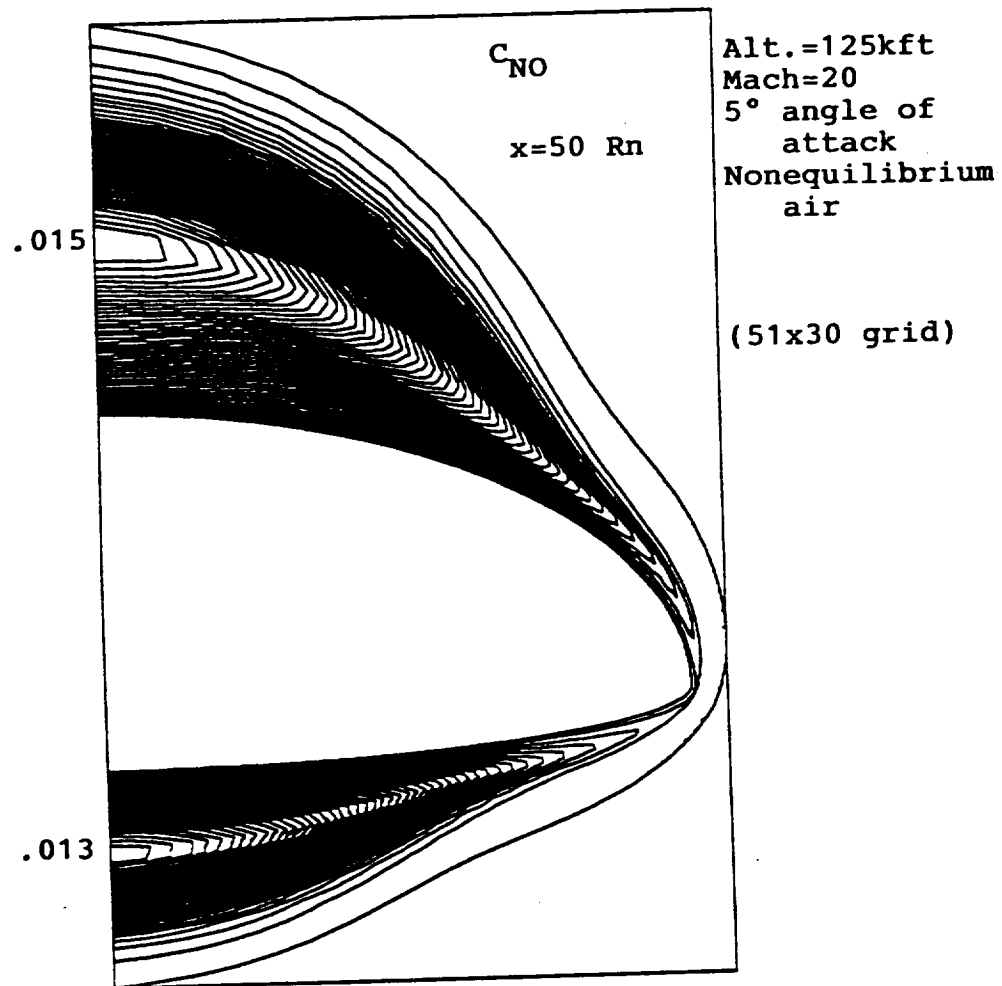
Fig. 38. Crossflow contours of NO concentration for Case 3a at x = 50Rn
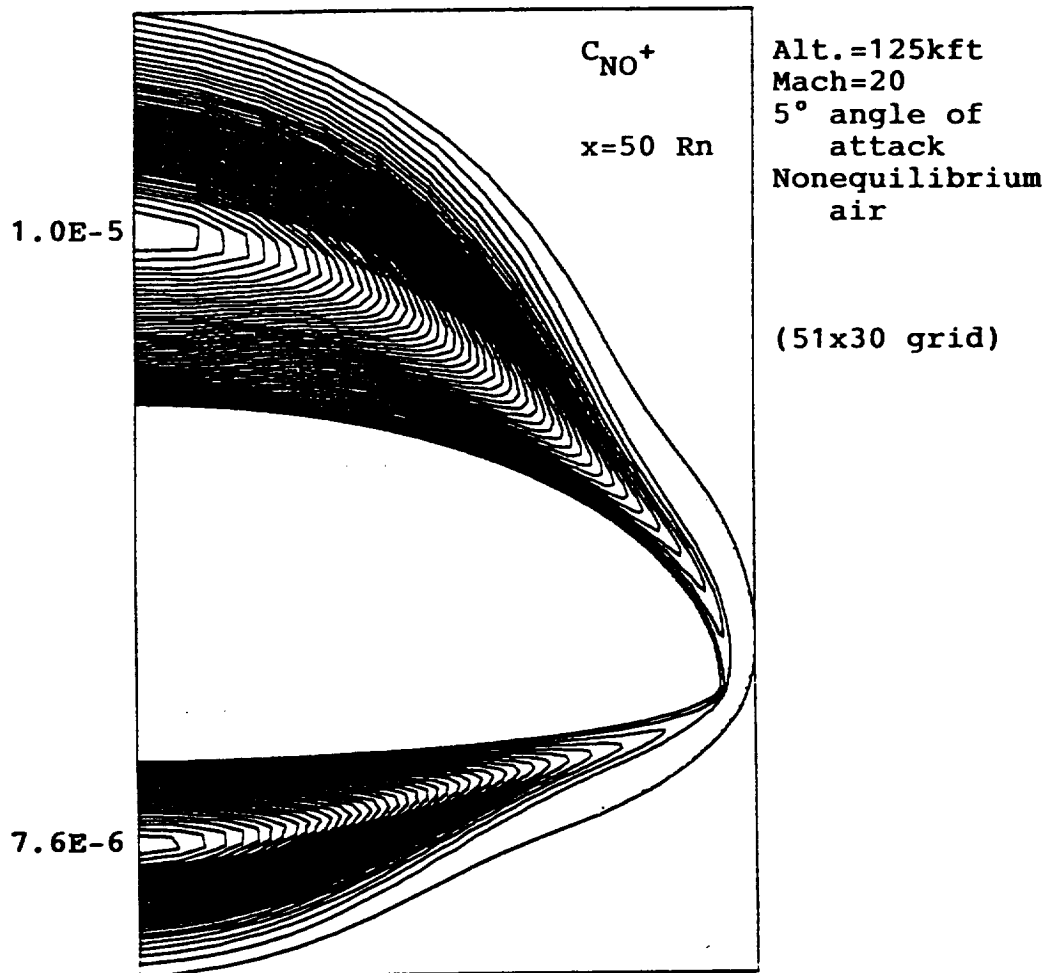
Fig. 39. Crossflow contours of NO+ concentration for Case 3a at x = 50Rn
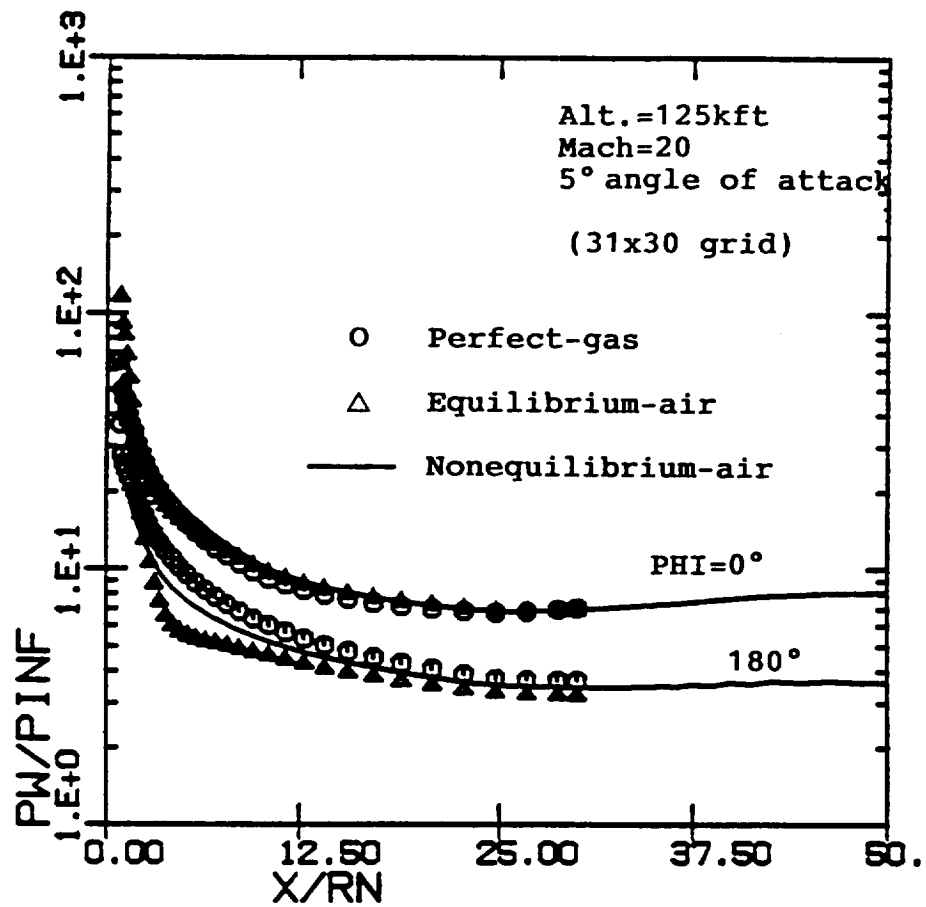
Fig. 40. Gas-model effects on the axial distribution of surface pressure
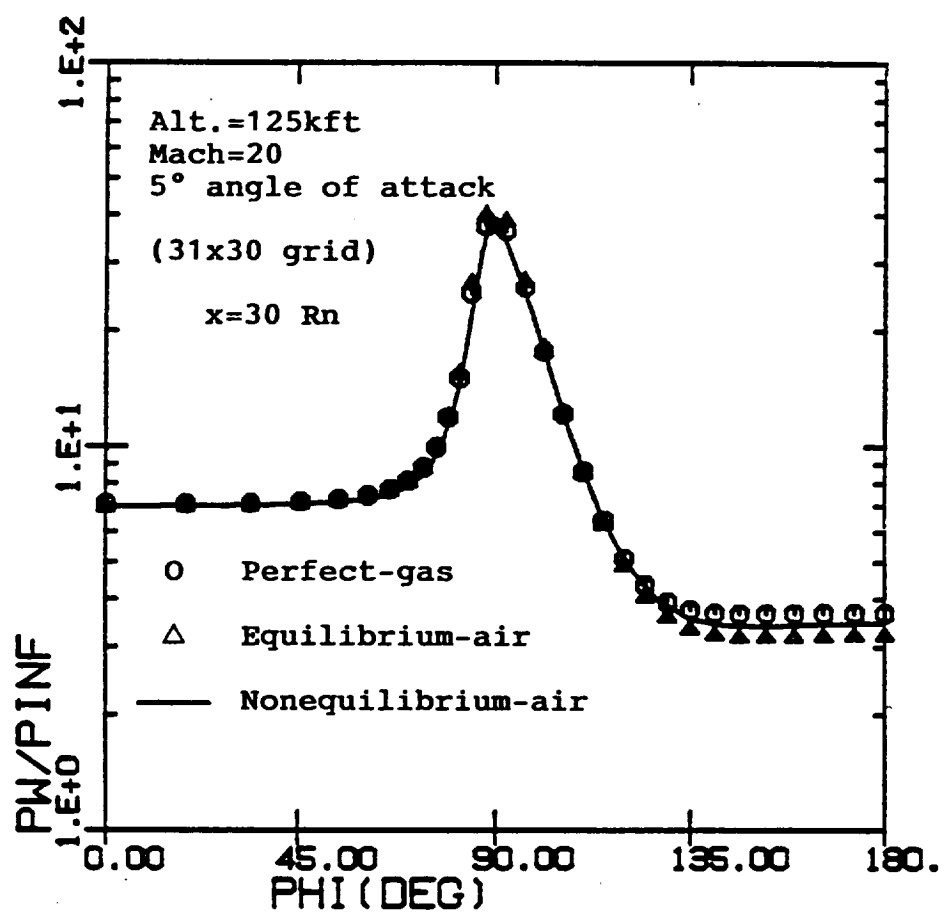
Fig. 41. Gas-model effects on the crossflow distribution of surface pressure at x = 30Rn
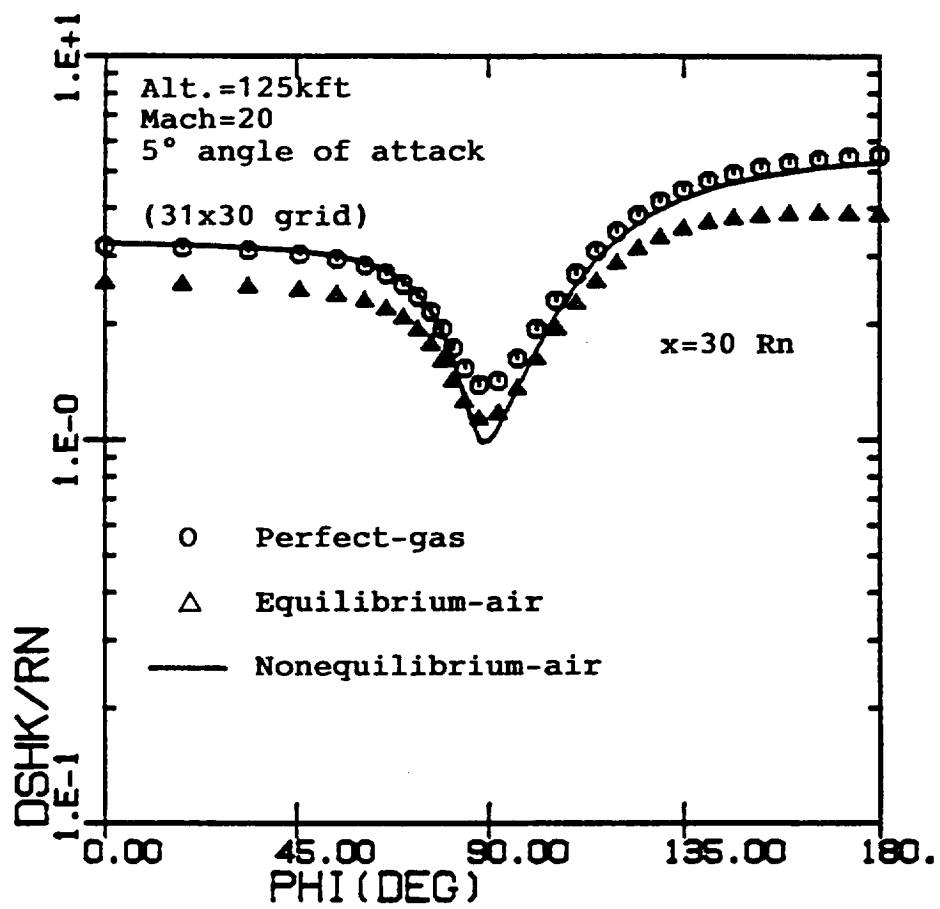
Fig. 42. Gas-model effects on the crossflow distribution of shock-standoff distance at x = 30Rn

Alt.=125 kft
Mach=20
5° angle of attack

(31x30 grid)

O   Perfect-gas

△   Equilibrium-air

——— Nonequilibrium-air

PHI=0°

180°

$-QW(BTU/F2/S)$

X/RN
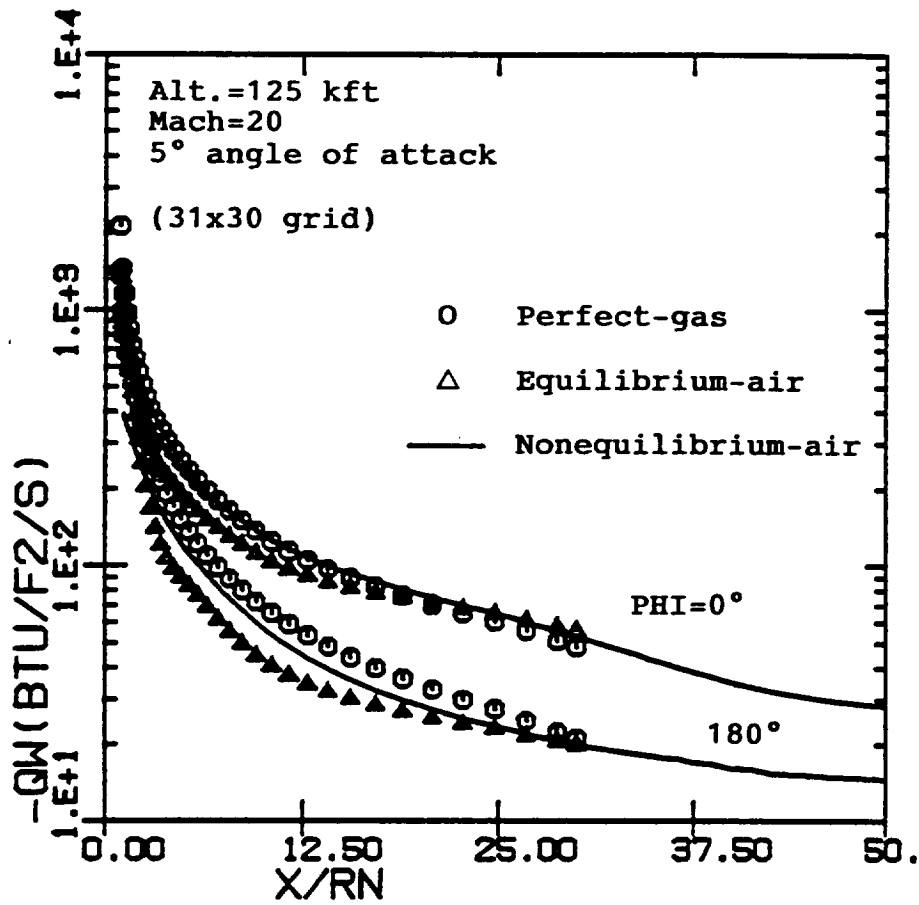
Fig. 43. Gas-model effects on the axial distribution of surface heat-transfer rate
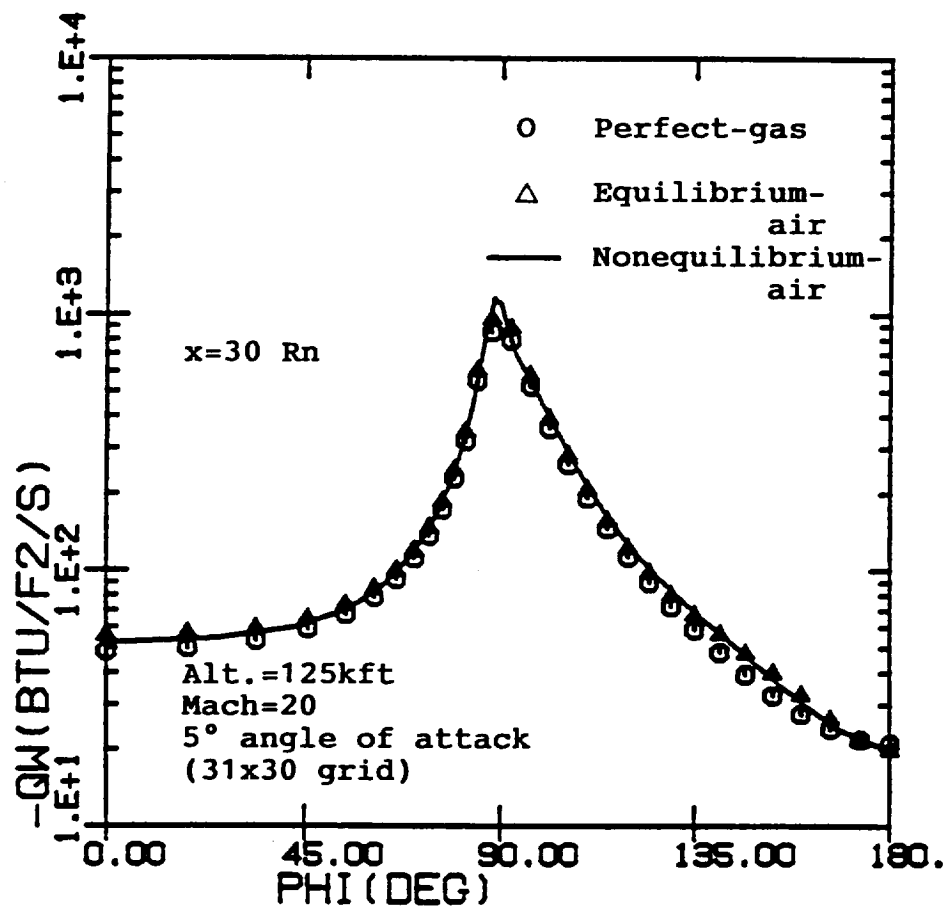
Fig. 44. Gas-model effects on the crossflow distribution of surface heat-transfer rate at
x = 30Rn
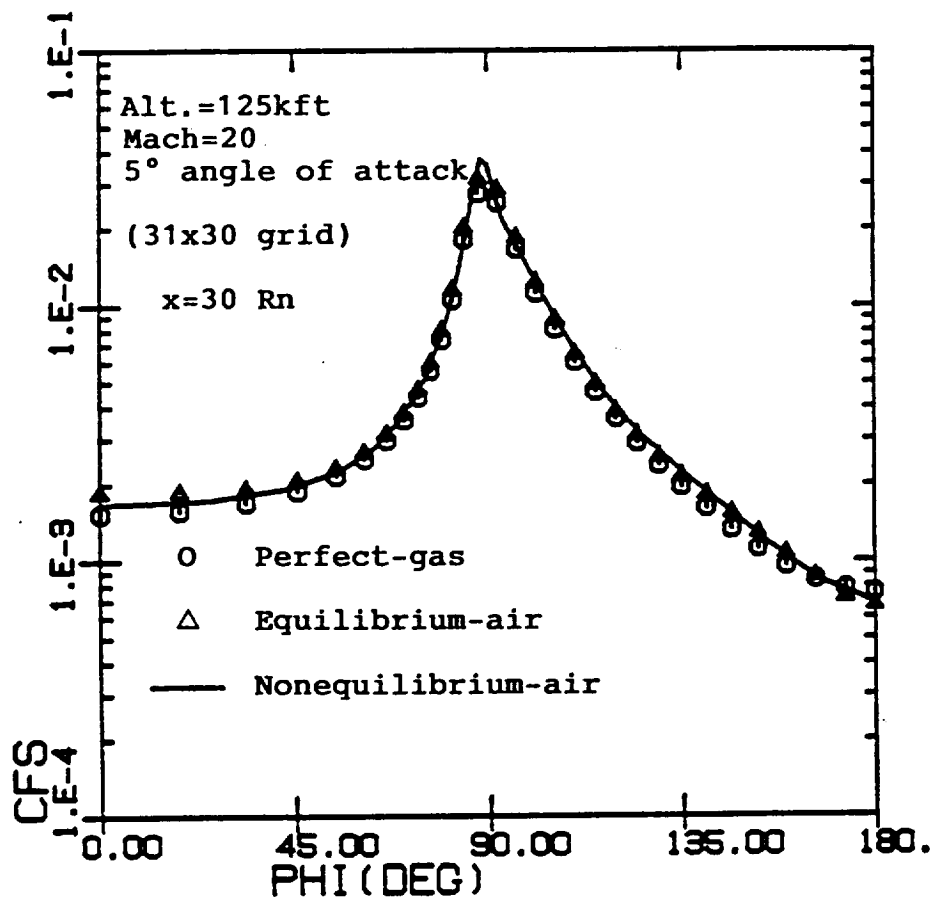
Fig. 45. Gas-model effects on the crossflow distribution of skin-friction at x = 30Rn
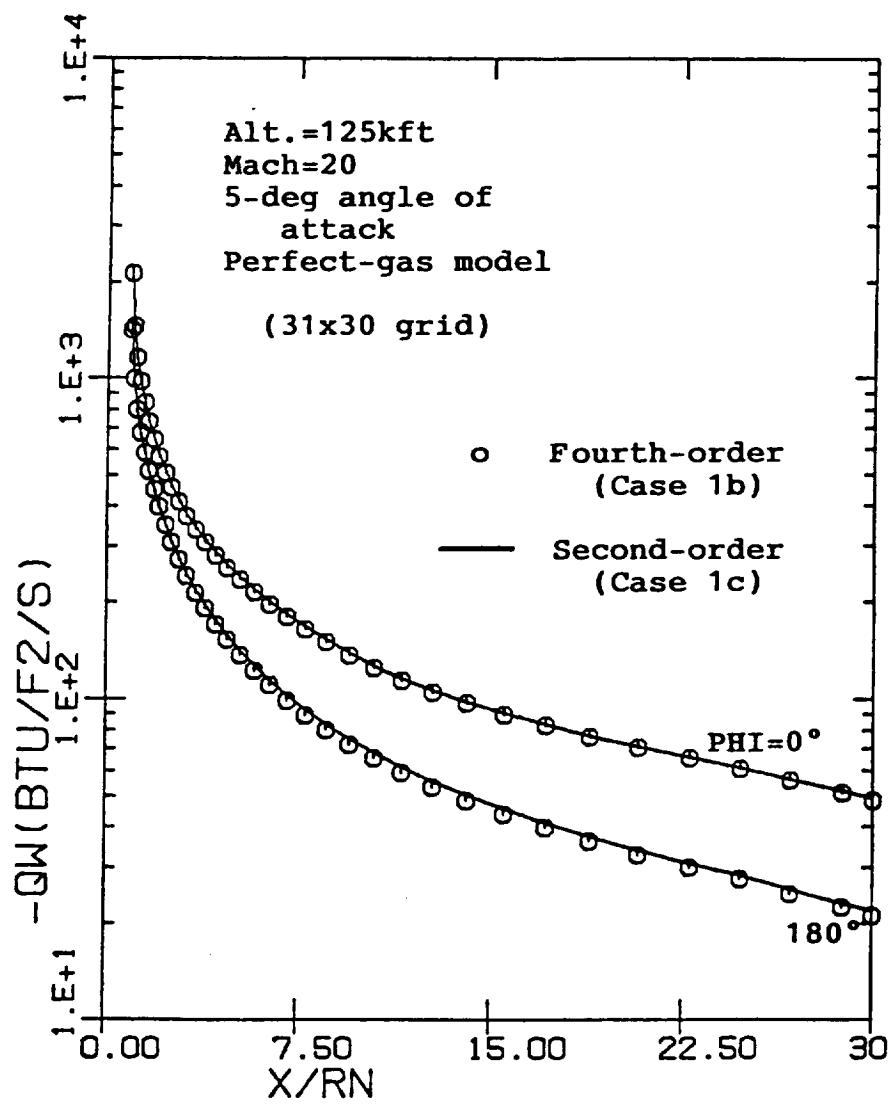
Fig. 46. Smoothing effects on the axial distribution of wall heat-transfer rates for Case 1
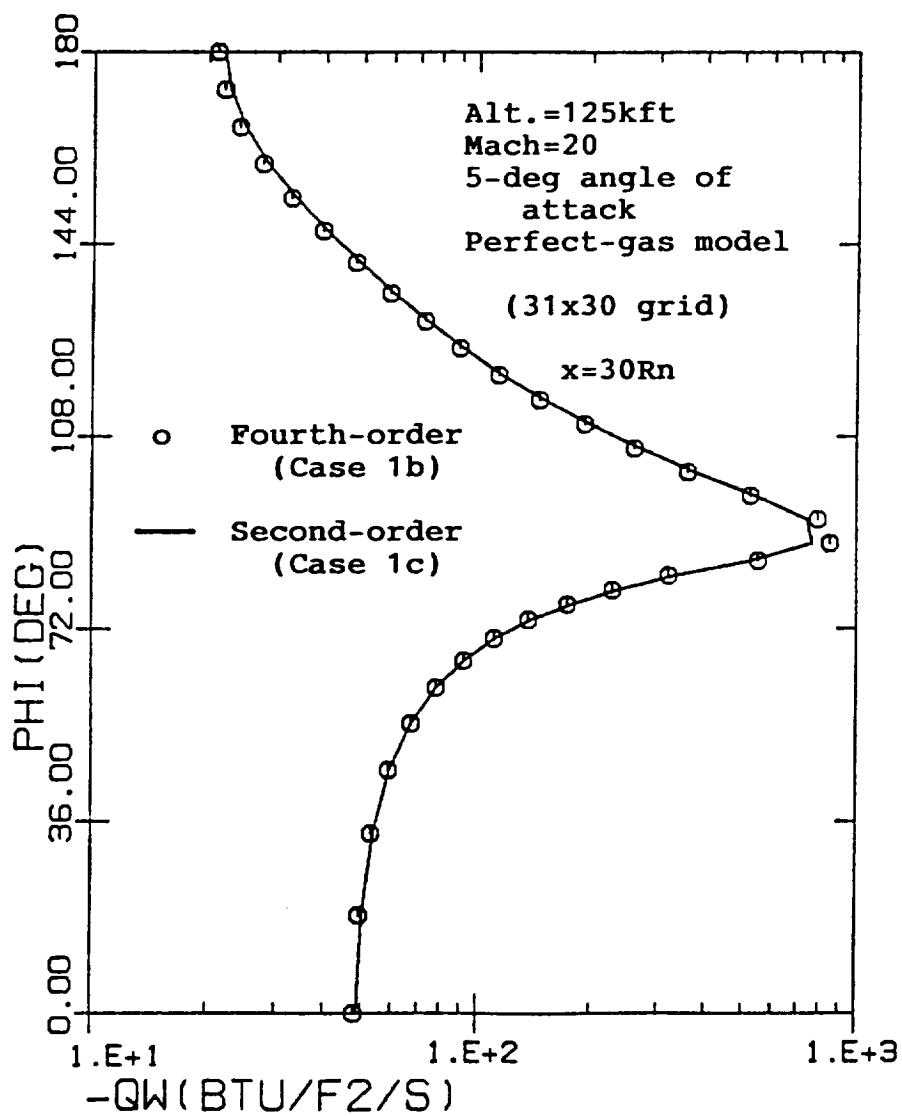
Fig. 47. Smoothing effects on the crossflow distribution of wall heat-transfer rates for Case 1
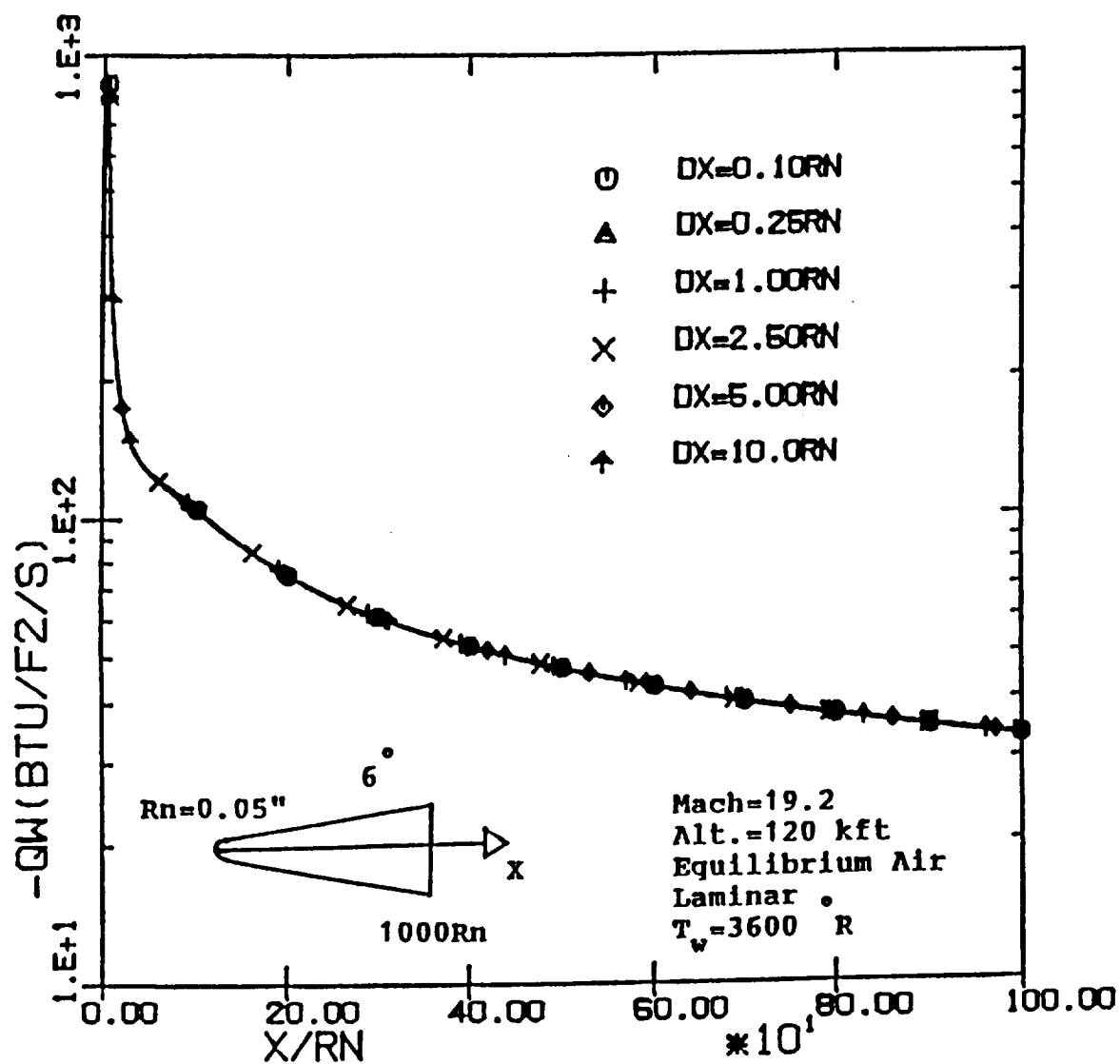
Fig. 48. Effects of axial step-size on wall heat-transfer rate for a 6-deg sphere-cone case
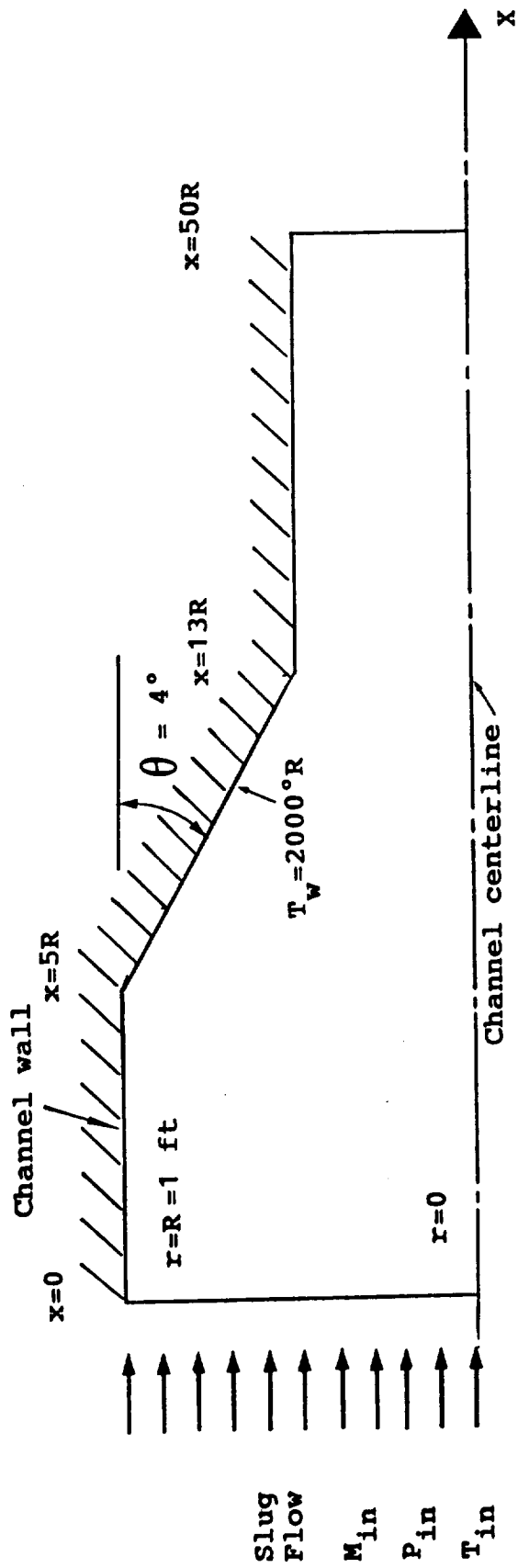
(Dimensions not to scale)

$M_{in}=6.7$, $P_{in}=142.2$ lbf/ft², $T_{in}=5332.89°R$

Fig. 49. Description of the inlet geometry for Case 4

180

2-D INLET FLOW :   MACH=6.7, R=1 FT, 4° COMPRESSION, REYNOLDS NO.=...

PINF=142.2 PSF, TINF=5332.89°R, TWALL=2000°R

Inviscid

Perfect-gas 3.2

2.97

4°

1.78

2.0

1.05

(P/PINF)

1.05

1.10

x=0.11R

x=15.77R

r=+R

r=0

r=-R

Equilibrium-air 3.2

Perfect-gas 3.2

2.0

1.9

2.0

1.1

1.05

1.1

1.05

1.1

Nonequilibrium-air 3.1

Perfect-gas 3.2

2.0

1.85

2.0

1.05

1.05

1.0

1.1

1.05

1.0
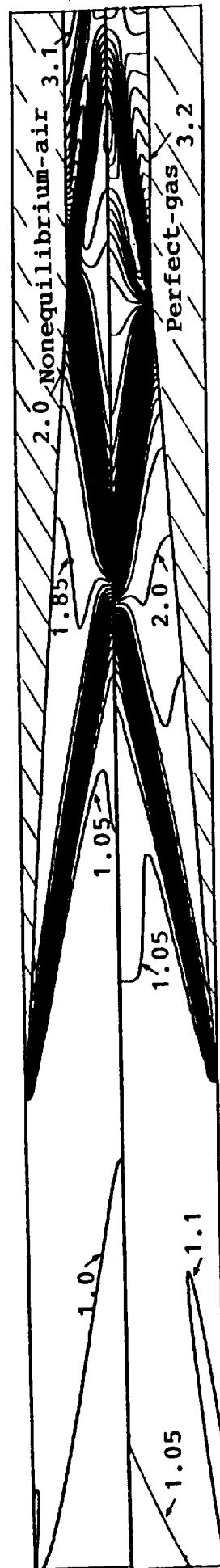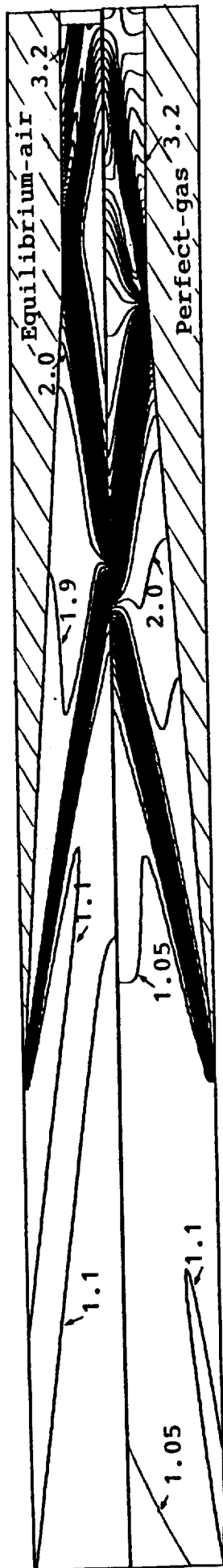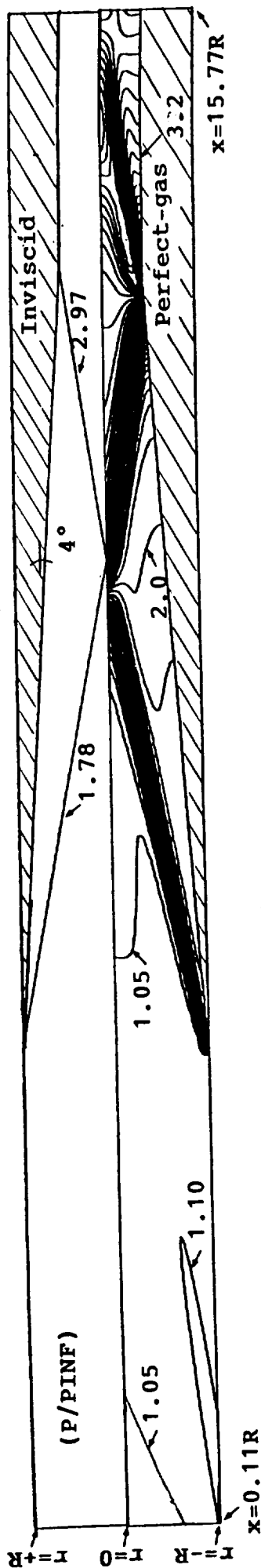
Fig. 50. Pressure contours for Case 4 calculations from x = 0.11 R to x = 15.77 R

181

C-3

2-D INLET FLOW : MACH=6.7, R=1 FT, 4° COMRESSION, REYNOLDS NO.=2.33x10^5/FT
PINF=142.2 PSF, TINF=5332.89°R, TWALL=2000°R
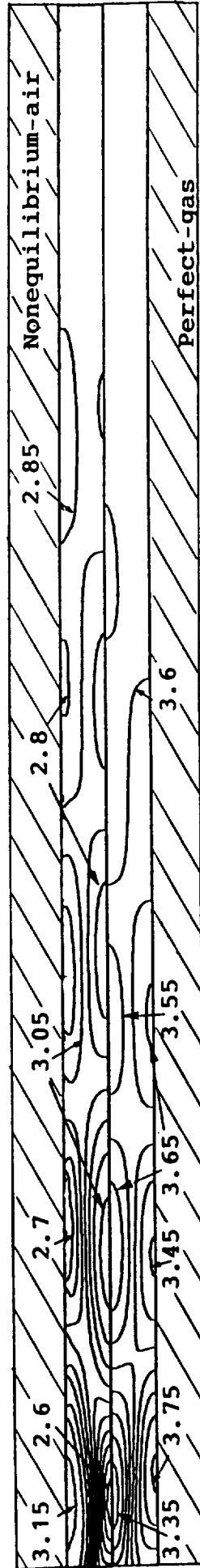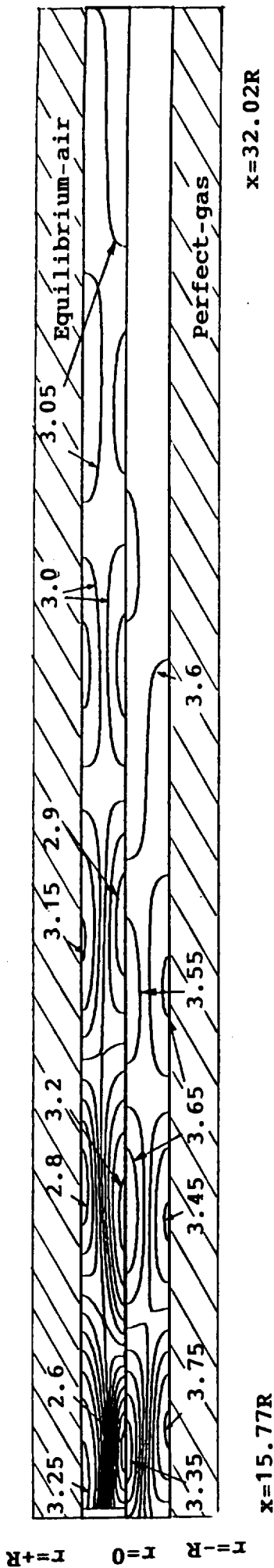
Fig. 51. Pressure contours for Case 4 calculations from x = 15.77 R to x = 32.02 R

182

2-D INLET FLOW : MACH=6.7, R=1 FT, 4° COMPRESSION, REYNOLDS NO.=2.33x10^5/FT
PINF=142.2 PSF, TINF=5332.89°R, TWALL=2000°R
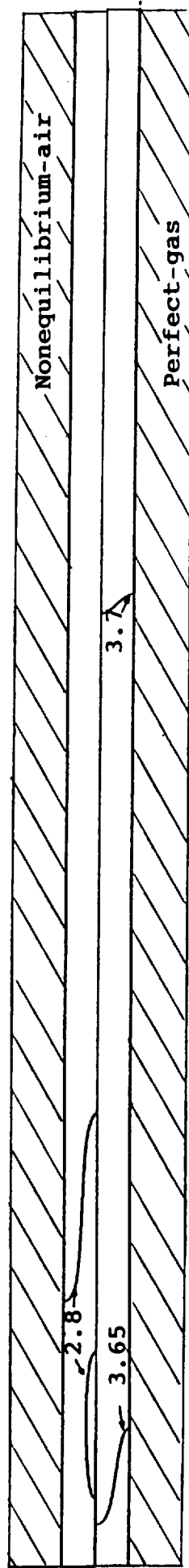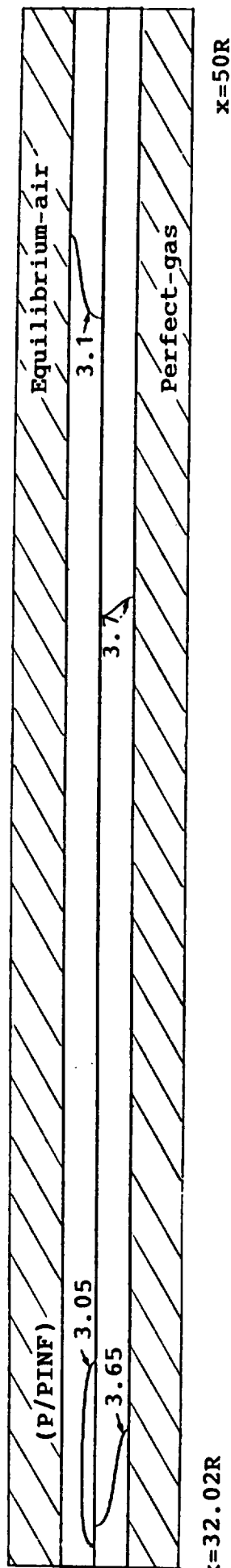
Fig. 52. Pressure contours for Case 4 calculations from x = 32.02 R to x = 50.0 R

183
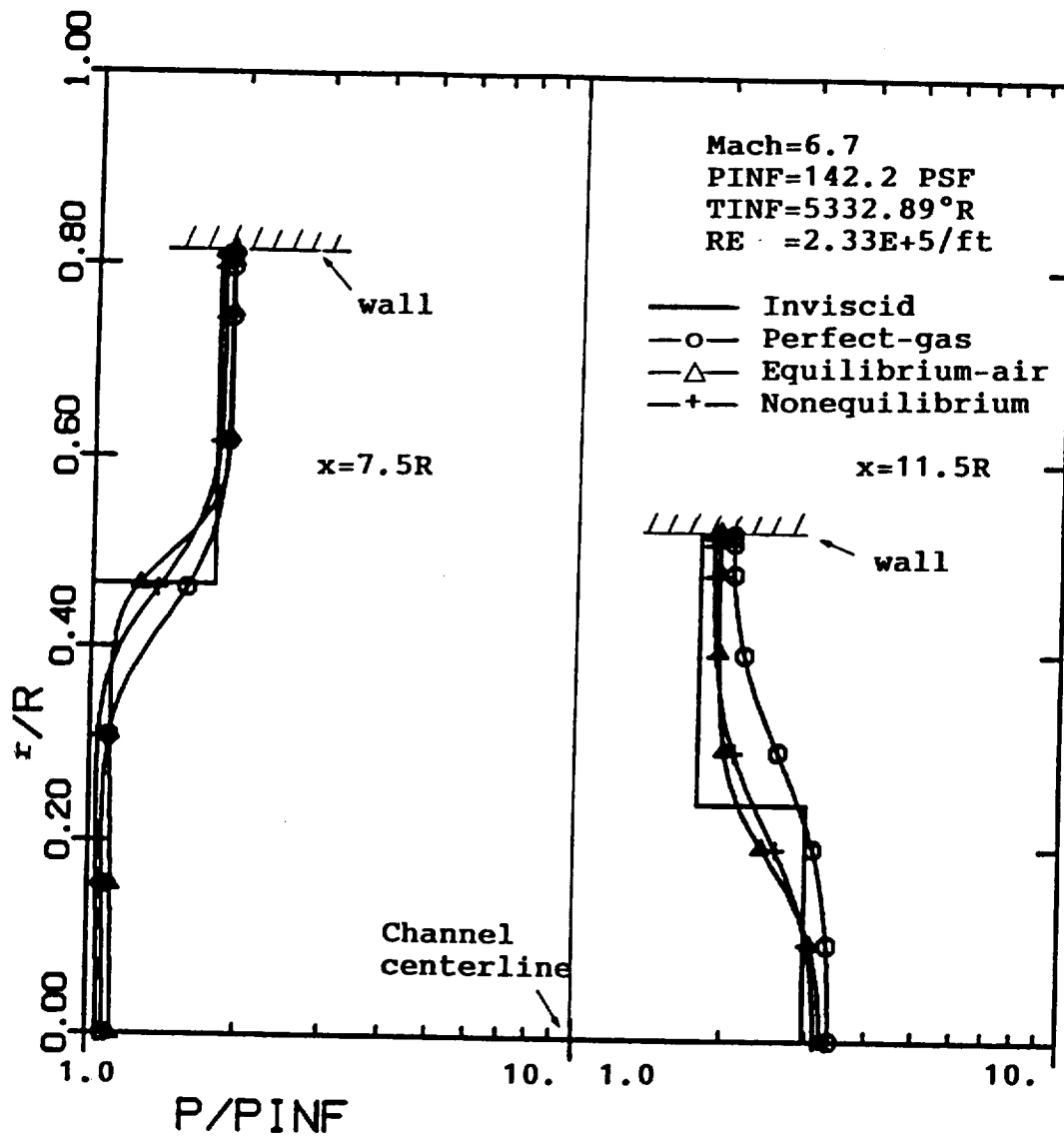
Fig. 53. Pressure profiles for Case 4 calculations
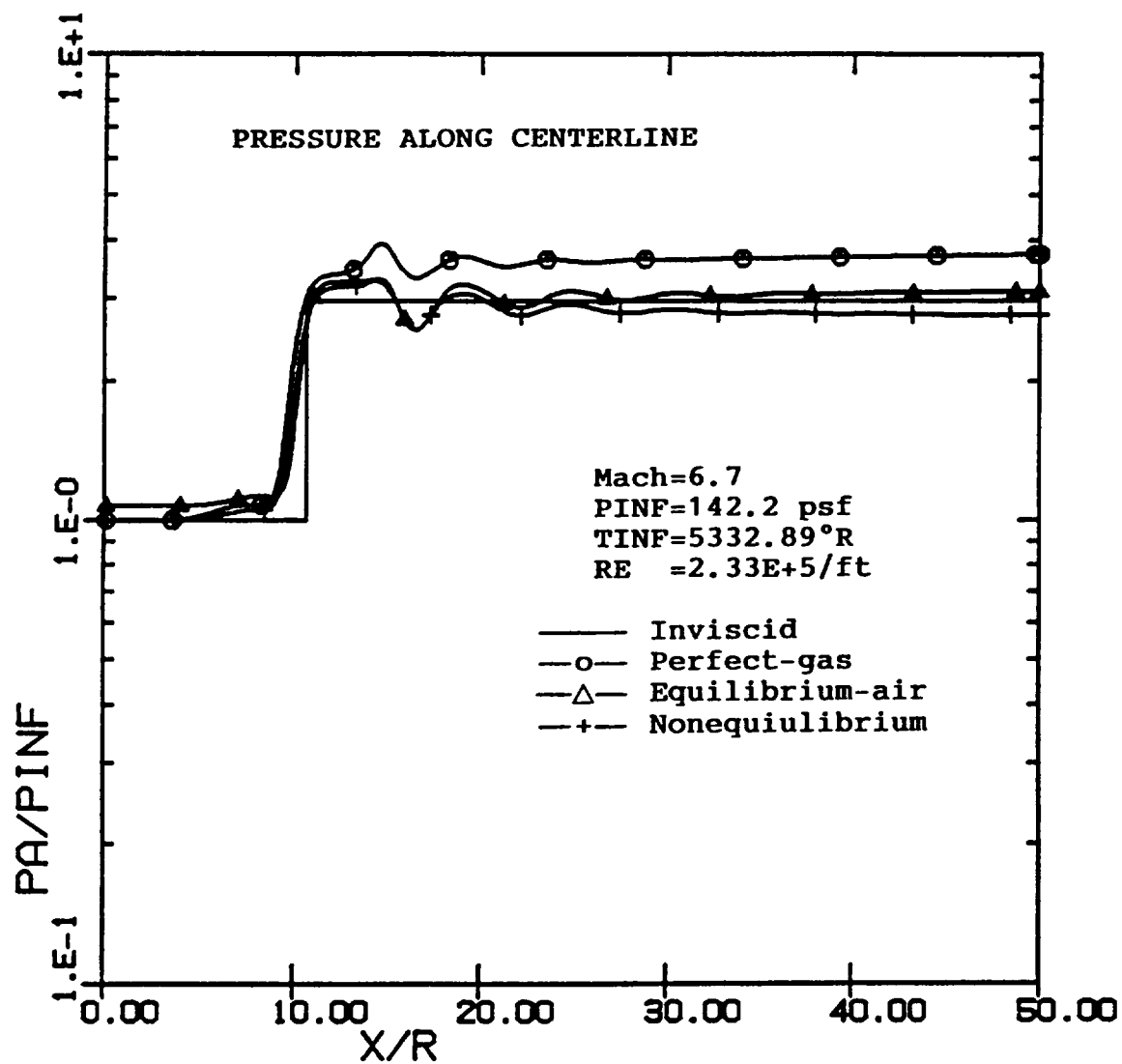
Fig. 54. Pressure distribution along the channel axis for Case 4
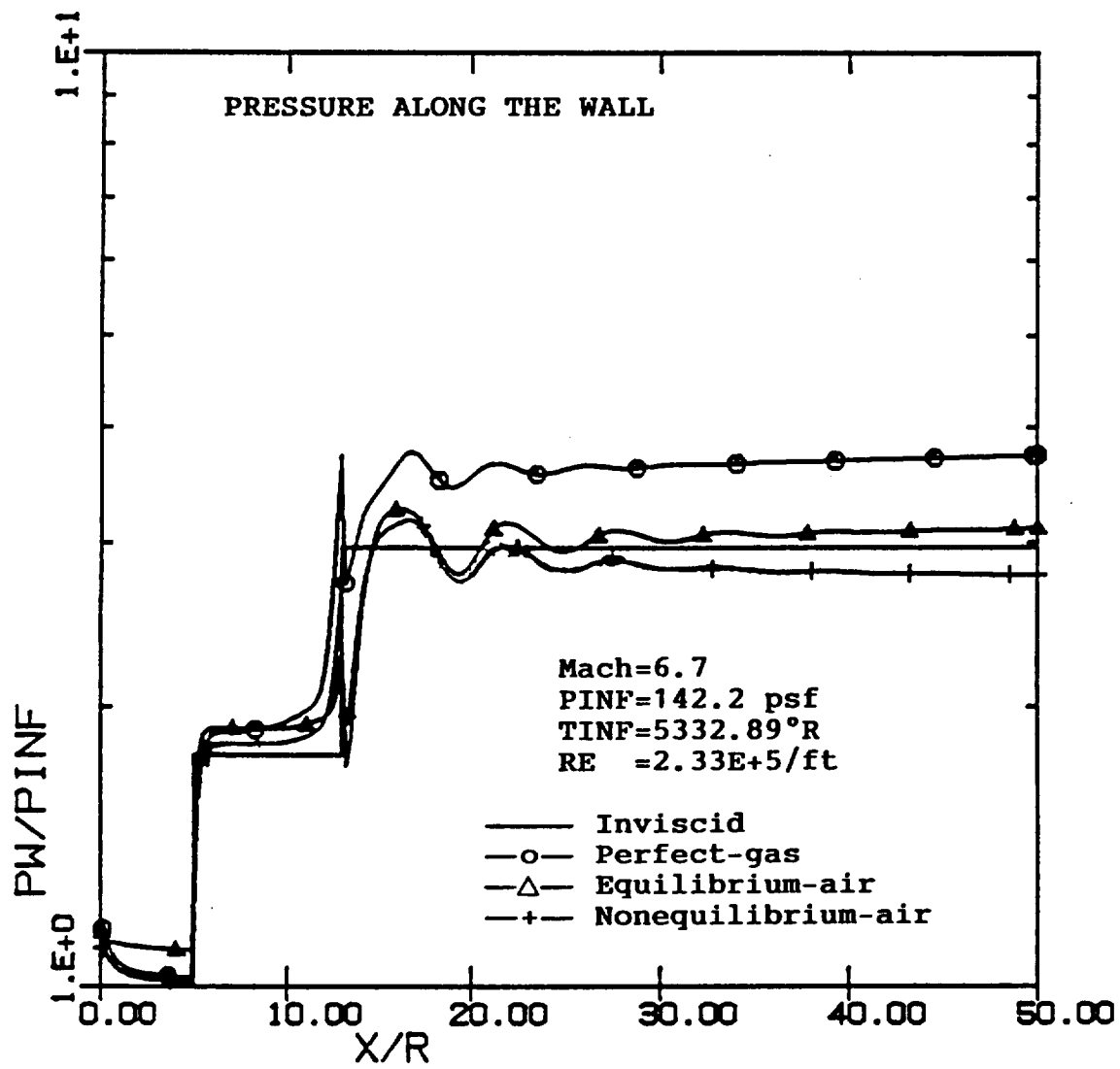
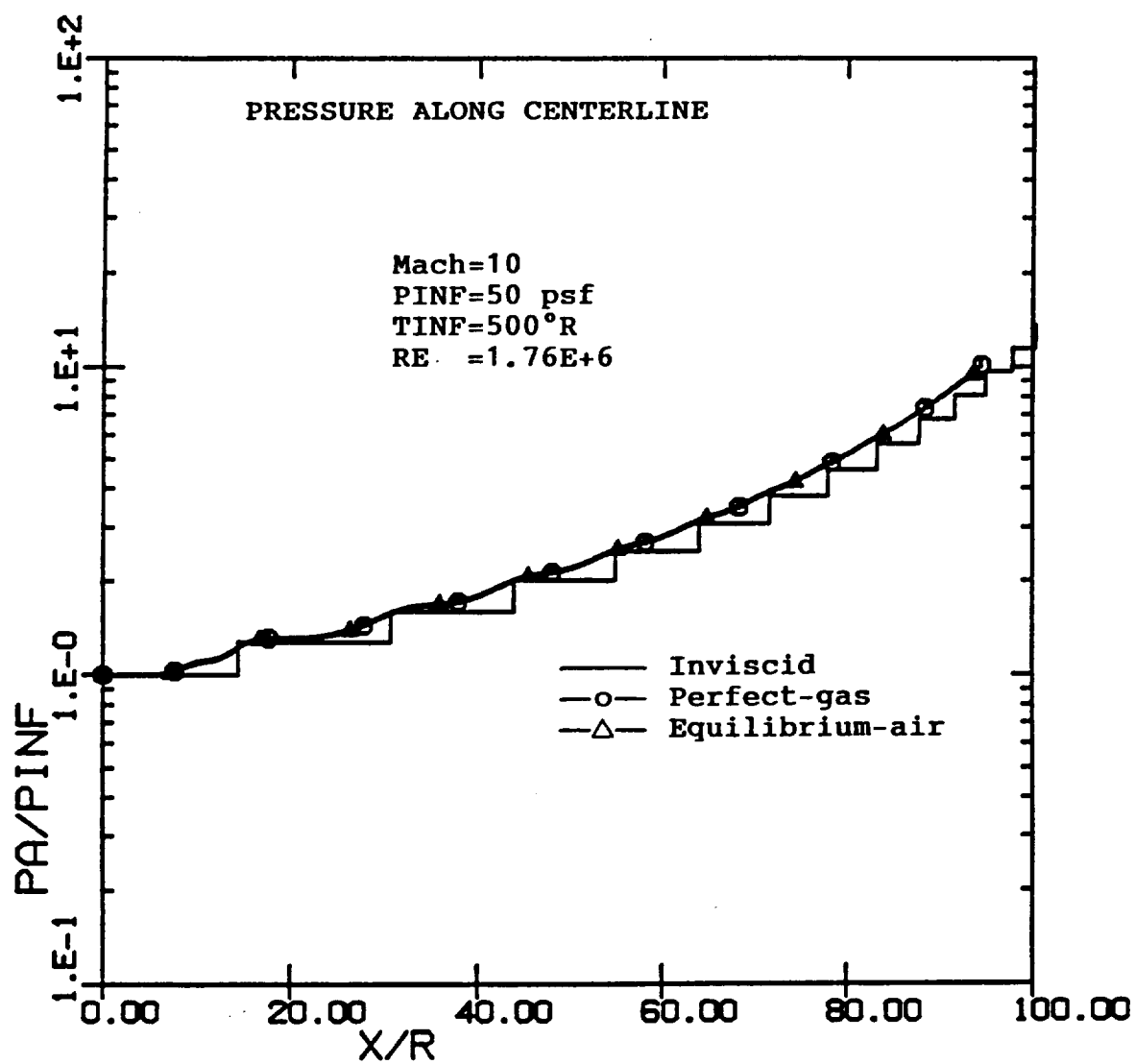Fig. 55. Pressure distribution along the channel wall for Case 4
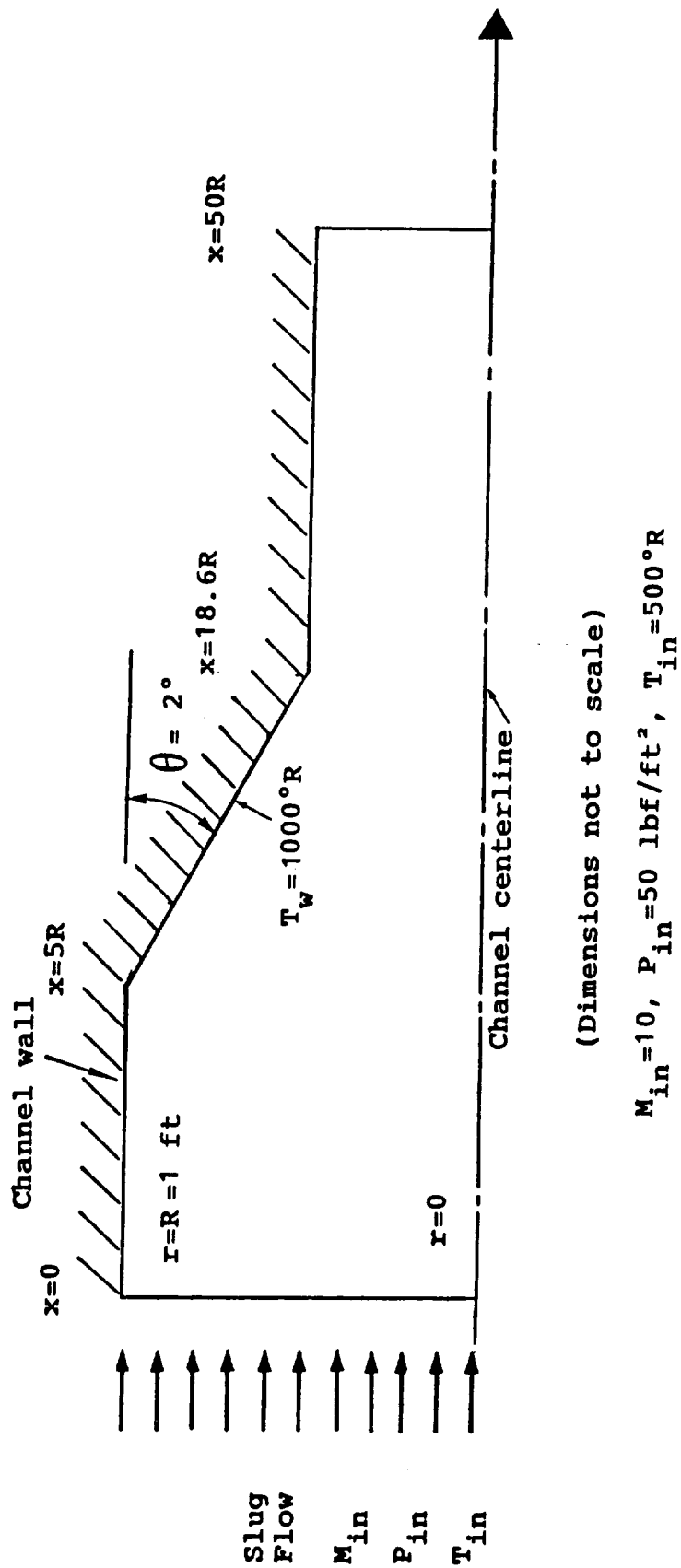
Fig. 56. Description of the inlet geometry for Case 5

Channel wall

x=0

x=5R

x=18.6R

x=50R

$\theta = 2°$

r=R =1 ft

$T_w = 1000°R$

Channel centerline

r=0

Slug
Flow

M_{in}

P_{in}

T_{in}

(Dimensions not to scale)

$M_{in} = 10$, $P_{in} = 50$ lbf/ft^2, $T_{in} = 500°R$

187
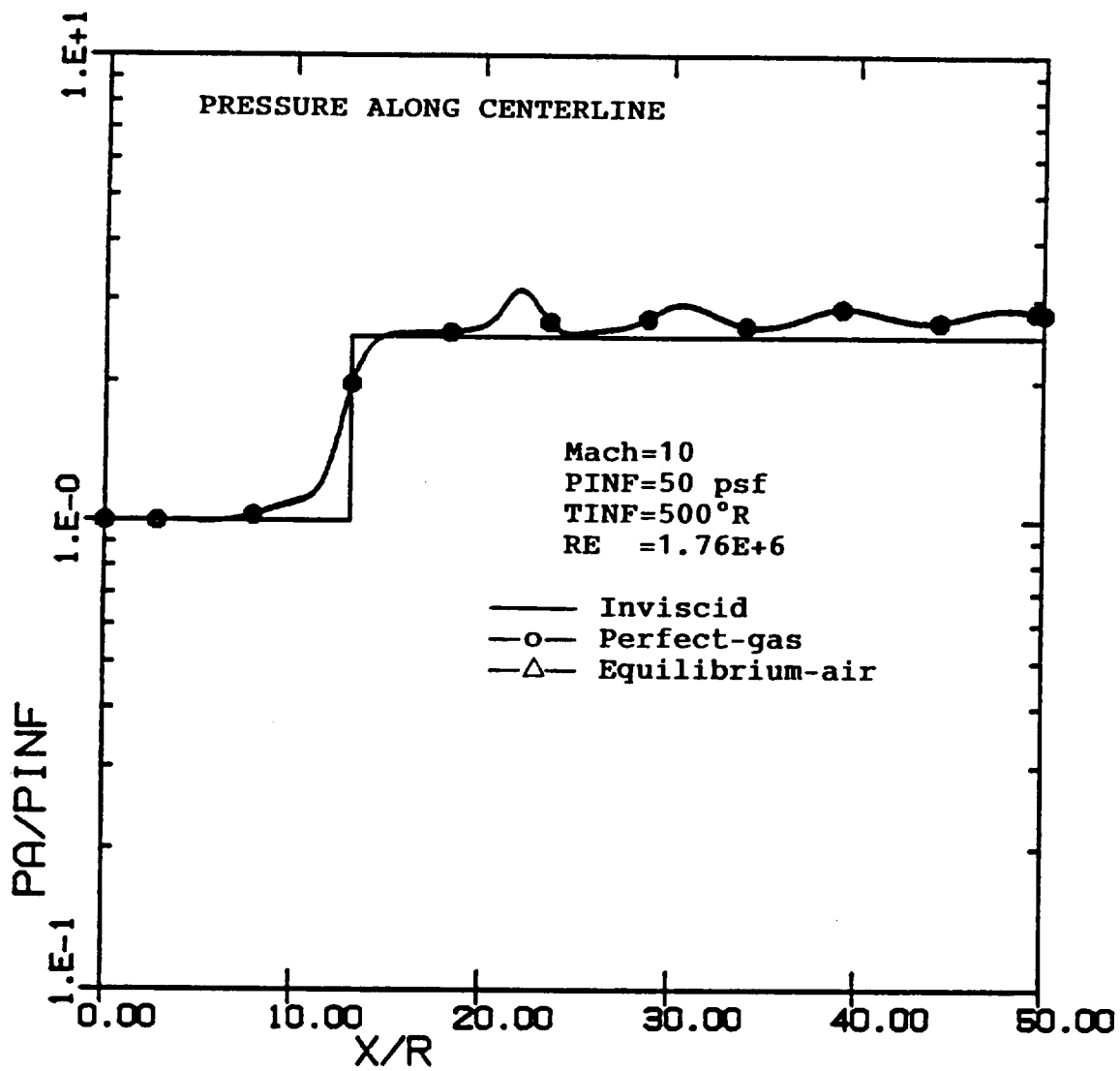
Fig. 57. Pressure distribution along the channel axis for Case 5
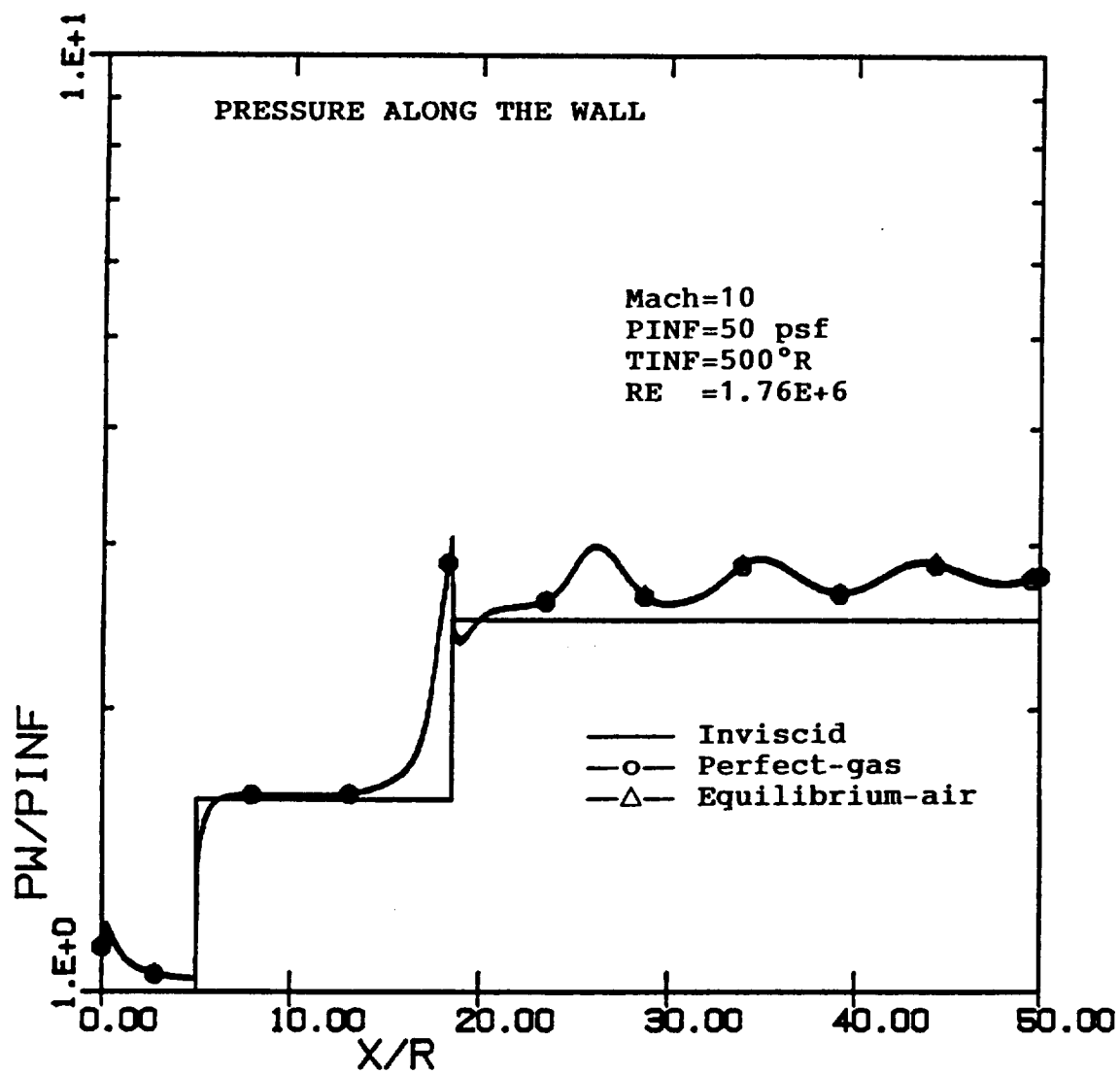
Fig. 58. Pressure distribution along the channel wall for Case 5

Fig. 59. Description of the inlet geometry for Case 6

Fig. 60. Pressure distribution along the channel axis for Case 6

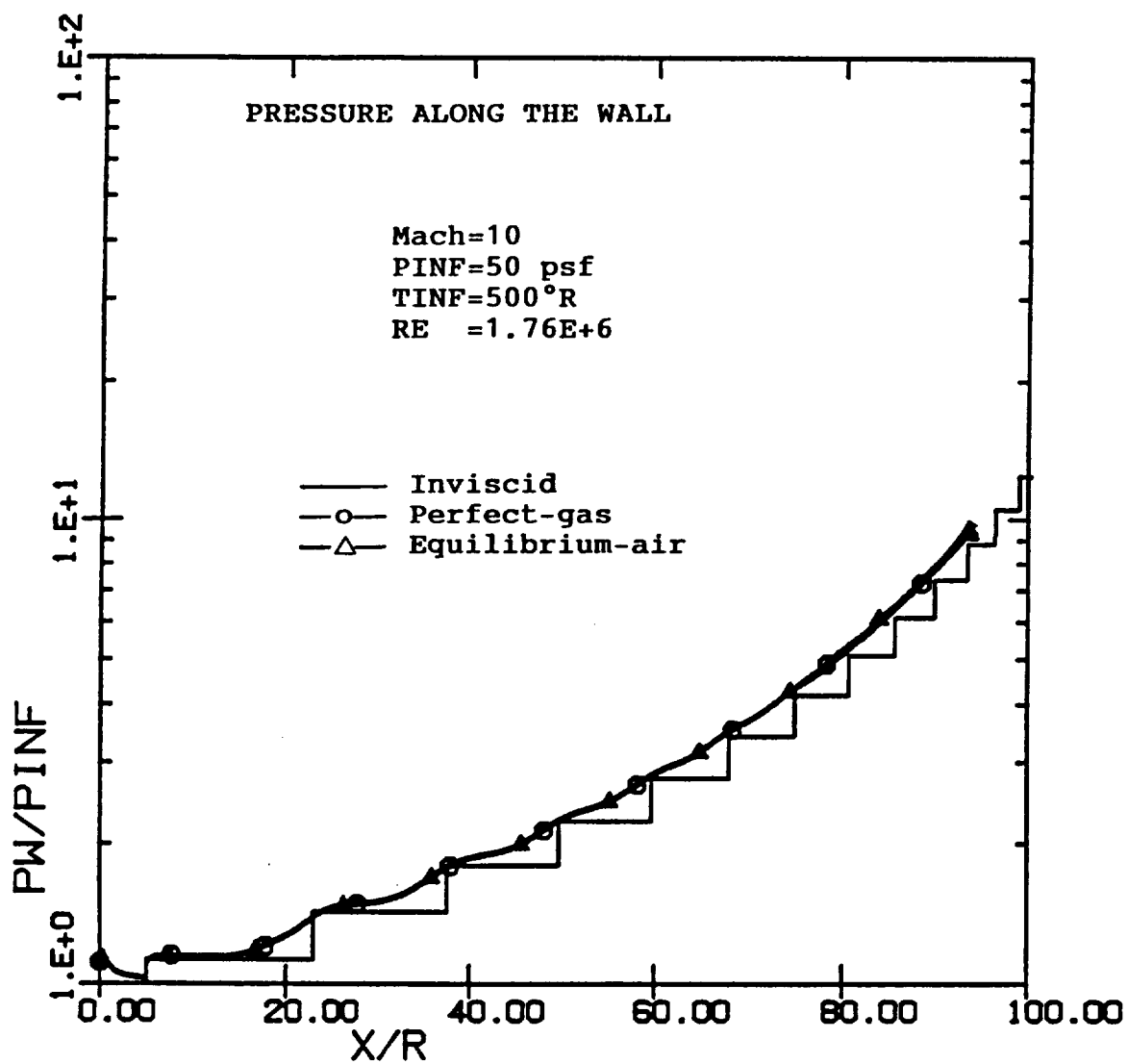Fig. 61. Pressure distribution along the channel wall for Case 6

ACKNOWLEDGEMENT